Multiscale Modeling and Simulation of Erosive Wear in Pelton Turbines

Thèse N° 7115

Présentée le 7 juin 2019

à la Faculté des sciences et techniques de l'ingénieur
Laboratoire de machines hydrauliques
Programme doctoral en énergie

pour l'obtention du grade de Docteur ès Sciences

par

Sebastián Camilo LEGUIZAMÓN SARMIENTO

Acceptée sur proposition du jury

Prof. S. Haussener, présidente du jury
Prof. F. Avellan, directeur de thèse
Prof. G. V. Messa, rapporteur
Dr S. Fréchinet, rapporteur
Prof. J.-F. Molinari, rapporteur

2019

ÉCOLE POLYTECHNIQUE
FÉDÉRALE DE LAUSANNE

Nature uses only the longest threads to weave her patterns, so each small piece of her fabric reveals the organization of the entire tapestry.

—Richard Feynman

Acknowledgements

This thesis would not have been possible without the unconditional support of Prof. François Avellan, head of the Laboratory for Hydraulic Machines at EPFL, who gave me the exceptional opportunity to conduct my doctoral research under his supervision. In particular, I acknowledge the trust and freedom he gave me in addressing the research topic and the chance of presenting my work at numerous international conferences.

I am grateful to General Electric Renewable Energy for the technical assistance and financial support granted to the GPU-SPHEROS project within which this thesis is framed. I would like to thank Dr. Claire Ségoufin, Dr. Stéphane Fréchinet, Antoine Bombenger and Rajesh Panchal for their enthusiastic involvement and guidance. Their agreement to publish the thesis results on international journals and conference proceedings is delightedly acknowledged.

This work was supported by a grant from the Swiss National Supercomputing Centre (CSCS) under project ID s777, by the Swiss Commission for Technology and Innovation (CTI) with grant No. 17568.1 PFEN-IW, by the Swiss Competence Center for Energy Research - Supply of Electricity (SCCER-SoE), and by the Swiss Federal Office of Energy (SFOE) - Research Programme Hydropower with grant No. SI/501786-01. It goes without saying that these grants were instrumental to the successful completion of the investigation.

I would like to sincerely thank the jury members, Prof. Jean-François Molinari, Prof. Gianandrea Vittorio Messa and Dr. Stéphane Fréchinet for their valuable time spent in reviewing this thesis and for their insightful and encouraging comments during the oral exam, and the jury president, Prof. Sophia Haussener, for agreeing to preside over it.

My work at LMH would have been overwhelming had I not privileged from the assistance of the SPHEROS team members. I would like to thank Dr. Ebrahim Jahanbakhsh for countless answers regarding programming and mechanics, as well as his relentless bug hunting activities, Dr. Audrey Maertens for her sharp suggestions and for sharing her deep understanding of a variety of topics, Siamak Alimirzazadeh for his advice on GPU programming, Dr. Christian Vessaz for his help on handling the Hydraulic Turbomachines course, and Takashi Kumashiro for the productive scientific collaboration. I am grateful for a whole lot of things I learned from you all. I truly enjoyed the conferences, workshops and the summer school that we shared, as well as the detailed technical conversations we delved into.

Acknowledgements

I acknowledge the precious help I received from Charly Euzenat, Dr. Bastien Durand and Pierre Quillery from ENS Cachan as well as Alain Renaud, Sébastien Dutoit and Raymond Fazan from LMH during the preparation and execution of the split-Hopkinson bar experimental campaign. I also thank Dr. Philippe Cerrutti for the technical support and Isabelle Stoudmann for the administrative assistance and for her everlasting cheerfulness.

I would like to thank the doctoral students with whom I shared this experience: Siamak Alimirzazadeh for his peculiar points of view and overall kindness, João Gomes Pereira for always trying to bring us together, Dr. João Gomes Borga for sharing his informed opinions and love of books, Dr. Outi Supponen for her endless laughter and tenacious optimism, Dr. Elena Vagnoni for her fun stories and delicious cooking, Dr. Keita Yamamoto for the conversations on photography and CFD, Dr. Simon Pasche for the shared interest in multiscale modeling, Ali Amini for stimulating short discussions on physical phenomena, and Alexis Papagiannopoulos for his subtle humor. I would also like to thank Dr. Pascal Clausen for thought-provoking dialogue and debate during lunch breaks, and Dr. Mohamed Farhat for the fascinating conversation topics at coffee breaks.

I am grateful to all the visiting students, engineers and interns, namely Takashi Kumashiro, Dr. Xiaoran Zhao, Dr. David Valentín, Mònica Egusquiza, Dr. Qin Wu, Dr. Ran Tao, Shahab Eghbali, Federico Martínez, Sayaka Kamata, Masashi Sakamoto, Dara Vahidi, Armand Sibier, Huaiyu Cheng and Prof. Yuchuan Wang for invaluable cultural exchanges and lively conversations during these four long years. I would also like to thank the preceding generation of doctoral students and postdocs, Dr. Andres Müller, Dr. Arthur Favrel, Dr. Christian Landry, Dr. Christian Vessaz, Dr. Matthieu Dreyer, Dr. Loïc Andolfatto and Dr. Philippe Kobel for the traditions and dynamic atmosphere they kindled within the lab.

My warmest gratitude to my friends outside the lab: Bharath Narayanan and Sandra Siby for lovely dinners and engaging conversations, Heather Chan for the delightful music recording sessions and cooking afternoons, et Eva Benzo pour sa chaleureuse hospitalité. Agradezco a Catalina Villabona por años de amistad y soporte a pesar de la distancia, a Juan Sebastián Ochoa y Diego Mariño por innumerables conversaciones sobre política, economía y religión, y por compartir conmigo esa pasión por la mecánica, y a Juan José Umaña, Juan Santiago García y Nicolás Williamson por fomentar mi curiosidad por temas tan diversos.

Quisiera agradecer muy especialmente a mi mamá Verónica, a mi papá Camilo, a mi abuelita Mariela, a mi hermano Juan Pablo y a mi tío Carlos por años de consejo, educación y amor incondicional; ésta tesis no hubiera sido posible sin su apoyo invariable, lleno de esfuerzos que reconozco agradecido.

Por último, agradezco a mi esposa Ginna por tanto cariño, consentimiento, comprensión, tantísima enseñanza y amor en este corto tiempo. Gracias por compartir tu vida conmigo.

Lausanne, May 22, 2019 Sebastián

Abstract

Hydropower has been identified as a key technology to mitigate climate change due to its very low lifecycle greenhouse gas emission intensity and its capacity to integrate intermittent renewable energy sources such as wind and solar into the electrical grid. One of the problems that limits a wider adoption of hydropower is the erosive wear that hydraulic turbines are subject to when operated under sediment-laden water; it entails efficiency degradation, outage for expensive repairs and an augmented risk of cavitation. This problem is bound to become increasingly important due to the expected deployment of hydropower on young geological formations such as the Himalayas and the Andes, and the increased sediment yield caused by retreating glaciers around the globe.

The technical capacity to predict the erosion process of prototype-scale machines is instrumental to the optimization of the runner designs and the operation strategies of hydroelectric plants. However, this technical capacity is lacking: neither laboratory experiments nor traditional numerical simulations are capable of delivering quantitative predictions. Whereas the reduced-scale experimental results are not transposable to prototype-scale due to an inherent non-similarity regarding the erosion conditions, traditional numerical models rely on uncertain erosion correlations that decidedly compromise their accuracy.

The difficulty of simulating the erosion process is explained by its multiscale character: it is a very gradual modification of large surfaces, yet it is the consequence of trillions of ephemeral impacts by microscopic sediments. Traditional numerical models confront this problem by neglecting the simulation of the sediment impacts altogether, instead settling for the use of erosion correlations that define the amount of mass removed by any given impact, but sacrificing accuracy and transferability in the process. This thesis presents a novel multiscale model of erosion that bypasses the need for erosion correlations by explicitly simulating the sediment impacts, without sacrificing the scope to simulate the long-term erosion process of an industrial-scale component. The proposed model is composed of two sequentially coupled submodels: the microscale model describes the particle impacts with all the detail required to accurately capture the high strain rate thermomechanical process involved; the macroscale model describes the turbulent sediment transport and the accumulation of erosion on the domain of interest. A projective integration scheme is used together with the multiscale model to simulate the long-term transformation of the surface and its effects on the hydrodynamics and subsequently on the erosion rate.

Abstract

After introducing the model formulation, a detailed discussion of the simplifications inherent to the multiscale approach and the modeling assumptions is presented. The finite volume particle method used to discretize the governing equations is introduced next, followed by the experimental characterization of the runner material, *i.e.* model parameter identification.

Four case studies are used to assess, verify and validate the proposed multiscale model. The first case study deals with the erosion of a flat plate by an impinging jet; convergence, parametric and sensitivity analyses of the microscale and macroscale models are presented, as well as a first satisfactory validation. The second case study demonstrates the use of projective integration to predict the long-term surface transformation of a 2D bucket and its effects on the outlet angle and reaction force; a feedback whereby the surface alteration increases the erosion rate is evidenced. The third case study deals with the erosion of a static prototype-scale Pelton bucket whereas the fourth case study involves a rotating prototype-scale Pelton runner; satisfactory validations of the erosion distribution results are presented for both cases.

The results obtained, namely quantitative predictions of the erosion of industrial-scale components, have no precedent in the literature. Furthermore, the model is shown to provide physically sound descriptions of the underlying impact condition distributions that explain the erosion distributions obtained. Overall, it can be said that the multiscale model is a significant improvement over the state-of-the-art models in regard to accuracy and transferability.

Keywords: multiscale modeling, erosion, wear, hydraulic turbine, Pelton turbine, numerical simulation, particle-based method, finite volume particle method, projective integration

Résumé

L'hydroélectricité a été identifiée comme une technologie clé pour atténuer les changements climatiques en raison de ses faibles émissions de gaz à effet de serre sur son cycle de vie et de sa capacité à intégrer des sources d'énergie renouvelable intermittentes telles que l'éolienne ou la solaire dans le réseau électrique. L'un des problèmes qui limite une adoption plus large de l'énergie hydroélectrique est l'érosion à laquelle sont soumises les turbines hydrauliques lorsqu'elles fonctionnent dans des eaux chargées de sédiments ; cela implique une dégradation du rendement, des interruptions pour des réparations coûteuses et un risque accru de cavitation. Ce problème deviendra de plus en plus important en raison du déploiement prévu de l'hydroélectricité sur de jeunes formations géologiques telles que l'Himalaya et les Andes, ainsi que de l'augmentation de la production de sédiments provoquée par le recul des glaciers partout dans le monde.

La capacité technique permettant de prévoir le processus d'érosion des machines à l'échelle du prototype est déterminante pour l'optimisation de la conception des roues et des stratégies d'opération des centrales hydroélectriques. Cependant, cette capacité technique fait défaut : ni les expériences de laboratoire ni les simulations numériques traditionnelles ne sont en mesure de fournir des prévisions quantitatives. Alors que les résultats expérimentaux à échelle réduite ne sont pas transposables à l'échelle du prototype en raison d'une absence inhérente de similitude concernant les conditions d'érosion, les modèles numériques traditionnels s'appuient sur des corrélations d'érosion incertaines qui compromettent considérablement leur précision.

La difficulté à simuler le processus d'érosion s'explique par son caractère multi-échelles : il s'agit d'une modification très progressive de vastes surfaces, alors que c'est la conséquence de trillions d'impacts éphémères par des sédiments microscopiques. Les modèles numériques traditionnels résolvent ce problème en négligeant complètement la simulation des impacts des sédiments, se contentant de l'utilisation de corrélations d'érosion qui définissent la quantité de masse enlevée par un impact donné, mais en sacrifiant la précision et la transférabilité. Cette thèse présente un modèle d'érosion novateur multi-échelles qui contourne le besoin de corrélations d'érosion en simulant explicitement les impacts des sédiments, sans sacrifier la portée pour simuler le processus d'érosion à long terme d'un composant à l'échelle industrielle. Le modèle proposé est composé de deux sous-modèles couplés séquentiellement : le modèle à l'échelle microscopique décrit les impacts des particules avec tout le détail nécessaire pour

capturer avec précision le processus thermomécanique de vitesse de déformation élevée qui est impliqué ; le modèle à l'échelle macroscopique décrit le transport turbulent des sédiments et l'accumulation de l'érosion sur le domaine concerné. Un schéma d'intégration projective est utilisé avec le modèle multi-échelles pour simuler la transformation de la surface à long terme et ses effets sur l'hydrodynamique et, par conséquent, sur le taux d'érosion.

Après l'introduction de la formulation du modèle, une discussion détaillée des simplifications inhérentes à l'approche multi-échelles et des hypothèses de modélisation est présentée. La méthode des volumes particulaires finis, utilisée pour discrétiser les équations gouvernantes, est ensuite introduite, suivie de la caractérisation expérimentale du matériau des roues, c'est-à-dire de l'identification des paramètres du modèle.

Quatre études de cas sont utilisées pour évaluer, vérifier et valider le modèle multi-échelles proposé. La première étude de cas porte sur l'érosion d'une plaque plane par un jet incident ; des analyses de convergence, paramétriques et de sensibilité des modèles microscopique et macroscopique sont présentées ainsi qu'une première validation satisfaisante. La deuxième étude de cas démontre l'utilisation de l'intégration projective pour prédire la transformation superficielle à long terme d'un auget 2D et ses effets sur l'angle de sortie et la force de réaction ; un bouclage par lequel l'altération de la surface augmente le taux d'érosion est mise en évidence. La troisième étude de cas traite l'érosion d'un auget Pelton statique à l'échelle du prototype, tandis que la quatrième étude de cas porte sur une rue de turbine Pelton en rotation à l'échelle du prototype ; des validations satisfaisantes des distributions de l'érosion résultantes sont présentées pour les deux cas.

Les résultats obtenus, à savoir les prévisions quantitatives de l'érosion des composants à l'échelle industrielle, n'ont pas de précédent dans la littérature. En outre, il est montré que le modèle fournit des descriptions physiquement valables des distributions sous-jacentes des conditions d'impact qui expliquent les distributions d'érosion obtenues. Globalement, on peut dire que le modèle multi-échelles est une amélioration significative par rapport aux modèles de pointe existants en termes de précision et de transférabilité.

Mots-clés : modélisation multi-échelles, érosion, usure, turbine hydraulique, turbine Pelton, simulation numérique, méthode particulaire, méthode des volumes particulaires finis, intégration projective

Contents

List of Figures

List of Tables

Nomenclature

Latin Characters

A	Surface area	$[m^2]$
A_i	Johnson-Cook constitutive model parameters	[–]
a	Numerical speed of sound	$[m \cdot s^{-1}]$
a_b	Wave speed in split-Hopkinson pressure bars	$[m \cdot s^{-1}]$
a_g	Bulk speed of sound in the solid or sediment	$[m \cdot s^{-1}]$
$\boldsymbol{B}_i$	FVPM boundary interaction vector	[–]
B_2	Maximum internal width of a Pelton bucket	[m]
$\boldsymbol{b}$	Particle centroid	[m]
$\boldsymbol{C}$	Velocity vector	$[m \cdot s^{-1}]$
$\boldsymbol{C}_{r,f}$	Relative velocity vector between fluid and sediment	$[m \cdot s^{-1}]$
$\boldsymbol{C}_{r,m}$	Relative velocity vector between sediment and solid	$[m \cdot s^{-1}]$
$\boldsymbol{C}_{r,w}$	Relative velocity vector between fluid and wall	$[m \cdot s^{-1}]$
C_1	Absolute jet velocity	$[m \cdot s^{-1}]$
$C_{1\epsilon}$	Turbulence model parameter	[–]
$C_{2\epsilon}$	Turbulence model parameter	[–]
C_k	Menter's turbulence production limiter clip factor	[–]
C_μ	Turbulence model parameter	[–]
C_τ	Shear velocity	$[m \cdot s^{-1}]$
$C_\circ$	Reference velocity	$[m \cdot s^{-1}]$
c_d	Drag coefficient	[–]
c_p	Specific heat capacity	$[J \cdot kg^{-1} \cdot K^{-1}]$
c_v	Sediment concentration by volume	[–]
c_w	Sediment concentration by weight	[–]
D_0	Jet diameter	[m]
D_1	Pitch diameter of a Pelton runner	[m]
D_b	Split-Hopkinson bar diameter	[m]
D_i	Johnson-Cook damage model parameters	[–]
d	Sediment diameter	[μm]
d_x	Sediment diameter below which x % of the cumulative mass lies	[μm]
E	Specific energy $E = gH$	$[J \cdot kg^{-1}]$
E_e	Young's elasticity modulus	[Pa]
E_k	Wall function empirical constant	[–]

$\dot{e}$	Erosion rate	$[g \cdot h^{-1}]$
e_d	Erosion depth	[mm]
e_r	Erosion ratio	$[mg \cdot kg^{-1}]$
$\boldsymbol{F}$	Vector of flux functions	[–]
F_1	Near-wall drag correction factor	[–]
$\boldsymbol{f}$	Volumetric and surface forces per unit volume	$[N \cdot m^{-3}]$
f_r	Radial return factor	[–]
$\boldsymbol{G}$	Random vector drawn from a Gaussian distribution	[–]
G_e	Shear modulus	[Pa]
G_i	Drag correlation sediment sphericity functions	[–]
g	Gravitational acceleration	$[m \cdot s^{-2}]$
H	Hydraulic head	[m]
HR	Hardness ratio between the sediment and the surface	[–]
HV	Vickers hardness number	$[kgf \cdot mm^{-2}]$
h	FVPM particle radius	[m]
$\boldsymbol{I}$	Identity tensor	[–]
J_s	Sediment flux	$[kg \cdot m^{-2} \cdot s^{-1}]$
J^*	Finite Reynolds number correction to the shear lift force	[–]
K	Von Kármán constant	[–]
K_e	Bulk modulus	[Pa]
k	Turbulence kinetic energy	$[m^2 \cdot s^{-2}]$
k_c	Penetration penalty contact model parameter	[–]
k_f	Friction force parameter defining the static-dynamic transition	[–]
L	Length	[m]
m	Mass	[kg]
m_σ	Johnson-Cook constitutive model thermal softening exponent	[–]
N	Number of FVPM particles	[–]
$\boldsymbol{n}$	Normal unit vector	[–]
n	Normal distance from the wall	[m]
n_v	Sediment impact velocity exponent	[–]
n_σ	Johnson-Cook constitutive model strain hardening exponent	[–]
P_k	Production rate of turbulence kinetic energy	$[kg \cdot m^{-1} \cdot s^{-3}]$
p	Pressure	[Pa]
p_c	Interparticle penetration	[m]
p_γ	Equation of state pressure	[Pa]
Q	Discharge	$[m^3 \cdot s^{-1}]$
$\dot{q}$	Heat sources and sinks per unit volume	$[W \cdot m^{-3}]$
$\dot{q}_p$	Thermoplastic heating per unit volume	$[W \cdot m^{-3}]$
$\dot{q}_f$	Frictional heating per unit volume	$[W \cdot m^{-3}]$
$RC_\parallel$	Parallel restitution coefficient	[–]
$RC_\perp$	Perpendicular restitution coefficient	[–]
r_d	Threshold distance above which additional damping is applied	[m]

r_s	FVPM discretization resolution	[–]
$\boldsymbol{S}$	Strain rate tensor	[s^{-1}]
$\boldsymbol{S}_l$	Surface vector of subsurface l	[m^2]
S	Linear Hugoniot slope coefficient	[–]
$\boldsymbol{s}$	Deviatoric part of the Cauchy stress tensor	[Pa]
$\hat{\boldsymbol{s}}$	Deviatoric part of the trail Cauchy stress tensor	[Pa]
T	Temperature	[K]
T_h	Homologous temperature	[K]
T_m	Melting temperature	[K]
$T_\circ$	Reference temperature	[K]
$\boldsymbol{U}$	Vector of conserved variables	[–]
U	Peripheral velocity of the runner	[$m \cdot s^{-1}$]
V	Volume	[m^3]
v	Sediment impact velocity	[$m \cdot s^{-1}$]
W	Relative velocity between the jet and the bucket	[$m \cdot s^{-1}$]
W_i	FVPM kernel	[–]
$\boldsymbol{x}$	Particle position	[m]
y^+	Dimensionless normal distance from the wall	[–]
z_0	Number of jets	[–]
z_b	Number of buckets	[–]

Greek Characters

α	Sediment impact angle	[°]
α_s	Auxiliary variable in the drag correlation anisotropy function	[–]
β	Contact angle between wall particle and sediment	[°]
β_p	Inelastic heat fraction	[–]
β_w	Reference angle between wall particles	[°]
γ	Tait equation of state material parameter	[–]
$\gamma_\circ$	Grüneisen equation of state material parameter	[–]
ΔT^i	Inner integration time interval	[s]
ΔT^o	Outer integration time interval	[s]
Δt	Simulation time step	[s]
Δx	Reference particle spacing	[m]
δ	Solid model damage parameter	[–]
$\delta(\boldsymbol{x})$	Dirac's delta function	[–]
δ_d	Interpolation distance normal to the wall	[m]
δ_s	Normalized distance between the wall and the sediment surface	[–]
δ_t	Boundary layer thickness	[m]
$\boldsymbol{\varepsilon}$	Strain tensor	[–]
$\dot{\boldsymbol{\varepsilon}}$	Strain rate tensor	[s^{-1}]
ϵ	Dissipation rate of turbulence kinetic energy	[$m^2 \cdot s^{-3}$]
$\dot{\varepsilon}$	Equivalent strain rate	[s^{-1}]

ε_p	Plastic strain	[–]
η	Fraction of friction heat transferred to the solid	[–]
θ	Jet impingement angle	[°]
κ	Thermal conductivity	$[\mathrm{W \cdot m^{-1} \cdot K^{-1}}]$
λ	Particle velocity correction parameter	[–]
λ_R	Smoothing mass flux parameter	[–]
μ	Dynamic viscosity	$[\mathrm{Pa \cdot s}]$
μ_a	Artificial viscosity	$[\mathrm{Pa \cdot s}]$
μ_b	Bulk viscosity	$[\mathrm{Pa \cdot s}]$
μ_f	Friction coefficient	[–]
$\mu_{f,d}$	Dynamic friction coefficient	[–]
$\mu_{f,s}$	Static friction coefficient	[–]
μ_g	Relative density variation in the Grüneisen equation of state	[–]
μ_t	Turbulence viscosity	$[\mathrm{Pa \cdot s}]$
ν	Specific speed	[–]
ν_p	Poisson's ratio	[–]
ξ	Dimensionless strain rate	[–]
ρ	Density	$[\mathrm{kg \cdot m^{-3}}]$
$\rho_\circ$	Reference density	$[\mathrm{kg \cdot m^{-3}}]$
$\boldsymbol{\sigma}$	Cauchy stress tensor	[Pa]
$\overset{\triangle}{\boldsymbol{\sigma}}$	Jaumann objective rate of the Cauchy stress tensor	$[\mathrm{Pa \cdot s^{-1}}]$
σ	Surface tension	$[\mathrm{N \cdot m^{-1}}]$
σ_k	Turbulence model parameter	[–]
σ_v	Von Mises equivalent stress	[Pa]
σ_w	FVPM kernel summation	[–]
σ_y	Yield stress	[Pa]
σ_ϵ	Turbulence model parameter	[–]
$\boldsymbol{\tau}$	Viscous stress tensor	[Pa]
$\boldsymbol{\tau}_t$	Reynolds stress tensor	[Pa]
τ_s	Sediment relaxation time	[s]
τ_t	Turbulence time scale	[s]
τ_w	Wall shear stress magnitude	[Pa]
$\Phi(\boldsymbol{x})$	Gaussian weighting kernel	[–]
ϕ_{B_2}	Discharge coefficient	[–]
ϕ_s	Sediment shape parameter used in the microscale simulations	[–]
ϕ_d	Sediment sphericity used in the macroscale drag correlation	[–]
ψ	FVPM basis function	[–]
ψ_1	Energy coefficient	[–]
$\boldsymbol{\Omega}$	Vorticity tensor	$[\mathrm{s^{-1}}]$
Ω	Domain	[–]
$\boldsymbol{\omega}$	Material spin tensor	$[\mathrm{s^{-1}}]$
ω	Angular speed	$[\mathrm{rad \cdot s^{-1}}]$

Non-dimensional Numbers

Fr	Froude number	[–]
Re	Reynolds number	[–]
Ro	Rossby number	[–]
St	Stokes number	[–]
We	Weber number	[–]

Subscripts

e	Eroded
f	Related to the fluid
i	Related to a sediment impact
j	Related to the impinging jet
m	Related to the base material
p	Related to the flat plate
r	Relative
s	Related to the sediment
t	Related to the turbulent fluctuations
w	Related to the wall
$\parallel$	Related to the parallel direction
$\perp$	Related to the perpendicular direction
1	Before impact
2	After impact

Acronyms

CFD	Computational Fluid Dynamics
CFL	Courant-Friedrichs-Lewy
CSCS	Swiss National Supercomputing Centre
CSM	Computational Solid Mechanics
EPFL	École Polytechnique Fédérale de Lausanne
FEM	Finite Element Method
FVM	Finite Volume Method
FVPM	Finite Volume Particle Method
GPU	Graphics Processing Unit
LMH	Laboratory for Hydraulic Machines
MPI	Message Passing Interface
MSS	Martensitic Stainless Steel
SM	Streaming Multiprocessor
SPH	Smoothed Particle Hydrodynamics

Introduction Part I

The history of science is rich in the example of the fruitfulness of bringing two sets of techniques, two sets of ideas, developed in separate contexts for the pursuit of new truth, into touch with one another.

—Robert Oppenheimer

1 Problem Overview

1.1 Energy Context

The world is only now starting to face the consequences of decades of unrestrained emission of greenhouse gases. If left unattended, climate change might result catastrophic for life on the planet. Foreseeable effects include increased likelihood of extreme weather events such as droughts, hurricanes and floods, changes in precipitation patterns, sea level rise and disruptions of food supply chains [54]. In turn, these effects will increase the risk of regional conflicts and will imply massive migration due to food and water shortages.

In 2010, the energy supply sector accounts for 35 % of anthropogenic greenhouse gas emissions [23], making it the largest sector contributor to global emissions. Furthermore, the growth rate of the sector accelerated from 1.7 % per year from 1990-2000 to 3.1 % per year from 2000-2010. Figure 1.1 presents the composition of the energy supply sector emissions between 1970 and 2010. The supply of electricity and heat accounts for more than 70 % of the sector emissions in 2010.

A recent Intergovernmental Panel on Climate Change report [82] highlights that an immediate and significant response is required to limit the warming of the planet to 1.5 °C above pre-industrial levels. There is scientific consensus about the fact that above this threshold the effects of climate change will be significantly more expensive for humanity.

Even though there are many possible pathways to reduce emissions, each of which includes a wide portfolio of mitigation measures, the energy supply sector plays a preponderant role in all of them for a variety of reasons. Not only is it the largest sector as of today; it is also expected to increase its share in global emissions with the electrification of transportation that is already underway. Furthermore, contrary to other sector, there is a range of commercially available renewable energy technologies at present that have the capability of mitigating the greenhouse gas emissions of the sector, provided they are deployed extensively. Within the set of renewable energy technologies, hydropower plays a key role, instrumental for the integration of other renewable energy sources that are intermittent in nature.

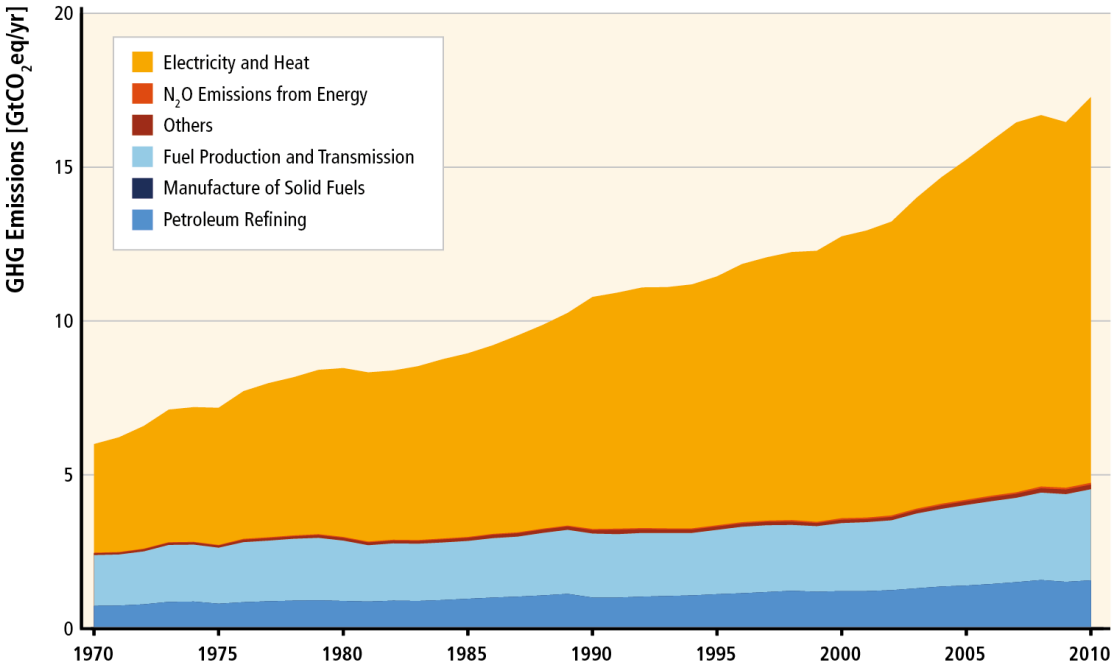

Figure 1.1 – Greenhouse gas emissions between 1970 and 2010, in CO_2 equivalent terms, for the energy supply sector and its subsectors [23].

1.1.1 The Role of Hydropower

With a total installed capacity of 1,114 GW as of 2017, hydropower accounts for 62 % of global renewable electricity production [167], as presented in Figure 1.2. However, non-renewable electricity accounts for 74 % of global electricity production, which explains the high greenhouse gas emissions the electricity supply subsector is responsible for. A rapid transition to 100 % renewable electricity is required to limit climate change and its associated risks; indeed, many nations have already set aggressive targets and policy to encourage the transition.

The extensive deployment of renewable energy technologies based on intermittent sources such as the sun and the wind is problematic. On the one hand, the electricity demand curve does not usually match the availability of the resource, *e.g.* the peak demand tends to occur in the evening when the sun is no longer shining. On the other hand, these resources are stochastic in nature, with unpredictable high-frequency variations. These two circumstances highlight the urgent need for electricity storage solutions for a successful integration of the fastest-growing renewable electricity technologies, *i.e.* wind and solar.

Pumped storage, which consists in storing energy by pumping water to a higher altitude, accounts for 96 % of the global energy storage capacity, with a total of 153 GW installed as of 2017 [167]. The high capacity of reservoirs and fast response time of the hydraulic turbomachines renders this solution very attractive, together with its round-trip efficiency of 75-85 % and low cost. Recent research efforts, such as the HYPERBOLE European project [45],

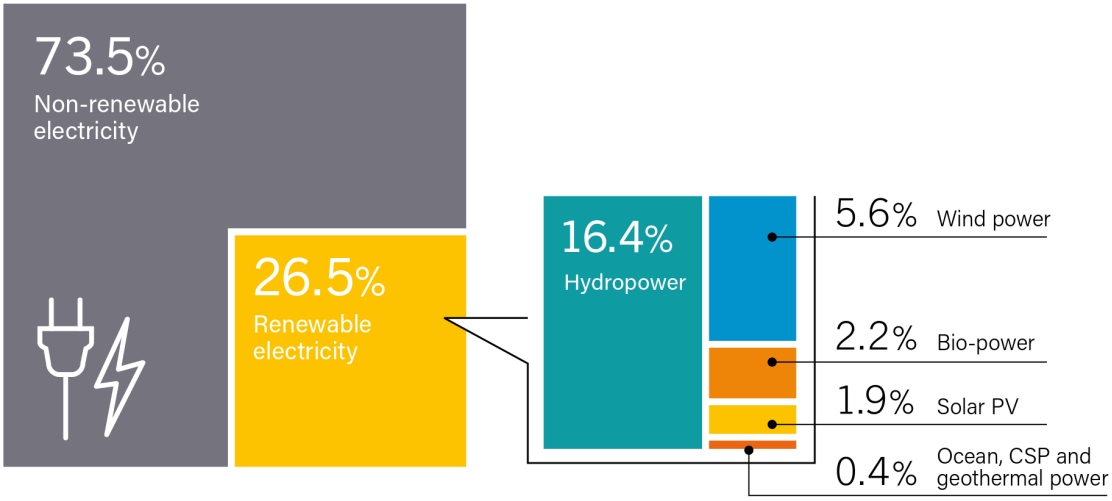

Figure 1.2 – Share of renewable electricity in the global production in 2017 [167].

have focused on extending the operating range of hydraulic turbomachines, diminishing their response time and increasing their flexibility, in order to bolster the use of hydropower as an integrating tool for intermittent renewable energy sources.

Apart from the aforementioned integrating role, hydropower is very attractive in its own right. The median lifecycle greenhouse gas emission intensity of electricity generated by hydropower is estimated to be 25 gCO_2eq/kWh, much lower than the global average of 530 gCO_2eq/kWh and comparable to solar photovoltaic (45 gCO_2eq/kWh), nuclear (13 gCO_2eq/kWh) and wind (12 gCO_2eq/kWh) [23]. Furthermore, hydropower is perhaps the least expensive technology, with a levelized cost of electricity of 35-160 USD_{2016}/MWh, comparable to natural gas in combined cycle (76-100 USD_{2016}/MWh) and less expensive than nuclear (100-180 USD_{2016}/MWh), wind (84-245 USD_{2016}/MWh) and solar photovoltaic (160-315 USD_{2016}/MWh) [23].

There is still plenty of hydropower to be exploited. Whereas in 2015 the global electricity generated by hydropower reached 4,000 TWh, it is estimated that the technically feasible potential is 14,000 TWh per year [34], meaning that the installed capacity could be more than tripled. In fact, it is expected to be almost doubled by 2050, reaching some 2,000 GW worldwide [34].

1.2 The Erosive Wear Problem

In spite of being a proven technology, the field of hydraulic turbomachines is an active area of research because there are many aspects of their design and operation that need to be further understood and improved. This is especially true nowadays since the way the machines are being used has to change to accommodate the increasing share of intermittent renewables.

One of the everlasting problems faced by hydraulic machines is the erosive wear they suffer

when they use sediment-laden water, as described in detail in Section 2.2. This problem is bound to become increasingly important for two reasons. On the one hand, the expected deployment of hydropower coincides geographically with regions that have hydraulic resources with high sediment concentrations due to relatively young geological formations, as is the case for important mountain ranges around the globe: the Himalayas, Andes, Alps and the Rocky Mountains. On the other hand, the sediment concentration will further increase as glaciers retreat due to global warming, further aggravating the problem.

It is necessary to study the erosive wear phenomenon to develop tools that will allow optimized designs and operation strategies for hydraulic turbines facing sediment-laden water, with the aim of reducing costs, increasing flexibility and efficiency. Hopefully, this will contribute to enabling the energy supply transition that is much required to face the threat of climate change.

2 Literature Review

2.1 Hydraulic Turbines

Machines that transform hydraulic energy into rotating mechanical energy are termed hydraulic turbines, a kind of hydraulic turbomachine. Primitive hydraulic turbines have been used for more than a thousand years, although only in the last 150 years did they settle into the four well-known families: Pelton, Francis, Kaplan and Bulb. In spite of their long history, the design of these turbines has continued to improve, especially in the last three decades with the advent of modern computer-aided design and manufacturing methodologies [29].

Hydraulic turbines are characterized by their *specific speed*, defined as

$$\nu = \frac{\omega\sqrt{Q}}{\sqrt{\pi}\,(2E)^{\frac{3}{4}}}, \tag{2.1}$$

where ω is the angular speed, Q is the discharge and E is the available specific energy; the specific speed therefore depicts the link between the machine's rotational speed and the site's hydraulic conditions. As illustrated in Figure 2.1, each family of hydraulic turbines reaches its highest efficiency for different values of ν, and are therefore best suited for different site conditions, *i.e.* different Q and E combinations.

2.1.1 The Pelton Turbine

Sites characterized by low discharge and high specific energy are best exploited by Pelton turbines, defined by their low specific speed. As illustrated in Figure 2.2, Pelton runners are composed of a given number of buckets z_b of characteristic size B_2. The runner is impinged by a given number of jets z_0, each of which is defined by an average speed C_1 and diameter D_0. The jet axis is tangent to the circle defined by the turbine pitch diameter D_1.

The energy transfer mechanism is fairly easy to understand. As presented in Figure 2.3, the impinging jet is divided by the bucket splitter, inverting its direction and significantly reducing

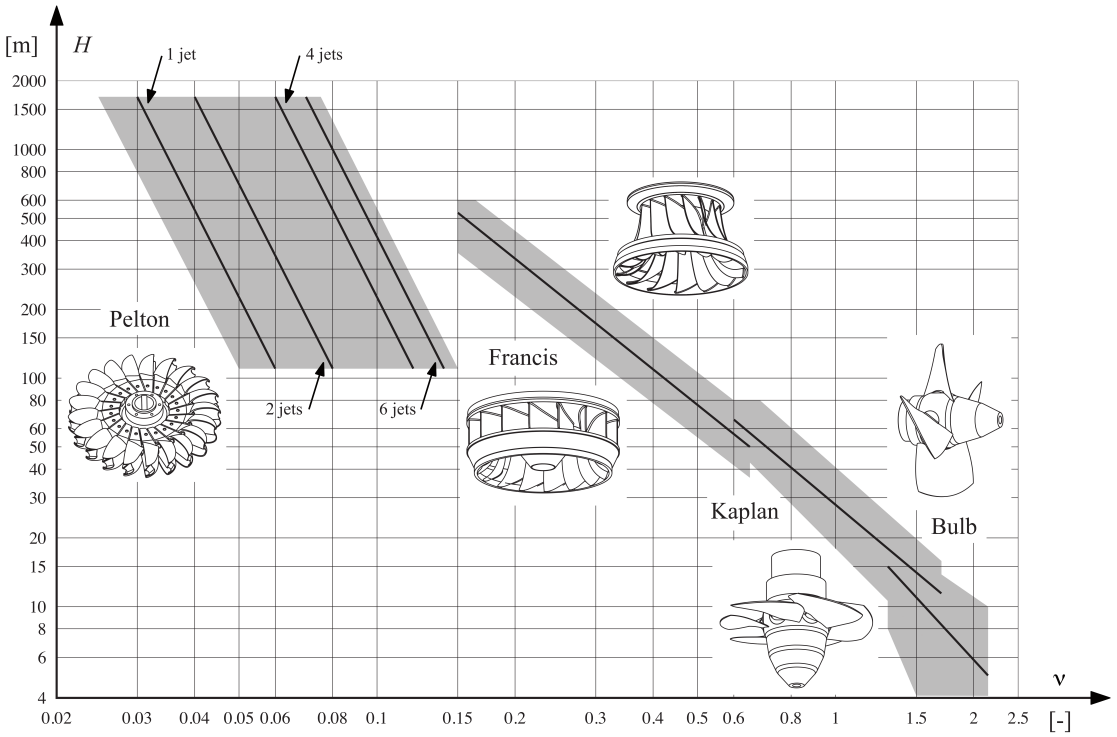

Figure 2.1 – Typical operating range for the different turbine families [10].

its absolute velocity. By conservation of momentum, the turbine is subject to a torque that results in extracted mechanical energy.

2.1.2 Principles of Similarity

Dimensional analysis allows defining the concept of similarity between a full-scale prototype and a reduced-scale model. *Geometric similarity* is achieved as long as the model is proportional to the prototype. *Cinematic similarity* is maintained so long as the operating conditions between the model and the prototype are identical, as defined by non-dimensional numbers. For Pelton turbines, the energy coefficient ψ_1 and the discharge coefficient ϕ_{B_2} completely characterize the operating condition; they are defined as [160]:

$$\psi_1 = \frac{2E}{U^2}, \qquad \phi_{B_2} = \frac{2C_1 D_0^2}{\omega D_1 B_2^2 z_0}. \tag{2.2}$$

Dynamic similarity is obtained once all the relevant dimensionless numbers that describe the hydrodynamics are identical in the model and the prototype. Provided the three similarities are met, it is possible to exactly know the prototype behavior, including the efficiency, by studying the reduced-scale experimentally. Model testing constitutes a fundamental step of designing hydraulic turbines and a very effective way to study the turbine hydrodynamics without the complications and costs associated with instrumenting a full-scale machine.

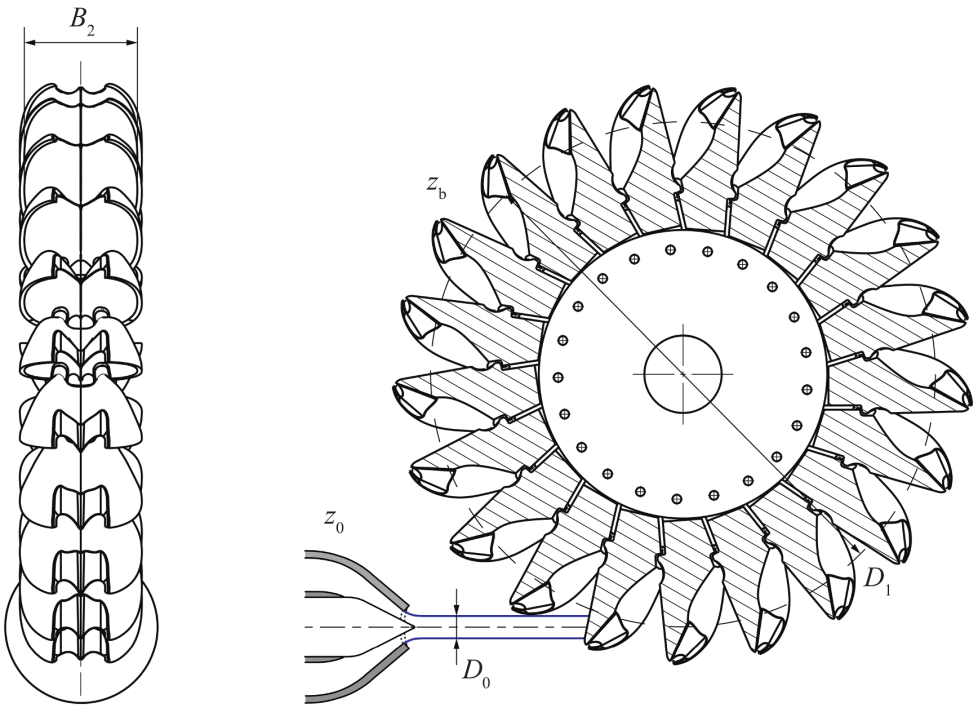

Figure 2.2 – Sketch of a Pelton runner with one injector and impinging jet [188].

The dimensionless numbers that characterize the hydrodynamics of a Pelton turbine are the following. The *Reynolds number* Re, which is defined as the ratio between inertial and viscous forces; the *Froude number* Fr, which measures the importance of inertia with respect to gravity; the *Weber number* We, which is defined as the ratio between inertial and surface tension forces; the *Rossby number* Ro, which is the ratio between inertial and Coriolis forces [160]. They are defined as

$$\mathrm{Re} = \frac{\rho B_2 C_1}{\mu}, \qquad \mathrm{Fr} = \frac{C_1}{\sqrt{g B_2}}, \qquad \mathrm{We} = \frac{\rho B_2 C_1^2}{\sigma}, \qquad \mathrm{Ro} = \frac{C_1}{B_2 \omega}, \tag{2.3}$$

where ρ is the fluid density, μ is its dynamic viscosity, g is the gravitational acceleration and σ is the surface tension.

Figure 2.3 – Jet impingement on a reduced-scale Pelton runner [158].

In spite of the beauty of the theory of similarity, in practice it is oftentimes not applicable. For Francis, Kaplan and Bulb turbines, for which only the Reynolds number matching is required to achieve dynamic similarity, it is not technically possible to ensure it because of the extremely high specific energy that would be required for the model test. Consequently, step-up empirical formulae have been derived to estimate the prototype efficiency based on the model tests, although the transposition of other turbine characteristics, such as its dynamic behavior at off-design conditions, is still a topic of research.

For the case of Pelton turbines, it is not even conceptually possible to ensure dynamic similarity because of the incongruence between the four dimensionless numbers involved. The effects of non-similarity on the turbine efficiency have been studied in detail; it has been found that the effects of Fr are the greatest. For this reason, reduced-scale model tests are performed under the Froude similarity, and an empirical step-up procedure has been developed to calculate the prototype efficiency [160]. However, some phenomena, such as jet interference [144], remain inaccessible to reduced-scale experimental investigation. Another example is erosive wear, as detailed in Section 2.2.3.

2.2 The Erosive Wear Phenomenon

A surface that is exposed to a sediment-laden flow will suffer removal of material, a kind of wear that is usually termed *hydroabrasive erosion* in the field of hydraulic machines [39]. Abrasive wear is defined as the material removal caused by particles that are forced to slide against a surface, continuously cutting it. Although cutting certainly is an important wear mechanism in the case of hydraulic machines, it does not occur through sliding, but when sediments impact the surface at a glancing angle [143, 145, 203]. Therefore, the wear suffered by these machines is best described as erosive in nature, *i.e.* caused by sediment impacts rather than by an abrasive action [163]. Hereafter the erosive wear caused by sediment impacts is referred to simply as *erosion*.

The following definitions are used throughout the document. The *erosion rate* is the amount of mass removed from a surface per unit of time; it is denoted as $\dot{e}$ [mg $\cdot$ h^{-1}]. The *erosion ratio* is the amount of mass removed per unit of sediment mass; it is denoted as e_r [mg $\cdot$ kg^{-1}]. The *erosion depth* is the normal depth of the erosion pit at a given point; it is denoted as e_d [μm].

There are four main mechanisms of erosion: Cutting, accumulation of plastic deformation, fatigue and shearing. A simplified description can be drawn as follows [17, 18, 39]. For ductile materials, at large impact angle and velocity, the sediments plastically deform the material leading to strain hardening and an increase in yield strength; eventually the ultimate strength is reached and the material fails. If the velocity is not high enough to generate plastic deformation or if the material is brittle, the sediment impacts produce elastic deformation that promotes crack propagation and eventually failure by fatigue or brittle fracture. At low impact angle, the sediments cut through the material provided the velocity is high enough for them to penetrate; if they do not do so, they still produce shearing by means of the frictional

contact, which can also lead to material failure.

In reality, the situation is not so simple since all these mechanisms may act simultaneously; they are part of the same phenomenon. For instance, every impact that produces plastic deformation also induces some fatigue due to the elastic component of the deformation. Another example is ploughing, a failure mechanism that occurs at moderate impact angles: it involves some cutting, but also accumulation of deformation on both sides of the cut, somewhat similar to the crater formation that occurs at higher impact angles.

One of the most important effects in the particle impact erosion phenomenon is the extremely high strain rate the material is subject to [17, 175], which is of the order of 1×10^7 s^{-1} [199, 200]. Such a high deformation rate significantly modifies the material response, an effect termed *strain rate hardening*. The extremely short impact duration, responsible for the strain rate, also implies adiabatic temperature increases [56, 163, 175] that may lead to *thermal softening* effects. At very high impact velocities not found in the domain of hydraulic machines, the concentrated heating and softening may lead to subsequent accumulation of deformation in the same spot, leading to failure by shear banding.

2.2.1 Main Influencing Parameters

The erosion damage caused by impacting sediments depends on many parameters, the most important of which are hereafter explained in detail. A special emphasis is placed in the conditions that occur in the erosion of hydraulic machines.

Impact Angle

The angle α at which sediments impact the surface determines the mechanism whereby the material erosion occurs [17, 18, 55, 56, 79]. At high values of α, a significant portion of the kinetic energy of the sediment is directed normal to the surface, and is therefore transferred directly to the material. As already discussed, under such conditions the failure mechanism in ductile materials is the accumulation of plastic deformation, whereas in brittle materials it is due to fracture if the ultimate stress is reached, or by fatigue otherwise. In the case of ductile materials, the impacts form pits and craters around which deformed material accumulates, a process termed *lip formation* [175], and eventually breaks loose. In the case of brittle materials, crack propagation leads to pieces of the material breaking off.

At low values of α, only a small fraction of the kinetic energy of the sediment is directed towards the surface, and only minor energy transfer occurs. However, the tangential motion of the sediment may cut through the material provided it is able to penetrate it. Whereas ductile materials tend to have low surface hardness and are therefore very sensitive to cutting, brittle materials tend to have higher hardness values and are therefore less prone to the cutting mechanism dominant at low impact angle.

The typical behavior of the erosion of brittle and ductile materials is well known: whereas the erosion rate $\dot{e}$ is maximum at normal incidence for the former, it reaches its maximum value at about $\alpha = 30°$ on the latter. The heat treatment may alter the erosion behavior of a material by modifying its microstructure and therefore its hardness. For instance, Figure 2.4a presents the erosion ratio for 0.55 % carbon steel impacted by SiC particles of diameter $d = 250$ μm at 107 m $\cdot$ s^{-1} [163]. Whereas the microstructure conformed by ferrite and pearlite exhibits a typical ductile erosion behavior, the martensitic microstructure presents a significantly more brittle response. Figure 2.4b shows the ductile behavior of aluminum eroded by $d = 325$ μm SiO_2 particles at three different velocities [153].

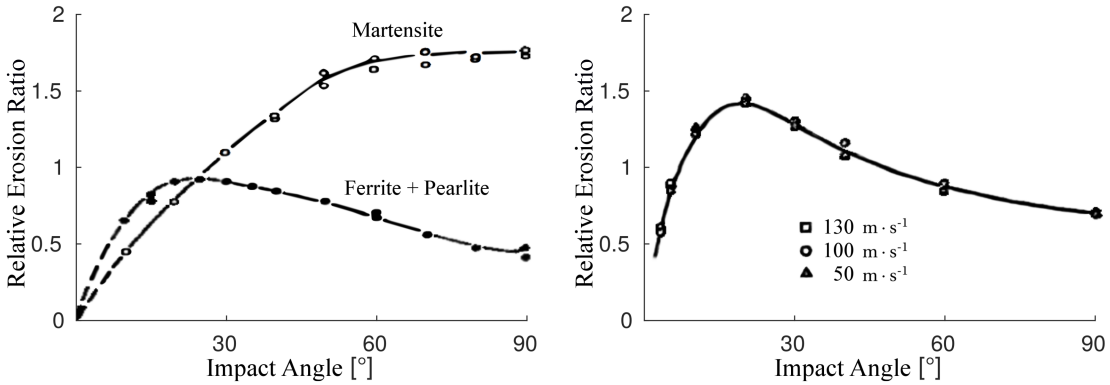

(a) Effect of microstructure on the erosion of 0.55 % carbon steel by 250 μm SiC particles at 107 m $\cdot$ s^{-1} [163].

(b) Effect of impact velocity on the erosion ratio dependence on impact angle [153].

Figure 2.4 – Typical erosion ratio behavior of ductile and brittle materials as a function of the impact angle [153, 163].

The sediment impact angles that occur during the operation of hydraulic machines cover the whole range, from almost normal incidence at the Pelton bucket splitter tip, to very low angles on the injector needle, where they tend to travel parallel to the surface. Hydraulic turbines are oftentimes made of *martensitic stainless steel* (MSS) 13Cr-4Ni [8, 26, 177], whose erosion behavior is similar to the results for martensitic carbon steel presented in Figure 2.4a, namely a maximum erosion ratio in the range of α = 60-90° [176].

Figure 2.5 presents scanning electron micrographs of the eroded surface of MSS 13Cr-4Ni by SiC particles of d = 500-700 μm at 120 m $\cdot$ s^{-1} [26]. Whereas cuts and ploughing marks are visible at low impact angle (see Figure 2.5a), pits and craters are most common at high impact angle (see Figure 2.5b). Note that these experiments were performed using a gas jet impingement apparatus [26] such that the sediment impact angle is very similar to the jet impingement angle; in slurry jet apparatus, the sediments follow the fluid streamlines more closely and the effective sediment impact angle is widely distributed about the jet impingement angle.

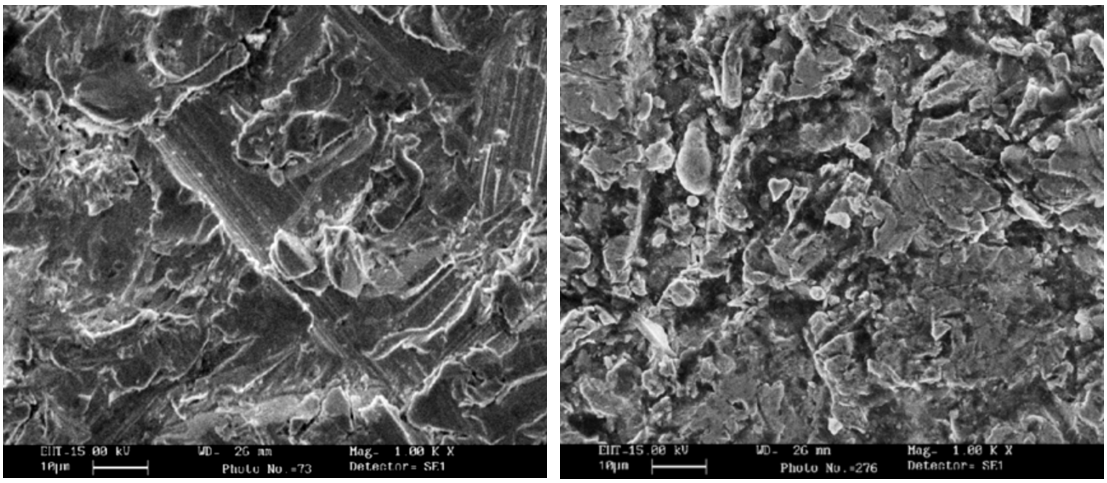

(a) Impact angle $\alpha = 30°$.

(b) Impact angle $\alpha = 90°$.

Figure 2.5 – Scanning electron micrographs of the eroded surface of 13Cr-4Ni martensitic stainless steel by SiC particles of d = 500-700 μm at 120 m $\cdot$ s^{-1} [26].

Impact Velocity

The velocity at which the sediments impact the material define the erosion mechanism, as already mentioned. There is a threshold velocity below which only elastic deformation is caused on the target, such that the material will fail by fatigue after many such impacts. Provided the impact velocity is above the threshold, a transition towards other erosion mechanisms takes place: either brittle fracture or accumulation of plastic deformation.

A number of experiments has established that the erosion ratio dependence on the sediment impact velocity v is well described by a power relation $e_r \propto v^{n_v}$. From energetic considerations alone, the erosion ratio should be proportional to the kinetic energy of the sediment, *i.e.* $n_v = 2$. However, experiments have shown that the exponent usually lies in the range n_v = 2.0-3.4 for metals [140, 152, 163, 175].

As evidenced in Figure 2.4b, the effect of the impact velocity on the erosion behavior of a material is orthogonal to the impact angle effect. In other words, the velocity exponent is not a function of the impact angle, such that the graph of $e_r = f(\alpha)$ is uniformly scaled by changes in impact velocity [153]. Consequently, the erosion ratio can be described as $e_r \propto f(\alpha) \cdot v^{n_v}$.

The fluid velocity in hydraulic turbines is proportional to the available specific energy E, therefore not all turbine families are equally prone to erosion. Whereas the characteristic fluid velocity for Bulb and Kaplan turbines is 5-9 m $\cdot$ s^{-1}, that of Francis turbines is about 8-12 m $\cdot$ s^{-1}; the relative velocity in Pelton turbines is 70-190 m $\cdot$ s^{-1} in the injector and 40-110 m $\cdot$ s^{-1} in the buckets, considering the runner's angular speed and the fluid acceleration in the bucket [75]. It is expected that the sediments will impact at about the fluid velocity, although their interactions with turbulence and the boundary layer render the impact velocity highly variable.

Sediment Size

The sediment size affects the erosion of a component by both indirect and direct pathways. Indirectly, it determines how the sediment interacts with the flow field and therefore at which angle and velocity it impacts the surface. For instance, small sediments closely follow the turbulent fluid streamlines, whereas larger ones move more loosely. Thus, depending on the flow characteristics, either relatively smaller or larger sediments will become most erosive.

The sediment size directly determines the energetic content of an impact for a fixed velocity, and therefore the larger the sediment, the greater the damage. However, considering the erosion ratio e_r, the normalized quantity defined as the eroded mass over the sediment mass, the picture is not so clear anymore. It has been proposed that above $d = 100$ μm, the erosion ratio stays constant, but below this threshold it decreases somewhat [56]. More recent data suggests that the sediment size dependence follows a power relation $e_r \propto d^{0.18\text{-}0.22}$ for SiO_2 particles in the range $d = 49\text{-}428$ μm eroding a variety of materials at an impact velocity $v = 100$ m $\cdot$ s^{-1} [152], that is, a mild increase in erosion ratio with particle size. Note that SiO_2 is the most common erodent of hydraulic machines.

It has also been shown that very small sediments of the order of 5 μm cause a transition to ductile erosion behavior in ideally brittle materials such as glass: cutting and plastic deformation appear [174]. Since the brittle behavior depends on the distribution of faults on the material, applying the stress at sufficiently small scales bypasses the activation of delicate faults that characterizes brittle fracture.

The sediment size has no effect on the erosion velocity exponent n_v [152]. Furthermore, it has been found that the impact angle dependence $f(\alpha)$ is not affected by the particle size either [56]. Therefore, the erosion ratio can be described as $e_r \propto f(\alpha) \cdot v^{n_v} \cdot d^{0.18\text{-}0.22}$.

Most rivers transport a wide range of sediment sizes, typically from a few microns to several millimeters in diameter. However, hydraulic turbines are oftentimes not exposed to the largest particles: Either a reservoir or sand traps are used to exclude sediments larger than ≈ 300 μm. Based on these representative sizes and the fluid velocities characteristic of hydraulic turbines, it is safe to say that the particles are transported in *suspension* [48], *i.e.* floating around the fluid volume, occupying it almost uniformly.

The heaviest erosion can be roughly attributed to sediments with $d = 50\text{-}300$ μm [65], although this is very much dependent on the site's particular *sediment size distribution*, which changes over time. A sediment size distribution can be characterized by a set of values d_x, where each d_x is the sediment diameter below which x % of the cumulative mass distribution lies. For example, a given distribution can be defined by a set d_{10}, d_{50}, d_{90}, where by definition d_{50} is the median particle size.

Sediments below 4 μm, classified as *clay*, are so small that they tend not to touch the turbine surface and are therefore not very erosive [65]. The particles that most affect hydraulic turbines

fall under the categories of *coarse silt* (20-63 μm) and *fine sand* (63-200 μm) [48], but they will continue to be referred to as simply sediments.

Sediment Concentration

Below a given threshold, there is a linear relationship between the sediment concentration and the erosion rate $\dot{e}$ of a given sample [39, 67, 145, 156]; simply put, the higher the number of sediments per unit of volume, the greater the number of impacts the sample will receive per unit of time. However, if the concentration is above the critical threshold, inter-sediment interference dominates and the relationship becomes sublinear. Indeed, when there are too many sediments in the fluid, the rebounding particles may impact incoming ones, effectively protecting the surface from some impacts; this phenomenon is termed *shielding effect*.

The critical sediment concentration below which linearity holds is estimated based on a *critical sediment flux*, which is highly variable. Whereas it is about 100 $\mathrm{kg \cdot m^{-2} \cdot s^{-1}}$ for elastomers, it can reach about 10,000 $\mathrm{kg \cdot m^{-2} \cdot s^{-1}}$ for metals impacted by large particles [178]. Based on these figures, it is reasonable to assume a value of 5,000 $\mathrm{kg \cdot m^{-2} \cdot s^{-1}}$ for the case of hydraulic machines.

Table 2.1 compiles the concentration values on a variety of conditions related to hydraulic turbines; given that the unit *parts per million* (ppm) is mass based, the unit conversion to % *by weight* ($\%_w$) is transparent. For the unit conversion to % *by volume* ($\%_v$), the water density is assumed to be $\rho_f = 999\ \mathrm{kg \cdot m^{-3}}$, and the sediment density $\rho_s = 2{,}650\ \mathrm{kg \cdot m^{-3}}$, that of quartz. The great variability between sites and even between different moments on a single site is highlighted. Indeed, the sediment concentration can increase dramatically in a matter of minutes [48].

Table 2.1 also presents the sediment flux computed using typical Pelton turbine conditions, namely a relative velocity between the jet and the bucket $W = 100\ \mathrm{m \cdot s^{-1}}$, which corresponds to the higher end of typical conditions, and the aforementioned sediment density. The sediment flux is computed as

$$J_s = c_v \rho_s W, \tag{2.4}$$

where c_v is the sediment concentration by volume. It can be seen in Table 2.1 that only under the most extreme conditions corresponding to the peak concentration during a strong monsoon does the assumption of linearity come into question, with $J_s = 6{,}228\ \mathrm{kg \cdot m^{-2} \cdot s^{-1}}$, greater than the estimated threshold value of $\approx 5{,}000\ \mathrm{kg \cdot m^{-2} \cdot s^{-1}}$. Therefore, assuming that the erosion rate increases linearly with the sediment concentration is a good approximation for the case of hydraulic turbines.

Table 2.1 – Typical Sediment Concentration and Flux Values.

Description	Concentration [ppm]	[$\%_w$]	[$\%_v$][1]	Sediment flux[1] [$kg \cdot m^{-2} \cdot s^{-1}$]
Zermatt power station, 1989 average [65]	200	0.02	0.008	21
Aletsch-Mörel river, 2008 average [40]	400	0.04	0.015	42
Yangtze river, 1983 average [123]	600	0.06	0.023	62
Low value on an average monsoon [155]	2,000	0.20	0.076	208
Aletsch-Mörel river, 2008 peak [40]	5,000	0.50	0.189	519
High value on an average monsoon [155]	6,000	0.60	0.227	623
Typical laboratory experiment [156, 179]	10,000	1.00	0.379	1,038
Peak value on an average monsoon [155]	20,000	2.00	0.763	2,076
Peak value on a strong monsoon [155, 181]	60,000	6.00	2.350	6,228

[1] Assuming typical values for Pelton turbines: $\rho_f = 999\ kg \cdot m^{-3}$, $\rho_s = 2{,}650\ kg \cdot m^{-3}$ and $W = 100\ m \cdot s^{-1}$.

Sediment Shape

It is well known that angular particles cause more erosion than rounded ones. Sharp edges act as stress concentrators, so angular sediments generate deeper cuts and craters. Estimations of the erosion potential of sharp particles compared to spherical ones lie in the range of 1.7 [150] to 4.0 [118]. Furthermore, the fact that the sediment sharpness increases the erosion at low impact angles especially has been verified both experimentally [35] and by numerical simulation [125] for the case of ductile metals. Not surprisingly, it is the cutting mechanism that is most sensitive to the sediment shape, with sharp edges greatly increasing the cutting potential.

The viscous drag dependence on the sediment shape generates an indirect effect of the particle angularity on the erosion of a component. Spherical sediments possess a minimal surface area per unit volume, so they are less affected by drag [71]. Consequently, inertial effects aside, the trajectory a sediment will follow through the flow field and therefore its impact location, velocity and angle depend on its shape.

There is experimental evidence that the sediment angularity has a negligible effect on the dependence of the erosion ratio on the sediment size [152]. However, the velocity exponent does depend on the kind of erodent used; this fact is mostly explained by the differences in erodent hardness, but possibly also on their shape [152]. Considering a sediment shape parameter ϕ_s, the erosion ratio can therefore be described as $e_r \propto f(\alpha, \phi_s) \cdot v^{n_v(\phi_s)} \cdot d^{0.18\text{-}0.22}$.

Material Properties

It goes without saying that the material properties of the sediment and the component are paramount in the erosion process. One evident parameter is the sediment density, which determines its inertial interaction with the transporting flow, as well as the energetic content of the impact. Another indisputable characteristic is the mechanical behavior of the material,

namely the yield and ultimate strengths and their dependence on strain and strain rate hardening; these, together with the maximum strain, determine how much energy per unit volume the material is able to accommodate before failing, *i.e.* its toughness.

One of the most important properties for erosion resistance is the surface hardness. The erosion dependence on the *ratio of sediment to surface hardness* $HR = \frac{HV_{\text{sediment}}}{HV_{\text{surface}}}$ has been described multiple times [40, 145, 185]: Below $HR \approx 0.8$ the sediments are not able to erode the surface; the erosion potential increases linearly until $HR \approx 1.3$, above which no further increment is evidenced.

As already presented in Figure 2.4a, the material hardness can significantly alter the erosion mechanism and therefore its dependence on the impact angle. Considering this effect, the aforementioned ramp-like erosion potential dependence on HR and the fact that the impact velocity exponent also depends on it [152], the erosion ratio can be described according to $e_r \propto f(\alpha, \phi_s, HR) \cdot g(HR) \cdot v^{n_v(\phi_s, HR)} \cdot d^{0.18\text{-}0.22}$.

Table 2.2 compiles hardness values for some of the most common sediments found in hydraulic installations, as well as for two turbine materials: MSS 13Cr-4Ni and tungsten carbide cobalt-chromium (WC-CoCr), the most frequently used coating. The hardness ratios HR_i show that the least hard minerals such as biotite and muscovite do not erode any of the turbine materials; the erosion potential of feldspar and quartz is complete ($HR >\approx 1.3$) on the bare MSS 13Cr-4Ni, whereas the application of a WC-CoCr coating significantly reduces it but does not completely prevent it ($HR >\approx 0.8$).

Due to the hardness effect, it is important to know the composition of the sediments if an assessment of the erosion potential of a site is to be performed. Oftentimes very hard sediments, *e.g.* quartz and feldspar, constitute ≈70-95 % of the particles [165, 181, 198].

Table 2.2 – Typical Material Hardness Values.

Material	Hardness		$HR_{\text{13Cr-4Ni}}$	$HR_{\text{WC-CoCr}}$
	[Mohs]	[HV]	[–]	[–]
Quartz [11, 165, 177]	7.0	1,000-1,200	3.13-4.44	0.83-1.33
Feldspar [11, 40, 165]	6.0	700-900	2.19-3.33	0.58-1.00
Biotite [165]	2.5-3.0	80-100	0.25-0.37	0.07-0.11
Muscovite [165]	2.0-2.5	16-18	0.05-0.07	0.01-0.02
WC-CoCr coating [40, 49]	6.5-7.0	900-1,200	–	–
MSS 13Cr-4Ni [8, 26, 40, 48, 66, 99, 130]	4.5-5.0	270-320	–	–

Other Considerations and Summary

In general it can be said that the erosion rate of a surface is constant in time, at least in the time frame of several hours [39, 145, 156]. Intuitively, the number of impacts is proportional

to the amount of time the sample is subject to erosion, and therefore the damage is linear in time.

However, the erosion rate does change over time under two distinct circumstances. First, on very short timescales, when a ductile material is first subject to sediment impacts, there is a gradual accumulation of plastic deformation and subsequent strain hardening, a period termed *incubation* [59] within which the erosion rate gradually increases. Only after this initial transient does the system stabilize to a *steady-state erosion rate*. Second, on very long timescales, the erosion rate is modified as a consequence of the erosion itself: As the sample loses mass, its contour changes, affecting the hydrodynamics and sediment impact conditions, therefore altering the erosion rate.

Apart from these circumstances, there are two indirect ways in which the erosion rate of a component may change. First, laboratory experiments that reuse sediments usually evidence a reduction of the erosion rate as a consequence of the breaking and rounding of the sediments as they impact the sample repetitively. Second, the surface modifications caused by the erosion can induce *cavitation*; the synergetic interaction between sediment erosion and cavitation erosion has been highlighted [62, 89, 120, 177], but remains an elusive subject of study.

Fluid *turbulence* is a major contributor to the erosion process of hydraulic machines [39]. The chaotic velocity fluctuations present in most moving fluids agitate the sediments being transported, especially the smallest particles, increasing their chance of impacting the surface. Moreover, the increased wall roughness caused by the erosion stimulates turbulence production in the boundary layer [173], further reinforcing the process.

The main parameters affecting erosion have been discussed in detail. They can be classified into three broad categories: Geometric sediment characteristics, such as their size, shape and concentration; impact conditions, such as angle and velocity, which depend on the flow field, the sediment transport process, and turbulence; material properties, such as hardness, yield and ultimate stress, toughness and ductility. The severe interaction among these influencing parameters has also been highlighted.

Based on the current knowledge of the phenomenon, the erosion ratio, which describes the amount of mass eroded per unit of sediment mass impacted, can be expressed as

$$e_r \propto f(\alpha, \phi_s, HR) \cdot g(HR) \cdot v^{n_v(\phi_s, HR)} \cdot d^{0.18\text{-}0.22}. \tag{2.5}$$

2.2.2 Effects of Erosion on Hydraulic Turbines

The alteration due to erosion of the carefully designed contours of hydraulic turbines leads to a significant decrease in their efficiency, which can be explained by an increased dissipation through turbulence production, proliferation of secondary flow structures, modified velocity triangles and pressure distributions. Decreases of hydraulic efficiency of several percentage points in one year are not uncommon [39, 48], and lead to important revenue losses and a

waste of hydraulic resources.

As already mentioned, the surface modifications induced by erosion stimulate the appearance of cavitation, creating a synergy that is significantly more damaging than any of the two phenomena alone. With or without cavitation, as the erosion process advances, the removal of material leads to increased vibration and structural damage that can eventually pose a threat to the integrity of the installation.

Pelton turbines are the most prone to erosion as a consequence of the high velocity flows they face, as discussed in Section 2.2.1. Several examples of erosion in uncoated Pelton turbines are presented in Figure 2.6.

The highest relative flow velocity is found at the injector and its needle. Considering the average flow only, it can be said that the velocity is parallel to the locally flat surfaces, so the entrained sediments would seldom impact the wall. However, in reality the flow is highly unsteady; the main mechanism that drives sediments towards impacting the wall is the *turbulence in the boundary layer*: the chaotic velocity fluctuations that are superposed on the average flow have a component normal to the wall. These small scale, rapid fluctuations increase the flux of sediments towards the wall, especially for the smallest particles that are much more responsive to the high frequency forcing. This explains why the needle erosion is predominantly caused by the smallest sediments, roughly $d < 50$ μm [39, 145, 155].

The relative flow velocity on the bucket is about half the jet velocity because of the angular speed of the runner. Even though the flow turbulence continues to promote the flux of sediments against the walls, the main mechanism that drives the sediments towards the bucket is the *flow acceleration*, which is commonly 12,000-35,000 $\mathrm{m} \cdot \mathrm{s}^{-2}$ [75], depending on the specific energy and the bucket curvature. Whereas the smallest sediments follow the fluid closely as it accelerates through the bucket due to their small inertia to drag ratio, the larger ones cannot follow and deviate towards the wall. This size-dependent mechanism explains why it is especially the larger sediments, d = 80-300 μm, which are most damaging to the buckets [39, 145, 155].

The two most eroded zones are the bucket outlet and the edges of the splitter and cutout. In the latter, the jet impinges directly and most sediments cannot avoid impacting at high angle. In the former, the sediment segregation caused by the fluid acceleration has deviated most sediments towards the wall, such that the local concentration is maximum, as is the number of impacts and subsequent damage.

Trade-offs in the Design and Operation of Pelton Turbines Facing Erosion

There exist a variety of possible measures to mitigate the erosion of Pelton turbines, each one of which involves a cost and an expected benefit. Provided one is able to accurately assess these costs and benefits, it is possible to optimize the design and operation of Pelton turbines that face erosive conditions.

(a) Pelton injector needle after 165 operating hours under severe erosion conditions [203].

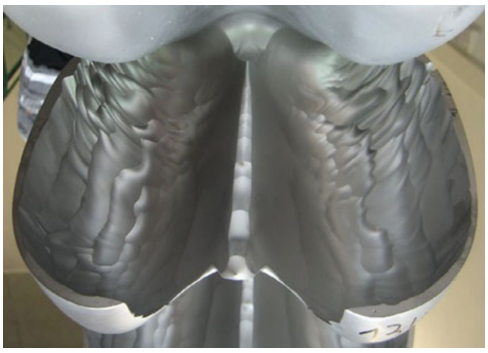

(b) Advanced splitter and outlet erosion of a bucket [203].

(c) Uncoated bucket at the Emosson power plant [50].

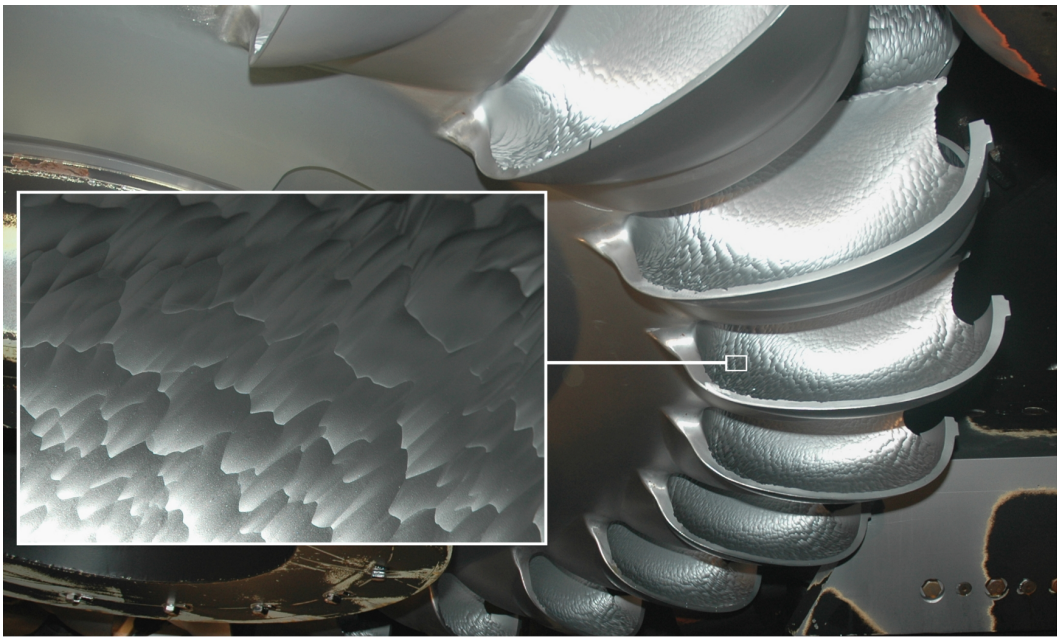

(d) Ripple erosion pattern on the outlet of a Pelton bucket.

Figure 2.6 – Examples of erosion in uncoated Pelton turbines.

One design possibility is the use of *thermally sprayed hard-coatings*, most commonly tungsten carbide cobalt-chromium. An immediate benefit is the substantial reduction of erosion and its related efficiency degradation. However, the initial efficiency of coated turbines is smaller than that of uncoated machines because of their higher roughness [48]. Furthermore, the coating implies greater initial and maintenance costs. Depending on the site conditions, this approach might be the most beneficial [32].

Another design choice, both for coated and uncoated turbines, is the *size of the buckets*. For a given site, there are several combinations of angular speed and runner diameter that are compatible with the available specific energy. Larger turbines have buckets with lower curvature and are thus less susceptible to erosion; however, they are also more expensive, both because of the amount of steel required and because of the low speed generator necessary [158].

A third design choice is the *number of jets*. Again, we find a trade-off between the turbine cost and its erosion sensitivity. For a given discharge, fewer jets implies a larger jet diameter, an increased ratio of fluid volume to contact surface, and therefore less erosion. However, larger jets require wider buckets, and therefore an overall greater cost [39].

The efficiency degradation caused by the erosion, together with the frequent need to perform turbine maintenance, imply a significant loss of revenue for the operator. Depending on the specific erosion conditions of each site, these costs might be greater than the capital cost increments associated with the aforementioned design choices to minimize the erosion sensitivity of a turbine. However, an accurate assessment of the *optimum solution* requires the *technical capacity to predict the erosion* a given turbine design will suffer under the conditions specific to the site.

Furthermore, this predictive capacity would also allow the plant owner to define, based on the specific site conditions, an *optimal operation strategy*. One example is assessing whether it is more economical to invest in a better sand trap to reduce the amount of sediments traversing the machine, rather than invest in frequent maintenance, as has been suggested for one site [20].

Another example is the choice faced by run-of-the-river plant owners: when to perform a *preventive shutdown* of the turbines. There is a sediment concentration threshold above which it becomes less expensive to shut down the machine, with the associated losses in revenue, rather than pay for the repair costs that would otherwise be induced by the erosion. However, this concentration threshold is very site dependent: values in the range 0.1-1.0 % have been proposed [19, 20, 46, 48, 66].

Moreover, the operators of storage plants have to assess what is the best solution for the problem of *reservoir sedimentation*, which gradually reduces the available storage volume and therefore the sustainability of the operation [81, 172]. Perhaps the least expensive strategy in the long term is to promote the evacuation of sediments through the water feeding the turbines, in which case erosion mitigation strategies become more urgent.

2.2.3 Approaches to Estimate the Erosion of Turbines

The technical capacity to predict the erosion of a hydraulic turbine, required to assess the aforementioned trade-offs, is a very challenging objective. Three possible approaches are hereafter explained.

Erosion Correlations

Mathematical descriptions that are used to calculate the erosion of a component as a function of a number of input parameters and constants are termed *erosion correlations*. Generally speaking, there is no single erosion correlation that is applicable to a wide set of conditions; in fact, increased accuracy is usually achieved by a reduction of generality [39, 185].

The 1995 analysis by Meng and Ludema [132] illustrates the point. They found that between 1957 and 1992, 182 correlations, involving more than 100 distinct variables and constants, were proposed to predict a series of different wear conditions. By restricting the analysis to correlations that describe the erosion by solid particle impacts, and after disregarding those that were judged inconsistent with logic, nature or experiments, they ended up with 28 equations involving 33 different variables and constants. Their conclusion is that no equation or group of equations could be found for general and practical use.

Several erosion correlations have been proposed for hydraulic turbines, but they are very case-dependent, contain large numbers of tuning parameters and are not able to predict the erosion rate in absolute terms. Instead, they can only be used to schedule maintenance cycles after a first erosion assessment has been used to tune the correlation coefficients to fit the specific turbine installation and operating condition [11, 39, 48, 145, 155, 156, 181].

The failure of the correlation approach can be explained in the following terms. On the one hand, as explained in Section 2.2.1, the erosion phenomenon depends on many parameters that are highly coupled, and on processes that are nonlinear, such as the turbulent sediment transport and the material mechanical response. On the other hand, it is remarkably difficult to experimentally determine many of the important parameters. For instance, the average fluid velocity of the system is oftentimes used as a proxy for the sediment impact velocity, which is in fact a distribution over the surface of interest, a function of the sediment size and shape distributions and the chaotic dynamics of the fluid velocity and pressure fields [39].

Experimental Testing

A fundamental part of research consists in performing laboratory experiments, although it is oftentimes complicated to extrapolate the findings to the scale of a real machine. One example is the ranking of materials according to their erosion resistance. The results of these laboratory experiments hardly coincide with the field experience on full-size turbines [39], the reason being that the mechanisms and extent of erosion are very sensitive to a wide range of

parameters that are not faithfully reproduced in the experiments.

Section 2.1.2 illustrates the concept of similarity and how reduced-scale models are used to predict the behavior of prototype-scale turbines. A clear option would be to develop a methodology to achieve *erosion similarity* in order to be able to link the model and prototype results. However, this approach is not realistic as explained hereafter.

Consider geometric similarity, the minimum requirement to achieve dynamic similarity. The model is commonly 10-20 times smaller than the prototype, and thus the model erosive particles would be significantly smaller than realistic sediments. However, the erosion mechanism is completely different for very small particles, as explained in Section 2.2.1, rendering the results unusable.

Assuming that the erosion mechanism remains unaltered under the scaling, other problems arise. Consider the turbulent sediment transport: assuming that the involved variables are the fluid density ρ_f, the sediment density ρ_s, the bucket size B_2 or associated curvature R, the sediment diameter d, the fluid relative velocity W and the fluid viscosity μ, then dimensional analysis states that the problem is defined by three independent non-dimensional variables, namely

$$\frac{\rho_f B_2 W}{\mu}, \qquad \frac{\rho_f d W}{\mu}, \qquad \frac{\rho_s d}{\rho_f R}. \tag{2.6}$$

The first one is the Reynolds number based on the bucket, which define the hydrodynamics (neglecting Fr, We and Ro); the second one is the Reynolds number based on the sediment, which determines the drag coefficient; the third one is the ratio of centrifugal to drag forces, which is related to the paths taken by the sediments. In other words, two additional constraint on similarity would arise for a problem that is already overconstrained by the four dimensionless numbers that define the hydrodynamic behavior of Pelton turbines: Re, Fr, We and Ro, Equation 2.3. Unless the sediment transport similarity is respected, the particles will not impact at equivalent angles, velocities and locations in the model and the prototype, rendering the results incompatible.

Further assuming that dynamic similarity is achievable or accurate step-up methodologies are developed to mitigate the non-similarity, there remains the problem of feasibility. The erosion of Pelton turbines is a very slow process, and it takes hundreds of hours to achieve measurable results; this inconvenient would be significantly greater in the model scale because of the lower fluid velocities involved. In short, developing a feasible similarity methodology for studying the erosion of Pelton turbines by means of model-scale experiments is unrealistic, for the time being.

A few erosion experiments on model Pelton turbines have been reported [156, 157], but they rely on questionable procedures to accelerate the process. On the one hand, the runners are not made of stainless steel, but of copper alloys that have a completely different erosion behavior. On the other hand, the sediments used are roughly 100 times larger than what

geometric similarity would require, significantly changing the sediment transport process. No attempt at complying with the similarity criteria expressed in Equation 2.6 is done.

In a nutshell, given the number of parameters that define the erosion process, the severe interaction among them and the nonlinear sensitivity to them, an experiment that would faithfully reproduce the erosion behavior of a Pelton turbine would no longer be a laboratory experiment but a full-scale prototype test [39].

Numerical Simulation

The numerical simulation of computational models is one of the three branches of scientific endeavor, together with theoretical developments and experimental studies. It finds its most prolific application in domains that are theoretically mature and where experiments are too expensive, infeasible or impossible to perform. Computational methods have been applied to the design, optimization and investigation of hydraulic turbines in particular, and engineering in general, for some 40 years [22, 29, 52, 83, 87, 93, 103, 104, 117, 188].

The numerical approach is instrumental in the study of a number of problems that do not lend themselves to experimental manipulation. Simply put, there are some phenomena that are too quick, or extremely small, or astronomically large, or too slow for experiments to be feasible or economical.

For the case of erosion, one can straightforwardly establish a set of equations and boundary conditions that would describe the hydrodynamics, turbulent sediment transport and solid mechanics of the full-scale turbine under study, without requiring similarity conditions and unconcerned about how to measure given quantities.

However, the great disadvantage of the approach is that the formulated computational model might turn out to be too complex to be solved, or too approximative to be of any use. As will be explained in Chapter 3, this is the current state-of-the-art on the modeling of the erosion problem.

2.3 Multiscale Problems and Their Modeling

Some of the most interesting problems in science and engineering have a *multiscale nature:* Their overall behavior emerges from the interaction of processes that take place on a variety of spatial and temporal scales [53]. Oftentimes independent physical models are used to describe the phenomena that take place at each scale, forming a hierarchy of models; Figure 2.7 illustrates such a hierarchy for the specific case of materials science.

For some problems, the details of the microscopic interactions are unimportant: the most general model is accurate enough for the purpose at hand. For example, the Navier-Stokes equations are an accurate description of flowing water, and all information about the molecules

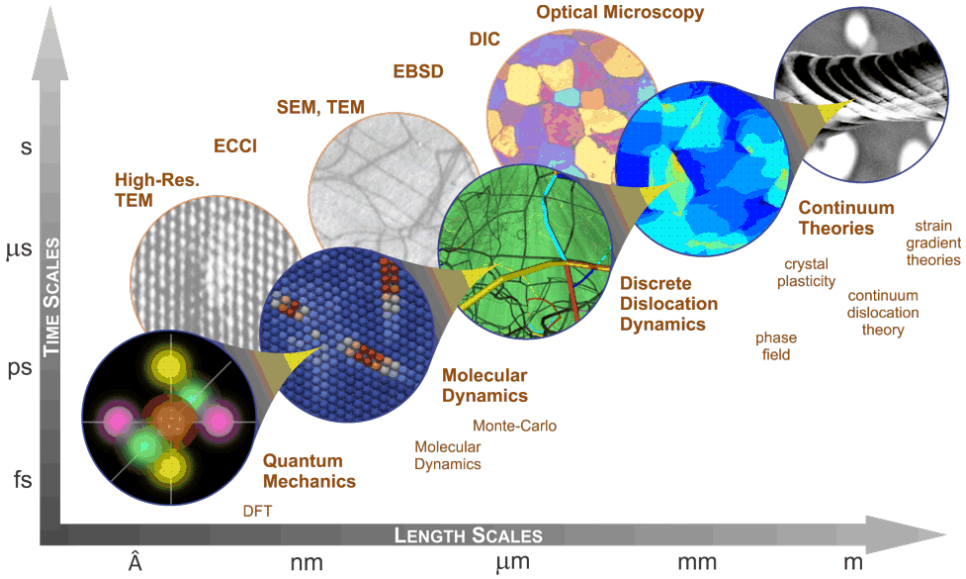

Figure 2.7 – Hierarchy of physical models in materials science [100].

that conform the fluid are irrelevant. So is the case for a metallic structure under mild bending: the continuum theory of linear elasticity is perfectly suitable, even if in reality the macroscopic behavior is determined by quantum mechanics.

However, other problems do not lend themselves to the most general models, and considering a more fundamental perspective is necessary. Applying the more detailed, microscopic model might result too costly for the problem of interest, in which case a coupling of models across scales is necessary: a *multiscale model*. In other words, by looking at the problem simultaneously at different levels of detail one hopes to achieve a description that shares the efficiency and scope of the macroscopic model and the accuracy of the microscopic model [1, 41].

Conceptually speaking, there is no limit to the number of levels in a multiscale model; however, most models proposed to date only have two levels. A *microscale model*, which includes the more accurate but expensive description, and a *macroscale model*, which describes the domain of interest in a simplified way. The microscale model provides information that is used to close the macroscale description or improve it in some way. It can be used either locally around singularities or it may be required everywhere.

2.3.1 Sequential and Concurrent Multiscale Modeling

Depending on the specificities of the problem being solved, the most efficient coupling between the microscale and macroscale models might be either sequentially or concurrent. In the *sequential multiscale coupling* paradigm the microscale model is used to produce data that will be fed to the macroscale model in a later stage. These data can be, for example, a multidimensional set of tabulated values, solutions to some set of functions required by

the macroscale description; function values not found in the table can be calculated by interpolation during the solution of the macroscale model. This coupling algorithm is also known as *precomputing* or *microscopically-informed modeling* [1, 41].

When the unknown information depends on many variables, a sequential coupling might be too costly, because a very large set of variable value combinations have to be precomputed. This approach is usually restricted to problems where the unknown information is function of no more than 3 variables, although this figure can be higher provided efficient algorithms are used for the microscale computations and subsequent interpolation.

In the *concurrent multiscale coupling* approach, the microscale computations are performed whenever they are required by the macroscale model, *i.e.* on demand. This approach is used whenever precomputing is unfeasible, or if the microscale and macroscale models need to be fully coupled. Whereas the microscale provides closure to the macroscale, the latter provides constraints, *e.g.* boundary conditions, to the former.

2.3.2 Some Multiscale Model Examples

A typical example of sequential multiscale coupling occurs in gas dynamics, where the equation of state is precomputed based on the kinetic theory of gases, and stored as a table that is interpolated upon when solving the Euler equations under a variety of conditions [1]. A more interesting example occurs in the domain of multiphase flows through porous media. The permeability describes the ability of a porous material to allow flow through it, relating the pressure gradient across the medium with a given flow rate, *i.e.* Darcy's law. However, the permeability is simply a macroscale proxy for the very complex flow through the microscopic pores, and thus depends on several parameters of the pore network structure. Sequential multiscale models have been proposed in which the effective permeability tensor is precomputed by running detailed microscale simulations of the flow through a representative volume of the medium, considering all the pore network intricacy, under a range of conditions; these results are then used to provide closure to the macroscopic model that describes the domain of interest [41]. Other more elaborate multiscale models for flow through porous media have recently been proposed [98, 201].

The constitutive model assumed in the Navier-Stokes equations, namely a linear relation between the stress and the velocity gradient, works well for water under most circumstances, but does not accurately describe the behavior of complex flows such as polymers. Complicated constitutive models have been proposed for such cases, with mixed success. Another possibility is to fall back on concurrent molecular dynamics simulations to calculate the stress based on some boundary conditions defined by the macroscale [41]. Another example of multiscale modeling in fluid dynamics occurs in the domain of turbulence, where the assumption of an isotropic eddy viscosity is bypassed by using analytical solutions of the fine scales to close the resolved scales [15].

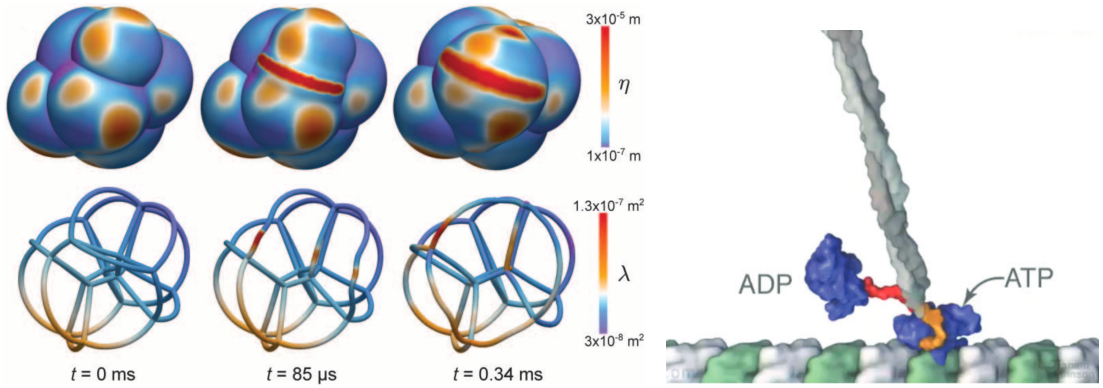

(a) Dynamics of evolving foams [171].

(b) Kinesin walking on a microtubule [90].

Figure 2.8 – Examples of complex systems revealed by multiscale models.

Figure 2.8a illustrates yet another multiscale model recently formulated. It describes the dynamics of evolving foams, which include processes as topological rearrangement and membrane drainage that occur at very disparate time and length scale [171].

The 2013 Nobel Prize in Chemistry concerned the formulation of multiscale models with application to the study of complex chemical systems. By enhancing molecular dynamics models with quantum mechanical potentials, instead of common ad hoc potentials, on the locations where reactions are expected to take place, models with the scope to simulate large systems and with the accuracy of quantum mechanics have been formulated [90]. Figure 2.8b illustrates the simulation of a walking kinesin, a very complex molecular mechanism present in eukaryotic cells.

A somewhat similar methodology has been proposed to simulate the fluid flow around a C540 fullerene nanostructure with important applications to materials science and nanotechnology. Whereas the space around the nanostructure has to be simulated with molecular dynamics, the far field does not require that level of sophistication and is modeled with the Lattice Boltzmann method [193]. Figure 2.9a shows that there is a series of overlapping regions used to couple the models.

The multiscale approach can also be applied in the time dimension. Some chemical systems include two or more coupled reactions that operate at very different time scales. Multiscale models have been formulated that take advantage of the temporal scale separation between reactions to achieve simulation speedups of up to 600,000 times [102].

A final example consists in the coupling of molecular dynamics and continuum models to solve the problem of crack propagation [1]. Whereas the continuum description is perfectly fine for the far field, the accuracy of atomistic models is exploited at the crack tip, as illustrated in Figure 2.9b. Provided that a consistent coupling is formulated between the models, an efficient concurrent multiscale model is achieved.

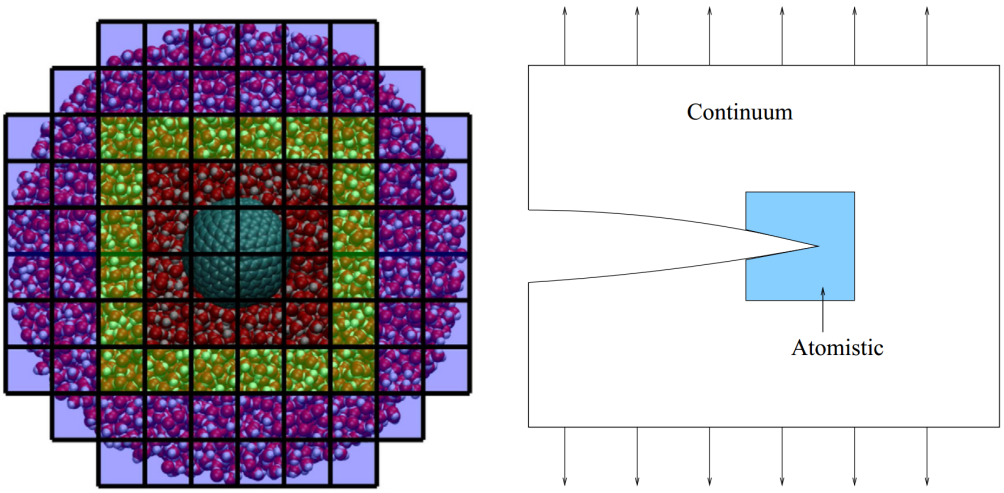

(a) Flow around a C540 fullerene nanostructure [193].

(b) Crack propagation model combining continuum and atomistic descriptions [1].

Figure 2.9 – Concurrent heterogeneous multiscale model examples.

2.3.3 From Projective Integration to Patch Dynamics

Some systems are characterized by a large gap in their eigenvalue spectrum, meaning that their evolution involves very fast and very slow dynamics only. Whereas one may be interested in the long-term evolution of the slow dynamics in the system, these depend on an accurate solution of the fast ones, rendering the system very stiff. A set of techniques, generally referred to as *projective integration*, has been developed to solve this kind of problem in an efficient manner [60, 92, 96, 97].

Two time integration steps are used in projective integration. First, a series of very small steps, at a scale corresponding to the fast time constants in the system, is performed until these components have been damped, revealing the behavior of the slow manifold; this first step is termed *inner integration*. Then, the rate of change of the slow dynamics is estimated based on the solution within the period of the inner integration, and used to perform an extrapolation, termed *outer integration*, with a time step commensurate with the slow time constant [60, 92].

As an example, consider a generic variable M that changes slowly in time as a consequence of some process of very fast character. By defining the inner and outer time intervals, ΔT^i and ΔT^o respectively, a Taylor expansion yields

$$M(t+\Delta T^i+\Delta T^o) \approx M(t+\Delta T^i)+\Delta T^o \frac{\partial M}{\partial t}\Big|_{(t+\Delta T^i)}. \tag{2.7}$$

In other words, the inner integrator solves for M within the interval ΔT^i using a small enough time step to ensure stability of the fast dynamics. Then, M is calculated after the interval ΔT^o using the solution time derivative calculated using the available values in the inner interval. This idea is illustrated in Figure 2.10. Provided $\Delta T^o \gg \Delta T^i$, projective integration provides a

significant computational advantage since the expensive inner integration is only used in the inner interval ΔT^i. Although the aforementioned scheme is a simple first-order forward Euler, higher-order projective integrators have also been developed [108].

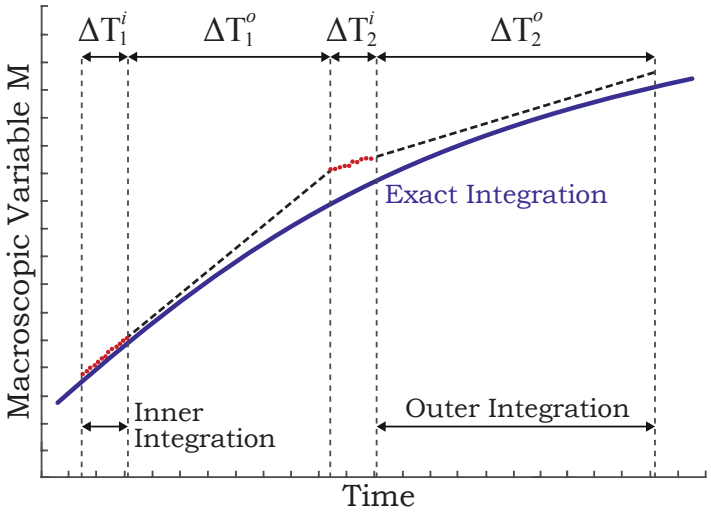

Figure 2.10 – Schematic representations of the projective time integration of a macroscopic observable.

The projective integration approach can be interpreted as a multiscale model in which the macroscopic, slow dynamics of a system are calculated using only a microscopic, fast dynamics integrator and appropriate polynomial projection in between the active calculation intervals. This idea has also been applied in the spatial dimension, a method termed the *gap-tooth scheme*. The microscale model is solved on a series of subdomains with appropriate boundary conditions; these subdomains, or patches, are distributed over the macroscale domain, although they only cover a small fraction of it. As seen in Figure 2.11a, the microscale results within each patch are used to build a polynomial reconstruction in space, covering the whole macroscopic domain and defining the boundary conditions for the following step [80, 96, 97].

The combination of the gap-tooth scheme in space and projective integration in time gives rise to an approach known as *patch dynamics*, or *equation-free modeling*. As presented in Figure 2.11b, the evolution of a macroscopic system over large time scales is computed based on a series of simulations of the microscale model that are linked via spatial interpolation and temporal projection [80, 96, 97]. Interestingly, the macroscopic behavior *emerges* from the microscopic model, *i.e.* no macroscopic model is being solved, thus the name equation-free modeling.

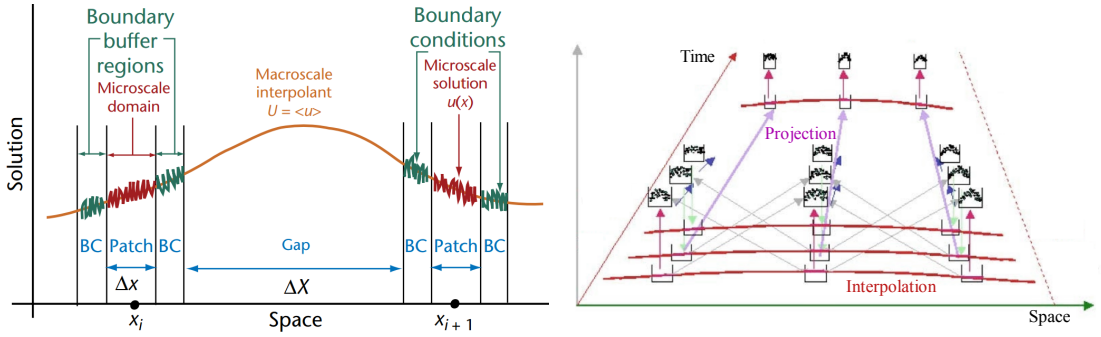

(a) Gap-tooth scheme [80].

(b) Patch dynamics scheme [95].

Figure 2.11 – Schematic representations of the gap-tooth and patch dynamics schemes.

3 State-of-the-Art on the Modeling of Erosion

Having introduced the most relevant information concerning the erosion phenomenon on hydraulic turbines in Chapter 2, together with an overview of possible approaches to predicting its outcomes, this chapter concentrates on the numerical simulation approach, and the reasons why there is currently no model that can be used to predict the erosion in hydraulic machines.

3.1 Computational Fluid Dynamics

The computational methodology used to solve mathematical models of moving fluids is known as *Computational Fluid Dynamics* (CFD). It involves defining a computational domain with given initial and boundary conditions, formulating a discretized version of the governing equations (*e.g.* the Navier-Stokes or Euler equations), together with supplementary models and constitutive laws, and solving the equations using a variety of computational techniques [52].

The most common technique for modeling the sediments in CFD simulations is termed *Lagrangian particle tracking*, whereby they are considered as point masses subject to some predefined set of forces. Given that the fluid is oftentimes solved on an Eulerian reference frame, this techniques is also known as the *Eulerian-Lagrangian approach*. Sediment transport models have also been proposed in which the particles are modeled as an Eulerian dispersed phase [58, 137], *i.e.* an *Eulerian-Eulerian approach*. Even though their low computational cost is advantageous, they are not well suited for simulating erosion nor for considering a wide range of particle sizes simultaneously, and have shown less accurate results than Lagrangian particle tracking for unsteady flows [159, 204].

The volumetric sediment concentration determines the particle-laden turbulent flow regime and therefore the kind of coupling that is present [43], as shown in Table 3.1. For very low concentration values, the particles do not influence the turbulence, so only the forces applied by the fluid on the particles need be considered, a regime known as *one-way coupled*. At higher concentration, the effects of the particles on the turbulence are no longer negligible, a regime

termed *two-way coupled*. When the particles are so close together that they start to interact, a transition to the *four-way coupled* regime occurs. A comparison between Tables 2.1 and 3.1 reveals that, for the case of erosion in hydraulic turbines, the regime is two-way coupled under most conditions, although very high concentration events, *e.g.* yearly peaks or high monsoon averages, fall under the four-way coupled regime.

Table 3.1 – Dominant Coupling Regimes in Particle-Laden Turbulent Flows [43].

Flow regime	Concentration [$\%_v$]
One-way coupled: fluid $\longrightarrow$ particle	$< 10^{-4}$
Two-way coupled: fluid $\longleftrightarrow$ particle	$10^{-4} - 10^{-1}$
Four-way coupled: fluid $\longleftrightarrow$ particle $\longleftrightarrow$ particle	$> 10^{-1}$

Simulating the effects of the transported particles on the turbulence is an area of active fundamental research [51, 127]. The *direct numerical simulation* approach commonly used to capture such effects is not applicable to macroscopic domains at high Reynolds numbers. Another approach has been proposed in which the turbulence attenuation or augmentation, function of the particle size, is considered by means of source terms on the turbulence transport equations [129]. However, no article in the literature of erosion simulation has ever considered the influence of the sediments on the fluid turbulence. Furthermore, the effect of the particles on the mean flow, sometimes wrongly referred to as two-way coupling, has been shown to be completely negligible for concentrations as high as 5,000 ppm [135], which is about 0.19 $\%_v$ for typical sediment densities.

In short, when considering the Lagrangian particle tracking approach, neglecting the influence of the sediments on the turbulence, it can be said that under most conditions relevant to the erosion of hydraulic turbines only the effect of the fluid on the sediments is important, *i.e.* one-way coupling applies. The effects of the interparticle interactions become relevant at the aforementioned very high concentration events only.

The information provided by the particle tracking is combined with one of several available erosion correlations in order to estimate the erosion on the domain walls. That is to say, whenever the trajectory of a sediment intersects a wall, a given amount of eroded mass is accumulated at that wall position based on some of the impact parameters, such as the velocity or angle. Similarly, the sediment rebound velocity is calculated by means of correlations for the *restitution coefficients*, which are the fraction of the initial sediment velocity, parallel and perpendicular to the wall, which is conserved after the impact.

3.1.1 Examples of CFD Simulations of Erosion

Almost all of the examples of CFD erosion simulations deal with a single test case: the erosion of a flat plate impinged by a slurry jet [135, 136, 148, 149, 194, 202]. This test case is the simplest expression of the erosion problem: it is steady and characterized by an elementary geometry,

yet it involves a variety of impact velocities and angles, turbulent dispersion and sediment size and shape effects.

In the above cited investigations, a total of eleven different erosion correlations and four different restitution coefficient correlations were tested. Lagrangian particle tracking is used in all studies, together with a one-way coupled scheme that takes into account the turbulent dispersion of the sediments; five different turbulence models were tested.

Wang et al. [194] compared the CFD results with experimental data for the distribution of erosion on the plate. Among the six erosion correlations tested, three resulted in *qualitative* disagreement with the experiment, whereas the other three resulted in a reasonable *quantitative* agreement. The authors highlight the importance of considering the turbulence effects on the sediment dispersion.

Nguyen et al. [149] validated their sediment transport model, and then studied the effect of the geometry on the sediment impact condition distributions and subsequent erosion rate. Their experimental eroded plate geometry was used to run independent simulations at four different instants of the process, from the initial flat geometry to a very eroded state. The experimental erosion rate was shown to decrease over time as a consequence of the change in impact conditions implied by the geometry and flow alteration. This trend was well captured by their CFD simulations, although the average absolute error of the erosion rate was 64 %.

In a more recent study, Nguyen et al. [148] investigated the effect of the particle size on the shape of the erosion scar. Whereas large particles tend to impact near the jet axis, forming a kind of Gaussian erosion depth distribution, smaller particles are deviated by the stagnation region and form a torus-shaped scar. Somewhat surprisingly, the simulated erosion rate matches their experimental results to within 5 %.

Zhang et al. [202] studied in some detail the effect of turbulence models, near-wall treatment and grid refinement on the resulting impact condition distributions and erosion rate. The *Standard k-ϵ model* with *wall function* provided the most accurate results, even compared with more sophisticated models such as the *Realizable k-ϵ*, *RNG k-ϵ*, *SST k-ω* and *Reynolds Stress Model*. The authors recommend using different mesh refinement degrees and near-wall treatments depending on the sediment size. They also compared four restitution coefficient correlations and found negligible variation in the erosion rate predictions. The most accurate model combination they report resulted in an average error in the erosion rate distribution of about 45 %.

Perhaps the most significant recent investigation was performed by Messa et al. [135], who did a systematic study of the effect of a variety of models and parameters commonly used in CFD erosion simulations. Importantly, they used a range of different experimental data sets in the literature to assess the erosion predictions; they did not run any experiments, nor are they proponents of an erosion correlation. First, they corroborated the aforementioned finding related to the restitution coefficients: they have a negligible effect on the results.

Even assuming that the impacts are perfectly elastic, *i.e.* that the particle velocity magnitude remains unchanged, has no effect on the erosion results. This is so because shortly after each impact the sediment velocity is overridden by its interaction with the flow. They also found that the turbulence model and near-wall treatment has a mild influence on the results. Furthermore, the effect of the sediments on the mean flow is negligible even for relatively large particles of $d = 150$ μm at a high concentration of 5,000 ppm; therefore they justify the use of one-way coupling. Moreover, it was found that drag is the dominant force in the turbulent transport of the sediments; taking into consideration the sediment shape on the drag force estimation significantly alters the transport behavior and erosion predictions.

The authors report that the most significant source of uncertainty is the erosion correlation used. They systematically compared the erosion rate predictions of the four most popular erosion correlations, including the one used in the investigations of Nguyen et al. [148, 149]; a total of 13 different test cases covering a wide range of test conditions were used for the comparison. The results speak by themselves: the *best* correlation achieves an average absolute error of 178 %, that decreases to 40 % if one only takes into account the best 6 test case results out of the 13 reported. They conclude that this level of accuracy is the best than can be obtained from CFD simulations for the time being.

CFD Erosion Simulations of Hydraulic Turbines

If for the simple flat plate erosion by an impinging jet the CFD simulation results achieve qualitative agreement with significant absolute error, the simulations of hydraulic turbine erosion do no better. In fact, very few results can be found in the literature.

Neopane [145] performed the first CFD simulations of the erosion of a Francis turbine. No quantitative comparison with experiments was presented, and it is hard to say that there is even a qualitative agreement with the known behavior of erosion. As presented in Figure 3.1, the predicted erosion appears in isolated spots, or saturated regions, unlike the smooth fields that would be expected. Not only is it a matter of the two erosion correlations employed: in retrospect, their numerical setup seems to be incapable of accurately simulating the hydrodynamics, mainly because of the unacceptable quality of the discretization grid employed.

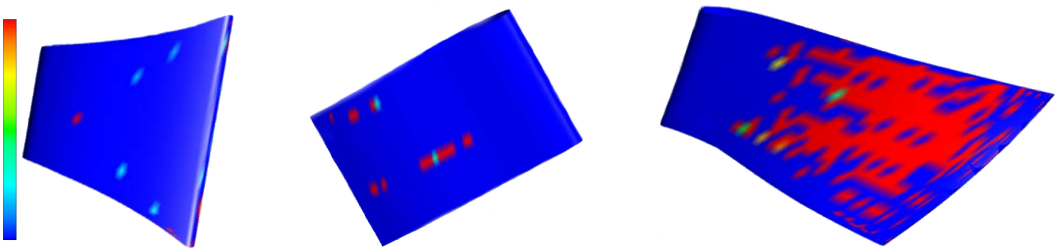

(a) Stay vane. (b) Guide vane. (c) Runner blade.

Figure 3.1 – Erosion rate distribution on the components of a Francis turbine [145].

Chongji et al. [28] used a multiphase approach and particle tracking to simulate the free-suface flow in a Pelton turbine injector. The steady-state simulation considered only particles with $d = 50$ μm, and a rather simple erosion correlation. Perhaps this explains their results, which are inconsistent with what is known about the erosion of these components. Instead of having the maximum amount of erosion near the needle tip, where the velocity is highest, it appears at the needle base. Furthermore, the erosion distribution does not follow the expected axisymmetry; instead, unexplained hot spots with no correspondence with reality appear on both the needle and the nozzle, as illustrated in Figures 3.2a and 3.2b.

Recently, Messa et al. [138] performed similar simulations with two different erosion correlations; their results are presented in Figures 3.2c and 3.2d. The erosion distribution follows the expected axisymmetry, and increases towards the nozzle exit where the flow velocity is highest. The global erosion ratio is studied as a function of the injector opening, revealing that the maximum wear occurs when it is almost closed, in agreement with experimental trends. The relative difference between the erosion rate predictions from the two correlations used amounts to 30-50 %. However, no quantitative comparison with experimental measurements is performed.

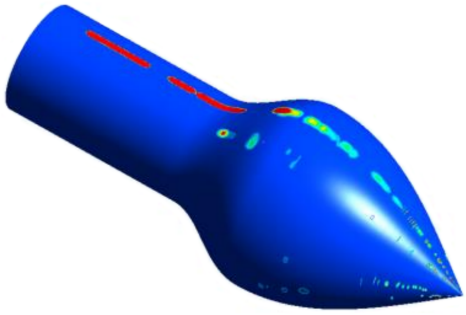

(a) Injector needle [28].

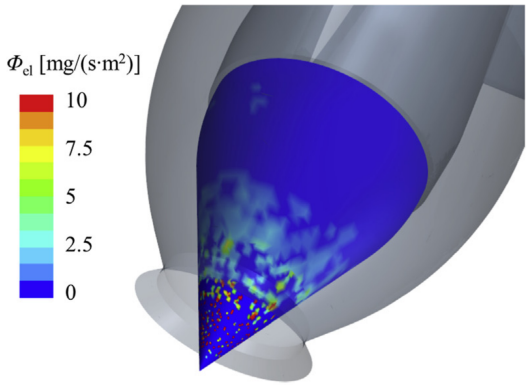

(c) Injector needle [138].

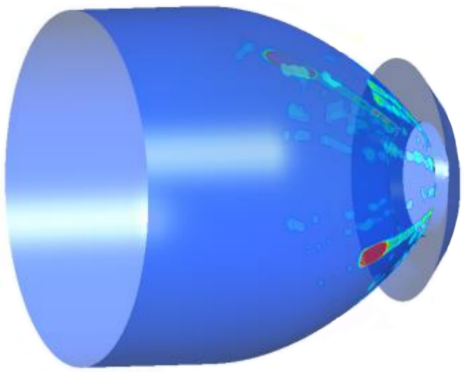

(b) Injector nozzle [28].

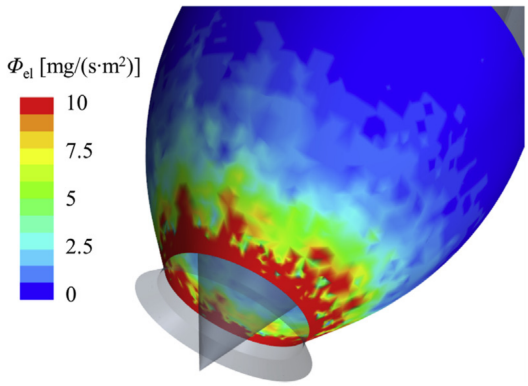

(d) Injector nozzle [138].

Figure 3.2 – Erosion rate distribution on the components of a Pelton turbine injector [28, 138].

The unsteady free-surface flow characteristic of the interaction between the jet and the rotating Pelton buckets is much more complex than the steady-state injector flow. Not a single erosion simulation of a Pelton bucket has been report to date in the literature, except for the articles associated with this thesis.

3.2 Computational Solid Mechanics

The computational methodology used to solve mathematical models that describe the mechanics of solid bodies is known as *Computational Solid Mechanics* (CSM). Similar to CFD, CSM involves defining a domain, its initial and boundary conditions, formulating the governing equations, generating a discretization of the system and solving the resulting set of equations with the help of a variety of computational techniques.

The erosion phenomenon can be studied using CSM by performing simulations of the sediment impacts against the target material, although neglecting the transporting fluid. In order to obtain accurate results, the governing equations must appropriately reflect the material behavior. As highlighted in Section 2.2, important aspects include: strain hardening, strain rate hardening, thermal softening, friction and adiabatic thermoplastic heating. Most of the investigations in the literature [38, 44, 121, 122, 125, 180, 196, 197, 199, 200] use the *Johnson-Cook model* [88], fully detailed in Section 6.5.3, coupled with thermal and frictional models to capture these aspects of the problem. Other material models, such as the *Cowper-Symonds model* [31], have also been used [12, 121, 122, 180].

The *Finite Element Method* (FEM) is by far the most common discretization method in CSM. For the specific case of solid impact simulations, *Smoothed Particle Hydrodynamics* (SPH) and other particle methods have also been used [38, 116, 180, 197]; discretizing the domain with particles bypasses the excessive mesh distortion and tangling that becomes problematic in FEM within the highly distorted region being impacted [197, 200].

CSM impact simulations have been used to study the response of materials to the parameters influencing the erosion process, providing insight into the governing mechanisms. These results generally compare well with experiments that use air as conveying medium, since in that case the fluid influence is negligible. Three examples of impact simulation results are illustrated in Figure 3.3.

Molinari et al. [140] studied high velocity impacts on mild steel plates; the impacting particles were modeled as spherical and elasto-plastic. It was found that shear banding dominates at velocities above 1,300 $m \cdot s^{-1}$, whereas at much lower velocities plastic flow is most important, with friction playing a significant role at low impact angles. Similar conclusions were drawn by Yildirim et al. [200] for copper using similar modeling assumptions; a snapshot of one of the high velocity impacts is presented in Figure 3.3a.

ElTobgy et al. [44] modeled the erosion of titanium alloy Ti-6Al-4V impacted at several angles

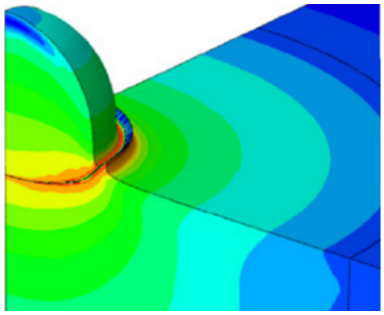

(a) Stress distribution during normal impact at $v = 500\ \mathrm{m \cdot s^{-1}}$ on copper [200].

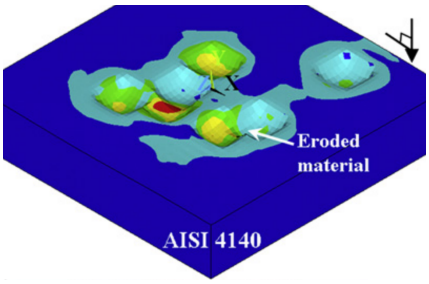

(b) Stress distribution after seven normal impacts at $v = 200\ \mathrm{m \cdot s^{-1}}$ on AISI 4140 [12].

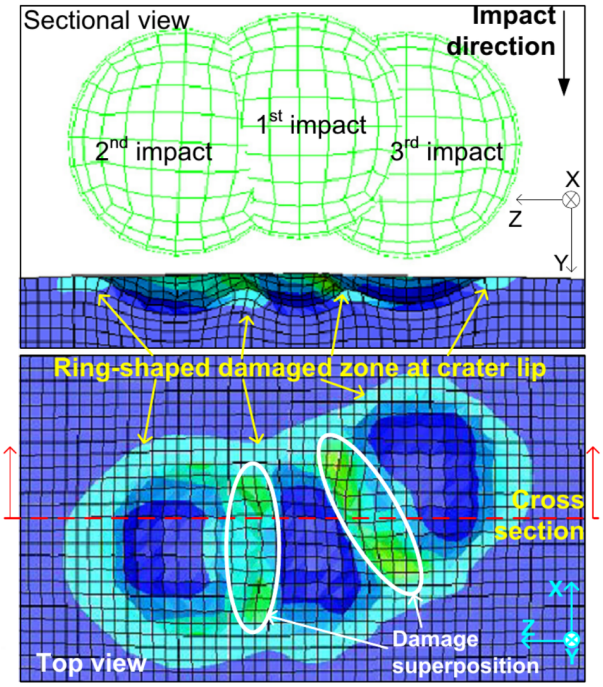

(c) Damage distribution after 3 impacts at $\alpha = 90°$ and $v = 500\ \mathrm{m \cdot s^{-1}}$ on AISI 4340 steel [121].

Figure 3.3 – Examples of solid particle impact simulation results.

and velocities by particles assumed spherical and rigid. The erosion velocity exponent n_v was predicted to within 5 % of the experimental value; the angle dependence behavior agrees qualitatively with the experiment, but no quantitative comparison is reported. For the same case and under identical modeling assumptions, Wang et al. [196, 197] predicted n_v to within 4 %; the angle dependence behavior qualitatively agrees with the experiment, although a uniform overprediction of about 30 % was found.

Some investigations improve upon the assumption of spherical particles. Takaffoli et al. [180] simulated the impact of aluminum alloy Al6061-T6 by rigid rhomboidal particles, and successfully reproduced the corresponding experimental crater shapes at several angles and velocities. Liu et al. [125] verified that sharper particles, modeled as rigid polyhedra, increase the erosion of Ti-6Al-4V at lower impact angles due to their cutting potential, similar to the results of Dong et al. [38], where additionally a transition in erosion mechanism is evidenced.

The assumption of rigid particles has also been bypassed in some instances. Yildirim et al. [199] investigated the effect of the surface roughness on the impact of circular elasto-plastic particles on copper. It was found that the roughness implies significant stress concentration, depending on the ratio between its length scale and the impacting particle diameter. Li et al. [121, 122] simulated the impact of AISI 4340 alloy steel by spherical elasto-plastic particles at high velocities. The crater volumes are compared with experimental data, revealing an error below 10 %. The overlap region between craters is highlighted as the most erosion-prone

location, as seen in Figure 3.3c; furthermore, the crater lips act as stress concentrators for subsequent impacts.

Perhaps the most advanced simulation to date was reported by Balu et al. [12]. Elastic polyhedral particles impacting coated and uncoated AISI 4140 alloy steel are simulated; the coating material is nickel-tungsten carbide. Figure 3.3b illustrates the bare steel sample after seven impacts at normal incidence. Quantitative comparison with experiments yields an average error for the erosion rate as a function of impact angle of 6 % for the bare steel case, and 24 % for the coated steel case.

Concerning the application of CSM to the problem of erosion in hydraulic machines, there are no investigations in the literature dealing with 13Cr-4Ni stainless steel. However, the relevant impact conditions for hydraulic turbines, namely the range of angles, velocities and diameters, overlap with some of the aforementioned investigations, some of which also deal with steel alloys. This, together with the rather accurate erosion results that can be obtained, indicate that CSM may be a valuable tool in studying the erosion of hydraulic machines. The main problem is that these simulations neglect the important effect of water and are limited to a microscopic domain.

3.3 SPHEROS

In 2010 the Laboratory for Hydraulic Machines (LMH) at EPFL begun development of a numerical simulation code, SPHEROS, designed to study the erosion of hydraulic turbines. Governing equations for both the fluid dynamics and the solid mechanics are fully coupled, and solved in the framework of the *Finite Volume Particle Method* (FVPM), all the details of which are given in Chapter 7.

The great advantage is that it is, in theory, possible to simulate the macroscopic erosion of a component without falling back on uncertain erosion correlations; instead, the solid mechanics model is solved, including plastic deformation and damage accumulation, as well as material removal, to estimate the erosion process.

Consider a water jet of $D_0 = 5$ mm, carrying sediments with $d = 300$ μm, that impinges on a flat plate. The 2D version of such test case has been simulated with SPHEROS, as presented in Figure 3.4. However, the resulting model is too expensive to be simulated under realistic conditions. First, the impact simulations have to be done in 3D to accurately represent the phenomenon, greatly increasing the computational cost. Second, the solid discretization needs to be significantly higher than what is presented in Figure 3.4, further skyrocketing the simulation cost. Third, the time frame for achieving a steady-state erosion rate distribution over the surface of interest is much greater than what is feasible to run. These complications are much more significant when dealing with larger cases, such as a turbine, a consequence of the multiscale nature of the problem.

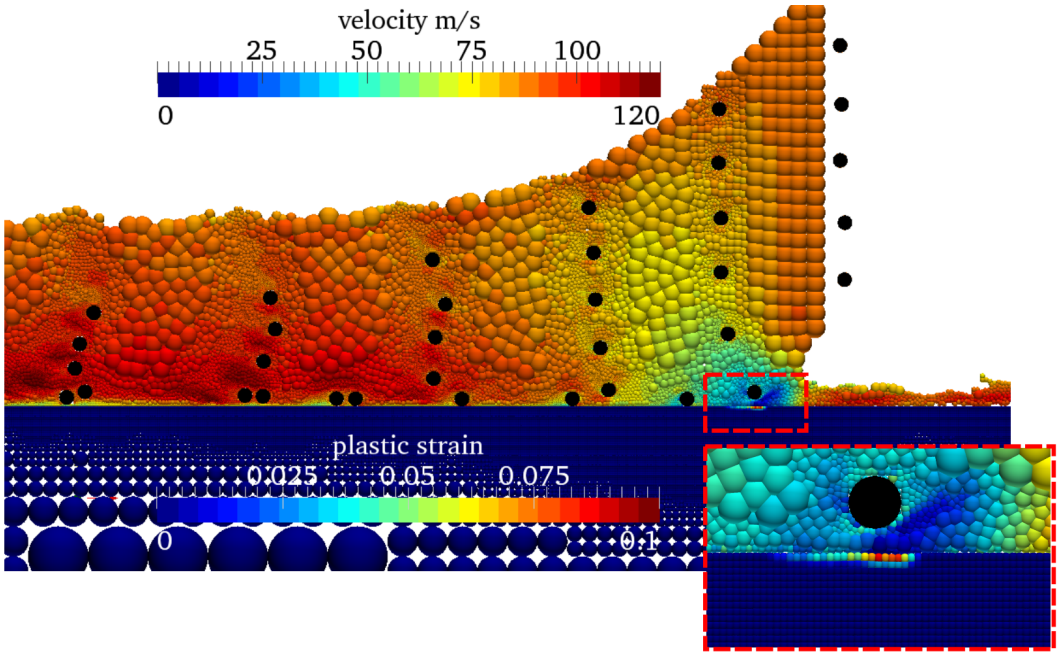

Figure 3.4 – 2D simulation of the erosion of a flat plate by an impinging slurry jet [83]. The solid plate is colored by plastic strain, the fluid according to its velocity magnitude, and the sediments are black. The jet impinges at 45° from right to left.

3.3.1 Author Contribution Statement

The main achievement of this thesis is formulating the erosion problem in a way that allows a solution, even for the challenging case of a rotating Pelton turbine runner. However, these results would not have been possible without the previous and concurrent work of my teammates, as explained hereafter.

Ebrahim Jahanbakhsh wrote most of SPHEROS as part of his Ph.D. thesis [83], with the collaboration of Christian Vessaz [191]. Before the present thesis, SPHEROS was a functional software that had been validated on a number of test cases, and had been parallelized for use on CPU supercomputers. During the initial two years of this work, Siamak Alimirzazadeh ported the code, with the help of Ebrahim Jahanbakhsh, to *Graphics Processing Units* (GPUs), achieving a significantly better performance, see Chapter 7, that was instrumental for the large test cases presented in Chapters 12 and 13.

At the start of this thesis, the models implemented in SPHEROS were not appropriate for the problem at hand, or were inexistent. Part of my work consisted in selecting, implementing and validating physical model, such as the Johnson-Cook constitutive and damage models, an improved equation of state, the k-ϵ turbulence model and wall function, friction and thermal models, and a turbulent sediment transport model. I also ported these models into the GPU version of the code, according to a preestablished data structure.

These models are not novel, and were only a prerequisite for the most significant contribution of my work: the formulation of a *multiscale model of erosion*, its validation and application to problems that would have otherwise been intractable, improving the state-of-the-art on the modeling of erosion both in terms of accuracy and scope.

4 Problem Statement

This chapter synthesizes the gist of the present thesis, having already introduced in great detail the problem of erosion and the current state-of-the-art on its modeling. After presenting the overall project goal, the research topic is delimited to allow for the formulation of concrete, specific objectives. Then, the chapters that constitute the present document, arranged into four blocks, are outlined.

4.1 Goal and Objectives

As detailed in Section 2.2.2, the erosion of hydraulic turbines generates significant losses of revenue due to decreased efficiency and frequent maintenance periods. In order to engineer an *optimal turbine design* for erosion-prone sites, it is necessary to have the technical capacity to predict the erosion rate of a given turbine design under the specific site conditions; this would allow assessing the competing mitigation strategies in view of their costs and predicted erosion reduction potential.

An analogous situation can be drawn with respect to the choices faced by the plant owner: Provided the aforementioned technical capacity is available, the *optimal operation strategy* for a specific turbine and site can be established.

With this in mind, the *overarching goal* of the present work is to contribute to the development of the technical capacity to predict the erosion process of hydraulic turbines, with envisioned applications in the optimization of their design and operation strategy.

The aforementioned goal is very broad and ambitious, so some clarifications are in order. The scope of this thesis is limited to *uncoated Pelton turbines* only: By restricting the turbine type and material, the involved erosion mechanisms and the range of the governing parameters is greatly decreased, allowing for an in-depth investigation. The numerical simulation approach is the main tool, supplemented by a few experiments that are required to find some of the model material parameters.

The *specific objectives* of this work, in line with the aforementioned goal, are as follows:

- Perform a broad literature review to understand the erosion phenomenon, the main influencing parameters, and the state-of-the-art on its numerical modeling.
- Select, implement and validate all the physical models required to accurately simulate the sediment turbulent transport and impact processes.
- Develop a novel multiscale model of erosion, in line with the multiscale nature of the phenomenon, to allow solving realistic problems.
- Validate the model in a series of case studies, ranging from very simple configurations to full-scale Pelton turbines.

4.2 Thesis Outline

The present work is organized into four main parts, as outlined hereafter.

Part I contains the general introduction to the problem. Chapter 1 presents an overview of the topic and highlights the global motivation for the investigation. Chapter 2 is a detailed literature review that contains all the introductory information required to fully understand the rest of the work. Chapter 3 contains a summary of the state-of-the-art on the modeling of erosion, laying the necessary foundations upon which the proposed model is built. Having introduced all the fundamental aspects, Chapter 4 states the goal and objectives of this contribution.

Part II describes the methodology. First, the novel multiscale model of erosion is presented in Chapter 5, together with a discussion on the simplifications it implies. Then, the mathematical formulation of the model is introduced in Chapter 6, including a discussion on the modeling assumptions. Chapter 7 details the Finite Volume Particle Method, the discretization framework that is used to solve the computational model. A short description of the computational resources used throughout this work is contained in Chapter 8, whereas Chapter 9 presents the experiments used to characterize the materials simulated.

Part III is constituted by the four case studies used to assess and validate the proposed erosion model. Chapter 10 describes the first case study, the impingement of a jet on a flat plate, where the most basic model features are tested and validated. The second case study, the impingement of a jet on a 2D static bucket geometry, is introduced in Chapter 11; it demonstrates one of the model features, projective integration. Having achieved successful results in these simplified cases, Chapter 12 presents the third case study, the jet impingement on a 3D static prototype-scale Pelton bucket of medium size, serving to validate the model on an industrial-scale problem. The fourth case study, involving a 3D rotating prototype-scale Pelton turbine of large size impinged by a jet, is described in Chapter 13, providing the final model validation on a more challenging industrial-scale erosion problem.

Part IV contains the overall thesis conclusions. Chapter 14 recapitulates the main outcomes and conclusions of the present work in view of the case study results. Additionally, based on these, a series of perspectives and recommendations is drawn in Chapter 15.

Methodology Part II

The underlying physical laws necessary for the mathematical theory are thus completely known, and the difficulty is only that the exact application of these laws leads to equations much too complicated to be soluble.

—Paul Dirac

5 A Multiscale Model of Erosion

In this chapter a novel multiscale model of erosion is introduced. However, all the details of the computational model, including the mathematical formulation of the submodels, are presented in Chapter 6. Part of the contents of this chapter have already been published in Leguizamón et al. [112, 115].

5.1 On the Multiscale Character of the Erosion Phenomenon

The erosive wear of hydraulic turbines has an inherently *multiscale character*: Whereas it is a very gradual process that affects large surfaces in the time frame of hundreds or thousands of hours of operation, it is the direct consequence of uncountable microscopic sediment impacts that last a fraction of a microsecond. In other words, it is a process that spans some 12 orders of magnitude in time and 5 in space.

One additional complication is the sheer number of sediments involved. Consider a large Pelton turbine like the ones used in the San Carlos hydropower station in Colombia. The nominal discharge per turbine is $Q = 33.37\ \mathrm{m}^3 \cdot \mathrm{s}^{-1}$ [75], with an average sediment concentration of only $0.02\ \%_w$ [107] and median diameter $d_{50} = 14.1\ \mu\mathrm{m}$ [78]. This means that, on average, each turbine receives some 17.1×10^{11} sediments *per second, i.e.* one order of magnitude greater than the number of stars in the Milky Way galaxy plus the number of neurons in the human brain, each of them estimated at about 1×10^{11} [61, 192].

These two circumstances make the approach presented in Section 3.3, where both the fluid dynamics and the solid mechanics are solved throughout the domain in a coupled manner, prohibitively expensive for the decades to come. Figure 5.1 illustrates the time and length scales present in the simulation of the erosion process of a Pelton turbine, together with the two main subprocesses: the sediment impacts and the turbulent transport. The left and right length scale bounds represent the discretization size required to achieve converged results and the overall domain size, respectively, for each of the two subprocesses. Similarly, the lower and upper time scale bounds of each box represent the time step required for stability and the

overall simulation duration, respectively.

In short, if one were to discretize the whole runner surface with the extremely fine discretization size required to properly model the sediment impacts, the number of nodes would be overwhelming. Similarly, the time step, which is of the order of 0.2 ns, would be too restrictive for the simulation of the hydrodynamics, let alone the long-term erosion process.

As reviewed in Section 2.3, there are a number of techniques that have been designed to tackle multiscale problems. The Pelton turbine erosion is a prime candidate for such a treatment because of the marked *scale separation* that characterizes it: The two subprocesses involved are fairly separated in both space and time scales, and the time frame in which the erosion becomes significant is several orders of magnitude greater than the time scales of the two subprocesses that define it. Furthermore, the details of one scale are not necessarily relevant for the others, *e.g.* the elastic deformations that would continuously propagate through the turbine as a consequence of the sediment impacts are almost imperceptible to the flow.

It looks promising to separate the sediment impacts and their transport by the fluid into two distinct submodels. By solving them independently, the mismatch of time and length scales is no longer a problem: The short time steps and discretization size are restricted to where they are required the most, the simulation of the sediment impacts, whereas the simulation of the hydrodynamics takes advantage of a larger time step and discretization size, in line with their slow macroscopic dynamics. The main challenge is to formulate a coupling strategy between the submodels such that the original problem is reproduced accurately.

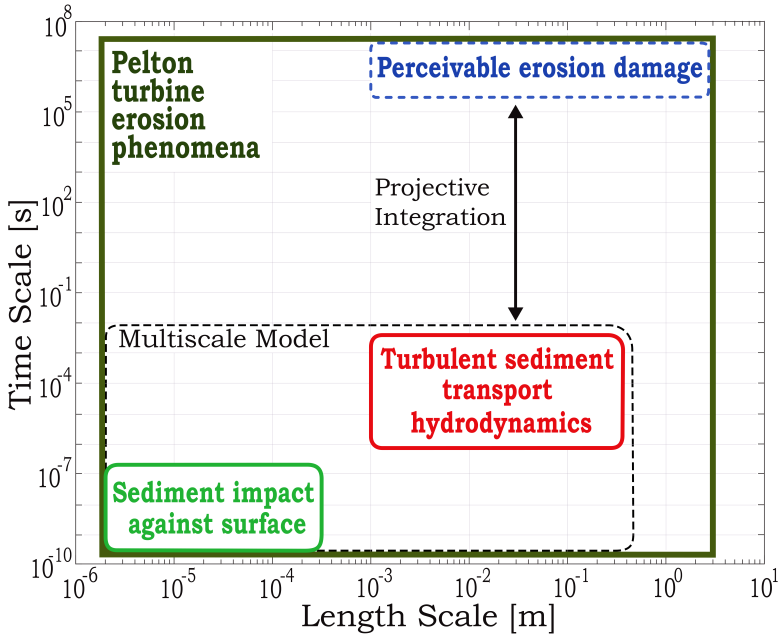

Figure 5.1 – Time and length scales involved in the simulation of the erosion of a Pelton turbine. The proposed multiscale coupling and projective integration are highlighted.

As illustrated in Figure 5.1, a multiscale model of erosion is proposed. It is composed of a *microscale model*, which considers the sediment impacts, and a *macroscale model*, which describes the turbulent sediment transport. Furthermore, a *projective integration* scheme is proposed to bridge the time scale separation towards perceivable erosion damage.

In what follows, the proposed multiscale model will be described in view of the discretization scheme used, see Chapter 7. FVPM is a particle-based method, so the computational nodes used to discretize the domain will be termed *FVPM particles* hereafter. However, note that the proposed multiscale model is independent of the discretization scheme used to solve the governing equations.

5.2 Sequential Multiscale Coupling Algorithm

Initially a concurrent multiscale algorithm was considered: For each FVPM particle used to discretize the macroscopic erodible surface, an independent microscopic domain is defined in which the detailed sediment impacts are carried out. Due to scale separation, each microscopic domain is significantly smaller than the associated macroscopic FVPM particle, such that the total number of particles is not excessive. Whenever an impact is detected by a macroscale FVPM particle, a detailed sediment impact simulation is performed in the associated microscale domain, such that by the end of the macroscale simulation the surface erosion is well described by the set of microscale domains.

This idea was abandoned because the cost of performing detailed impact simulations for every impact instance renders such a model impractical; an enormous number of impacts occurs for every problem of interest. This same fact renders a *sequential multiscale coupling* algorithm the best approach for the erosion problem.

Consider the 1×10^{12} sediment impacts that may occur every second on a large Pelton runner. Factoring out the parameters that define the impact, there is a kind of *similarity* between impact instances. That is to say, two impacts at identical conditions that occur at different locations along the runner surface at different times are in principle similar, so precomputing a given set of impacts might provide enough information to close the macroscopic model.

5.2.1 Microscale Model

The microscale model describes the details of the sediment impacts against the solid being eroded; see Section 6.5 for the formulation of the solid model. The fluid is neglected in the microscale, as discussed in Section 5.4.

The microscale model is used to characterize the space of impact conditions in terms of the erosion ratio e_r, and the restitution coefficients for the parallel and perpendicular velocities, $RC_{\parallel}$ and $RC_{\perp}$ respectively. This characterization is performed using independent microscale simulations at constant impact conditions, for a given set of impact condition combinations.

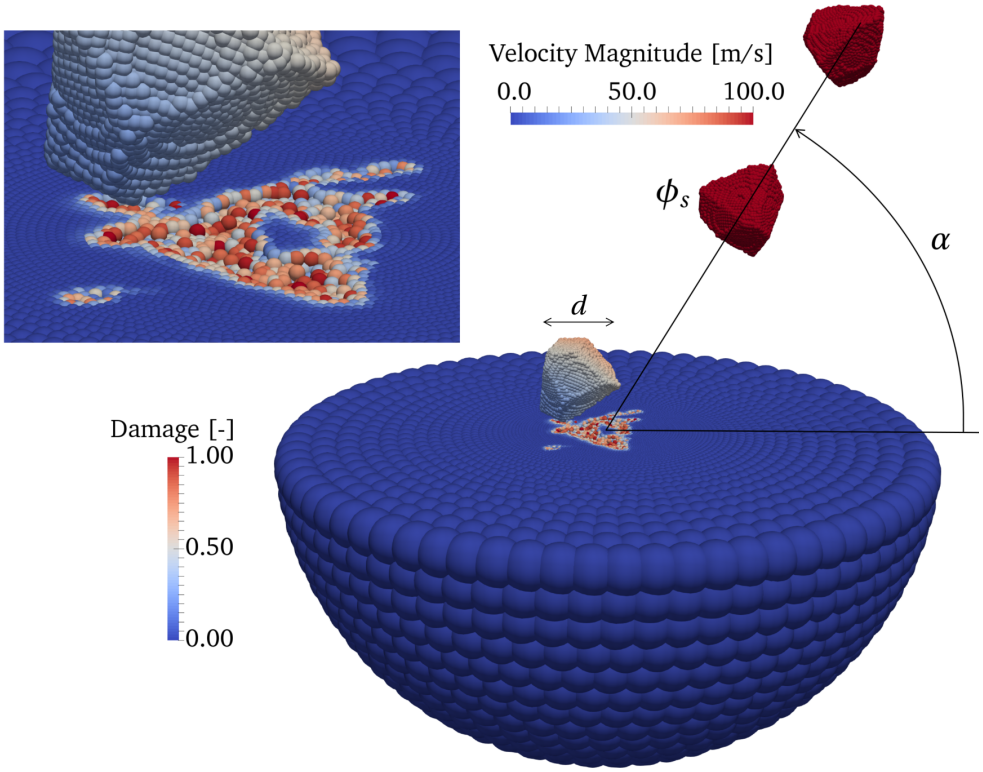

Figure 5.2 – Computational domain of a microscale simulation after 20 impacts. The FVPM particles are colored according to velocity magnitude for the sediments and damage parameter δ for the solid specimen.

Figure 5.2 illustrates the computational domain of a microscale simulation: It comprises a hemispherical solid specimen that is successively impacted by sediments of characteristic size d whose shape is defined by the parameter ϕ_s, see Appendix B.1; the impacts occur at a fixed velocity v and angle α. The initial position of each sediment is displaced by a random amount in such a way that they impact the solid within a circular area of size comparable to d. A complete convergence analysis has been performed to determine the discretization resolution, distance between incoming sediments, domain size and impact area size; see Appendix B.2 for the details.

The successive impacts cause plastic deformation on the material, which is related to a damage parameter δ according to the material formulation in Section 6.5. When an FVPM particle is completely damaged, $\delta > 1.0$, it is removed from the system, *i.e.* its associated mass is said to have been eroded. The erosion ratio is defined as

$$e_r = \frac{\partial m_e}{\partial m_s}, \tag{5.1}$$

where m_e is the eroded mass and m_s is the impacting sediment mass. In practice, an average e_r is calculated as the slope of the graph of accumulated eroded mass as a function of accumulated sediment mass that has impacted. As presented in Figure 5.3a, this slope becomes

linear after an initial incubation period where the material accumulates plastic deformation without eroding much. Depending on the impact conditions, between 50 and 100 impacts are required to accurately estimate this *steady-state erosion ratio*.

In Section 2.2.1 is was shown that, for a fixed material combination, the erosion ratio can be written as $e_r = f(\alpha, v, \phi_s, d)$, see Equation 2.5. In general, e_r can be calculated by running microscale simulations for a large set of impact conditions, *i.e.* combinations of α, v, ϕ_s, and d, in order to have the required information to close the macroscale model. However, one can take advantage of the known features of the erosion ratio to drastically reduce the number of points that need to be probed. For example, given the orthogonality between the impact angle and velocity effects, $e_r(\alpha, v)$ can be characterized by first calculating $e_r(\alpha, v_{ref})$ at a reference impact velocity v_{ref}; then, the velocity dependence is characterized by computing $e_r(\alpha_{ref}, v) = kv^{n_v}$ at a reference impact angle α_{ref}, which can be used to fit the velocity exponent n_v. The erosion ratio is then computed as

$$e_r(\alpha, v) = \left(\frac{v}{v_{ref}}\right)^{n_v} \cdot e_r(\alpha, v_{ref}). \tag{5.2}$$

Figure 5.3b illustrates the approach: $e_r(\alpha, v_{ref})$ is calculated by interpolation between 5 microscale simulations results, and then Equation 5.2 is used to span the rest of the space; the velocity exponent n_v is calculated using 4 microscale simulation results; a total of 8 microscale simulations are used to reconstruct $e_r(\alpha, v)$.

It is straightforward to perform a similar reconstruction by interpolation for the whole space spanned by the parameters (α, v, ϕ_s, d). However, given that the most important parameters

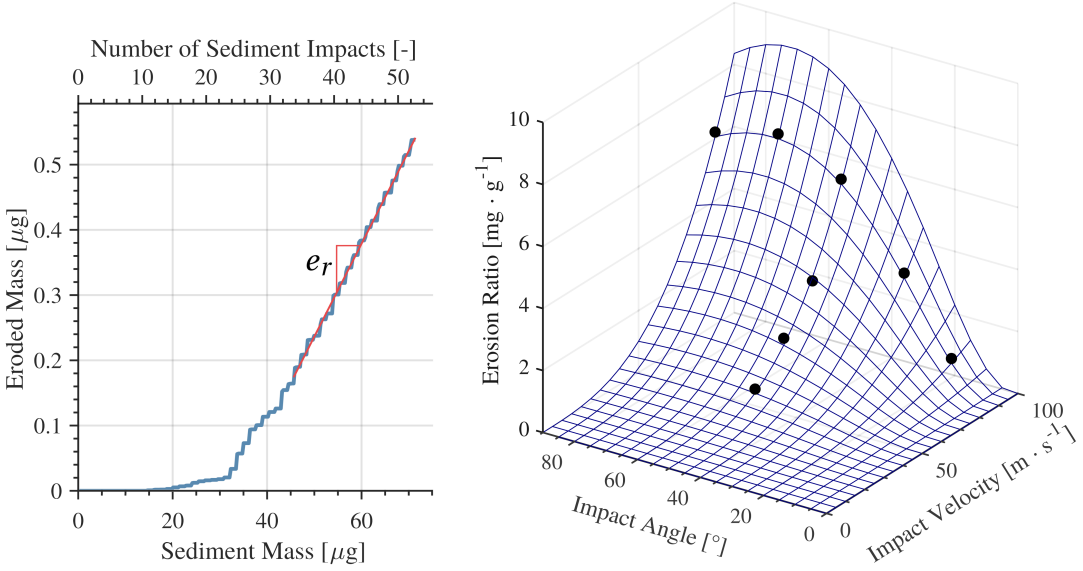

(a) Estimation of the erosion ratio e_r for a single impact condition (α, v, ϕ_s, d).

(b) Erosion ratio $e_r(\alpha, v)$ reconstruction based on 8 microscale model results.

Figure 5.3 – Examples of the microscale model erosion ratio results.

are α and v, to reduce the computational burden microscale simulations are only performed for a representative value of ϕ_s and d, depending on the case study. The error induced by this simplification is expected to be small. On the one hand, the sediment size has a very mild effect on e_r, as revealed by Equation 2.5. On the other hand, choosing a representative sediment shape ϕ_s means that the greater damage caused by sharper sediments is compensated by the lower damage caused by rounder ones, at least to some extent.

A similar reconstruction by interpolation is performed for the restitution coefficients $RC_\parallel(\alpha, v)$ and $RC_\perp(\alpha, v)$. For a given microscale simulation, the velocity of all impacted sediments is stored before and after impact. Then, the restitution coefficients are calculated as

$$RC_\parallel = \frac{\overline{v_{\parallel_2}}}{v_{\parallel_1}}, \qquad RC_\perp = \frac{\overline{v_{\perp_2}}}{v_{\perp_1}}, \tag{5.3}$$

where $\overline{v_{\parallel_2}}$ is the average parallel velocity after impact, $v_{\parallel_1}$ is the parallel velocity before impact, and similarly for the perpendicular components.

Once all the necessary microscale simulations have been run, enough detailed information has been collected in terms of $e_r(\alpha, v)$, $RC_\parallel(\alpha, v)$ and $RC_\perp(\alpha, v)$ to provide closure to the macroscale model.

5.2.2 Macroscale Model

The macroscale model describes the details of the turbulent sediment transport and the erosion accumulation on the macroscopic component under study; see Section 6.2 for the formulation of the fluid and sediment transport models.

The computational domain of a macroscale simulation is comprised of a set of FVPM particles that discretize the surface being eroded, the fluid and the sediments. Figure 5.4 illustrates the example of a jet impinging on a flat plate. Throughout the simulation, FVPM fluid particles are injected through the domain inlet according to a prescribed mass flux. Similarly, the sediments are injected at fixed intervals that are calculated such that the predefined sediment concentration is respected; their diameters are selected randomly following a prescribed size distribution.

During the transport process sediments tend to impact the wall. Whenever a contact is detected between a sediment and a wall particle, the microscale results are used to determine the outcome of the impact. For a given impact condition (α_i, v_i), the rebound velocity is calculated as $v_j = v_{i,\parallel} \cdot RC_\parallel(\alpha_i, v_i) \cdot \hat{\parallel} - v_{i,\perp} \cdot RC_\perp(\alpha_i, v_i) \cdot \hat{\perp}$, where the velocity has been decomposed into parallel and perpendicular components according to the unit vectors $\hat{\parallel}$ and $\hat{\perp}$.

Similarly, the eroded mass is calculated as $m_e = m_i \cdot e_r(\alpha_i, v_i)$, where m_i is the mass of the impacting sediment. The wall particle stores the impact conditions (α_i, v_i) as well as a cumulative value of eroded mass m_e.

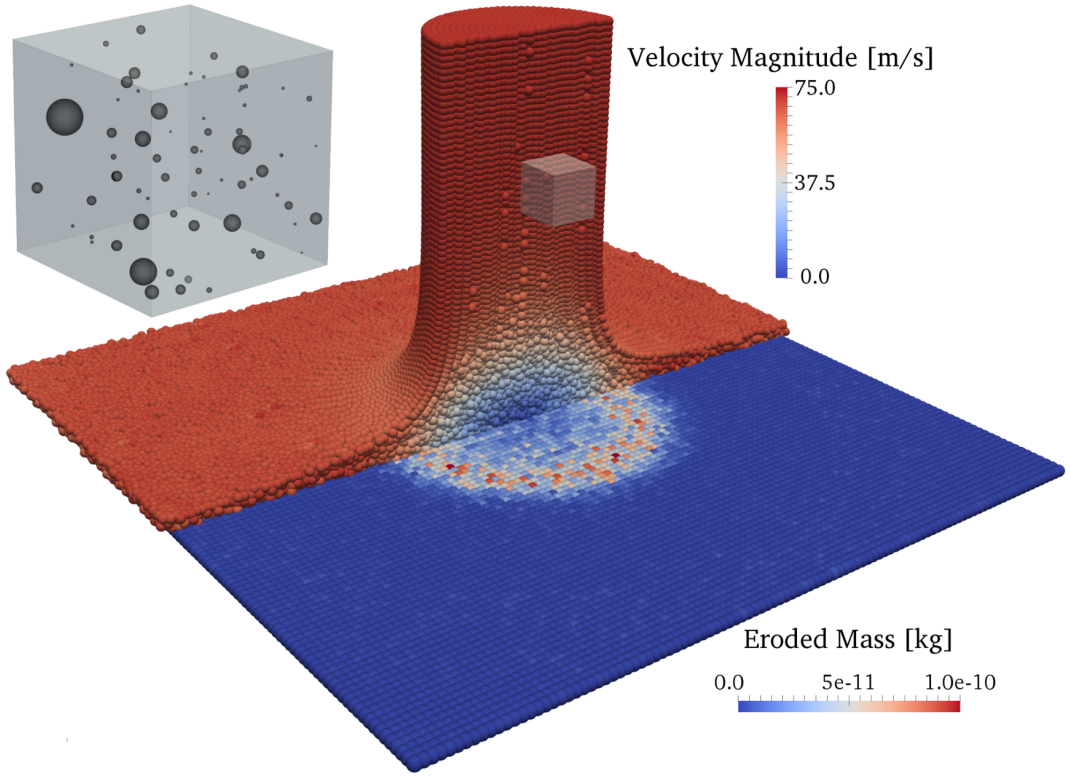

Figure 5.4 – Macroscale simulation computational domain example: jet impingement on a flat plate. Only the sediments within a cube are rendered.

The turbulent sediment transport has a chaotic character, such that the macroscale model shares some characteristics with a Monte Carlo method. Indeed, a large number of sediments have to be injected through the domain inlet before the erosion and impact condition distributions on the wall converge. Depending on the case study, between 5×10^4 and 1×10^6 sediments are simulated.

As a summary, the proposed multiscale model is schematically represented in Figure 5.5.

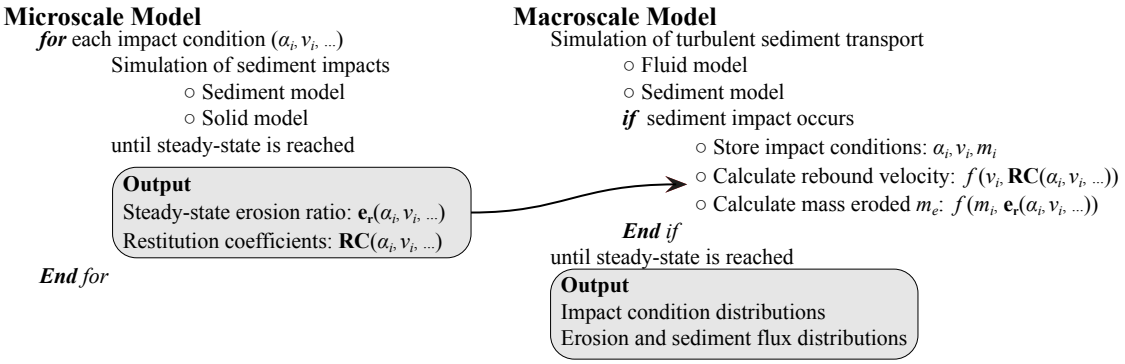

Figure 5.5 – Schematic representation of the multiscale model.

5.3 Projective Integration to Circumvent the Time Scale Separation

The main result of running the multiscale model is a distribution of eroded mass on the surface of interest; together with the known injected sediment mass and simulation duration, the distributions of erosion ratio e_r and erosion rate $\dot{e}$ follow directly. The spatial integration of these quantities are known as the *global erosion ratio* and *global erosion rate*, respectively.

However, multiscale simulations are only feasible in the time frame of the hydrodynamics, *e.g.* the tens of milliseconds it takes for the water to interact with a bucket. Extending these simulations to the time frame of the erosion, hundreds of hours, is only feasible with a projective integration scheme, as proposed in Figure 5.1.

Consider the time evolution of the erosion depth e_d at a point, as presented in Figure 5.6. The proposed scheme involves two steps: First, the multiscale model is used to calculate the converged erosion rate distribution within a short time period, the inner integration; then, a large projective step is taken in which the position of the wall particles is updated according to the computed erosion. The displacement $\boldsymbol{r}_j$ due to erosion is expressed as

$$\boldsymbol{r}_j = \Delta T^o \frac{m_{e,j}}{\rho A_j \Delta T^i} \boldsymbol{n}_j = \Delta T^o \frac{\dot{e}_j}{\rho A_j} \boldsymbol{n}_j, \tag{5.4}$$

where ΔT^o and ΔT^i are the outer and inner integration time intervals, respectively, $m_{e,j}$ is the accumulated eroded mass, ρ is the material density, A_j is the surface area, and $\boldsymbol{n}_j$ is the unit vector normal to the surface. Equation 5.4 is equivalent to the last term of Equation 2.7, a first-order forward Euler projective integration scheme.

After the wall particle positions have been updated, a new instance of the multiscale model is run; only the macroscale model is run provided the microscale results are still useful, *e.g.* if the expected impact condition ranges remain unchanged. The eroded mass variable is reset, such that the inner integration provides a new estimation of the converged erosion rate distribution, which is expected to be different because of the updated wall geometry.

The inner integration time interval is chosen long enough to ensure that the distributions of impact conditions and erosion have converged, whereas the outer integration time intervals are chosen small enough to secure stable and accurate integration of the slow dynamics of the wall. For example, in Chapter 11, ΔT^o is chosen such that the maximum displacement $\boldsymbol{r}_j$ in the domain is less than h_i, the respective FVPM particle radius.

With the combination of projective integration and multiscale modeling, it becomes feasible to study the long-term evolution of the erosion process of a turbine based on detailed simulations of the sediment impacts themselves, in spite of the significant time and length scale separation that characterizes the problem.

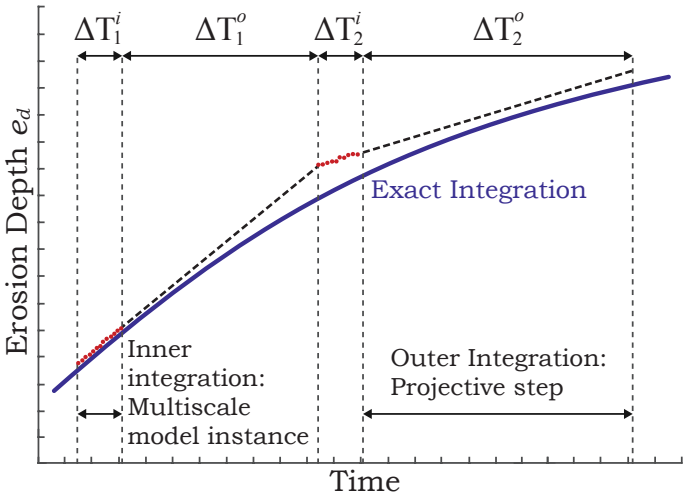

Figure 5.6 – Scheme of the projective integration of the local erosion depth.

5.4 Discussion on the Approach Simplifications

One seemingly strong assumption is neglecting the fluid in the microscale model. First, it is important to note that the significant effect of the fluid before and after the impact is fully taken into consideration in the macroscale model; for example, the lubrication force or *squeeze film effect*, which is important when the sediment is very near the wall, is considered by an appropriate modification of the drag force, see Section 6.3. The macroscale model thus accurately describes the sediment dynamics up to the moment of impact, and immediately afterwards.

The core assumption is really that the fluid has a negligible effect on the dynamics of the sediment impact *during the instant it lasts*. It has been suggested by an order of magnitude analysis that the time scale of an impact is short relative to the boundary layer development around a rapidly accelerating particle, such that the effect of the fluid might be negligible [73]. A similar argument has been proposed, with the additional consideration of the relative magnitude of the contact and viscous forces during the impact [94].

A quantitative estimation of the effect of the fluid during the sediment impact is given by the Stokes number, defined as

$$\mathrm{St} = \frac{\rho_s v d}{9\mu_f}, \tag{5.5}$$

where μ_f is the dynamic viscosity of the fluid and ρ_s is the sediment density. Experiments by Joseph, reported by Ruiz-Angulo et al. [170] reveal that for sufficiently high Stokes number, $\mathrm{St} \approx 1 \times 10^3$, the fluid effect is indeed negligible. Figure 5.7 presents their results, together with the Stokes number ranges for 4 representative sediment sizes. The ranges are computed using the properties of quartz and water, and an impact velocity range v = 30-100 m $\cdot$ s^{-1}.

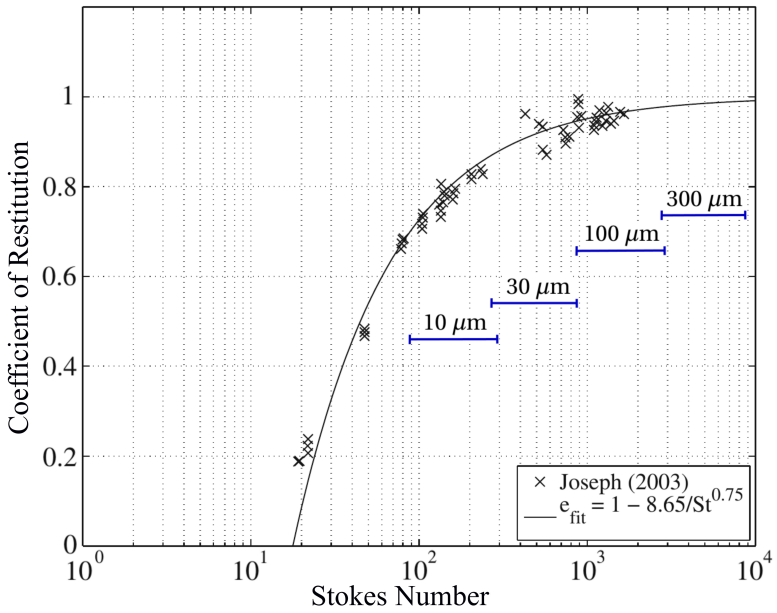

Figure 5.7 – Influence of the Stokes number on the restitution coefficient, adapted from [170].

Whereas it seems justified to assume that the fluid effect is negligible for all relevant impact conditions for particles of $d > 100$ μm, for the smallest sediments at low impact velocity the fluid effect reduces the rebound velocity by up to 30 %; a similar discrepancy in the erosion ratio estimation is presumed. However, the fact that it is precisely the smallest particles at low impact velocity that produce the least erosion suggests that neglecting the fluid in the microscale simulations has an overall small effect on the model predictions.

An implicit assumption of the multiscale model is that the erosion by successive impacts can be well approximated by the *linear superposition* of their individual effects. For example, consider two impacts, at low and high angle, at the same location. Whereas in the model the impact order is irrelevant, *i.e.* the total erosion is the sum of the average eroded mass by each impact, in reality this might not be exactly true. The crater lips generated by a normal impact might get eroded away by a second one at glancing angle in a way that would not occur if the order were inverted. It is difficult to quantify the magnitude of these nonlinear effects, or assess whether they cancel out *on average*. Only the global error, including other modeling and discretization errors, is quantified in the validation of the model.

The microscale model erosion ratio estimation changes with the size of the area sediments are allowed to impact. For example, if it is too small, successive sediments do not have the chance to hit the lips of existing craters, and the erosion ratio is reduced. By increasing the impact area, the erosion ratio quickly converges to a fixed value representative of the successive impact of sediments on a large region. In practice, the impact area is selected as small as possible in order to reach the steady-state erosion ratio with fewer impacts, although large enough to avoid the aforementioned effect; see Appendix B.2 for the details of this convergence behavior.

The FVPM particles that get eroded in the microscale simulations are immediately removed from the system under the assumption that the flow would quickly dispose of the detached matter before the following impact. However, note that when an impact occurs in the macroscale the eroded mass is not injected to the flow for further transport and impact. This disregard is justified by the fact that the eroded mass is negligible compared to the sediment mass ($e_r \ll 1$), and its erosion potential is insignificant because its hardness is that of the base material.

The global erosion ratio changes in time by two distinct effects, both of them captured by the proposed model. On the one hand, the incubation period whereby the material gets work hardened as it accumulates plastic deformation leads to an initially low erosion ratio; this transient is seen in the microscale model, as illustrated in Figure 5.3a, and bypassed by simulating enough impacts until the steady-state erosion ratio is reached. Thus it is congruent to use those results to simulate the long-term erosion process in the macroscale.

On the other hand, the global erosion ratio changes as a consequence of the flow field modification, itself induced by the alteration of the surface. For instance, a change in the flow field might cause an increased flux of sediments against the wall, resulting in a greater amount of mass eroded per unit mass of sediments in the domain. The projective integration scheme allows describing the long-term changes to the surface position, within the resolution provided by the discretization, revealing the erosion ratio variations. The surface alterations that fall below the discretization resolution, *e.g. roughness changes*, can be in principle considered within the boundary condition formulation; however, in this work the changes in roughness induced by the erosion are neglected, as discussed in Section 6.6.

Finally, note that the projective integration scheme is applicable thanks to the time scale separation between the fluid dynamics and the wall evolution. Indeed, the wall movement due to erosion is so slow that, from the perspective of the flow, it is effectively frozen. This justifies the fact that, during a macroscale simulation, the eroded mass is simply stored as a scalar value at each wall particle, without implying any wall displacement.

6 Computational Model

An overview of the multiscale model of erosion is introduced in Chapter 5. A specific set of submodel formulations is hereafter presented; note that these submodels are not unique, and their choice is independent of the overall multiscale methodology. In Section 6.6 the modeling assumptions and limitations are discussed.

6.1 Governing Equations

Conservation laws for mass, linear momentum and energy constitute the core of the governing equations used to describe the fluid, solid and sediments. They are expressed, respectively, as

$$\frac{d\rho}{dt} + \rho \nabla \cdot \boldsymbol{C} = 0, \qquad \rho \frac{d\boldsymbol{C}}{dt} = \nabla \cdot \boldsymbol{\sigma} + \boldsymbol{f}, \qquad \frac{dT}{dt} = \frac{\kappa}{\rho c_p} \nabla \cdot (\nabla T) + \frac{\dot{q}}{\rho c_p}, \tag{6.1}$$

where ρ is the mass density, $\boldsymbol{C}$ is the velocity, $\boldsymbol{\sigma}$ is the Cauchy stress, $\boldsymbol{f}$ is the sum of volumetric and surface forces per unit volume, c_p is the specific heat capacity, T is the temperature, κ is the thermal conductivity, $\dot{q}$ is the sum of heat sources and sinks per unit volume, and $\frac{d}{dt}$ denotes the material derivative.

6.2 Fluid Constitutive and Turbulence Models

6.2.1 Newtonian Isothermal Weakly Compressible Flow

The fluid is assumed *isothermal*, in line with the flow regime found in hydraulic turbines, so the energy conservation equation needs not be solved.

The *weakly compressible* fluid model is assumed: the incompressibility constraint is bypassed by allowing a given level of artificial compressibility, which is arbitrarily modulated by means of a *numerical speed of sound a*; see the discussion in Section 6.6. As detailed in Appendix A.1, by assuming a Newtonian fluid and Boussinesq's *eddy viscosity* hypothesis, the momentum

conservation equation leads to the compressible Navier-Stokes equation, expressed as

$$\rho \frac{d\boldsymbol{C}_f}{dt} = -\nabla p_\gamma + \nabla \cdot \left\{ 2\left(\mu + \mu_t\right) \left[\boldsymbol{S} - \frac{1}{3}\left(\nabla \cdot \boldsymbol{C}_f\right) \boldsymbol{I} \right] - \frac{2}{3}\rho k \boldsymbol{I} + \left(\mu_b + \mu_a\right)\left(\nabla \cdot \boldsymbol{C}_f\right) \boldsymbol{I} \right\}, \tag{6.2}$$

where $\boldsymbol{C}_f$ is the fluid velocity, p_γ is the pressure, μ is the dynamic viscosity, μ_t is the turbulence viscosity, $\boldsymbol{I}$ is the identity, k is the turbulence kinetic energy, μ_b is the bulk viscosity, μ_a is the artificial viscosity, and $\boldsymbol{S}$ is the strain rate, defined as

$$\boldsymbol{S} = \frac{1}{2}\left[\nabla \boldsymbol{C}_f + \left(\nabla \boldsymbol{C}_f\right)^T\right]. \tag{6.3}$$

An equation of state is used to compute the pressure as a function of density variations with respect to a reference density $\rho_\circ$. The following form of the Tait equation is commonly used

$$p_\gamma = \frac{\rho_\circ a^2}{\gamma}\left[\left(\frac{\rho}{\rho_\circ}\right)^\gamma - 1\right], \tag{6.4}$$

where γ is a material parameter set to 7 for water [14].

6.2.2 The Standard *k*-ϵ Model

The standard k-ϵ turbulence model is used to calculate the turbulence viscosity as

$$\mu_t = \rho C_\mu \frac{k^2}{\epsilon}, \tag{6.5}$$

where ϵ is the dissipation rate of turbulence kinetic energy and C_μ is a model parameter defined further down. The equations that describe the rate of change of k and ϵ, due to convection, diffusion, production and dissipation, are

$$\frac{d(\rho k)}{dt} + \rho k \nabla \cdot \boldsymbol{C}_f - \nabla \cdot \left(\frac{\mu_t}{\sigma_k}\nabla k\right) = 2\mu_t\left(\boldsymbol{S}{:}\boldsymbol{S}\right) - \rho\epsilon, \tag{6.6}$$

$$\frac{d(\rho \epsilon)}{dt} + \rho \epsilon \nabla \cdot \boldsymbol{C}_f - \nabla \cdot \left(\frac{\mu_t}{\sigma_\epsilon}\nabla \epsilon\right) = C_{1\epsilon}\frac{\epsilon}{k} 2\mu_t\left(\boldsymbol{S}{:}\boldsymbol{S}\right) - C_{2\epsilon}\rho\frac{\epsilon^2}{k}. \tag{6.7}$$

The standard values of the model parameters are used: $C_\mu = 0.09$, $\sigma_k = 1.0$, $\sigma_\epsilon = 1.3$, $C_{1\epsilon} = 1.44$ and $C_{2\epsilon} = 1.92$ [52].

A wall function is used to describe the fluid near the walls; it is applied to the fluid particles that intersect any wall particle, *i.e.* all the finite volumes that discretize the fluid and that intersect the wall boundary. The wall function defines the velocity magnitude, parallel to the wall, as

$$C_f = C_\tau \frac{1}{K}\ln\left(E_k y^+\right) = C_\mu^{\frac{1}{4}} k^{\frac{1}{2}} \frac{1}{K}\ln\left(E_k y^+\right), \tag{6.8}$$

where it is assumed that the flow is in local equilibrium [52], *i.e.* the shear velocity $C_\tau = C_\mu^{\frac{1}{4}} k^{\frac{1}{2}}$.

Here the von Kármán constant $K = 0.41$, E_k is an empirical constant set to 9.793 for smooth surfaces, and y^+ is the dimensionless normal distance from the wall, defined as

$$y^+ = \frac{\rho C_\tau n}{\mu} = \frac{\rho C_\mu^{\frac{1}{4}} k^{\frac{1}{2}} n}{\mu}, \tag{6.9}$$

where n is the normal distance from the wall.

Equation 6.8, together with the definition of the shear stress magnitude at the wall $\tau_w = \rho C_\tau^2$, leads to

$$\tau_w = \frac{\rho C_\mu^{\frac{1}{4}} k^{\frac{1}{2}} K}{\ln\left(E_k y^+\right)} C_f, \tag{6.10}$$

which is used as boundary condition at the interface between fluid and wall, instead of the shear stress calculated from the no-slip condition, to enforce the wall function.

Furthermore, the last two terms of Equation 6.6, the production and dissipation terms of turbulence kinetic energy, are replaced by

$$2\mu_t \left(\boldsymbol{S}{:}\boldsymbol{S}\right) - \rho\epsilon \implies \tau_w \frac{C_\mu^{\frac{1}{4}} k^{\frac{1}{2}}}{Kn} - \rho\epsilon^* = \frac{\rho C_\mu^{\frac{1}{4}} k^{\frac{1}{2}} K}{n} \left[\frac{C_f}{\ln\left(E_k y^+\right)}\right]^2 - \rho \frac{C_\mu^{\frac{3}{4}} k^{\frac{3}{2}}}{Kn}, \tag{6.11}$$

whereas the value of ϵ is directly specified as

$$\epsilon^* = \frac{C_\mu^{\frac{3}{4}} k^{\frac{3}{2}}}{Kn}. \tag{6.12}$$

These modifications, applied only to the fluid particles in contact with a wall, are a consequence of the assumption of equilibrium, *i.e.* the turbulence production and dissipation are equal [52].

6.2.3 Turbulence Production Limiters

One disadvantage of eddy viscosity turbulence models is the overproduction of turbulence near stagnation regions. Two formulations are commonly used to limit the turbulence production, resulting in better agreement with experiments.

The first turbulence production limiter that is applied is due to Menter [133], and is defined as

$$P_k = \min\left[2\mu_t \left(\boldsymbol{S}{:}\boldsymbol{S}\right), C_k \rho\epsilon\right], \tag{6.13}$$

where C_k is a parameter set to 10, and P_k is the turbulence kinetic energy production term, the second-to-last term of Equation 6.6. This equation states that the turbulence production is limited to a maximum value of 10 times the dissipation rate; it has been noted that even in shear layers of complex flows this ratio only reaches about 2 [133], so the procedure does not

affect the overall solution accuracy, simply prevents the unphysical turbulence accumulation in stagnation regions.

The second turbulence production limiter is due to Kato and Launder [91], and can be expressed as

$$P_k = \min\left[2\mu_t\left(\boldsymbol{S}{:}\boldsymbol{S}\right), 2\mu_t\left(\boldsymbol{S}{:}\boldsymbol{\Omega}\right)\right], \tag{6.14}$$

where $\boldsymbol{\Omega}$ is the vorticity, defined as

$$\boldsymbol{\Omega} = \frac{1}{2}\left[\nabla \boldsymbol{C}_f - \left(\nabla \boldsymbol{C}_f\right)^T\right]. \tag{6.15}$$

6.3 Turbulent Sediment Transport Model

In the macroscale, the sediments are assumed *rigid* and *isothermal*; the mass and energy conservation equations are therefore not solved. The momentum conservation equation simplifies to Newton's second law [147], namely

$$m_s \frac{\partial \boldsymbol{C}_s}{\partial t} = m_s \boldsymbol{g} + \boldsymbol{f}_h + \boldsymbol{f}_c, \tag{6.16}$$

where m_s is the sediment mass, $\boldsymbol{C}_s$ is its velocity, $\boldsymbol{g}$ is the gravitational acceleration, $\boldsymbol{f}_h$ is the sum of hydrodynamic forces, and $\boldsymbol{f}_c$ is the sum of contact forces, as defined in Section 6.4.

6.3.1 Contributions to the Hydrodynamic Force

The hydrodynamic force includes the effects of drag, pressure gradient, added mass, lift and buoyancy: $\boldsymbol{f}_h = \boldsymbol{f}_d + \boldsymbol{f}_p + \boldsymbol{f}_a + \boldsymbol{f}_l + \boldsymbol{f}_b$. The formulations are presented hereafter.

The drag force is computed as

$$\boldsymbol{f}_d = \frac{1}{2}\rho_f \frac{\pi}{4} d^2 \, C_{r,f} \, c_d\left(\mathrm{Re}, \phi_d\right) \cdot \boldsymbol{C}_{r,f}, \tag{6.17}$$

where ρ_f is the fluid density, d is the sediment diameter, $\boldsymbol{C}_{r,f}$ is the relative velocity between the fluid and the sediment, and Re is the sediment Reynolds number, defined as

$$\mathrm{Re} = \frac{\rho_f C_{r,f} d}{\mu}. \tag{6.18}$$

The drag coefficient c_d is a function of the sediment sphericity ϕ_d, which is defined as

$$\phi_d = \frac{\pi^{\frac{1}{3}}\left(6V\right)^{\frac{2}{3}}}{A}, \tag{6.19}$$

where V is the sediment volume and A is its surface area. As presented in Appendix B.1, there is a consistent mapping $\phi_d = f(\phi_s)$, where ϕ_s is the sediment shape parameter used in the algorithm to generate random sediment discretizations for the microscale simulations. In

other words, for a given problem where the sediment population has been characterized by an average sphericity ϕ_d, to be used in the macroscale simulation, the aforementioned mapping allows selecting the corresponding sediment shape parameter ϕ_s, to be used in the generation of the microscale sediment discretizations.

When the sediment is near a wall there is a certain degree of drag anisotropy. In that case, $\boldsymbol{C}_{r,f}$ is decomposed into parallel and perpendicular directions relative to the wall, as defined by the unit vectors $(\hat{\parallel}, \hat{\perp})$; two different drag coefficients are computed as a function of the direction, the normal distance to the wall, n, measured from the sediment center, and the sediment diameter. The drag force is then computed as

$$\boldsymbol{f}_d = \frac{1}{2}\rho_f \frac{\pi}{4} d^2 \, C_{r,f} \cdot \left[c_d^{\parallel}\left(\mathrm{Re}, \phi_d, n, d\right) C_{r,f}^{\parallel} \cdot \hat{\parallel} + c_d^{\perp}\left(\mathrm{Re}, \phi_d, n, d\right) C_{r,f}^{\perp} \cdot \hat{\perp} \right]. \tag{6.20}$$

The drag coefficient is estimated using the correlation by Haider and Levenspiel [71] for non-spherical sediments, whose range of applicability, $1 \times 10^{-2} < \mathrm{Re} < 1 \times 10^{5}$, completely covers the range of sediment Reynolds numbers found in hydraulic machines, $1 \times 10^{-1} < \mathrm{Re} < 1 \times 10^{4}$. The drag coefficient is written as

$$c_d\left(\mathrm{Re}, \phi_d, n, d\right) = \frac{24}{\mathrm{Re}}\left[F_1(n,d) + G_1(\phi_d)\,\mathrm{Re}^{G_2(\phi_d)}\right] + \frac{G_3(\phi_d)}{1 + G_4(\phi_d)\,\mathrm{Re}^{-1}}, \tag{6.21}$$

where G_i are functions of the sediment sphericity given by

$$\begin{aligned} G_1(\phi_d) &= \exp(2.3288 - 6.45810\,\phi_d + 2.4486\,\phi_d^2), \\ G_2(\phi_d) &= 0.0964 + 0.5565\,\phi_d, \\ G_3(\phi_d) &= \exp(4.9050 - 13.8944\,\phi_d + 18.4222\,\phi_d^2 - 10.2599\,\phi_d^3), \\ G_4(\phi_d) &= \exp(1.4681 + 12.2584\,\phi_d - 20.7322\,\phi_d^2 + 15.8855\,\phi_d^3). \end{aligned} \tag{6.22}$$

F_1 is a near-wall correction factor, which also introduces a level of anisotropy, function of the normalized gap between the sediment and the wall: $\delta_s(n,d) = \frac{2n-d}{d}$. It is defined as [27]

$$F_{1,\parallel}(n,d) = \exp\left\{1.465 \exp\left[-0.03176\,\left(\ln\left(\delta_s\right) + 6.150\right)^2\right] - 0.1\right\}, \tag{6.23}$$

$$F_{1,\perp}(n,d) = \begin{cases} \exp\left\{4.526 \exp\left[-0.0662\,\left(\ln\left(\delta_s\right) + 5.217\right)^2\right]\right\}, & \text{if } \delta_s < 0.5, \\ \frac{2}{\alpha_s^2} + 0.4 \ln\left(\frac{1}{\alpha_s}\right) + 1.04, & \text{otherwise,} \end{cases} \tag{6.24}$$

with

$$\alpha_s(n,d) = \ln\left(\frac{2n}{d} + \sqrt{\delta_s^2 + 2\delta_s}\right). \tag{6.25}$$

Although these correlations look obscure, Figure 6.2 in Section 6.6 clarifies their behavior.

The second force considered is due to the pressure gradient. It is expressed as

$$\boldsymbol{f}_p = \frac{4}{3}\pi\left(\frac{d}{2}\right)^3 \cdot \left(-\nabla p\right) = \frac{1}{6}\pi d^3 \cdot \left(\rho_f \boldsymbol{C}_f \cdot \nabla \boldsymbol{C}_f\right), \tag{6.26}$$

where the pressure gradient is estimated as $-\nabla p \simeq \rho_f \boldsymbol{C}_f \cdot \nabla \boldsymbol{C}_f$. This approximation comes from the momentum equation, assuming inviscid and steady flow.

The third contribution to the hydrodynamic force is the added mass effect, computed as

$$\boldsymbol{f}_a = \frac{1}{12}\rho_f \pi d^3 \cdot \dot{\boldsymbol{C}}_{r,f}, \tag{6.27}$$

where $\dot{\boldsymbol{C}}_{r,f}$ is the relative acceleration between the fluid and the sediment.

The shear lift force is computed as [131]

$$\boldsymbol{f}_l = -1.615\, J^* \rho_f d^2 \sqrt{\frac{\mu}{\rho_f \Omega}} \cdot \left(\boldsymbol{\Omega} \times \boldsymbol{C}_{r,f}\right), \tag{6.28}$$

where J^* is a finite Reynolds number correction defined as

$$J^* = \begin{cases} (1 - 0.3314\sqrt{\xi})\, \exp\left(-\frac{\mathrm{Re}}{10}\right) + 0.3314\sqrt{\xi}, & \text{if } \mathrm{Re} \leq 40, \\ 0.0524\sqrt{\xi \mathrm{Re}}, & \text{otherwise,} \end{cases} \tag{6.29}$$

and ξ is the dimensionless strain rate of the fluid, computed as

$$\xi = \frac{\sqrt{2\boldsymbol{S}:\boldsymbol{S}}}{C_r}\frac{d}{2}. \tag{6.30}$$

The buoyancy force is calculated according to

$$\boldsymbol{f}_b = -\frac{1}{6}\pi d^3 \rho_f \cdot \boldsymbol{g}. \tag{6.31}$$

6.3.2 The Continuous Random Walk Model of Turbulent Dispersion

Given that the Reynolds-averaged Navier-Stokes equations solved for the fluid represent time-averaged fields, the turbulent fluctuations that affect the dispersion of sediments must be included using an additional model. These turbulent fluctuations affect the forces that depend on the relative velocity between fluid and sediment, namely the drag, added mass and lift forces.

The relative velocity is expressed as

$$\boldsymbol{C}_{r,f} = (\boldsymbol{C}_f + \boldsymbol{C}_{f,t}) - \boldsymbol{C}_s, \tag{6.32}$$

where $\boldsymbol{C}_f$ is the fluid velocity, $\boldsymbol{C}_{f,t}$ is the turbulent velocity fluctuation and $\boldsymbol{C}_s$ is the sediment velocity.

The turbulent fluctuations are modeled by means of the stochastic Langevin equation [33], which can be expressed as

$$\boldsymbol{C}_{f,t}^{t+\Delta t} = \boldsymbol{C}_{f,t}^{t} \cdot \left(1 - \frac{\Delta t}{\tau_t}\right) + \sqrt{\frac{4}{3}\frac{k\,\Delta t}{\tau_t}} \cdot \boldsymbol{G}(0,1) + \nabla k \cdot \frac{\Delta t}{3\left(1 + \frac{\tau_s}{\tau_t}\right)}, \tag{6.33}$$

where Δt is the time step, τ_t is the turbulence time scale, defined as

$$\tau_t = \sqrt{\frac{3}{2}}\frac{C_\mu^{\frac{3}{4}} k}{\epsilon}, \tag{6.34}$$

τ_s is the sediment relaxation time, defined as

$$\tau_s = \begin{cases} \frac{\rho_s d^2}{18\mu}, & \text{if Re} \leq 1, \\ \frac{4\rho_s}{3\rho_f}\frac{d}{c_d\, C_{r,f}}, & \text{otherwise,} \end{cases} \tag{6.35}$$

where ρ_s is the sediment density, and $\boldsymbol{G}(0,1)$ is a vector whose components are randomly drawn from a Gaussian distribution with zero mean and unitary variance.

Equation 6.33 states that the fluctuating velocity at time $t + \Delta t$ depends on its value at time t, plus a random component proportional to the turbulence kinetic energy k, plus a drift correction proportional to the gradient of k. Importantly, the fluctuating velocity is not a field, but a variable stored in each sediment.

6.3.3 Near-Wall Velocity Correction

Whenever the hydrodynamic force components are evaluated, the required fluid properties are calculated at the sediment location by interpolating upon the known values, located at the fluid particle centroids. The interpolated values are second-order accurate, provided the sediment is well surrounded by fluid particles; see Section 7.3.2.

However, when the sediment is near a fluid boundary, for instance approaching the wall, the interpolation accuracy decreases significantly. The sediments are oftentimes much smaller than the fluid particles, so the region near the wall where interpolation is inaccurate is large relative to their size. Furthermore, the lack of particle refinement forbids discretizing the boundary layer; even if interpolation was accurate, it would not adequately describe the fluid velocity as the sediment approaches the wall.

With the objective of improving the near-wall modeling, considering its importance for accurately predicting the sediment impact conditions, the fluid velocity *experienced by the sediments* is defined according to the following approach.

First, the fluid velocity is interpolated at a distance δ_w normal to the wall; the vector pointing from the sediment position to the interpolation location is spanned by the wall normal, as illustrated in Figure 6.1a. The distance δ_w is selected to be equal to the average interparticle

distance Δx, such that the interpolation at that location is still second-order accurate and close enough to the wall to be representative. Whereas a much smaller value of δ_w would imply a decreased interpolation accuracy due to it being one-sided, a much larger value would be less representative of the near-wall behavior while not improving the interpolation accuracy any further.

The relative velocity between the fluid and the wall, at position δ_w, is then computed as

$$\boldsymbol{C}_{r,w}^{\delta_w} = \boldsymbol{C}_f^{\delta_w} - \boldsymbol{C}_w, \tag{6.36}$$

where $\boldsymbol{C}_f^{\delta_w}$ is the interpolated fluid velocity at position δ_w. The relative velocity is decomposed according to the parallel and perpendicular directions defined by the unit vectors $(\hat{\parallel}, \hat{\perp})$

$$\boldsymbol{C}_{r,w}^{\delta_w} = C_{r,w,\parallel}^{\delta_w} \cdot \hat{\parallel} + C_{r,w,\perp}^{\delta_w} \cdot \hat{\perp}. \tag{6.37}$$

The *1/7th power law velocity profile* is used to estimate the fluid velocity at the sediment location as

$$\boldsymbol{C}_f^n = \boldsymbol{C}_w + \left[C_{r,w,\parallel}^{\delta_w} \left(\frac{n}{\delta_w} \right)^{\frac{1}{7}} \cdot \hat{\parallel} + C_{r,w,\perp}^{\delta_w} \left(\frac{n}{\delta_w} \right)^{\frac{6}{7}} \cdot \hat{\perp} \right], \tag{6.38}$$

where n is the normal distance from the wall to the sediment position. The procedure is illustrated in Figure 6.1a, where $\boldsymbol{C}_w = 0$ is assumed.

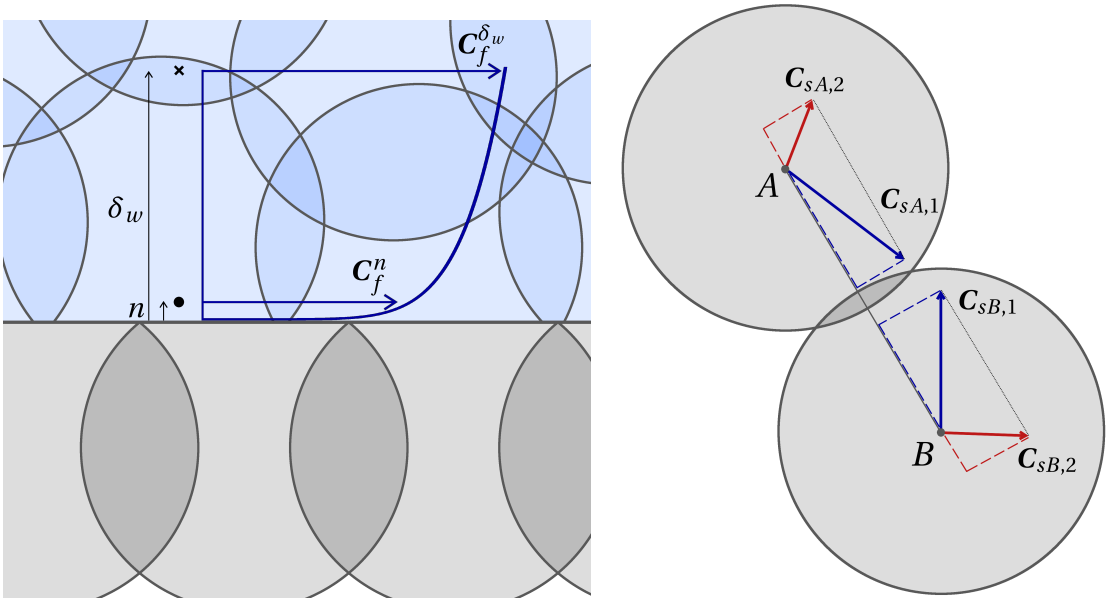

(a) Estimation of the fluid velocity experienced by a sediment near the wall based on the 1/7$^{\text{th}}$ power law velocity profile. Fluid and wall particles colored blue and gray, respectively.

(b) Inelastic collision between two identical sediments. The subscripts $_1$ and $_2$ denote the velocity before and after the collision, respectively.

Figure 6.1 – Illustrations of the near-wall velocity and inelastic contact formulations.

6.4 Sediment Contact Models

6.4.1 Contact in the Macroscale

The sum of contact forces felt by a sediment in the macroscale model, $\boldsymbol{f}_c$, considers interactions with the wall particles and with other sediments. The collisions between sediments are assumed inelastic, with a restitution coefficient $RC = 0.9$ representative of the flow regime, see Figure 5.7. A collision occurs whenever two sediments overlap, i.e. $\|\boldsymbol{x}_A - \boldsymbol{x}_B\| < \frac{1}{2}(d_A + d_B)$, where $\boldsymbol{x}_i$ denotes the position of sediment i. This formulation implies that the sediments are assumed spherical for the purpose of contact detection. Figure 6.1b illustrates a collision for the 2D case.

The velocity after collision for sediment A, $\boldsymbol{C}_{sA,2}$, is computed as

$$\boldsymbol{C}_{sA,2} = C^{\parallel}_{sA,2} \cdot \hat{\parallel} + C^{\perp}_{sA,2} \cdot \hat{\perp} = C^{\parallel}_{sA,1} \cdot \hat{\parallel} + \frac{RC\, m_B \left(C^{\perp}_{sB,1} - C^{\perp}_{sA,1}\right) + m_A C^{\perp}_{sA,1} + m_B C^{\perp}_{sB,1}}{m_A + m_B} \cdot \hat{\perp}, \quad (6.39)$$

where m_A and m_B are the masses of sediments A and B, respectively, the subscripts $_1$ and $_2$ denote the velocity before and after the collision, respectively, and the velocities have been decomposed into perpendicular and tangential components as $C^{\perp}_s = \boldsymbol{C}_s \cdot \hat{\perp}$ and $C^{\parallel}_s = \boldsymbol{C}_s \cdot \hat{\parallel}$. The unit vector $\hat{\perp}$ is defined as $\frac{\boldsymbol{x}_A - \boldsymbol{x}_B}{\|\boldsymbol{x}_A - \boldsymbol{x}_B\|}$, whereas $\hat{\parallel} = \left(\frac{\boldsymbol{C}_{sA,1} \times \boldsymbol{C}_{sB,1}}{\|\boldsymbol{C}_{sA,1} \times \boldsymbol{C}_{sB,1}\|}\right) \times \hat{\perp}$. In other words, each velocity is decomposed into two perpendicular components: one along the line of collision and another one tangent to the contact plane; whereas the tangent component is unaffected by the collision, the perpendicular component is computed according to a 1D inelastic collision.

A somewhat similar approach is followed whenever a sediment impacts a wall particle. The rebound velocity is calculated according to

$$\boldsymbol{C}_{s,2} = C^{\parallel}_{s,2} \cdot \hat{\parallel} + C^{\perp}_{s,2} \cdot \hat{\perp} = RC_{\parallel}(\alpha, C_{s,1})\; C^{\parallel}_{s,1} \cdot \hat{\parallel} - RC_{\perp}(\alpha, C_{s,1})\; C^{\perp}_{s,1} \cdot \hat{\perp}, \quad (6.40)$$

where $RC(\alpha, C_{s,1})$ are the restitution coefficients, functions of the impact angle and velocity magnitude, that are computed by interpolating the microscale simulation results. In this case $\hat{\perp}$ is the unit vector normal to the wall, and $\hat{\parallel} = \left(\frac{\boldsymbol{C}_{s,1} \times \hat{\perp}}{\|\boldsymbol{C}_{s,1} \times \hat{\perp}\|}\right) \times \hat{\perp}$. In spite of the fact that the wall is discretized using spherical FVPM particles, forming a *bumpy surface*, the sediments actually see a *locally flat surface*, as depicted in Figure 6.1a. This is achieved by computing an impact only when

$$\|\boldsymbol{x}_s - \boldsymbol{x}_w\| \;<\; \frac{d}{2} + h_w \cdot \min\left[1.0, \frac{\sin(\beta_w)}{\sin(\beta)}\right], \quad (6.41)$$

where $\boldsymbol{x}_s$ and $\boldsymbol{x}_w$ are the sediment and wall particle positions, respectively, d is the sediment diameter, h_w is the wall particle radius, and the angles β_w and β are defined as

$$\beta_w = \cos^{-1}\left(\frac{\Delta x_w}{\sqrt{2} h_w}\right), \qquad \beta = \sin^{-1}\left[\mathrm{abs}\left(\frac{\boldsymbol{x}_s - \boldsymbol{x}_w}{\|\boldsymbol{x}_s - \boldsymbol{x}_w\|} \cdot \hat{\perp}\right)\right], \quad (6.42)$$

where Δx_w is the interparticle spacing for the wall. Yet again, this contact criterion assumes that the sediments are spherical.

6.4.2 Contact in the Microscale

As presented in Figure 5.2, the sediments in the microscale model are discretized by using a large number of FVPM particles, fully describing their intricate shapes, unlike the sediments in the macroscale model that are discretized by a single FVPM particle. A novel algorithm for generating particle-based discretizations for sediments of different shapes, characterized by the shape parameter ϕ_s, is presented in Appendix B.1, where a consistent mapping $\phi_d = f(\phi_s)$ is also presented.

The sediments in the macroscale are modeled as elastic solids, see Section 6.5. The contact force, which acts as an external contribution to the momentum equation, is written as

$$\boldsymbol{f}_c = \boldsymbol{f}_p + \boldsymbol{f}_f, \tag{6.43}$$

where $\boldsymbol{f}_p$ is the reaction force to penetration and $\boldsymbol{f}_f$ is the friction force.

A contact force is calculated whenever a solid particle intersects a *sediment particle*, *i.e.* any of the FVPM particles that discretize the sediment; the resulting force is added to the momentum balance of both particles involved. The aforementioned contact criterion is written as $p_c = \max(0,\ h_m + h_s - \|\boldsymbol{x}_m - \boldsymbol{x}_s\|) > 0$, where p_c is the interparticle penetration, h is the particle radius, $_s$ denotes the sediment particle and $_m$ denotes the solid particle.

The reaction force resisting penetration is calculated as

$$\boldsymbol{f}_p = k_c p_c \bar{R}\bar{E} \cdot \hat{\perp}, \tag{6.44}$$

where k_c is the penetration penalty parameter, discussed in Section 6.6, and $\bar{R}$ and $\bar{E}$ are the effective contact radius and the effective Young's modulus, defined as

$$\bar{R} = \frac{h_m h_s}{h_m + h_s}, \qquad \bar{E} = \frac{E_{e,m} E_{e,s}}{\left(1 - \nu_{p,m}^2\right) E_{e,s} + \left(1 - \nu_{p,s}^2\right) E_{e,m}}, \tag{6.45}$$

where E_e and ν_p are the Young's modulus and Poisson's ratio of each material. The penalty force $\boldsymbol{f}_p$, used to enforce the *no-penetration constraint*, acts along the direction $\hat{\perp} = \left(\frac{\boldsymbol{x}_m - \boldsymbol{x}_s}{\|\boldsymbol{x}_m - \boldsymbol{x}_s\|}\right)$.

The friction force is computed by means of a simple Coulomb model, expressed as

$$\boldsymbol{f}_f = f_p\ \mu_f(\boldsymbol{C}_{r,m}) \cdot \hat{\parallel}, \tag{6.46}$$

where the friction coefficient is computed as

$$\mu_f(C_{r,m}) = \mu_{f,d} + \left(\mu_{f,s} - \mu_{f,d}\right) \exp\left(-k_f C_{r,m}^{\parallel}\right), \tag{6.47}$$

where $\mu_{f,d}$ is the dynamic friction coefficient, $\mu_{f,s}$ is the static friction coefficient, k_f charac-

terizes the exponential decay from static to dynamic friction coefficient, $\boldsymbol{C}_{r,m}$ is the relative velocity between the sediment particle and the solid particle, the tangential unit vector is defined as $\hat{\parallel} = \left(\frac{\boldsymbol{C}_{r,m}\times\hat{\perp}}{\|\boldsymbol{C}_{r,m}\times\hat{\perp}\|}\right)\times\hat{\perp}$, and $C^{\parallel}_{r,m} = \boldsymbol{C}_{r,m}\cdot\hat{\parallel}$. Throughout this work, $k_f = \frac{1}{3}$, such that for $C^{\parallel}_{r,m} \approx 2\ \mathrm{m}\cdot\mathrm{s}^{-1}$ the friction coefficient is halfway between the static and dynamic values.

6.5 Constitutive and Damage Models for the Solid and the Sediments

Conservation laws for mass, linear momentum and energy are solved for the solid and sediments in the microscale simulations, where constant values for c_p and κ are assumed, see Equation 6.1.

6.5.1 Homogeneous Isotropic Elasticity

Both materials are assumed as *homogeneous* and *isotropic*; whereas the solid is modeled as elasto-plastic, only elastic behavior is considered for the sediments. The linear stress-strain constitutive relation used in the elastic regime is written as

$$\boldsymbol{\sigma} = -p\boldsymbol{I} + \boldsymbol{s} = K_e\ \mathrm{tr}\,(\boldsymbol{\varepsilon})\,\boldsymbol{I} + 2G_e\left(\boldsymbol{\varepsilon} - \frac{1}{3}\mathrm{tr}\,(\boldsymbol{\varepsilon})\,\boldsymbol{I}\right), \tag{6.48}$$

where $\boldsymbol{\sigma}$ is Cauchy's stress, $\boldsymbol{s}$ is the deviatoric stress, K_e is the bulk modulus, G_e is the shear modulus, and $\boldsymbol{\varepsilon}$ is the elastic strain.

To calculate the pressure as a function of density and temperature variations with respect to their reference values $\rho_\circ$ and $T_\circ$, respectively, the temperature-corrected Mie-Grüneisen equation of state is used [101], which can be expressed as

$$p_\gamma = \rho_\circ a_g^2 \mu_g \frac{1 + \left(1 - \frac{\gamma_\circ}{2}\right)\mu_g}{\left[1 - (S-1)\,\mu_g\right]^2} + \gamma_\circ \rho_\circ c_p\,(T - T_\circ), \tag{6.49}$$

where $\mu_g = \frac{\rho}{\rho_\circ} - 1$, a_g is the bulk speed of sound, $\gamma_\circ$ is Grüneisen's parameter and S is the linear Hugoniot slope coefficient.

The material stress is updated in time by successive stress increments, each of which is computed using the *infinitesimal strain theory*; the approximation is justified by the small time step characteristic of the explicit integration scheme, see Section 7.3.3. The rate of change of $\boldsymbol{\sigma}$ is composed of an *objective stress rate* $\overset{\triangle}{\boldsymbol{\sigma}}$, which is related to the deformation of the material, and a *non-objective component* caused to the rotation of the material, which is unrelated to changes in strain. The Jaumann rate of the Cauchy stress, an objective measure of the stress rate, is defined as

$$\overset{\triangle}{\boldsymbol{\sigma}} = \dot{\boldsymbol{\sigma}} + \boldsymbol{\sigma}\cdot\boldsymbol{\omega} - \boldsymbol{\omega}\cdot\boldsymbol{\sigma}, \tag{6.50}$$

where $\dot{\boldsymbol{\sigma}}$ is the time derivative of the Cauchy stress and $\boldsymbol{\omega}$ is the material spin, defined as

$$\boldsymbol{\omega} = \frac{1}{2}\left[\nabla \boldsymbol{C}_m - (\nabla \boldsymbol{C}_m)^T\right], \tag{6.51}$$

where $\boldsymbol{C}_m$ is the material velocity. As presented in Appendix A.2, using Equations 6.48 and 6.50, together with the fact that the trace of a tensor is invariant to rotations, the rate of change of the Cauchy stress can be expressed as

$$\dot{\boldsymbol{\sigma}} = -\dot{p}\boldsymbol{I} + 2G_e\left(\dot{\boldsymbol{\varepsilon}} - \frac{1}{3}\mathrm{tr}\left(\dot{\boldsymbol{\varepsilon}}\right)\boldsymbol{I}\right) - \boldsymbol{s}\cdot\boldsymbol{\omega} + \boldsymbol{\omega}\cdot\boldsymbol{s} = -\dot{p}\boldsymbol{I} + \dot{\boldsymbol{s}}, \tag{6.52}$$

where $\dot{\boldsymbol{\varepsilon}}$ is the strain rate, computed as

$$\dot{\boldsymbol{\varepsilon}} = \frac{1}{2}\left[\nabla \boldsymbol{C}_m + (\nabla \boldsymbol{C}_m)^T\right]. \tag{6.53}$$

The rate of change of the pressure follows directly from Equation 6.49, and can be written as

$$\dot{p} = -\left(\nabla\cdot\boldsymbol{C}_m\right)\rho_\circ a_g^2\left\{\frac{1+2\mu_g\left(1-\frac{\gamma_\circ}{2}\right)}{\left[1-(S-1)\,\mu_g\right]^2} + \frac{2\mu_g\left(S-1\right)\left[1+\mu_g\left(1-\frac{\gamma_\circ}{2}\right)\right]}{\left[1-(S-1)\,\mu_g\right]^3}\right\} + \gamma_\circ\rho_\circ c_p\dot{T}, \tag{6.54}$$

where $\dot{T}$ is the rate of change of the material temperature, specified in Section 6.5.4.

Equation 6.52 allows calculating the rate of change of the Cauchy stress, and therefore the stress increments required to integrate it, as a function of the gradient and divergence of the material velocity, thus closing the system of governing equations.

6.5.2 Elasto-Plasticity

The solid elasto-plastic behavior is considered by means of the radial return plasticity algorithm. First, a trial stress is computed upon integration of the Cauchy rate of stress, assuming elastic behavior. The deviatoric component of the trail stress, $\hat{\boldsymbol{s}}$, is calculated as

$$\hat{\boldsymbol{s}} = \boldsymbol{s} + \dot{\boldsymbol{s}}\Delta t = \boldsymbol{s} + \left[2G_e\left(\dot{\boldsymbol{\varepsilon}} - \frac{1}{3}\mathrm{tr}\left(\dot{\boldsymbol{\varepsilon}}\right)\boldsymbol{I}\right) - \boldsymbol{s}\cdot\boldsymbol{\omega} + \boldsymbol{\omega}\cdot\boldsymbol{s}\right]\Delta t, \tag{6.55}$$

and is used to compute an equivalent von Mises stress, defined as

$$\sigma_v = \sqrt{\frac{3}{2}\hat{\boldsymbol{s}}:\hat{\boldsymbol{s}}}. \tag{6.56}$$

It is compared against the current yield stress, σ_y, specified in Section 6.5.3. If $\sigma_v < \sigma_y$, the material has not yielded and the elastic trail stress is retained, *i.e.* it is used to update the material stress variable.

However, if the yield criterion is met, $\sigma_v > \sigma_y$, the resulting plastic strain increment $\Delta\varepsilon_p$ and deviatoric stress $\boldsymbol{s}^{t+\Delta t}$ need to be computed. The trail stress is projected onto the yield surface, which results in $\boldsymbol{s}^{t+\Delta t} = f_r\hat{\boldsymbol{s}}$, where f_r is the radial return factor. The plastic strain

increment and radial return factor are calculated by requiring that the $\sigma_v(\boldsymbol{s}^{t+\Delta t}) = \sigma_y$; an iterative procedure is necessary because $\sigma_y = \sigma_y(\Delta\varepsilon_p)$.

It can be shown that the radial return factor is written as [72]

$$f_r = 1 - \frac{3G_e\Delta\varepsilon_p}{\sigma_v(\hat{\boldsymbol{s}})} = \frac{\boldsymbol{s}^{t+\Delta t}}{\hat{\boldsymbol{s}}} = \frac{\sigma_y}{\sigma_v(\hat{\boldsymbol{s}})}, \tag{6.57}$$

where the last equality is true when $\sigma_v(\boldsymbol{s}^{t+\Delta t}) = \sigma_y$.

The converged values of $\Delta\varepsilon_p$ and f_r, from which $\boldsymbol{s}^{t+\Delta t}$ can be calculated, are obtained using the following algorithm, which is Newton's method applied to the minimization of the error $\Delta\varepsilon_p^r = \|\Delta\varepsilon_p^i - \Delta\varepsilon_p\|$. The expressions for σ_y and ΔT_p, the temperature increment due to thermoplastic heating, are presented in Sections 6.5.3 and 6.5.4, respectively.

Algorithm 1: Radial return plasticity

Result: $\Delta\varepsilon_p$, $\boldsymbol{s}^{t+\Delta t}$
$\Delta\varepsilon_p^r = 1.0$
$\Delta\varepsilon_p^i = 0.0$
while *Error* $\Delta\varepsilon_p^r > 1\times10^{-8}$ **do**
  Calculate thermoplastic temperature increment: $\Delta T_p^i\left(\Delta\varepsilon_p^i\right)$
  Calculate yield stress: $\sigma_y^i\left[\varepsilon_p + \Delta\varepsilon_p^i,\ T + \Delta T_p^i\left(\Delta\varepsilon_p^i\right)\right]$
  Calculate radial return factor: $f_r^i = \min\left(1.0,\ \frac{\sigma_y^i}{\sigma_v(\hat{\boldsymbol{s}})}\right)$
  Calculate error $\Delta\varepsilon_p^r = \|\Delta\varepsilon_p^i - \frac{(1-f_r^i)\sigma_v(\hat{\boldsymbol{s}})}{3G_e}\|$
  Define plastic strain increment differential: $\delta\Delta\varepsilon_p = \Delta\varepsilon_p^r \times 10^{-3}$
  Estimate yield surface slope:
  $\frac{\partial\sigma_y}{\partial\Delta\varepsilon_p} = \frac{1}{\delta\Delta\varepsilon_p}\left\{\sigma_y\left[\varepsilon_p + \Delta\varepsilon_p^i + \delta\Delta\varepsilon_p,\ T + \Delta T_p\left(\Delta\varepsilon_p^i + \delta\Delta\varepsilon_p\right)\right] - \sigma_y^i\right\}$
  Apply correction to the plastic strain increment:
  $\Delta\varepsilon_p^i = \max\left[0.0,\ \Delta\varepsilon_p^i - \Delta\varepsilon_p^r\left(1 + \frac{1}{3G_e}\frac{\partial\sigma_y}{\partial\Delta\varepsilon_p}\right)^{-1}\right]$
end
$\Delta\varepsilon_p = \Delta\varepsilon_p^i$
$f_r = f_r^i$
$\boldsymbol{s}^{t+\Delta t} = f_r\hat{\boldsymbol{s}}$

6.5.3 The Johnson-Cook Model

The Johnson-Cook [88] constitutive model is used to calculate the yield stress of the solid. It considers the effects of nonlinear strain hardening, strain rate hardening and thermal softening. The model can be expressed as

$$\sigma_y = \left(A_1 + A_2\varepsilon_p^{n_\sigma}\right)\left(1 + A_3\ln\frac{\dot{\varepsilon}}{\dot{\varepsilon}_\circ}\right)\left(1 - T_h^{m_\sigma}\right), \tag{6.58}$$

where A_i are the material parameters, ε_p is the plastic strain, n_σ is the strain hardening exponent, $\dot{\varepsilon}$ is the equivalent strain rate, $\dot{\varepsilon}_\circ$ is a reference strain rate, T_h is the homologous temperature and m_σ is the thermal softening exponent.

The equivalent strain rate is defined as

$$\dot{\varepsilon} = \sqrt{\frac{3}{2}\dot{\boldsymbol{\varepsilon}}:\dot{\boldsymbol{\varepsilon}}}, \tag{6.59}$$

whereas the homologous temperature takes the form

$$T_h = \frac{T - T_\circ}{T_m - T_\circ}, \tag{6.60}$$

where T_m is the melting temperature.

The Johnson-Cook [88] damage model is used to calculate the failure plastic strain of the solid. The effect of stress triaxiality, strain rate and thermal softening are taken into account. The model can be written as

$$\varepsilon_{p_f} = \left[D_1 + D_2 \exp\left(D_3 \frac{p}{\sigma_v}\right)\right]\left(1 + D_4 \ln\frac{\dot{\varepsilon}}{\dot{\varepsilon}_\circ}\right)(1 + D_5 T_h), \tag{6.61}$$

where D_i are the material parameters.

The material damage is characterized by a scalar variable, δ, that accounts for the accumulation of plastic strain. It is defined as

$$\delta = \sum_i \frac{\Delta\varepsilon_p^i}{\varepsilon_{p_f}^i}, \tag{6.62}$$

where $\Delta\varepsilon_p^i$ is the plastic strain increment during time step i, and $\varepsilon_{p_f}^i$ is the failure plastic strain for time step i, computed using Equation 6.61.

As the microscale simulation advances, δ increases with the accumulation of plastic strain on the FVPM particles that discretize the solid. Once $\delta \geq 1.0$, the material fails: the affected FVPM particle is immediately removed from the system.

6.5.4 Thermal Model

Two contributions conform the heat source per unit volume, $\dot{q}$, in the energy conservation equation: thermoplastic and frictional heating, $\dot{q}_p$ and $\dot{q}_f$, respectively.

The thermoplastic heating, *i.e.* the dissipation of the plastic work in the form of thermal energy, is modeled as

$$\dot{q}_p = \beta_p\left(\boldsymbol{\sigma}:\dot{\boldsymbol{\varepsilon}}_p\right), \tag{6.63}$$

where $\dot{\boldsymbol{\varepsilon}}_p$ is the plastic strain rate and β_p is the inelastic heat fraction, *i.e.* the fraction of the plastic work converted to heat. Even though β_p is a function of strain rate and plastic strain [169], it is usually assumed constant and equal to 0.9 in metals [140, 200]. Within the radial return plasticity algorithm, the temperature increment at a given time step is written as

$$\Delta T_p = \frac{\dot{q}_p \Delta t}{\rho c_p} = \frac{\beta_p \left(\boldsymbol{\sigma} : \dot{\boldsymbol{\varepsilon}}_p\right) \Delta t}{\rho c_p} = \frac{\beta_p \left[\left(\boldsymbol{s}^{t+\Delta t}\right) : \left(\dot{\boldsymbol{\varepsilon}} \frac{(1-f_r)\sigma_v(\hat{\boldsymbol{s}})}{\sigma_v(\hat{\boldsymbol{s}}) - \sigma_v(\boldsymbol{s}^t)}\right)\right] \Delta t}{\rho c_p}, \tag{6.64}$$

where $\frac{(1-f_r)\sigma_v(\hat{\boldsymbol{s}})}{\sigma_v(\hat{\boldsymbol{s}}) - \sigma_v(\boldsymbol{s}^t)}$ is slightly less than unity, meaning that the elastic strain rate $\dot{\boldsymbol{\varepsilon}}_e$ is small compared to $\dot{\boldsymbol{\varepsilon}}_p$, that is, $\dot{\boldsymbol{\varepsilon}}_p = \dot{\boldsymbol{\varepsilon}} - \dot{\boldsymbol{\varepsilon}}_e \approx \dot{\boldsymbol{\varepsilon}}$.

The frictional heating is modeled as

$$\dot{q}_f = \eta \frac{\boldsymbol{f}_f \cdot \boldsymbol{C}_{r,m}}{V}, \tag{6.65}$$

where V is the particle volume and η is the fraction of the friction heat transferred to the solid. The material properties determine η according to the following expression [140]

$$\eta = \left(1 + \sqrt{\frac{(\rho \kappa c_p)_s}{(\rho \kappa c_p)_m}}\right)^{-1}, \tag{6.66}$$

where the subscripts $_s$ and $_m$ denote the sediment and solid, respectively.

6.5.5 Artificial Dissipation

Similar to the fluid in the macroscale, the solid and sediments in the microscale require some artificial dissipation to ensure stability. Spurious oscillations can lead to inconvenient instabilities than can nonetheless be suppressed by artificial viscosity without affecting the physical behavior of the material to a great extent.

The linear momentum conservation equation is modified as

$$\rho \frac{d\boldsymbol{C}}{dt} = \nabla \cdot \left\{ \boldsymbol{\sigma} + \mu_a \left[2\dot{\boldsymbol{\varepsilon}} + \frac{1}{3} \mathrm{tr}\left(\dot{\boldsymbol{\varepsilon}}\right) \boldsymbol{I} \right] \right\} + \boldsymbol{f}, \tag{6.67}$$

where μ_a is the artificial viscosity; note that it is applied in both the deviatoric and hydrostatic directions.

6.6 Discussion on the Modeling Assumptions

6.6.1 Fluid Models

Whereas water at 20 °C, the typical condition in hydraulic turbines, can be assumed Newtonian without accuracy concerns, assuming it weakly compressible might be questionable. Water

is not incompressible, but does have very low compressibility. The key modeling question is then *how weak* is weakly compressible.

In the weakly compressible model the amount of compressibility is dictated by the numerical speed of sound a. Since density variations scale as

$$\delta\rho_f \approx \rho_f \frac{C_f^2}{a^2}, \tag{6.68}$$

then setting $a = 10 \max\left(C_f\right)$ ensures density variations of the order of 1 % [141]. This level of density variation seems a reasonable compromise to avoid solving the incompressibility constraint, and is used in the case studies to define a. Less artificial compressibility can be obtained by increasing a, with the time step reduction this implies, but the effect on the results is minor [188]. A greater concern about the artificial compressibility is the noise it introduces in the pressure field, which can be partly filtered out by using a smoothing mass flux, see Section 7.3.5 for the details.

The need for artificial viscosity to ensure stability is ubiquitous in the field of numerical simulation; whereas some methods include enough intrinsic numerical dissipation, others require an explicit dissipation term. In this work, the artificial viscosity is applied in analogy to the bulk viscosity: proportional to $\nabla \cdot \boldsymbol{C}$. Therefore, only the compression and dilation dynamics are damped, leaving the shear component unaffected, *i.e.* it does not change the main fluid dynamics such as the velocity profiles.

Note that the fluid modeling only includes the liquid phase, whereas the gas phase is neglected. For the problems under study, namely free-surface water jets, the surrounding air induces some jet dispersion [203]. However, given that the distance traveled by the jets is usually small before impinging the target surface, the effect of this assumption is expected to be negligible.

The k-ϵ model implemented is the most robust and common model available, see Appendix B.5 for the implementation verification. The standard wall function is used to describe the flow near walls, since it is unfeasible to discretize the extremely thin boundary layer present at the high Reynolds numbers of interest without dynamic particle refinement, which is unavailable.

The turbulence model, which is based on the eddy viscosity hypothesis, assumes that the Reynolds stresses are isotropic. Within the boundary layer this is inaccurate: the velocity fluctuations parallel to the wall tend to be greater than the perpendicular ones. This inaccuracy has an influence in the sediment dynamics near the wall, and therefore in the impact condition predictions; however, turbulence models that bypass the isotropy assumption are much more complex and are out of the scope of this initial effort in modeling the erosion process.

The turbulence model wall function assumes that the flow is in equilibrium, meaning that the turbulence production and dissipation at the wall are equal; it is difficult to assess the level of inaccuracy of this supposition in the unsteady flow that occurs in Pelton turbine buckets. The implementation and assessment of a non-equilibrium wall function is left for future work.

For all its faults and simplifications, the standard k-ϵ model with equilibrium wall function provided the best results, in terms of impact condition distributions and erosion rate predictions, compared to more sophisticated models such as the Realizable k-ϵ, RNG k-ϵ, SST k-ω and the Reynolds Stress Model, in a recent systematic study of the jet impingement erosion case [202]. Furthermore, the wall function approach allows including the wall roughness, a consequence of the erosion, and its effect on the flow by means of a simple modification to the parameter E_k [57, 162, 173]. Yet again, the study of the effect of wall roughness on the erosion predictions is left for future work.

6.6.2 Sediment Transport Models

By far the most important force in the hydrodynamic transport of sediments is drag. The relative importance of the various forces depends on the flow field, sediment size, shape and density, but a representative estimation for sediments of $d = 100$ μm based on the case of jet impingement on a flat plate is as follows: drag accounts for ≈ 80 % of the hydrodynamic force, whereas the pressure gradient and added mass account for ≈ 12 % and ≈ 8 %, respectively. The lift and buoyancy forces are negligible for the aforementioned case, but are considered because they may become significant for very small sediments or large density ratios, respectively.

The correlation used to estimate the drag coefficient is plotted in Figure 6.2a as a function of Reynolds number and sediment sphericity; the values calculated far from the wall are illustrated by continuous lines, whereas the near-wall corrected values are shown with dotted lines. The near-wall correction applied corresponds to the component perpendicular to the wall, $c_d^{\perp}\left(F_{1,\perp}\right)$, at a normalized distance $\delta_s = 0.5$, meaning that the gap between wall and particle is equal to $0.5\frac{d}{2}$. Figure 6.2b illustrates the behavior of the correction factors $F_{1,\perp}$ and $F_{1,\parallel}$ for several values of δ_s.

The drag coefficient correlation covers the range of Reynolds numbers found in the transport of sediments: Figure 6.2a contains the range of Re for 4 typical sediment diameters, calculated using a representative range of relative velocity $C_{r,f} = 0.1\text{-}10$ m $\cdot$ s^{-1}. Whereas the sediment shape effect is predominant at higher Reynolds, affecting the larger particles, the near-wall correction is most important at lower Reynolds, affecting the smaller sediments.

The near-wall correction, whose behavior is illustrated in Figure 6.2b, increases as the sediment approaches the wall; the effect is much greater in the perpendicular direction, thus inducing an anisotropic drag coefficient. The effect of the thin liquid film between the sediment and the wall, which decreases the normal impact velocity, is thus reproduced by the near-wall drag correction, in spite of the fact that in the macroscale the fluid around each sediment, and thus the thin film, is not discretized.

The noisy pressure field induced by the weakly compressible character of the fluid model renders the estimation of ∇p very error-prone. It was found that, even after filtering out some noise by means of the smoothing mass flux, the estimated pressure gradient induced

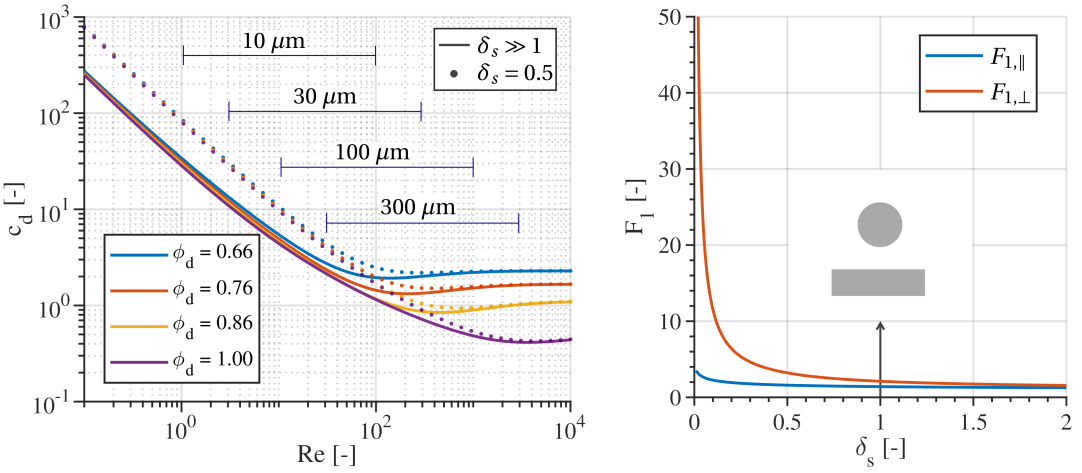

(a) Drag coefficient $c_d(\mathrm{Re}, \phi_d)$ far from the wall, $F_1(\delta_s \gg 1)$, and near the wall, $F_{1,\perp}(\delta_s = 0.5)$. The range of Re for 4 representative sediment diameters is presented, assuming a range of relative velocity $C_{r,f} = 0.1\text{-}10\ \mathrm{m \cdot s^{-1}}$.

(b) Near-wall drag correction factor $F_1(\delta_s)$. At $\delta_s = 1$, the gap between the sediment and the wall is equal to the sediment radius.

Figure 6.2 – Drag force behavior as a function of Re, ϕ_d and δ_s.

significant error on the sediment dynamics. The alternative form $-\nabla p \simeq \rho_f \boldsymbol{C}_f \cdot \nabla \boldsymbol{C}_f$ assumes inviscid and steady flow, thus injecting some error. However, it was found that this source of error is smaller than the alternative, directly calculating ∇p from the computed pressure field. Furthermore, the pressure gradient force constitutes a small contribution to the hydrodynamic force, so the overall error induced by the assumption is negligible. The only exception to this assertion occurs at the boundary layer, where viscosity is dominant and the strong velocity gradient overestimates the pressure gradient force; therefore $\boldsymbol{f}_p$ is neglected if the sediment is near the wall, *i.e.* if the closest fluid particle is subject to the turbulence wall function.

The assumed $1/7^{\text{th}}$ power law velocity profile experienced by the sediments very close to the wall is a reasonable assumption for steady flow, but does induce some error for the unsteady flow characteristic of Pelton turbines. In spite of this, the approach is significantly more accurate than extrapolating the velocity based on the fluid particles near the wall. Furthermore, as the fluid discretization is refined, the zone where the velocity profile is assumed gets smaller; in other words, the velocity experienced by the sediments converges under refinement.

As discussed in Section 3.1, considering the effect of sediments on the fluid turbulence is necessary, in principle, at the concentrations present on hydraulic turbines. However, that interaction is complex and expensive, and a research topic in its own right; it has been neglected in all previous investigations of macroscale sediment transport, and it will be neglected in this work. However, note that neglecting the effect of the sediments on the mean flow *is* justified at the concentrations relevant to this work, *i.e.* the 1-way coupling scheme assumed should induce negligible errors.

The continuous random walk model of turbulent dispersion was verified in a simple test case

where the drift of sediments of various sizes under homogeneous turbulence was monitored, see Appendix B.6. The expected physical behavior was verified: smaller sediments closely follow the turbulent fluctuations, whereas larger ones are less sensitive to the high frequency forcing they generate; moreover, the drift distance decreases with sediment size.

The continuous random walk model provides more realistic turbulent fluctuations compared to the discrete random walk model, see Appendix B.6. Consequently, it was verified that less sediments need to be injected on a given macroscale simulation to achieve converged sediment impact distribution results. One disadvantage shared by both approaches is the fact that the fluctuating velocity is calculated independently for each sediment, *i.e.* no fluctuating velocity field is computed. In other words, the fluctuating velocities are time-correlated for each sediment, but not space-correlated among sediments. To bypass this limitation, either a direct numerical simulation of the Navier-Stokes equations or a novel space-correlated random walk approach would be required.

The time step used to integrate the Langevin equation is subject to the constraint $\Delta t < 0.1\tau_s$, which greatly restricts the macroscale model time step. A *dual time stepping scheme* has been developed to bypass this restriction, as discussed in Section 7.3.3.

6.6.3 Contact Models

In the macroscale model, the inter-sediment collisions are considered in order to capture the effect they have on the erosion, which becomes important at very high sediment concentration, as discussed in Section 3.1. Even though assuming inelastic collisions may appear too simple, in fact it is accurate enough because the sediment velocities are defined by the hydrodynamic force almost instantly after the collision, such that the exactitude of the rebound velocity is inconsequential. The need to detect the inter-sediment collisions significantly restricts the macroscale simulation time step, as detailed in Section 7.3.3; if a more accurate contact algorithm were used, *e.g.* a no-penetration constraint enforced by a penalty force, the required time step would be some 20 times smaller, rendering the simulation impractical.

Note that the contact criterion in the macroscale assumes spherical sediments; the sediment sphericity ϕ_d is only used within the drag coefficient calculation. In the microscale, the sediment shape, defined by the shape parameter ϕ_s, is fully discretized by means of many FVPM particles. The contact force is computed independently for each pair of particles discretizing the sediment and the solid, respectively, with a contact criterion defined in terms of the overlap of the spherical FVPM particles.

Equation 6.44 describes a simple *penalty method*, which depends on the parameter k_c. As presented in Appendix B.2, the higher the value of k_c, the higher is the accuracy with which the no-penetration constraint is satisfied. However, increasing k_c also brings about instabilities due to the increasing stiffness of the contact, requiring a smaller time step. A value of $k_c = 20$ was found to be the best compromise between accuracy and computational cost.

Friction plays a predominant role in the erosion process, especially at lower impact angles. The friction model employed considers only a Coulomb friction coefficient, function of the slip velocity, so there is plenty of room for improvement. Some more complex models include an additional friction force proportional to the slip velocity, the pre-sliding effect, the hysteresis behavior and the lubricant effect [124]. These models might improve the accuracy of the microscale simulations, but their assessment is left for future work.

Moreover, the use of friction coefficients is a simplified macroscopic description of the complex microscopic interactions that underlie the phenomenon: inter-surface adhesion, surface deformation and roughness interactions. At the scale of the sediments, a macroscopic description might not be good enough, although a more fundamental description of friction might be too expensive for the problem at hand.

6.6.4 Material Models

Both the solid and the sediments in the microscale are assumed homogeneous and isotropic. Quartz, the most common sediment material, is homogeneous; however, its crystalline structure renders some of its mechanical properties anisotropic. The complexity of considering this subtlety being greater than the accuracy improvement it might cause, we opt for simply using an average value of the anisotropic Young's modulus within the aforementioned linear homogeneous isotropic elasticity model.

Martensitic stainless steel of the grade typically used in hydraulic machines, a micrograph of which is presented in Figure 6.3, is homogeneous and isotropic above a given scale dictated by the microstructure, at least in an average sense, *i.e.* over many impacts. Considering a circular region with $d = 5$ μm, which corresponds to the impact zone of a sediment with $d \approx 20$ μm, it can barely be justified that the microstructure is fine enough for the homogeneous and isotropic assumptions to hold. The accuracy of these assumptions degrades even further for smaller sediments. However, considering the range of sediment sizes important in hydraulic machines, 10-300 μm as detailed in Section 2.2.1, and the fact that the smallest sediments cause the least erosion, it can be said that the error introduced by these assumptions is not considerable. Furthermore, the use of a more detailed description of the solid, namely one which accounts for the microstructure, would render the multiscale model too expensive to be of any practical engineering use.

One implicit modeling assumption is that the sediments do not fracture. Depending on the impact velocity, it might be inaccurate: experiments have shown that the sediment size distribution changes after repeatedly using the same batch of sediments, implying that particles do tend to fracture. In the microscale model, the neglect of sediment fracture may introduce some error into the calculation of the erosion ratio and the restitution coefficients. In the macroscale model, it might be unnecessary to consider the sediment fracture because they only pass through the turbine once, such that assuming that their shape and size does not change might be a fair approximation. Deeper investigation into this aspect of the multiscale model is left for future work.

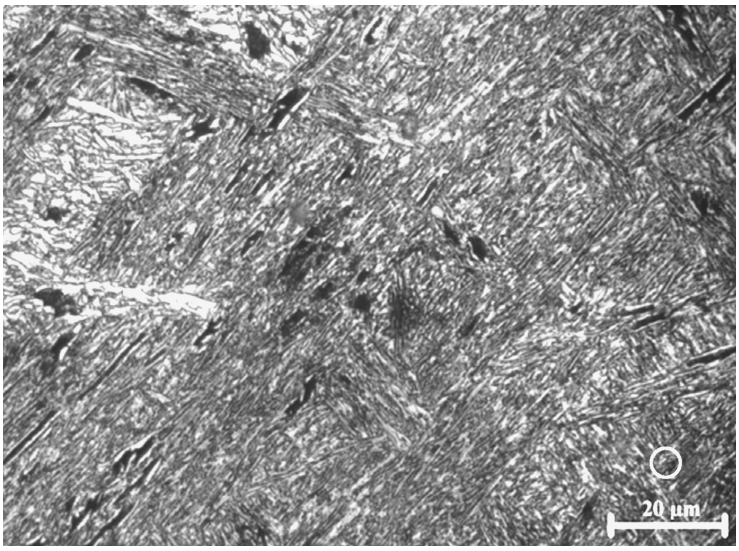

Figure 6.3 – Optical micrograph of the fine martensitic microstructure of 13Cr-4Ni [99]. The circle on the bottom right corner is 5 μm in diameter.

The solid matter that fails in the microscale is immediately removed from the system, consistent with what would happen in the macroscale: the fluid would quickly dispose of any detached material before subsequent sediment impacts.

Heat conduction is neglected within the microscale model. The impact dynamics is so fast that the heat generated has no time to diffuse, leading to an adiabatic temperature increase [122, 175]. To avoid unphysical heat accumulation during the microscale simulation, the temperature is relaxed back to the reference temperature in between impacts. By using this approach, the local temperature increase and its effect on the material response are considered, without the need to introduce long time intervals in between impacts that would render the simulation unfeasible.

The microscale solid is supposed to model part of the macroscopic domain, *i.e.* its extend should be much greater than the sediment size. However, as illustrated in Figure 5.2, only a hemispherical portion of the solid domain is considered in order to keep the problem size reasonable. The hemispherical boundary reflects the elastic waves generated at the impact location, waves that would otherwise propagate away and not interfere with subsequent impacts. To avoid unphysical accumulation of elastic deformation waves with successive impacts, a damping force is applied within the outermost hemispherical shell defined by $\|\boldsymbol{x}\| > r_d$, where $\boldsymbol{x}$ is the position and r_d is the threshold distance below which no damping is applied. The force is written as

$$\boldsymbol{f}_d = -0.05\frac{m}{\Delta t}\left[\frac{\max(0.0,\ \|\boldsymbol{x}\| - r_d)}{r_d}\right]^2 \cdot \boldsymbol{C}_m, \tag{6.69}$$

where m and $\boldsymbol{C}_m$ are the mass and velocity of the solid FVPM particle, respectively. The

damping coefficient 0.05 is selected such that the elastic waves have been damped significantly before the following sediment impact. The damping zone, characterized by r_d, is located sufficiently far away from the refined zone where impacts occur in order to ensure that it does not affect the impact results; see Appendix B.2 for the details.

The Johnson-Cook constitutive model coupled with the Mie-Grüneisen equation of state is the most common configuration for impact simulations in the literature [38, 101, 180, 196, 197]. Two equations of state and two constitutive models, including the Cowper-Symonds model, were compared with the aforementioned configuration to corroborate the trend in the literature. The results [116] indicate that indeed the Johnson-Cook constitutive model provides the greatest accuracy, and that including the effect of temperature on the equation of state is important, even if the temperature increase is minor.

The Johnson-Cook damage model, where it is assumed that failure occurs as a consequence of plastic deformation accumulation, is applicable to ductile metals. It is therefore well-suited for describing the erosion of *uncoated* hydraulic turbines. However, the model is clearly not adequate for simulating *coated* turbines because the dominant failure mechanism of hard coatings is fatigue by repeated elastic deformation without any plastic strain. The multiscale model of erosion is still applicable to the case of coated turbines, provided an adequate microscale damage model is used instead of the Johnson-Cook model. This is a possible direction of future development.

In spite of its popularity, the Johnson-Cook model has many limitations. For instance, it has been found that the model parameters change significantly depending on the experimental apparatus used to characterize the material [180]. Moreover, as explained in Chapter 9, the fitting of the experimental results is sometimes poor. These circumstances point to the fact that the model parameters are not really material constants, but simply empirical approximations to the complex microscopic interactions at the scale of the material microstructure.

The reader might wonder if there is any benefit in replacing erosion correlations, with their many parameters, with physical model that have as many parameters. After all, the Johnson-Cook model could be understood as a kind of correlation; why not directly use a correlation for the erosion instead? The answer is that the processes and interactions that are supposed to be captured by a material model are *more fundamental* than the ones captured by an erosion correlation, and therefore the *accuracy* and *transferability* should be better. Fitting the results of a complex erosion experiment with a correlation necessarily conflates the very different processes that take place; not surprisingly, when using the correlation on a different setup the predictions do not match reality. However, by fitting a material model one is trying to capture more fundamental aspects, for instance, how sensitive to the rate of strain the material is; this information should be transferable to any other setup in which the material is strained in a similar way.

In other words, by characterizing a more fundamental level of the hierarchy of interactions that define the behavior of a physical system, one hopes to bypass the problem of transferability

and improve the accuracy. The hope is well grounded: whereas the average error of the leading erosion correlation is about 180 %, that of impact simulations is 4-30 %, as illustrated in Sections 3.1 and 3.2, respectively.

An overview of all the model parameters is presented in Appendix C, together with a classification based on how physical and easily characterizable they are.

7 The Finite Volume Particle Method

The governing equations, detailed in Chapter 6, are discretized in the framework of the Finite Volume Particle Method (FVPM). However, note that both the multiscale model and the submodels that conform it are independent of the discretization scheme used.

FVPM, introduced in 2000 by Hietel et al. [77], is a particle-based method that can be understood as a generalization of the classical Finite Volume Method (FVM): the spherical volumes used to discretize the domain, *i.e. FVPM particles*, are allowed to move and overlap. Furthermore, it is based on an Arbitrary Lagrangian-Eulerian (ALE) formulation that allows computational nodes to move with an arbitrary velocity: they can remain fixed (Eulerian reference frame), they can move with the material velocity (Lagrangian reference frame), or anything in between.

Some of the desirable features of FVM, such as local conservation and consistency, together with the flexibility provided by the moving particles, render FVPM especially well-suited to handle complex free surface problems as well as cases where significant deformations are expected, such as impact simulations where traditional mesh-based methods suffer from excessive mesh distortion and tangling. Nonetheless, FVPM is computationally expensive and cannot reach high-order accuracy, limiting the scope of application of the method.

7.1 Derivation of the Discretization of a Generic Conservation Law

Consider a generic conservation law of the form

$$\frac{\partial \boldsymbol{U}}{\partial t} + \nabla \cdot \boldsymbol{F}(\boldsymbol{U}) = 0, \tag{7.1}$$

where $\boldsymbol{U}(\boldsymbol{x}, t)$ are the conserved variables and $\boldsymbol{F}(\boldsymbol{x}, t)$ the corresponding flux functions. For

the governing equations contained in Equation 6.1, these can be written as

$$\boldsymbol{U}(\boldsymbol{x},t)=\begin{bmatrix}\rho\\ \rho\boldsymbol{C}\\ \rho c_p T\end{bmatrix},\qquad \boldsymbol{F}(\boldsymbol{x},t)=\begin{bmatrix}\rho\boldsymbol{C}\\ \rho\boldsymbol{C}\otimes\boldsymbol{C}-\boldsymbol{\sigma}\\ \rho c_p T\boldsymbol{C}-\kappa\nabla T\end{bmatrix}. \tag{7.2}$$

We can write the *weak form* of Equation 7.1 by multiplying it by an arbitrary *test function* $\psi(\boldsymbol{x},t)$ and integrating over the domain Ω

$$\int_\Omega \frac{\partial \boldsymbol{U}(\boldsymbol{x},t)}{\partial t}\psi(\boldsymbol{x},t)\,dV+\int_\Omega \nabla\cdot\boldsymbol{F}(\boldsymbol{x},t)\,\psi(\boldsymbol{x},t)\,dV=0. \tag{7.3}$$

Provided this holds for any test function $\psi(\boldsymbol{x},t)$ on the Hilbert space, the weak form is equivalent to Equation 7.1.

Using the product rule for the partial derivative and the divergence leads to

$$\begin{aligned}&\int_\Omega \frac{\partial\,\boldsymbol{U}(\boldsymbol{x},t)\,\psi(\boldsymbol{x},t)}{\partial t}dV-\int_\Omega \boldsymbol{U}(\boldsymbol{x},t)\frac{\partial\psi(\boldsymbol{x},t)}{\partial t}dV\\ &\quad+\int_\Omega \nabla\cdot\big(\boldsymbol{F}(\boldsymbol{x},t)\,\psi(\boldsymbol{x},t)\big)\,dV-\int_\Omega \boldsymbol{F}(\boldsymbol{x},t)\cdot\nabla\psi(\boldsymbol{x},t)\,dV=0.\end{aligned} \tag{7.4}$$

Using Gauss's divergence theorem and Reynolds's transport theorem, knowing that the domain boundaries $\partial\Omega$ are allowed to move, we can write

$$\begin{aligned}&\frac{d}{dt}\int_\Omega \boldsymbol{U}(\boldsymbol{x},t)\,\psi(\boldsymbol{x},t)\,dV-\int_{\partial\Omega}(\dot{\boldsymbol{x}}_b\cdot\boldsymbol{n})\,\boldsymbol{U}(\boldsymbol{x},t)\,\psi(\boldsymbol{x},t)\,dS-\int_\Omega \boldsymbol{U}(\boldsymbol{x},t)\frac{\partial\psi(\boldsymbol{x},t)}{\partial t}dV\\ &\quad+\int_{\partial\Omega}\big(\boldsymbol{F}(\boldsymbol{x},t)\,\psi(\boldsymbol{x},t)\big)\cdot\boldsymbol{n}dS-\int_\Omega \boldsymbol{F}(\boldsymbol{x},t)\cdot\nabla\psi(\boldsymbol{x},t)\,dV=0,\end{aligned} \tag{7.5}$$

where $\dot{\boldsymbol{x}}_b$ denotes the boundary velocity and $\boldsymbol{n}$ is its outward pointing unit vector.

The Galerkin method is used to discretize the weak form of the equations. The following approximations are used for the conserved variables and corresponding flux functions

$$\boldsymbol{U}(\boldsymbol{x},t)\approx\sum_{j=1}^{N}\boldsymbol{U}_j(t)\,\psi_j(\boldsymbol{x},t),\qquad \boldsymbol{F}(\boldsymbol{x},t)\approx\sum_{j=1}^{N}\boldsymbol{F}_j(t)\,\psi_j(\boldsymbol{x},t), \tag{7.6}$$

where the domain has been discretized by a set of N particles, each of which has an associated *basis function* ψ_j. Under the Galerkin scheme, it is required that the spaces spanned by the test and basis functions are the same. This leads to [76]

$$\begin{aligned}&\frac{d}{dt}\sum_{j=1}^{N}\boldsymbol{U}_j(t)\int_\Omega \psi_j(\boldsymbol{x},t)\,\psi_i(\boldsymbol{x},t)\,dV-\sum_{j=1}^{N}\boldsymbol{U}_j(t)\int_{\partial\Omega}\psi_j(\boldsymbol{x},t)\,\psi_i(\boldsymbol{x},t)\,(\dot{\boldsymbol{x}}_b\cdot\boldsymbol{n})\,dS\\ &\quad-\sum_{j=1}^{N}\boldsymbol{U}_j(t)\int_\Omega \psi_j(\boldsymbol{x},t)\frac{\partial\psi_i(\boldsymbol{x},t)}{\partial t}dV+\sum_{j=1}^{N}\boldsymbol{F}_j(t)\cdot\int_{\partial\Omega}\psi_j(\boldsymbol{x},t)\,\psi_i(\boldsymbol{x},t)\,\boldsymbol{n}dS\\ &\quad-\sum_{j=1}^{N}\boldsymbol{F}_j(t)\cdot\int_\Omega \psi_j(\boldsymbol{x},t)\,\nabla\psi_i(\boldsymbol{x},t)\,dV=0,\end{aligned} \tag{7.7}$$

which holds for each of the N particles with associated basis function ψ_i.

Note that in building the scheme described by Equation 7.7 no simplifications have been made; the accuracy has not been compromised because the approximations in Equation 7.6 can be formulated to an arbitrary level of accuracy by enhancing the basis functions with additional degrees of freedom, as done in the discontinuous Galerkin method. Let us now consider the assumptions and approximations that will allow solving the scheme, but *will* hinder the accuracy of the method.

The chosen basis function in the current implementation of FVPM is the *Shepard function*, defined as

$$\psi_i(\boldsymbol{x},t) = \frac{W_i(\boldsymbol{x},t)}{\sigma_w(\boldsymbol{x},t)}, \tag{7.8}$$

where the kernel W_i and kernel summation σ_w are defined as

$$W_i(\boldsymbol{x},t) = \begin{cases} 1, & \text{if } \|\boldsymbol{x}-\boldsymbol{x}_i(t)\| < h_i, \\ 0, & \text{otherwise,} \end{cases} \qquad \sigma_w(\boldsymbol{x},t) = \sum_j W_j(\boldsymbol{x},t), \tag{7.9}$$

where $\boldsymbol{x}_i(t)$ is the time-dependent particle position and h_i is its radius, assumed constant. Figure 7.1 illustrates the Shepard function for one FVPM particle in 2D: it is a piecewise constant function with positive value within the particle support, and 0 elsewhere in the domain.

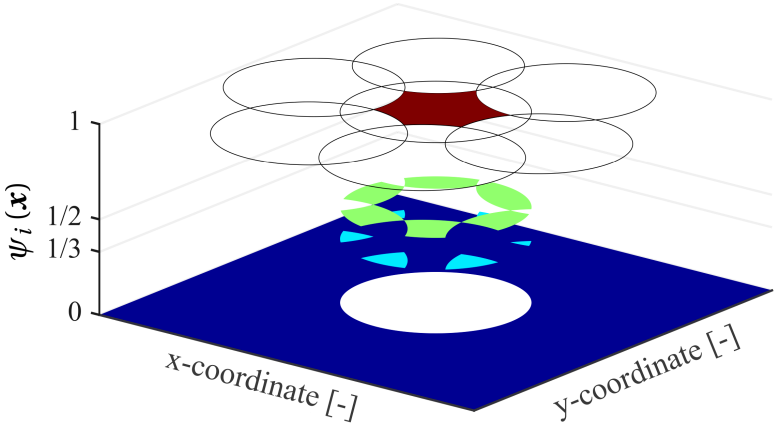

Figure 7.1 – Basis function $\psi_i(\boldsymbol{x})$ for one FVPM particle in 2D.

By construction, the set of Shepard functions conforms a partition of unity, *i.e.* $\sum_j \psi_j(\boldsymbol{x},t) = 1$, and as such it is only *first-order accurate*, meaning that it can only exactly reproduce a constant field. Formally speaking, this choice of basis function limits the accuracy of the discretization scheme to first-order [76].

The particle volume is defined as

$$V_i(t) = \int_\Omega \psi_i(\boldsymbol{x},t)\, dV, \tag{7.10}$$

whereas the cell average associated with the particle is defined as

$$\boldsymbol{U}_i(t) = \frac{1}{V_i}\int_\Omega \boldsymbol{U}(\boldsymbol{x},t)\,\psi_i(\boldsymbol{x},t)\,dV. \tag{7.11}$$

This cell average is a second-order accurate approximation of the field value at the particle centroid, defined as

$$\boldsymbol{b}_i(t) = \frac{1}{V_i}\int_\Omega \boldsymbol{x}\,\psi_i(\boldsymbol{x},t)\,dV, \tag{7.12}$$

whereas it is first-order accurate elsewhere within the particle support.

Let us consider the first term of Equation 7.7. It is approximated to first-order accuracy as

$$\begin{aligned}\frac{d}{dt}\sum_{j=1}^{N}\boldsymbol{U}_j(t)\int_\Omega \psi_j(\boldsymbol{x},t)\,\psi_i(\boldsymbol{x},t)\,dV &= \frac{d}{dt}\left[\boldsymbol{U}_i(t)\int_\Omega \psi_i(\boldsymbol{x},t)\,dV + \sum_{j=1,j\neq i}^{N} k_{ij}\left(\boldsymbol{U}_j(t)-\boldsymbol{U}_i(t)\right)\right]\\ &\overset{\mathcal{O}(h)}{\approx} \frac{d}{dt}\left[\boldsymbol{U}_i(t)\int_\Omega \psi_i(\boldsymbol{x},t)\,dV\right] = \frac{d}{dt}\left(\boldsymbol{U}_i V_i\right),\end{aligned} \tag{7.13}$$

where k_{ij} depend on the overlap between particles.

Consider now the second term of Equation 7.7. Note that $\psi_j\psi_i$ is non-zero only at the particle overlaps, or when $i=j$. Given that the particle overlaps are simply arc segments on the domain boundary, they do not contribute to the integral over the boundary surface. When $i=j$, the basis function product $\psi_j\psi_i = \psi_i = 1$ on the particle boundary shared with the domain boundary, so the term can we written as

$$\begin{aligned}\sum_{j=1}^{N}\boldsymbol{U}_j(t)\int_{\partial\Omega}\psi_j(\boldsymbol{x},t)\,\psi_i(\boldsymbol{x},t)\,(\dot{\boldsymbol{x}}_b\cdot\boldsymbol{n})\,dS &= \boldsymbol{U}_i(t)\int_{\partial\Omega}\psi_i(\boldsymbol{x},t)\,\dot{\boldsymbol{x}}_b\cdot\boldsymbol{n}dS\\ &\overset{\mathcal{O}(h)}{\approx} \boldsymbol{U}_b(t)\otimes\dot{\boldsymbol{x}}_b(t)\cdot\int_{\partial\Omega}\psi_i(\boldsymbol{x},t)\,\boldsymbol{n}dS = \boldsymbol{U}_b\otimes\dot{\boldsymbol{x}}_b\cdot\boldsymbol{B}_i,\end{aligned} \tag{7.14}$$

where $\boldsymbol{B}_i = \int_{\partial\Omega}\psi_i(\boldsymbol{x},t)\,\boldsymbol{n}dS$ is the surface of particle i shared with the domain boundary, also known as the boundary interaction vector. The above simplification takes advantage of the fact that, to within first-order accuracy, the boundary value $\boldsymbol{U}_b$ is equal to the particle cell average $\boldsymbol{U}_i$; moreover, the boundary velocity is constant within the particle support and equal to the particle velocity, also denoted $\dot{\boldsymbol{x}}_b$.

The fourth term of Equation 7.7 can be simplified in a similar manner

$$\sum_{j=1}^{N}\boldsymbol{F}_j(t)\cdot\int_{\partial\Omega}\psi_j(\boldsymbol{x},t)\,\psi_i(\boldsymbol{x},t)\,\boldsymbol{n}dS = \boldsymbol{F}_i(t)\cdot\int_{\partial\Omega}\psi_i(\boldsymbol{x},t)\,\boldsymbol{n}dS \overset{\mathcal{O}(h)}{\approx} \boldsymbol{F}_b\cdot\boldsymbol{B}_i, \tag{7.15}$$

where $\boldsymbol{F}_b$ is the flux at the domain boundary, a first-order approximation .

As presented in Appendix A.3, the third term of Equation 7.7 can be approximated to first-order

accuracy as

$$\sum_{j=1}^{N} \boldsymbol{U}_j(t) \int_\Omega \psi_j(\boldsymbol{x},t) \frac{\partial \psi_i(\boldsymbol{x},t)}{\partial t} dV \overset{\mathcal{O}(h)}{\approx} \sum_{j=1}^{N} \frac{1}{2} \left(\boldsymbol{U}_i + \boldsymbol{U}_j\right) \otimes \left(\dot{\boldsymbol{x}}_j \cdot \boldsymbol{\Gamma}_{ij} - \dot{\boldsymbol{x}}_i \cdot \boldsymbol{\Gamma}_{ji}\right), \tag{7.16}$$

where $\dot{\boldsymbol{x}}$ is the particle velocity and $\boldsymbol{\Gamma}$ is the *interaction vector*, defined as

$$\boldsymbol{\Gamma}_{ij} = \int_\Omega \frac{\psi_i(\boldsymbol{x},t)\ \nabla W_j(\boldsymbol{x},t)}{\sigma_w(\boldsymbol{x},t)} dV. \tag{7.17}$$

The interaction vectors are used to weight the flux exchanges between particles and as such, they are analogous to the area vectors defined between volumes in the traditional FVM.

Similarly, as presented in Appendix A.3, the fifth term of Equation 7.7 can be written as

$$\sum_{j=1}^{N} \boldsymbol{F}_j(t) \cdot \int_\Omega \psi_j(\boldsymbol{x},t) \nabla \psi_i(\boldsymbol{x},t)\, dV = -\sum_{j=1}^{N} \frac{1}{2} \left(\boldsymbol{F}_i + \boldsymbol{F}_j\right) \cdot \left(\boldsymbol{\Gamma}_{ij} - \boldsymbol{\Gamma}_{ji}\right). \tag{7.18}$$

By using the shorthands $\boldsymbol{U}_{ij} = \frac{1}{2}\left(\boldsymbol{U}_i + \boldsymbol{U}_j\right)$ and $\boldsymbol{F}_{ij} = \frac{1}{2}\left(\boldsymbol{F}_i + \boldsymbol{F}_j\right)$, together with the approximations developed in Equations 7.13 to 7.18, we can finally write

$$\frac{d}{dt}(\boldsymbol{U}_i V_i) = \sum_{j=1}^{N} \left[\boldsymbol{U}_{ij} \otimes \left(\dot{\boldsymbol{x}}_j \cdot \boldsymbol{\Gamma}_{ij} - \dot{\boldsymbol{x}}_i \cdot \boldsymbol{\Gamma}_{ji}\right) - \boldsymbol{F}_{ij} \cdot \left(\boldsymbol{\Gamma}_{ij} - \boldsymbol{\Gamma}_{ji}\right)\right] + (\boldsymbol{U}_b \otimes \dot{\boldsymbol{x}}_b - \boldsymbol{F}_b) \cdot \boldsymbol{B}_i. \tag{7.19}$$

Equation 7.19 describes the FVPM discretization of a generic conservation law. Formally, it is a *first-order accurate* method because of the piecewise constant basis functions used and because of the approximations done for each of the terms of Equation 7.7. In practice, however, both first-order convergence results [86, 128] and closer to second-order convergence results [84, 146, 164] have been reported. The effective convergence rate depends on the uniformity of the particle distribution, on the relative importance of different error terms, and on the boundary conditions used, *i.e.* it is problem-dependent.

7.2 Exact Computation of the Interaction Vectors

To solve the FVPM discretization scheme, it is necessary to compute the interaction vectors between each pair of particles. Based on the top-hat kernel definition, Equation 7.9, it follows that $\nabla W_j = 0$ everywhere except on the border of the particle support, $\partial\Omega_j$, where

$$\nabla W_j = -\delta_{\partial\Omega_j} \boldsymbol{n}_j, \tag{7.20}$$

with

$$\delta_{\partial\Omega_j}(\boldsymbol{x}) = \delta\left(f\left(\boldsymbol{x},\ \partial\Omega_j\right)\right), \tag{7.21}$$

where δ is Dirac's delta function, $\boldsymbol{n}_j$ is the outwards pointing normal to $\partial\Omega_j$, and $f\left(\boldsymbol{x},\ \partial\Omega_j\right)$ is

the signed distance from $\boldsymbol{x}$ to $\partial\Omega_j$. The interaction vector is then

$$\boldsymbol{\Gamma}_{ij} = \int_\Omega \frac{\psi_i \nabla W_j}{\sigma_w} dV = \int_\Omega \frac{W_i \nabla W_j}{\sigma_w^2} dV = \int_{\Omega_i \cap \partial\Omega_j} \int_{-\epsilon}^{+\epsilon} \frac{-\delta_{\partial\Omega_j} \boldsymbol{n}_j}{\sigma_w^2} df dS. \tag{7.22}$$

On $\partial\Omega_j$ we have $\nabla\sigma_w = \left(\sigma_w^+ - \sigma_w^-\right)\delta_{\partial\Omega_j}\boldsymbol{n}_j$, where σ_w^+ and σ_w^- denote the kernel summation outside and inside of $\partial\Omega_j$, respectively. It follows that

$$\begin{aligned}
\boldsymbol{\Gamma}_{ij} &= \int_{\Omega_i \cap \partial\Omega_j} \int_{-\epsilon}^{+\epsilon} \frac{-1}{\sigma_w^+ - \sigma_w^-} \frac{\nabla\sigma_w}{\sigma_w^2} df dS = \int_{\Omega_i \cap \partial\Omega_j} \int_{-\epsilon}^{+\epsilon} \frac{1}{\sigma_w^+ - \sigma_w^-} \nabla\left(\frac{1}{\sigma_w}\right) df dS \\
&= \int_{\Omega_i \cap \partial\Omega_j} \int_{-\epsilon}^{+\epsilon} \frac{1}{\sigma_w^+ - \sigma_w^-} \left(\frac{1}{\sigma_w^+} - \frac{1}{\sigma_w^-}\right) \delta_{\partial\Omega_j} \boldsymbol{n}_j df dS \\
&= \int_{\Omega_i \cap \partial\Omega_j} -\left(\frac{1}{\sigma_w^+ \sigma_w^-}\right) \boldsymbol{n}_j dS \int_{-\epsilon}^{+\epsilon} \delta_{\partial\Omega_j} df = -\int_{\Omega_i \cap \partial\Omega_j} \frac{1}{\sigma_w^+ \sigma_w^-} \boldsymbol{n}_j dS.
\end{aligned} \tag{7.23}$$

By partitioning $\Omega_i \cap \partial\Omega_j$ into M elementary surfaces with constant σ_w^+ and σ_w^- values, the integral can be evaluated exactly as

$$\boldsymbol{\Gamma}_{ij} = -\sum_{l=1}^{M} \frac{\boldsymbol{S}_l}{\sigma_{w,l}^+ \sigma_{w,l}^-}, \tag{7.24}$$

where $\boldsymbol{S}_l$ is the surface vector. Figure 7.2 illustrates the partition of $\partial\Omega_j$, the spherical suface of particle j, into elementary surfaces defined by the intersections with other particles. The σ_w^- values on $\partial\Omega_j$ are shown, as well as the surface vectors $\boldsymbol{S}_l$ within Ω_i.

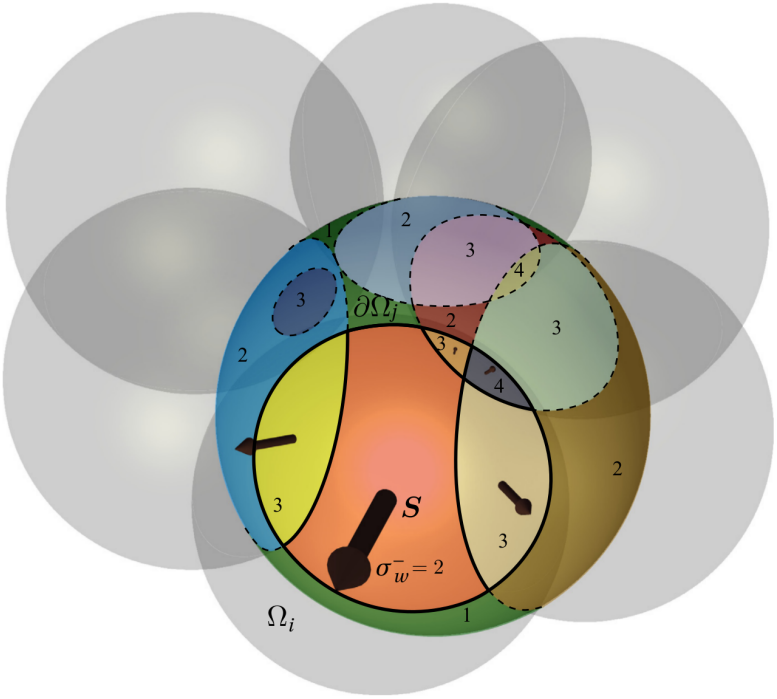

Figure 7.2 – Partition of $\partial\Omega_j$ into elementary surfaces defined by the intersections with other particles [84].

7.3 Some Details of the CPU and GPU Implementations of SPHEROS

SPHEROS is an in-house implementation of 3D FVPM with the aforementioned exact integration of the interaction vectors using spherical top-hat kernels. It has been under development since 2010, is written in C++, is parallelized using MPI and uses the HDF5 library for I/O. The code has recently been ported to Graphics Processing Units (GPUs), a version referred to as GPU-SPHEROS. It is written in CUDA C/C++ and also uses the MPI and HDF5 libraries.

GPU-SPHEROS is between 6 and 10 times faster than the CPU version [3, 4], allowing for the simulation of larger, more complex problems. Both SPHEROS [83–86, 112–116, 128, 188, 190, 191] and GPU-SPHEROS [2–4, 6, 7, 111] have been validated on a number of test cases. Some parallel scaling performance results are provided in Section 8.1.1.

The computation of the interaction vectors is by far the most expensive step of the FVPM algorithm, taking 60-70 % of the total execution time. Other necessary steps are the neighbor search, the flux computation and the time integration, as detailed hereafter.

7.3.1 Nearest Neighbor Search Algorithm

A necessary step before computing the interaction vectors and interparticle fluxes is to identify the neighbors of each particle, *i.e.* all the nearby particles that intersect a given particle. A simple distance check, taking into account the radius h of each particle, suffices; however, checking the distance for each particle with respect to all other particles is very expensive.

To avoid such an approach, the domain is first partitioned recursively, forming an *octree* in 3D or a *quadtree* in 2D; the refinement of the tree-like structure depends on the local distribution of particles, such that smaller branches are generated when the particles are smaller or closer together. The distance checking is then performed for each particle, but considering only particles located on the same branch or immediately contiguous branches. Figure 7.3 illustrates the partitioning of a simple 2D domain by means of a quadtree; for each of the blue particles, the distance is only checked with respect to green or blue particles.

The octree is a byproduct of using a space-filling curve, the *Morton curve*, to map the 3D particle distribution into a 1D representation whilst preserving locality. When storing the particles in memory, they are first sorted according to the Morton indices, such that particles that are nearby in the domain tend to be nearby in memory, significantly improving the memory access pattern and the overall GPU code performance.

A different octree is used to partition the domain for parallel computation. Each of the computing nodes is assigned a subdomain, a given number of branches to process. The subdomains are defined by segments of the 1D Morton curve; the points that define these segments are dynamically adapted to ensure that each subdomain has about the same computational load. This *dynamic load balancing* is fundamental because the distribution of particles within the domain may change significantly as the simulation advances.

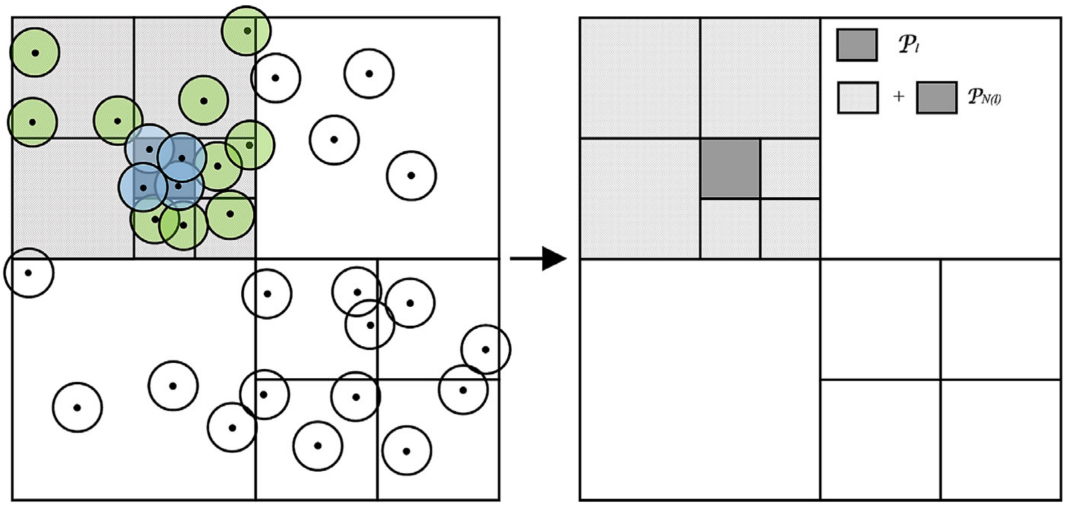

Figure 7.3 – Quadtree partition of a 2D domain [4]. For each of the blue particles, the distance is only checked with respect to green or blue particles.

7.3.2 Weighted Least Squares

A weighted least squares approach is used to fit a linear field through the scattered data provided by the particles. Such a linear fit is used to interpolate field variables in between the particle locations, for example to estimate the fluid velocity experienced by a given sediment. It is also used to estimate the gradients, for instance to calculate the solid strain rate $\dot{\boldsymbol{\varepsilon}}(\nabla \boldsymbol{C}_m)$.

Assuming that the cell average of a given field, U_i, is a second-order accurate approximation of the underlying field at the particle centroid, then the linear field reconstructed upon the cell averages is also second-order accurate. Note that the assumption may not hold for some cases, for example if first-order errors unrelated to the cell average definition become dominant. Furthermore, the accuracy also decreases if the field is extrapolated, *i.e.* if the location where the field value is estimated is not well surrounded by particles.

The weighted least squares formulation reads

$$\begin{pmatrix} \tilde{U}(\boldsymbol{x}) \\ \tilde{\nabla} U(\boldsymbol{x}) \end{pmatrix} = \begin{pmatrix} \sum_k \Phi_k(\boldsymbol{x}) & \sum_k (\boldsymbol{x}-\boldsymbol{b}_k)^T \Phi_k(\boldsymbol{x}) \\ -\sum_k (\boldsymbol{x}-\boldsymbol{b}_k)\Phi_k(\boldsymbol{x}) & \sum_k (\boldsymbol{x}-\boldsymbol{b}_k)(\boldsymbol{x}-\boldsymbol{b}_k)^T \Phi_k(\boldsymbol{x}) \end{pmatrix}^{-1} \begin{pmatrix} \sum_k \Phi_k(\boldsymbol{x}) U_k(\boldsymbol{b}_k) \\ \sum_k (\boldsymbol{x}-\boldsymbol{b}_k)\Phi_k(\boldsymbol{x}) U_k(\boldsymbol{b}_k) \end{pmatrix}, \tag{7.25}$$

where $\tilde{U}(\boldsymbol{x})$ and $\tilde{\nabla} U(\boldsymbol{x})$ are the estimated values of the field and its gradient, respectively, at an arbitrary position $\boldsymbol{x}$, and $U_k(\boldsymbol{b}_k)$ are the cell averages, which are associated with the particle centroid $\boldsymbol{b}_k$. The weighting kernel is a Gaussian function defined as

$$\Phi_k(\boldsymbol{x}) = \exp\left(-\left(\frac{\|\boldsymbol{x}-\boldsymbol{b}_k\|}{h_k}\right)^2\right), \tag{7.26}$$

such that $\Phi_k(\boldsymbol{b}_k) \approx 2.71 \times \Phi_k(\partial\Omega_k)$.

7.3.3 Time Integration

The second-order accurate explicit Runge-Kutta time integration algorithm is used. It is a two-step scheme defined as

$$\begin{aligned} \boldsymbol{U}^{t+\frac{\Delta t}{2}} &= \boldsymbol{U}^t - \nabla \cdot \boldsymbol{F}\left(\boldsymbol{U}^t\right)\frac{\Delta t}{2}, \\ \boldsymbol{U}^{t+\Delta t} &= \boldsymbol{U}^t - \nabla \cdot \boldsymbol{F}\left(\boldsymbol{U}^{t+\frac{\Delta t}{2}}\right)\Delta t. \end{aligned} \tag{7.27}$$

Due to its explicit character, the scheme is subject to the Courant-Friedrichs-Lewy (CFL) condition to ensure numerical stability. For the fluid, the solid and the sediment in the microscale, the time step is defined as

$$\Delta t = \mathrm{CFL}\,\min_i\left(\frac{h_i}{a_{\mathrm{CFL}} + \|\boldsymbol{C}_i\|}\right), \tag{7.28}$$

where a_{CFL} is the numerical speed of sound, a, for the fluid, or the bulk speed of sound, a_g, for the sediment and solid materials. For stability, CFL ≤ 1; it is commonly set to 0.5-0.7.

The sediments in the macroscale are not subject to the CFL condition since they are not discretized. However, they are subject to an even stiffer time step constraint because of the need to detect the inter-sediment collisions and the impacts against the wall. Furthermore, the Langevin equation solved to obtain the turbulent fluctuations is subject to the constraint $\Delta t < 0.1\tau_s$, where τ_s is the sediment relaxation time defined by Equation 6.35. The sediment time step in the macroscale simulations is therefore defined as

$$\Delta t = \min\left[\min_i\left(0.1\tau_{s,i}\right),\ 0.2\,\min_i\left(\frac{d_i}{\|\boldsymbol{C}_i\|}\right)\right]. \tag{7.29}$$

It is worth noting that the Langevin equation is integrated with a first-order Euler scheme, as expressed in Equation 6.33, because the velocity fluctuation should be correlated with its value on the previous time step, so including an intermediate step would deteriorate this correlation.

Dual Time Stepping Scheme

Whereas in the microscale simulations the solid and sediment time steps are similar, in the macroscale simulations the sediment time step is commonly 10-100 times smaller than the fluid time step for the case studies presented in Chapters 12 and 13. A dual time stepping scheme is used to bypass this problem.

The computation of interaction vectors is only required to calculate the flux between fluid particles; the sediment dynamics depend only on variables that can be interpolated from the flow field. It is therefore possible to integrate the sediment governing equations with the required time step, while only updating the fluid particles with their larger time step, thus significantly reducing the number of times the interaction vectors need to be computed. Time step synchronization renders this approach consistent.

7.3.4 Particle Velocity Correction

It is desirable to have a somewhat uniform particle distribution to minimize the discretization and interpolation errors. While this is straightforward for the solid, where the particles barely move relative to each other, the fluid motion may lead to non-uniformity if the particles move with exactly the material velocity.

The ALE formulation allows prescribing the particle velocity arbitrarily. To obtain a more uniform particle distribution for the fluid, the velocity of fluid particles is defined as

$$\dot{\boldsymbol{x}}_i = \begin{cases} \boldsymbol{C}_i + \dot{\boldsymbol{x}}_i' - \left(\dot{\boldsymbol{x}}_i' \cdot \boldsymbol{n}_i\right) \boldsymbol{n}_i, & \text{for the free-surface, } \textit{i.e.} \ \|\boldsymbol{B}_i\| \neq 0, \\ \boldsymbol{C}_i + \dot{\boldsymbol{x}}_i', & \text{otherwise,} \end{cases} \qquad \boldsymbol{n}_i = \frac{\boldsymbol{B}_i}{\|\boldsymbol{B}_i\|}, \tag{7.30}$$

where $\boldsymbol{C}_i$ is the fluid velocity, $\boldsymbol{n}_i$ is the outward pointing unit vector at the free-surface, and $\boldsymbol{B}_i$ is defined in Equation 7.14. The particle velocity correction reads

$$\dot{\boldsymbol{x}}_i' = -\lambda C_\circ \sum_j \left[\left(\frac{\Delta x}{\|\boldsymbol{x}_j - \boldsymbol{x}_i\|} \right)^3 - 1 \right] \cdot \frac{\boldsymbol{x}_j - \boldsymbol{x}_i}{\|\boldsymbol{x}_j - \boldsymbol{x}_i\|}, \tag{7.31}$$

where λ is a parameter set to 0.2-0.5, $C_\circ$ is the characteristic velocity of the problem and Δx is the reference interparticle distance. As formulated in Equation 7.30, the correction is not applied normal to the free surface to ensure the impermeability condition.

7.3.5 Smoothing Mass Flux

Given that both pressure and velocity are associated with the same point, the particle centroid, their coupling is weak and therefore checkerboard oscillations appear [52]. To filter out these spurious oscillations, a smoothing mass flux between fluid particles is applied. The formulation, adapted from Fatehi et al. [47] and Rhie et al. [168], can be written as

$$\boldsymbol{R}_{ij} = \lambda_R \frac{1}{2} \frac{h_i + h_j}{a} \left[\frac{1}{2} \left(\nabla p_i + \nabla p_j \right) - \tilde{\nabla} p_{ij} \right] \cdot \left(\boldsymbol{\Gamma}_{ij} - \boldsymbol{\Gamma}_{ji} \right), \tag{7.32}$$

where $\tilde{\nabla} p_{ij}$ is the weighted least squares estimation of the pressure gradient at the interface between particles i and j, a is the numerical speed of sound, h is the particle radius and λ_R is a parameter set to 0.12-0.25. This term is added to the discretized mass conservation equation, *i.e.* Equation 7.19 with $\boldsymbol{U} = \rho$ and $\boldsymbol{F} = \rho \boldsymbol{C}$.

8 Computational Resources

In Chapter 7 it was highlighted that the FVPM scheme used to discretize the governing equations, presented in Chapter 6, is computationally expensive. Apart from the method's inherent complexity, most of the simulations presented in Part III are large. This chapter presents a short description of the computational resources used is those simulations.

8.1 Piz Daint Supercomputer

Most of the simulations of Part III were performed on *Piz Daint*, Europe's most powerful supercomputer, and the world's third most powerful at the time the first simulations of this work were performed [182]. By the time of writing, Piz Daint is ranked fifth on the list of the most powerful supercomputer worldwide [183].

Piz Daint is located at the Swiss National Supercomputing Centre (CSCS) at Lugano, Switzerland. It is a hybrid CPU/GPU supercomputer model Cray XC50. The system specifications are presented in Table 8.1. The simulations of Chapters 10, 12 and 13 were performed using 4 to 32 nodes, depending on the number of particles involved.

Table 8.1 – Piz Daint Supercomputer Specifications [25, 184].

Number of nodes	5,704
Node composition	Intel® Xeon® E5-2690 v3 @ 2.60GHz (12 cores, 64GB) NVIDIA® Tesla® P100 (56 SMs, 16GB)
Node peak performance	4.76 TFlop/s
Total number of cores	387,872
Total system memory	365,056 GB
Peak performance	27,154 TFlop/s
Linpack performance	21,230 TFlop/s
Power consumption	2,384 kW

8.1.1 Parallel Scaling Performance Results

Parallel scaling tests are performed to identify the optimum number of GPUs for each type of computation. The first benchmark consists in a microscale model simulation featuring a sediment impact. A resolution of 40 particles per sediment diameter, for a total of 280,800 particles, is used to discretize the problem, which is run for 20 time steps. A *strong scaling* test is performed in which the same problem is solved with increasing numbers of GPUs; Figure 8.1a presents the obtained speed-up compared to the ideal speed-up. A parallel scaling efficiency of about 50 %, considered an optimum compromise according to the supercomputer's guidelines, is achieved by using 8 GPUs. This assessment suggests about 35,000 particles per GPU to achieve a reasonable scaling for a simulation of this size.

A strong scaling test is performed for a significantly larger macroscale simulation featuring a fluid jet impinging a flat plate. A resolution of 400 particles per jet diameter is used for a total of 75,500,000 particles; the simulation is run for 6 time steps. Figure 8.1b presents the ideal and benchmark speed-ups, which show that a scaling efficiency of about 40 % is achieved using 256 GPUs. According to these results, about 420,000 particles are required per GPU to achieve 50 % scaling efficiency for a simulation of this size.

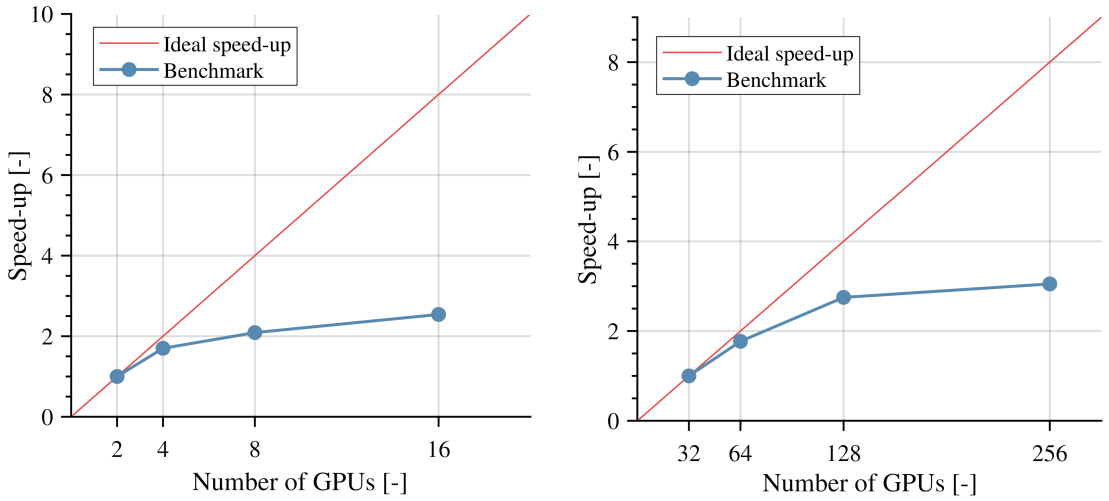

(a) Microscale simulation with 280,800 particles.

(b) Macroscale simulation with 75,500,000 particles.

Figure 8.1 – Strong scaling results for two representative simulations.

Whereas the strong scaling tests study the variation of solution time for a fixed problem size, *weak scaling* tests study its variation for a fixed problem size *per processor*. The macroscale simulation of a jet impingement on a flat plate is also used for a weak scaling analysis, which involves about 588,000 particles per GPU. One time step is performed on 4 to 256 GPUs for a total problem size of 2.35 to 150.5 million particles. As illustrated in Figure 8.2, GPU-SPHEROS achieves a sustained scaling efficiency of about 60 % on Piz Daint.

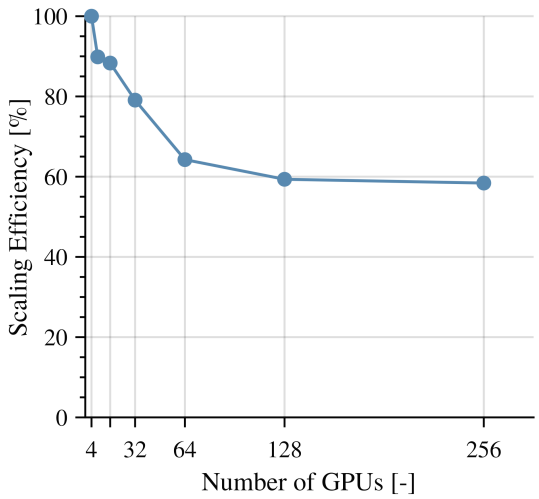

Figure 8.2 – Weak scaling efficiency using 588,000 particles per GPU.

8.2 NeXtScale Cluster

Some of the simulations of Chapters 10 and 11 were performed using the CPU version of the code, because the GPU version was under development. These simulations were run on the NeXtScale Cluster at the Laboratory for Hydraulic Machines. The cluster specifications are presented in Table 8.2.

Typically only one node, *i.e.* 20 cores, were used for each of the simulations. Indeed, the inter-node communication is relatively slow in this cluster so the scaling efficiency drops significantly if multiple nodes are used.

Table 8.2 – NeXtScale Cluster Specifications [189].

Number of nodes	8
Node composition	2× Intel® Xeon® E5-2660 v2 @ 2.20GHz (10 cores, 128GB)
Node peak performance	0.352 TFlop/s
Total number of cores	160
Total system memory	1,024 GB
Peak performance	2.816 TFlop/s

8.3 Personal Computer

The least expensive simulations, such as the 2D macroscale simulation of Chapter 11, were run on a personal laptop. Apart from these production runs, almost all the simulations that were run during the code development and testing were performed on this machine, whose specifications are presented in Table 8.3.

Table 8.3 – Personal Laptop Specifications.

CPU	Intel® Core™ i7-4810MQ @ 2.80GHz
Total number of cores	4
Total system memory	16 GB
Peak performance	0.179 TFlop/s

9 Characterization of Materials Studied

The physical models presented in Chapter 6 contain a significant number of parameters that depend on the materials under study. Before performing any simulations, all the material parameters have to be obtained either from the literature or through experimentation.

Four materials are simulated in this work:

- *Water*, the conveying fluid
- *Quartz*, the main component of sediments
- *Oxygen-free copper*, a well-characterized metal
- *Martensitic stainless steel 13Cr-4Ni*, the most common hydraulic turbine material

All the model parameters for the first three materials are found in the literature. Similarly, many of the thermomechanical properties and equation of state parameters for steel are fairly uniform across different grades and compositions, so a literature survey allowed estimating them for MSS 13Cr-4Ni, albeit with some small uncertainty. The model parameters for the four materials studied are reported in Tables 9.4 and 9.5.

By far the most critical parameters for the erosion simulations are those related to the Johnson-Cook constitutive and damage models; not unexpectedly, these were found to vary significantly across different steel grades. A partial calibration of these models for MSS 13Cr-4Ni was made possible by two experiments, as explained in detail hereafter. Given that all the related data are protected by a non-disclosure agreement, only normalized results are presented.

9.1 Split-Hopkinson Pressure Bar Experiment

The split-Hopkinson pressure bar experiments allow characterizing the material response under varying strain rates and temperatures. A sketch of the system is presented in Figure 9.1. It is composed of three bars: the *striker*, the *input* and the *output* bars, all of which are made of the same material and have the same diameter. A pressurized vessel is used to launch the

striker bar against the input bar, generating a compressive pulse that propagates downstream towards the specimen. Once it reaches it, part of the wave is reflected whilst the rest is transmitted to the output bar across the specimen.

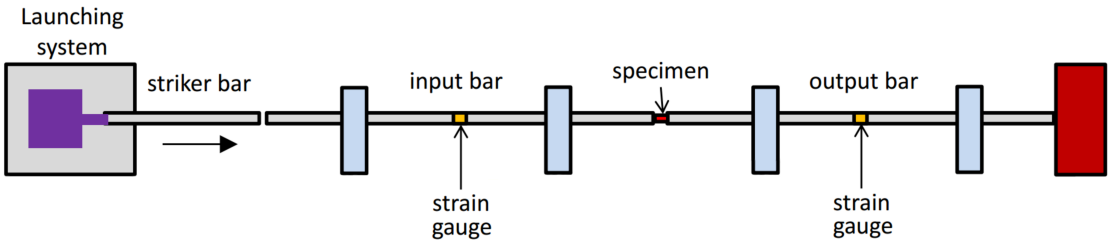

Figure 9.1 – Sketch of the split-Hopkinson pressure bar experiment, adapted from [139].

The specifications of the split-Hopkinson pressure bar system at École Normale Supérieure Cachan used for the experiments are presented in Table 9.1. The bars are made of X2NiCoMo18-8-5 high-strength steel, commercialized as Marval 18. Additional instrumentation, apart from the strain gauges in the input and output bars, includes a high-speed camera and a thermal camera filming the specimen, and another high-speed camera filming the striker-input interface. This footage is used to calibrate and corroborate the strain gauge measurements, as explained in Section 9.1.2. The experimental setup is shown in Figure 9.2a.

As presented in Figure 9.2b, the specimen circumference is covered by a thin paint layer that is used in the imaging processing step to estimate the strain field; the other side, not visible in the image, is painted black to obtain a uniform black-body radiation spectrum used to estimate the surface temperature by means of the thermal camera.

Specimens were tested at 6 different strain rates, each of which included 3 runs, rendering a total of 18 specimens tested. All the tests were conducted at ambient temperature. The test conditions are presented in Table 9.2. Although the launch vessel pressure was controlled for each run, the striker velocity is not exactly repeatable and therefore the strain rate the specimen is subject to is slightly different for each run within a vessel pressure level. Note that the measured strain rate for each run is used in the fitting step, Section 9.3, instead of the average strain rates presented in Table 9.2.

Table 9.1 – Split-Hopkinson Pressure Bar Specifications.

Striker bar length	L_{st}	1.25	[m]
Input bar length	L_i	4.0	[m]
Output bar length	L_o	2.0	[m]
Bar diameter	D_b	21.8	[mm]
Bar density	ρ_b	8,050	[kg · m^{-3}]
Bar Young's modulus	$E_{e,b}$	170.3	[GPa]
Wave speed in bars	a_b	4,600	[m · s^{-1}]
Specimen length	$L_{s,0}$	5.0	[mm]
Specimen diameter	$D_{s,0}$	5.0	[mm]

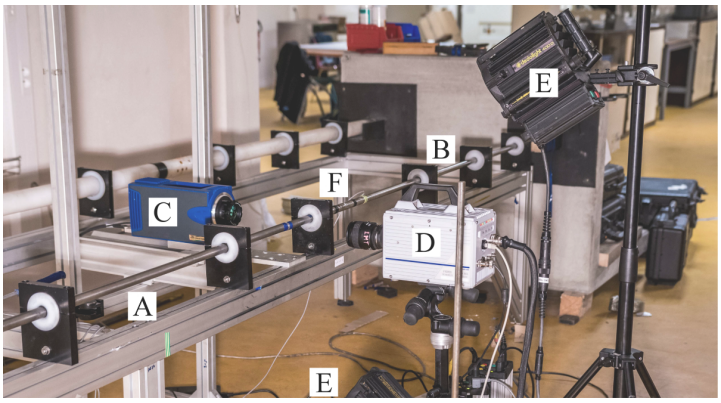

(a) Experimental setup including the input (A) and output (B) bars, the thermal (C) and high-speed (D) cameras, the spotlights (E), and one of the strain gauges (F).

(b) Cylindrical specimen with a thin paint layer used in the image processing.

Figure 9.2 – Split-Hopkinson pressure bar experimental setup and specimen.

The strain gauge raw data is processed to obtain true stress-true strain curves for the specimen at different strain rates. The theoretical description of the experiment that allows this data processing is introduced next.

Table 9.2 – List of Experimental Conditions Tested.

Launch vessel pressure	[kPa]	48	69	75	97	125	180
Average striker velocity	$[\mathrm{m}\cdot\mathrm{s}^{-1}]$	3.39	6.37	8.26	10.16	11.91	14.54
Average specimen strain rate	$[\mathrm{s}^{-1}]$	129	624	1,058	1,444	1,956	2,154

9.1.1 Theoretical Description of the Experiment

The split-Hopkinson pressure bar system is designed such that the one-dimensional wave propagation theory is a good approximation of the phenomena involved, and the impact velocity is limited in order for the bars to remain elastic throughout the experiments. The strain gauges are used to measure three pulses: the *incident pulse* generated by the striker impact, the *reflected pulse* from the input-specimen interface, and the *transmitted pulse* to the output bar. Let these measured strains be $\varepsilon_I(t)$, $\varepsilon_R(t)$ and $\varepsilon_T(t)$, respectively.

One-dimensional elastic wave propagation tells us that the particle velocity at the input-specimen interface is given by [166]

$$v_1(t) = a_b\left[\varepsilon_I(t) - \varepsilon_R(t)\right], \tag{9.1}$$

where a_b is the bar wave speed. Conversely, at the specimen-output interface it is given by

$$v_2(t) = a_b\left[\varepsilon_T(t)\right]. \tag{9.2}$$

The mean axial strain rate in the specimen is then given by

$$\dot{e}_s(t) = \frac{v_1(t) - v_2(t)}{L_{s,0}} = \frac{a_b}{L_{s,0}} \left[\varepsilon_I(t) - \varepsilon_R(t) - \varepsilon_T(t)\right], \tag{9.3}$$

where $L_{s,0}$ is the initial specimen length.

Knowing the bar elastic strains, the stresses and therefore the normal forces at the two interfaces can be computed as

$$F_1(t) = E_{e,b}\left[\varepsilon_I(t) + \varepsilon_R(t)\right] A_b, \qquad F_2(t) = E_{e,b}\left[\varepsilon_T(t)\right] A_b, \tag{9.4}$$

where $E_{e,b}$ is the Young's modulus of the bar material and A_b is its cross-section area, whose variation in time is neglected. The mean axial stress in the specimen can thus be written as

$$\bar{s}_s(t) = \frac{F_1(t) + F_2(t)}{2} \frac{1}{A_{s,0}} = \frac{E_{e,b}}{2} \frac{A_b}{A_{s,0}} \left[\varepsilon_I(t) + \varepsilon_R(t) + \varepsilon_T(t)\right], \tag{9.5}$$

where $A_{s,0}$ is the initial cross-section area of the specimen.

After several wave reflections within the specimen, F_1 and F_2 equilibrate and the stress becomes essentially uniform. This force equilibrium implies that $\varepsilon_I(t) + \varepsilon_R(t) = \varepsilon_T(t)$, which greatly simplifies the aforestated equations.

The strain rate on the specimen can then be estimated as

$$\dot{e}_s(t) = -\frac{2a_b}{L_{s,0}} \varepsilon_R(t), \tag{9.6}$$

and therefore its strain is

$$e_s(t) = \int_0^t \dot{e}_s(\tau) d\tau. \tag{9.7}$$

The stress can be computed as

$$s_s(t) = E_{e,b} \frac{A_b}{A_{s,0}} \varepsilon_T(t). \tag{9.8}$$

Finally, the change of the specimen's cross-section area in time can be taken into account to calculate the *true* quantities. The true strain in the specimen is computed as

$$\varepsilon_s(t) = -\ln\left[1 - e_s(t)\right], \tag{9.9}$$

which implies a true strain rate of the form

$$\dot{\varepsilon}_s(t) = \frac{\dot{e}_s(t)}{1 - e_s(t)}, \tag{9.10}$$

and, assuming plastic incompressibility, the true stress is obtained as

$$\sigma_s(t) = s_s(t)\left[1 - e_s(t)\right]. \tag{9.11}$$

These equations are exact under three assumptions: one-dimensional wave propagation through the bars, uniaxial stress, and stress equilibrium in the specimen. The first assumption never holds because of wave dispersion: wavelength-dependent wave speeds imply that the wave changes as it propagates through the bars, developing oscillations that appear in the strain measurements. Although it is possible to correct the results for the effects of dispersion, it requires additional calculations that are not straightforward. Moreover, these effects are mostly noise, so the experimental results are not compromised by their presence.

The assumption of uniaxial stress holds provided the interfaces are friction-free. The effects of friction are minimized by applying a lubricant on the interfaces. It was corroborated that the specimens deformed uniformly, with negligible barreling, suggesting an effectively uniaxial stress state on the specimen.

The assumption of stress equilibrium is fulfilled as long as the normal forces acting on the interfaces are equal. The results, presented in Section 9.1.3, indicate that this is a good approximation after a transient period of equilibration.

9.1.2 Strain Gauge Calibration

The strain gauge calibration is achieved with the raw data of a series of tests at various velocities without any specimen, in such a way that the same incident pulse propagates through the input and output bars. Knowing that the theoretical strain in that case is

$$\varepsilon_I = \frac{v_{st}}{2a_b}, \tag{9.12}$$

where v_{st} is the striker bar velocity, it is possible to find the calibration factor that relates the measured strain gauge voltage with the bar strain.

The striker velocity is measured precisely using the high-speed camera footage of the striker covered with a stripped pattern, knowing the stripe size and the camera's frame rate. Then, the calibration factor between strain gauge voltage and bar strain is found by solving the weighted least squares minimization problem between the measured strain and the theoretical strain, function of the striker velocity v_{st}, where the weights are inversely proportional to the velocity measurement uncertainty of each data point. This minimization is performed simultaneously over all the data, which involves a series of striker velocities; it is performed independently for each of the two strain gauges. The resulting calibration factors are presented in Table 9.3.

Table 9.3 – Strain Gauge Calibration Factors.

Input bar strain gauge	[V^{-1}]	2.360×10^{-4}
Output bar strain gauge	[V^{-1}]	2.474×10^{-4}

The theoretical and measured strain signals in the input bar for a series of striker velocities is presented in Figure 9.3a, where the calibration factors have been used to translate the

strain gauge voltages into strains. While the theoretical pulses look like a step, the measured pulses are characterized by finite rise and decay times, and present oscillations due to wave dispersion. These departures from the idealized case imply a non-negligible uncertainty.

9.1.3 Example of the Results

Once the strain gauge calibration has been obtained, the experimental results can be extracted as explained in Section 9.1.1. Hereafter the results for three runs are presented; they correspond to a launch vessel pressure of 75 kPa, with an average striker velocity of 8.26 $m \cdot s^{-1}$ resulting in an average strain rate of $1,058\ s^{-1}$. Although the nominal conditions are identical, the results present some dispersion.

Figure 9.3b contains the strain measurements for the incident, reflected and transmitted waves, for each of the three runs; it can be seen that the results are fairly repeatable. These strain measurements occur at different times; in order to operate on them they have to be synchronized as seen in Figure 9.3b. Given that the signals present uneven and finite rise times, this synchronization process is not exact. Some error is therefore induced in the variables that are computed based on the sum or difference between these signals; that is especially true for the first and last ~ 0.1 ms of the test due to the oscillations present, whose addition or subtraction is especially sensitive to the phase, which is affected by the synchronization uncertainty.

The velocities of the input-specimen and specimen-output interfaces are presented in Figure 9.4a, as computed from Equations 9.1 and 9.2, respectively. The input interface moves faster than the output interface, leading to the specimen compression.

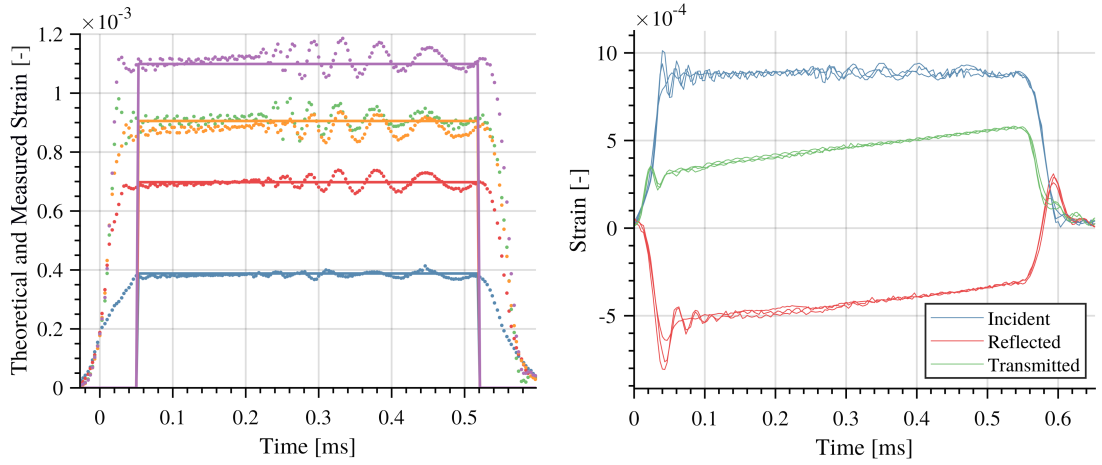

(a) Theoretical and measured strain on the input bar for a series of striker velocities.

(b) Strain signals for three experiment runs under identical nominal conditions.

Figure 9.3 – Examples of strain gauge calibration and experiment repeatability.

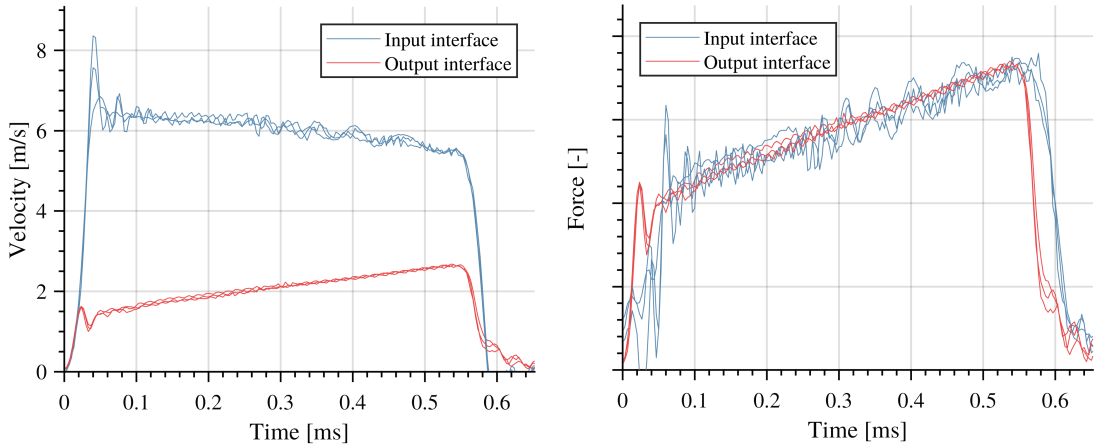

(a) Input and output interface velocities for three experiment runs under identical nominal conditions.

(b) Input and output interface forces for three experiment runs under identical nominal conditions.

Figure 9.4 – Velocity and force on the input and output interfaces.

Figure 9.4b contains the forces on the input and output interfaces based on Equation 9.4. It can be seen that after ~ 0.1 ms these forces equilibrate, although the input force is somewhat oscillatory due to wave dispersion in the input bar. The assumption of stress equilibrium therefore holds reasonably well after the initial transient.

The engineering and true stress on the specimen as functions of time, calculated according to Equations 9.8 and 9.11, respectively, are presented in Figure 9.5a. Due to the non-equilibrium of the forces on the specimen during the initial transient, the equations are not valid and therefore the stress in that period is incorrect. After ~ 0.1 ms, however, the stress calculation is valid and the three experiment runs are fairly similar, although somewhat oscillatory.

Figure 9.5b presents the engineering and true strain rate time histories, computed using Equations 9.6 and 9.10, respectively. It can be seen that the true strain rate is almost constant throughout the test, and that it is fairly repeatable between runs. The average true strain rates for these runs are within 2.5 % of the nominal 1,058 s^{-1} of the test condition.

The engineering and true strain time histories, calculated using Equations 9.7 and 9.9, respectively, are presented in Figure 9.6a. These results are valid up to ~ 0.55 ms, when the strain signals start to decay as illustrated in Figure 9.3b.

The final result of the experiments is the true stress-true strain curves, presented in Figure 9.6b for three experiment runs under identical nominal conditions. Given the non-equilibrium of forces before ~ 0.1 ms, which corresponds to a true strain of ~ 0.08 according to Figure 9.6a, the true stress-true strain curves are only valid above that strain value for this particular test condition.

It is evidenced that the curves present a non-negligible spread. Part of the difference is

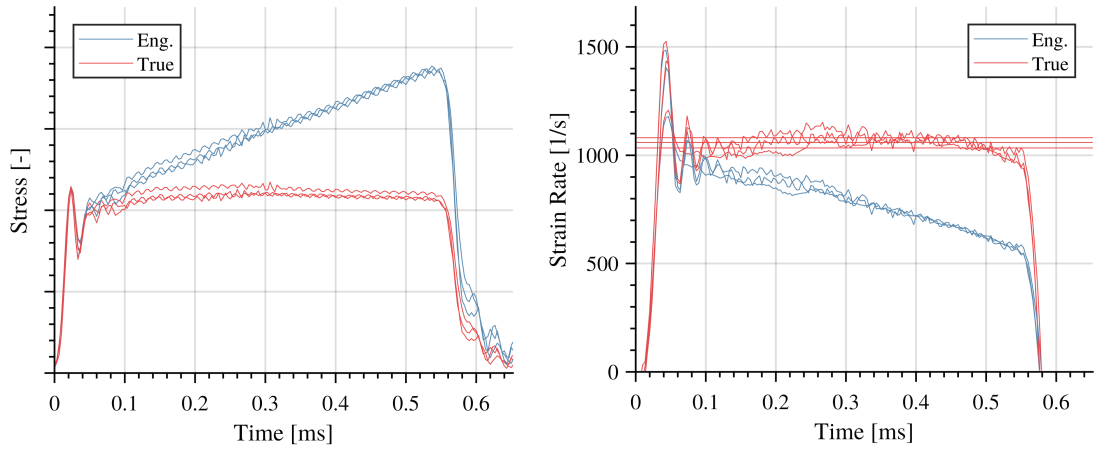

(a) Engineering and true stress time histories for three experiment runs under identical nominal conditions.

(b) Engineering and true strain rate time histories for three experiment runs under identical nominal conditions.

Figure 9.5 – Stress and strain rate on the specimen.

explained by the variation in effective strain rate, which is within 2.5 % of the group average. In an attempt to estimate the experimental uncertainty, this difference is factored out by linearly scaling the curves according to the effective strain rate variation: knowing that the stress increases with the strain rate, the true stress curves are multiplied by a factor $\frac{\dot{\varepsilon}_{s,g}}{\dot{\varepsilon}_s}$, where $\dot{\varepsilon}_{s,g}$ is the average strain rate of the group of experimental runs at equivalent nominal conditions. Then, the standard deviation between the 3 curves in each group is calculated, considering only the range of true strain within which the equations used to derive them are valid. The average standard deviation is ±5.8 %, which represents the *experimental uncertainty* of the true stress-true strain curves within the true strain range where they are valid.

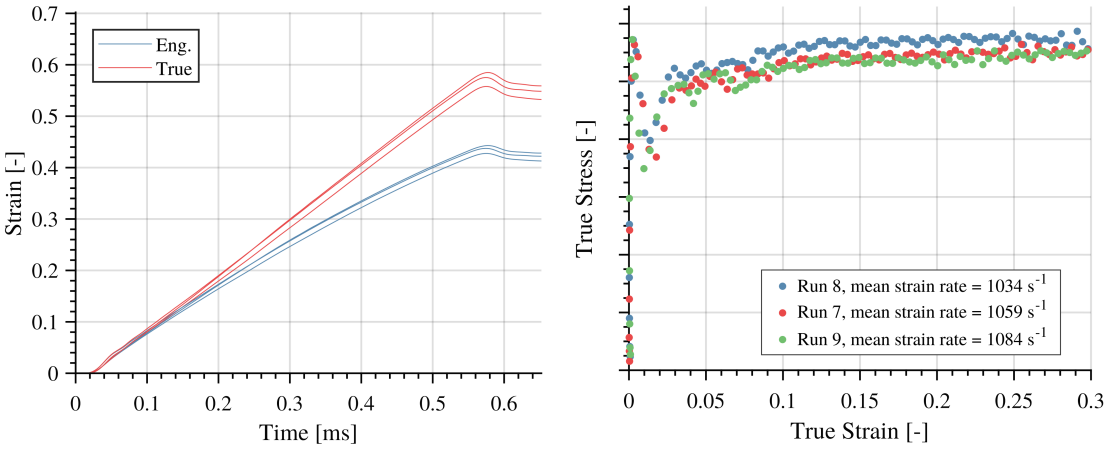

(a) Engineering and true strain time histories for three experiment runs under identical nominal conditions.

(b) True stress-true strain curves for three experiment runs under identical nominal conditions.

Figure 9.6 – Strain time histories and true stress-true strain curves.

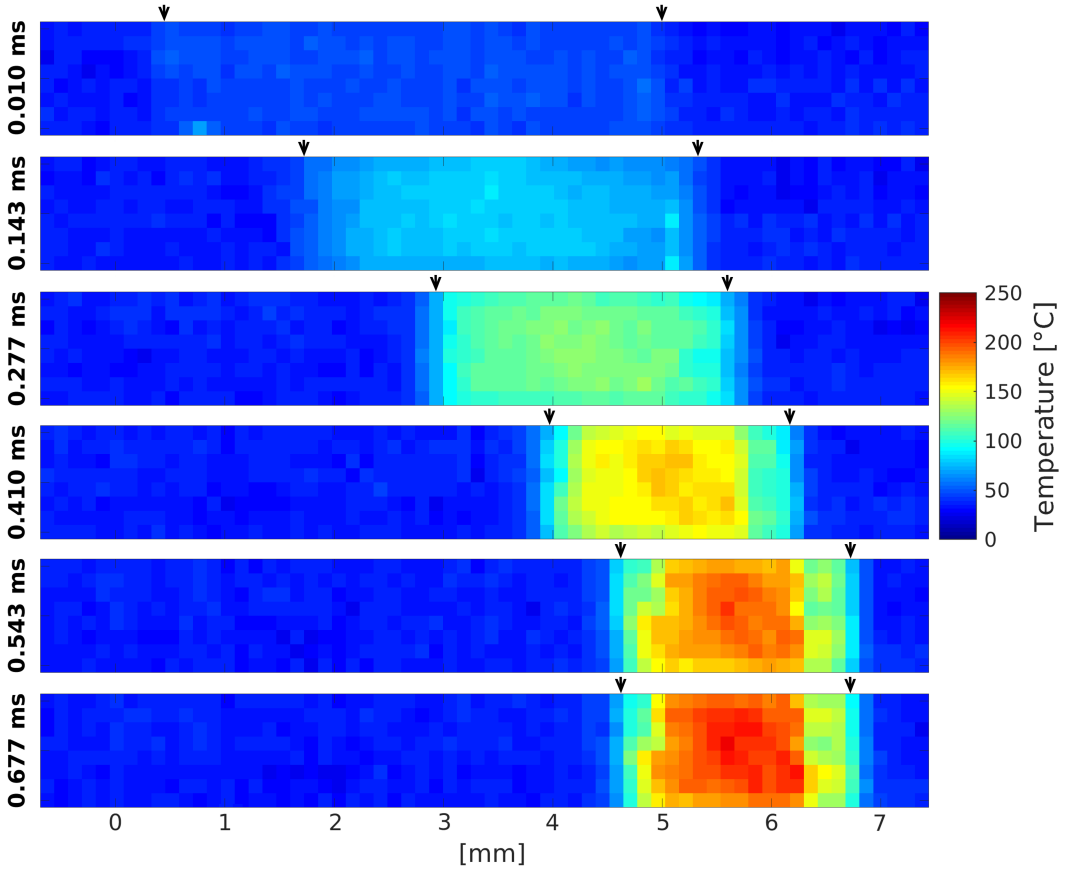

Figure 9.7 – Thermal camera footage of the specimen during a run with a mean strain rate of 2,057 s^{-1}. The approximate interface locations are indicated by arrows.

The specimen temperature is measured by means of a thermal camera. The uniform plastic deformation causes a uniform volumetric heating, therefore the surface temperature estimation provided by the camera is representative of the whole specimen. Figure 9.7 contains six frames of the camera footage; due to resolution constraints, only a 1 mm wide stripe covering the full specimen length is visible. The coordinate is centered at the initial position of the input interface. For this run with an average strain rate of 2,057 s^{-1}, the temperature reaches 250 °C, although it is lower for the tests at lower strain rate since the total strain is also lower.

9.2 Quasi-Static Tensile Experiment

The project's industrial partner provided the quasi-static strain rate characterization of MSS 13Cr-4Ni in the form of tensile experimental data. The tests were performed on *as received* as well as *heat-treated* material, to verify the magnitude of the effect of the heat treatment on the material behavior. The non-dimensional true stress-true strain curves are presented in Figure 9.8. Although noticeable, the effect of the heat treatment on the material response is rather small.

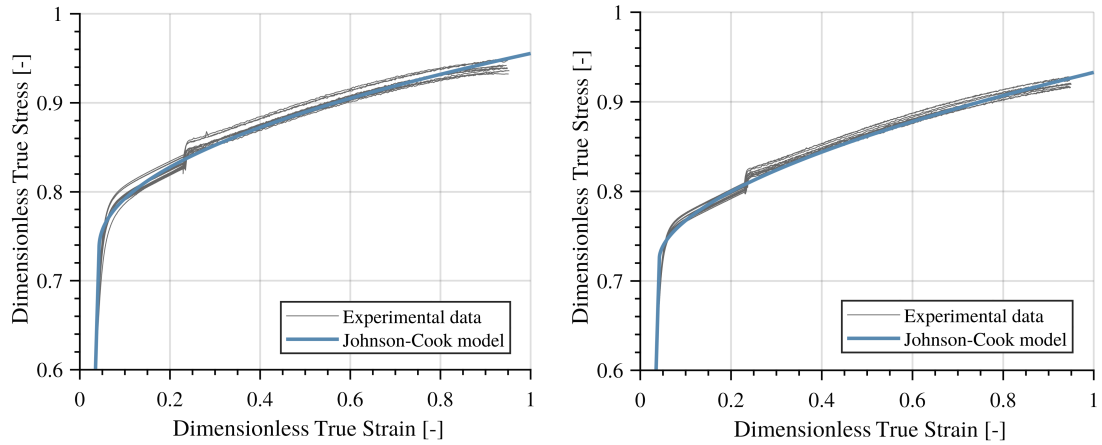

(a) As received material.

(b) Heat treated material.

Figure 9.8 – Johnson-Cook constitutive model fit to the quasi-static tensile test data.

9.3 Fitting of the Johnson-Cook Constitutive Model

The experimental data is used to fit the Johnson-Cook constitutive model, described by Equation 6.58. The *first term*, characterized by the parameters A_1, A_2 and n_σ, can be fitted using the quasi-static tensile data: under these conditions, the strain rate and temperature effects are negligible. Figure 9.8 presents the model fit to the experimental data of as received and heat treated material. The material behavior is well described by the non-linear strain hardening formulation.

Note that to fit the *third term* of the Johnson-Cook constitutive model, the thermal softening term characterized by the parameter m_σ, split-Hopkinson pressure bar experiments have to be performed for a series of different initial specimen temperatures. However, this was not possible on the experimental setup available. Since only the *second term* can be fitted, the strain rate hardening term characterized by the parameters A_3 and $\dot{\varepsilon}_\circ$, the fraction of the curves that may be affected by thermal softening need to be neglected.

In order to obtain a proper fit of the split-Hopkinson pressure bar data, only a fraction of each true stress-true strain curve is used since not all the curve is valid. Lower and upper bounds on the true strain are defined for each curve depending on the test conditions. On the one hand, the lower true strain bound is given by the stress equilibrium requirement, *i.e.* once the forces on the specimen interfaces have equilibrated. On the other hand, the upper true strain bound is given by the requirement that the thermal softening effects remain negligible; a maximum allowable temperature of ~ 130 °C, corresponding to $T_h = 0.07$, was found to be a reasonable threshold.

The data fitting is formulated as a weighted least squares minimization problem and solved using a genetic algorithm. The point weights are defined such that each test has the same

weight, irrespective of the number of data points contained in its bounded true stress-true strain curve. No bounds are enforced on the parameter values in the optimization process. However, when one of the parameters comes from the quasi-static tensile test data, *e.g.* the initial yield strength A_1, the bounds within which the parameter is allowed to evolve are defined by the uncertainty interval of the tensile test data fit.

Although it is common practice to fit the strain hardening term with data from a quasi-static tensile test, as presented in Figure 9.8, and use the split-Hopkinson bar data to fit the strain rate hardening term only, this approach did not yield satisfactory results, as illustrated in Figure 9.9a. Indeed, the material exhibits a weaker strain hardening behavior on the split-Hopkinson pressure bar experiment, perhaps because it involves compression, unlike the tensile experiment used to fit that part of the model. In other words, the material strain hardening is significantly higher on the quasi-static tension test than on the split-Hopkinson pressure bar test, and appears to be a function of strain rate.

Given that the split-Hopkinson compression data at high strain rate are more representative of the conditions encountered by the material during sediment impacts, it is decided to fit both the strain hardening and the strain rate hardening terms with the available split-Hopkinson pressure bar data, as presented in Figure 9.9b. This approach yields a significantly better fit to the data, as evaluated by the weighted least squares residual. The only model parameter fitted using the quasi-static tensile test data is A_1, the initial yield strength; A_2, n_σ, A_3 and $\dot{\varepsilon}_\circ$ are fitted using the split-Hopkinson pressure bar data.

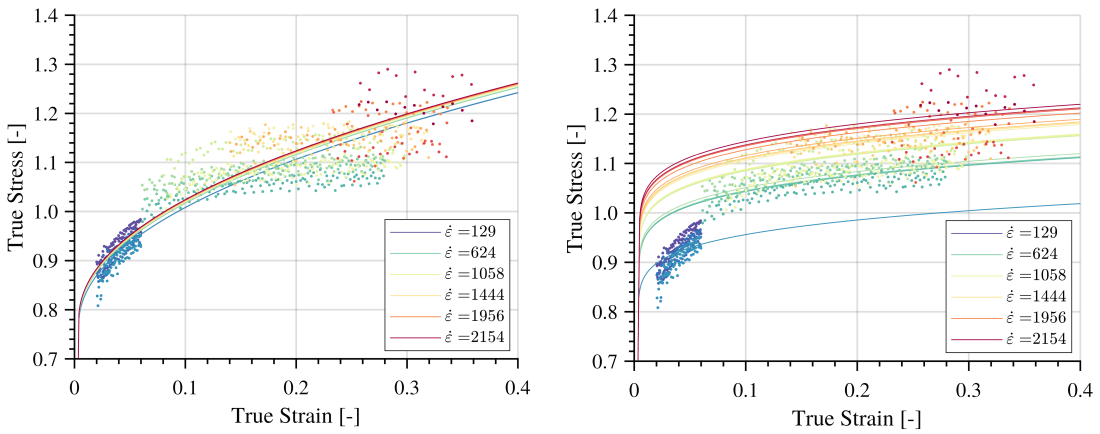

(a) Best fit of the strain rate hardening term (A_3, $\dot{\varepsilon}_\circ$), given the quasi-static tensile test fit for the yield stress and strain hardening term (A_1, A_2, n_σ).

(b) Best fit of the strain rate and strain rate hardening terms (A_2, n_σ, A_3, $\dot{\varepsilon}_\circ$), given the quasi-static tensile test fit for the yield stress (A_1).

Figure 9.9 – Johnson-Cook constitutive model fit to the split-Hopkinson pressure bar data. The strain rate is color-coded; only 6 out of the 18 different strain rate labels are shown.

Figure 9.10 presents the correlation between the Johnson-Cook model and the experimental data used to fit it. The dashed lines represent error bounds of ±4.1 %, which is the standard deviation of the ratio between model and experimental stress.

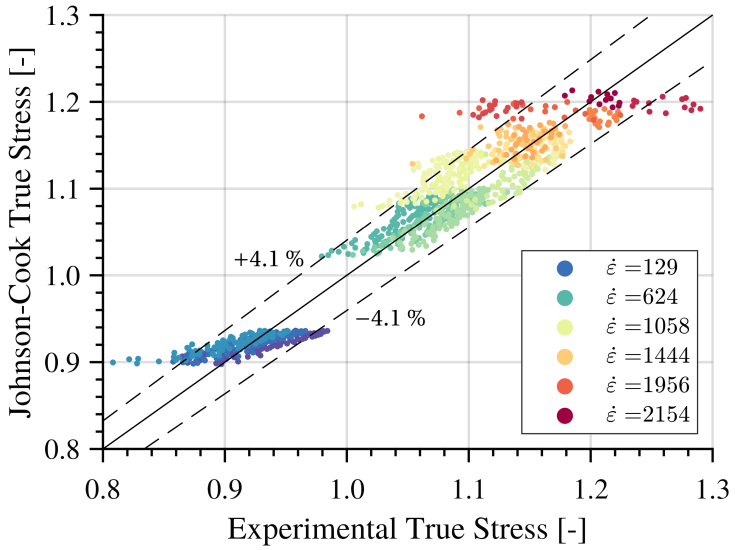

Figure 9.10 – Correlation between the Johnson-Cook model and the experimental data used to fit it. The strain rate is color-coded; only 6 out of the 18 strain rate labels are shown.

Given that the experimental uncertainty, ±5.8 %, is similar to the standard deviation of the fitting error, ±4.1 %, the procedure is judged satisfactory.

The strain rate hardening term of the Johnson-Cook constitutive model is fitted with data within the strain rate range $\dot{\varepsilon} = 1 \times 10^2$-$2 \times 10^3$ s^{-1}. However, the relevant range experienced by a material impacted by a sediment is $\dot{\varepsilon} \approx 1 \times 10^5$-$1 \times 10^7$ s^{-1} [116, 200]. Such an extrapolation is mandatory because no experimental characterization technique can reach these strain rates. Moreover, the extrapolation of the Johnson-Cook model up to $\dot{\varepsilon} \approx 1 \times 10^6$ s^{-1} for a material characterized with experiments of up to $\dot{\varepsilon} = 1 \times 10^3$ s^{-1} has been successfully validated by Wang and Shi [195].

9.4 Likely Range of the Unknown Johnson-Cook Model Parameters

The limitations of the experimental facilities used to characterize the MSS 13Cr-4Ni prevented us from fitting some of the Johnson-Cook material parameters. These include the thermal softening parameter of the constitutive model, m_σ, and the five parameters of the damage model, D_i.

An exhaustive literature review was performed to identify the *most likely range* of these unknown parameters. A total of 7 steels were used to estimate these ranges: stainless steels 12Cr-3Ni-4Mo [161], 304 [142] and 316L [186], and steels 4140 [126], 4340 [105], Weldox 460E [24], and ST37 [154]. As seen in Table 9.4, some parameters, such as m_σ and D_5, vary within ± 3-6 % of their mean value, whereas other, such as D_1 and D_2, vary within ± 40-80 %. These uncertainties are addressed and discussed in detail in Chapter 10.

9.5 Compilation of Model Parameters for Materials Studied

Except for the information protected by a non-disclosure agreement, all the material parameters or their most likely ranges are presented in Table 9.4. These solid materials, namely oxygen-free copper, MSS 13Cr-4Ni and quartz, are used in the simulations of Part III.

Table 9.4 – Material Model Parameters for Solids [9, 16, 24, 30, 37, 88, 101, 105, 126, 140, 142, 154, 161, 186, 200].

				Copper	13Cr-4Ni	Quartz
Thermomechanical	Reference density	$\rho_\circ$	[kg · m^{-3}]	8,960	7,750	2,650
	Young's modulus	E_e	[GPa]	125	205	80
	Poisson's ratio	ν_p	[–]	0.34	0.30	0.17
	Specific heat capacity	c_p	[J · kg^{-1} · K^{-1}]	383	460	710
	Thermal conductivity	κ	[W · m^{-1} · K^{-1}]	386	20	8
	Inelastic heat fraction	β_p	[–]	0.90	0.90	–
	Melting temperature	T_m	[K]	1,358	1,780	1,930
	Reference temperature	$T_\circ$	[K]	293	293	293
EoS	Linear Hugoniot slope	S	[–]	1.49	1.50	2.12
	Bulk speed of sound	a_g	[m · s^{-1}]	3,933	4,560	5,728
	Grüneisen's parameter	$\gamma_\circ$	[–]	1.99	2.00	0.72
J-C Constitutive	Yield stress	A_1	[MPa]	265	*	–
	Strain hardening parameter	A_2	[MPa]	292	*	–
	Strain rate parameter	A_3	[–]	0.025	*	–
	Strain hardening exponent	n_σ	[–]	0.31	*	–
	Thermal softening exponent	m_σ	[–]	1.09	0.80 ± 0.05	–
	Reference strain rate	$\dot{\varepsilon}_\circ$	[s^{-1}]	1.00	*	–
J-C Damage	Base parameter	D_1	[–]	0.54	-0.10 ± 0.08	–
	First triaxiality parameter	D_2	[–]	4.89	0.26 ± 0.10	–
	Second triaxiality parameter	D_3	[–]	3.03	0.52 ± 0.04	–
	Strain rate parameter	D_4	[–]	0.014	0.018 ± 0.004	–
	Thermal softening parameter	D_5	[–]	1.12	0.60 ± 0.02	–

* Confidential data protected by a non-disclosure agreement.

Table 9.5 contains all the material parameters for water at a reference temperature of 20 °C, as well as the typical artificial viscosity value used in the simulations of Part III.

Table 9.5 – Material Model Parameters for Water at 293 K [14, 74, 151].

Reference density	$\rho_\circ$	[kg · m^{-3}]	998
Tait equation of state parameter	γ	[–]	7.0
Dynamic viscosity	μ	[Pa · s]	0.0010
Bulk viscosity	μ_b	[Pa · s]	0.0025
Artificial viscosity	μ_a	[Pa · s]	0.0100

Validation Case Studies Part III

One thing I have learned in a long life: that all our science, measured against reality, is primitive and childlike—and yet it is the most precious thing we have.

—*Albert Einstein*

10 Jet Impingement on a Flat Plate

The first case study consists of a slurry jet impinging on a flat plate at various angles and velocities. In spite of the very simple geometry, this case study includes all the physical interactions that need to be validated before applying the multiscale model to more interesting problems. Part of the contents of this chapter have been previously published in Leguizamón et al. [112, 113].

10.1 Description of the Case Study

A 2D diagram of the case study is presented in Figure 10.1. A jet of diameter D_0 impinges on a square flat plate of length L_p. The jet is oriented at an impingement angle θ, and is injected at a distance L_j from the plate at an average velocity C_1. Sediments are uniformly distributed on the jet volume with a concentration c_w, and their diameters are randomly chosen following either a Weibull or a log-normal probability distribution fitted to the experimental sediment size distribution. The sediment shape is described by the microscale shape parameter ϕ_s and by the macroscale sediment sphericity ϕ_d.

The experimental Reynolds number and the distribution pipe length suggest a fully developed turbulent flow at the inlet for all the test cases considered. Consequently, Nikuradse's [173] velocity and turbulence profiles for straight pipe flow are specified on the inlet boundary. After an initial transient in which the fluid impacts the plate, the system reaches a steady-state condition after which the sediments are injected at the inlet boundary with a velocity equal to that of the fluid.

The erosion depth is insignificant with respect to the jet diameter for all of the test cases considered, such that it can be assumed that the modification of the plate geometry does not affect the hydrodynamics nor the erosion rate. For this reason, the projective integration approach is not required and a single macroscale simulation is sufficient to calculate the erosion distribution on the plate.

The case study is composed of three test cases, as described hereafter. All the geometric parameters that define them are reported in Table 10.1.

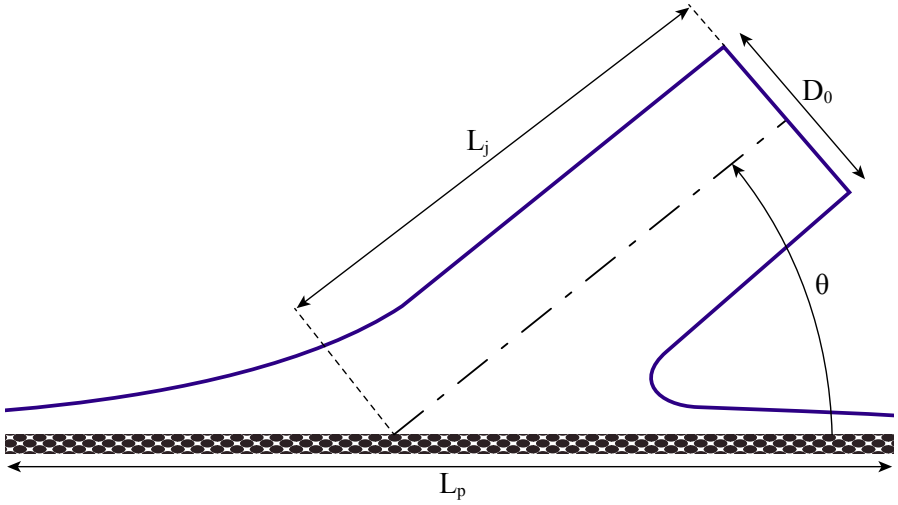

Figure 10.1 – Jet impingement case study diagram.

10.1.1 Test Case 1

The first test case follows the experiment by Sugiyama, Harada and Hattori [179], which involves slurry erosion tests on oxygen-free copper. Given that all the material parameters are available in the literature, and that the experimental results include the global erosion rate as well as erosion depth profiles, this test case constitutes the most thorough validation of the multiscale model.

The microscale simulations are performed for the impact angles α = [30, 45, 60, 90]° and impact velocities v = [50, 80, 100] m · s^{-1}. The sediments are assumed rigid and spherical (ϕ_s = 1.0), with a diameter d = 100 μm. Given that spherical sediments underestimate the cutting damage that occurs at low impact angles, artificially high friction coefficients are used in order to limit the error induced by the assumed sediment shape, as explained in more detail elsewhere [116]. Note that this correction was necessary only for this run of the microscale model, given that the final sediment model, including the particle elasticity and shape, was not yet implemented. The static and dynamic friction coefficients used in the microscale

Table 10.1 – Geometric Parameters of Case Study 1.

		Test Case 1	Test Case 2	Test Case 3	
Jet velocity	C_1	10.0	19.8	70.0, 90.0	[m · s^{-1}]
Jet diameter	D_0	3.0	30.0	6.0	[mm]
Jet length	L_j	5.0	50.0	12.0	[mm]
Impingement angle	θ	15, 30, 60, 90	90	45, 90	[°]
Plate length	L_p	10.0	100.0	27.0	[mm]
Sediment concentration	c_w	1.0	0.32	0.20	[%$_w$]
Microscale sediment shape	ϕ_s	1.0	1.0	0.5	[–]
Macroscale sediment sphericity	ϕ_d	0.76	1.0	0.66, 0.76, 0.86	[–]

simulations are $\mu_{f,s} = 0.7$ and $\mu_{f,d} = 0.6$, respectively, chosen to be thrice the typical value used in particle impact simulations [38, 122, 125, 180, 199, 200]; note that these values were fixed prior to the simulations and were not changed a posteriori, *i.e.* their value was not tuned for the simulation results to agree with the experiments.

In the macroscale simulations, the sediment sphericity is set to $\phi_d = 0.76$, a typical value for semi-sharp sediments [135], in qualitative agreement with the experiment, where no quantitative characterization of the particle sphericity is given. A Weibull distribution is fitted from the experimental sediment size distribution. The resulting shape and scale parameters are 0.80 and 16 μm, respectively, rendering a volume-weighted average sediment size of 80 μm. The sediment size distribution is truncated with the following cutoff values: 10 μm and 200 μm.

A convergence analysis of the macroscale simulation was performed to determine the FVPM discretization resolution required to achieve converged results, as well as the number of sediments needed to obtain converged erosion and impact condition distributions on the plate. The results, presented in Appendix B.4, reveal that a resolution of 40 FVPM particles per jet diameter and about 2.0×10^5 injected sediments are needed to achieve converged results. The total number of FVPM particles used to discretize the macroscopic domain at a given instant is about 2.5×10^5.

10.1.2 Test Case 2

The second test case deals with the erosion of oxygen-free copper by sediments of different sizes. No experimental data is available, so this test case is only a verification of the expected behavior of the macroscale sediment transport model. It is also a first assessment of the multiscale model robustness: the physical size of the macroscale domain is ten times larger than that of test case 1, as seen in Table 10.1, implying a greater scale separation between hydrodynamics and sediment impact dynamics.

The microscale simulation results of test case 1 are used in the present test case, such that only the macroscale simulations need to be run. These are performed for four different sediment size distributions. As presented in Table 10.2, they are described by Weibull distributions compactly defined around the nominal diameters $d = [10, 50, 125, 250]$ μm. For all the size groups a sediment sphericity $\phi_d = 1.0$ is selected arbitrarily. Given the similarity with test case 1, the same FVPM discretization resolution and number of injected sediments is used.

Table 10.2 – Sediment Size Groups of Test Case 2.

Nominal diameter	10	50	125	250	[μm]
Weibull shape factor	25	25	25	25	[–]
Weibull scale factor	10	50	125	250	[μm]
Lower cutoff diameter	9	45	112	225	[μm]
Upper cutoff diameter	11	55	138	275	[μm]

10.1.3 Test Case 3

The third test case follows the experiment performed at General Electric Renewable Energy, namely slurry erosion tests on stainless steel 13Cr-4Ni. As explained in Chapter 9, it was not possible to characterize all the material parameters of MSS 13Cr-4Ni due to the limitations of the experimental facility available; however, a literature review allowed drawing ranges of maximum likelihood for the missing parameters. The present test case is used to assess different combinations of the unknown material model parameters in order to pinpoint their optimum value for the validation case studies presented in Chapters 12 and 13.

It would be best to directly find the missing material parameters by means of characterization experiments, but an alternative approach had to be used due to the lack of access to suitable facilities. The fact that the multiscale model was successfully validated for the case of copper, together with the fact that the missing parameter ranges were established a priori, lends confidence to the use of the experimental slurry erosion data to pinpoint the missing values. Furthermore, this approach serves as a sensitivity analysis of the multiscale model predictions to variation of the microscale material parameters.

A total of six microscale model parameter sets, referred to as MS-i, are assessed in test case 3. All the parameter values used are within the maximum likelihood ranges defined a priori, as presented in Table 10.3. Only four of the parameters are varied because the uncertainty of D_5 is small and its effect almost negligible given that the temperature increment experienced by the material is insufficient to cause significant thermal softening. It is clear that six parameter sets are insufficient to exhaustively explore the combinations of the four parameters under study, but further exploration of the parameter space was impossible due to the computational cost associated with each set.

Table 10.3 – Microscale Model Parameter Sets Evaluated in Test Case 3.

Johnson-Cook damage model parameter			Maximum likelihood range	MS-1	MS-2	MS-3	MS-4	MS-5	MS-6
Base parameter	D_1	[–]	-0.10 ± 0.08	-0.10	-0.10	-0.10	-0.06	-0.02	-0.02
Triaxiality parameter 1	D_2	[–]	0.26 ± 0.10	0.26	0.26	0.36	0.36	0.36	0.36
Triaxiality parameter 2	D_3	[–]	0.52 ± 0.04	0.52	0.56	0.56	0.56	0.56	0.56
Strain rate parameter	D_4	[–]	0.018 ± 0.004	0.018	0.018	0.018	0.018	0.018	0.022
Thermal softening parameter	D_5	[–]	0.60 ± 0.02	0.60	0.60	0.60	0.60	0.60	0.60

Microscale simulations are performed for the impact angles α = [15, 30, 50, 70, 90]° and impact velocities v = [45, 60, 75, 90] m · s^{-1} for each parameter set MS-i. The sediments are modeled as elastic and sharp, with a shape parameter ϕ_s = 0.5 and diameter d = 100 μm; see Appendix B.1 for the sediment shape discretization algorithm and Appendix B.3 for a study of the effects of the sediment elasticity and shape on the erosion ratio of MSS 13Cr-4Ni. The static and dynamic friction coefficients used in the microscale simulations are $\mu_{f,s}$ = 0.4 and $\mu_{f,d}$ = 0.3, respectively, within the range typical of particle impact simulations [38, 122, 125,

180, 199, 200]. As with the first test case, these values were fixed prior to the simulations and were not changed a posteriori, *i.e.* their value was not tuned for the simulation results to agree with the experiments.

Table 10.4 – Jet Impingement Configurations Studied in Test Case 3.

		Case A	Case B	Case C	Case D	
Jet velocity	C_1	70.0	70.0	90.0	70.0	[m · s^{-1}]
Impingement angle	θ	45	45	45	90	[°]
Log-normal shape factor		0.19	0.18*	0.19*	0.19*	[–]
Log-normal scale factor		195	59*	195*	195*	[μm]
Lower cutoff diameter		100	30	100	100	[μm]
Upper cutoff diameter		325	150	325	325	[μm]

* Approximate values with indeterminate uncertainty.

Four jet impingement configurations are studied in test case 3. They involve two jet velocities, two impingement angles and two sediment size distributions that are fitted with a log-normal distribution, as presented in Table 10.4. The experimental sediment size distribution is only known for Case A; for the other three configurations only the cutoff diameters are known, so an approximate size distribution is assumed in the simulations.

A sensitivity analysis is performed for the macroscale sediment sphericity parameter ϕ_d. Macroscale simulations are run with the microscale simulation results of parameter set MS-3 using ϕ_d = [0.66, 0.76, 0.86], representative of the full range of sphericity values typically found in sediments [119, 135]. All the other macroscale simulations are run with $\phi_d = 0.76$, assumed to be a representative value for the experiments. Given the similarity with test case 1, the same FVPM discretization resolution and number of injected sediments is used for all the macroscale simulations of test case 3.

10.2 Results and Validation for Test Case 1

The simulation results that will allow a better understanding of the quantitative erosion results, namely the distributions of sediment flux and impact conditions on the flat plate, are first presented, followed by the erosion predictions and their validation.

10.2.1 Distributions of Sediment Flux and Average Impact Conditions

The azimuthally-averaged sediment flux as a function of the radial distance from the jet axis for impingement at $\theta = 90°$ is presented in Figure 10.2a. Note that the flux integrals over the inlet and against the plate need not be equal since not every sediment entering the domain impacts the surface once; some impact it more than once while others never do. The highest sediment flux against the plate occurs below the jet inlet, where the sediments struggle to follow the highly curved fluid streamlines. This inertia-driven process depends on the

sediment diameter, with smaller sediments following the fluid more closely. This explains why the average diameter of impacting sediments, also shown in Figure 10.2a, is highest below the inlet. The sediment flux does not vanish even when the mean fluid velocity is parallel to the surface ($r\frac{2}{D_0} >\sim 2.0$) because of the effect of turbulence. As expected, such turbulent velocity fluctuations have a greater effect on low-inertia sediments, as evidenced by the low average sediment diameter in that region.

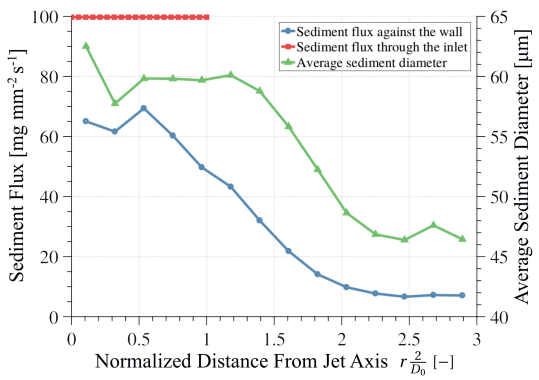

(a) Sediment flux through the inlet and against the copper surface, and average diameter of impacting sediments.

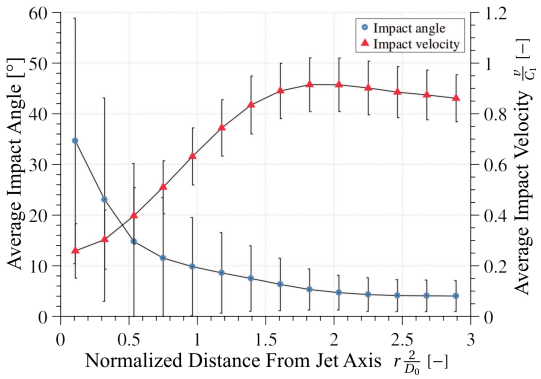

(b) Average impact angle and impact velocity normalized by the jet velocity C_1. The error bars represent ± one standard deviation.

Figure 10.2 – Distributions of sediment flux, average diameter and average impact conditions as functions of the radial distance r from the jet axis normalized by the jet radius $\frac{D_0}{2}$.

The sediment flux is not the only variable that determines the erosion distribution; at least as important are the impact conditions. The azimuthal averages of the average impact angle and impact velocity distributions as functions of the radial distance from the jet axis for impingement at $\theta = 90°$ are presented in Figure 10.2b. The standard deviation, depicted by the error bars, represents the average impact condition variability at a given radial position; it is not a measure of azimuthal variability, which is almost nonexistent due to the axisymmetry. The sediment transport behavior can be described as follows: the area underneath the jet inlet is characterized by low-velocity, high-angle impacts due to the stagnation region and the jet orientation, respectively; conversely, the sediments that follow the fluid streamlines to a greater extent avoid the stagnation region and end up impacting at higher velocity and lower impact angle further downstream. Note that the impact condition for a given sediment does not only depend on its size, but also on its initial position on the inlet boundary and on turbulence-induced randomness. These circumstances explain the relatively high standard deviations in both distributions.

The average impact angle and impact velocity distributions over the plate for three jet impingement angles are presented in Figure 10.3. Even though the stagnation region shrinks and moves as the impingement angle is decreased, the overall behavior of the impact condition distributions is analogous to the aforementioned $\theta = 90°$ configuration.

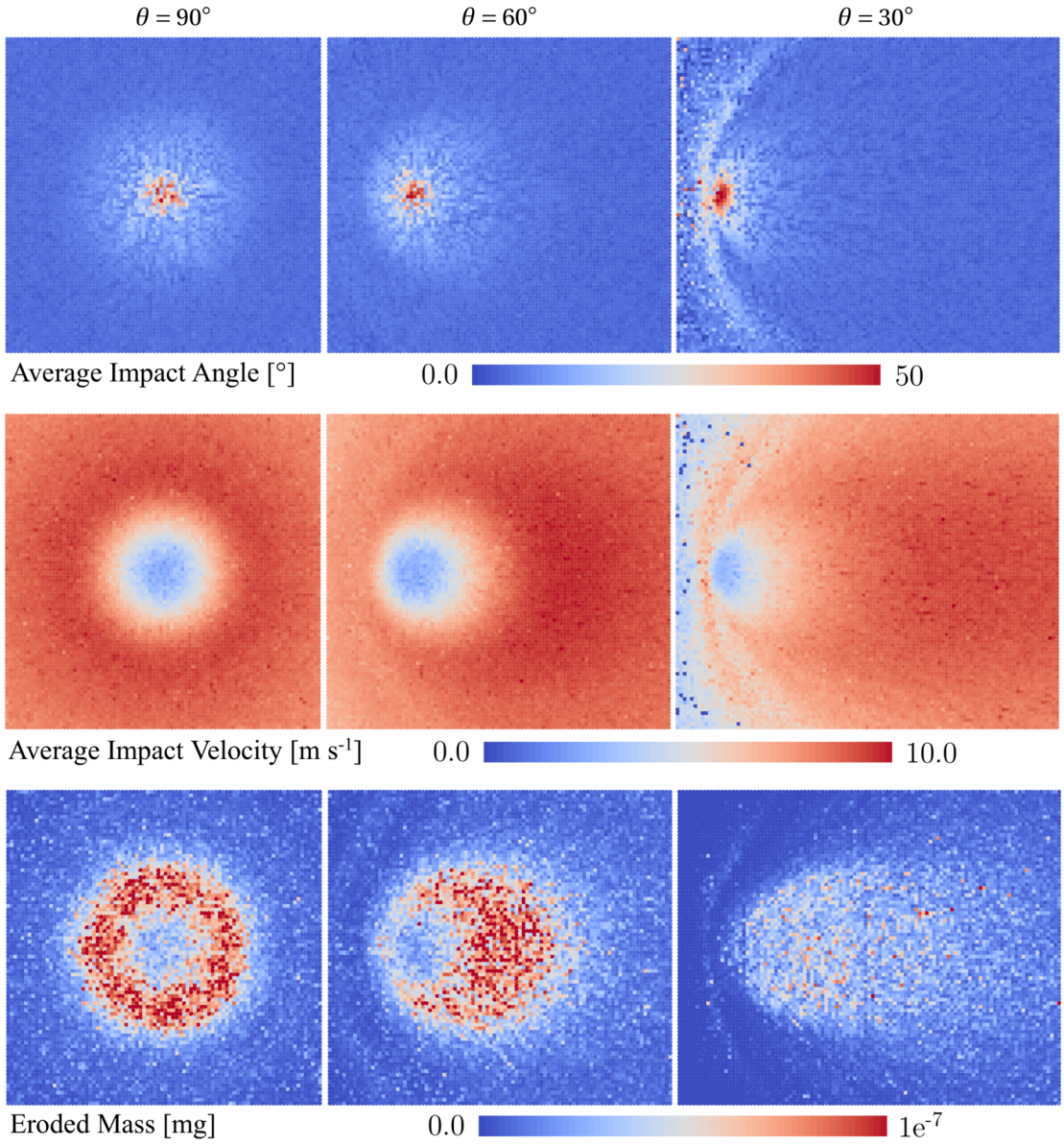

Figure 10.3 – Distributions of the average impact angle, average impact velocity and total eroded mass on the copper plate for three jet impingement angles. The jet impinges from left to right for $\theta = [60,\ 30]°$.

10.2.2 Erosion Depth Distribution and Global Erosion Ratio

The interaction of the microscale erosion model results and the distributions of impact conditions and sediment flux gives rise to the eroded mass distributions also presented in Figure 10.3 for three jet impingement angles. Whereas the $\theta = 90°$ configuration presents a toroidal erosion topology, the $\theta = 30°$ configuration shows an almost uniform erosion scar; for $\theta = 60°$, the erosion distribution is somewhat in between.

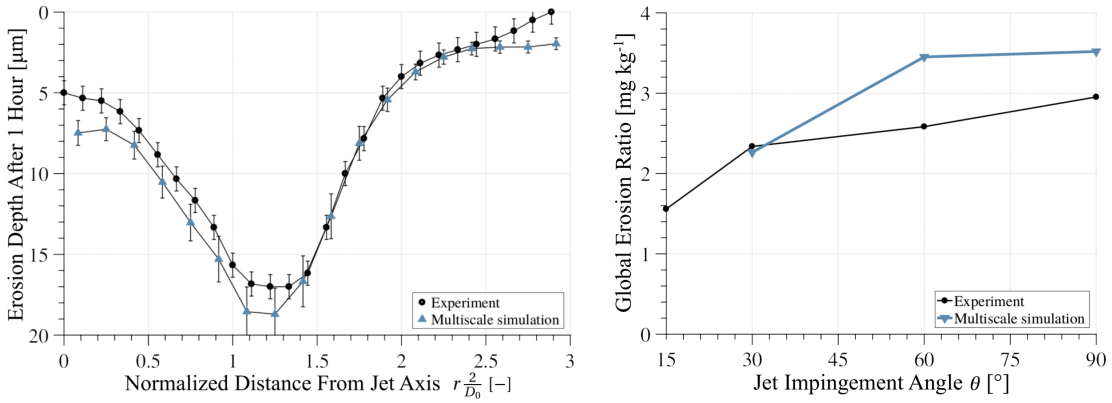

(a) Erosion depth profile after one hour of jet impingement at $\theta = 90°$.

(b) Global erosion ratio as a function of the jet impingement angle.

Figure 10.4 – Comparison of the multiscale erosion simulation predictions and the corresponding experimental data [179].

The results thus far presented are obtained after the injection of about 2.0×10^5 sediments; even though the elapsed physical time is only a fraction of a second, they have converged to a steady-state. In order to compare with the hour-long experiment of Sugiyama, Harada and Hattori [179], the simulation results are linearly extrapolated in time by assuming that the erosion rate stays constant, as discussed in Section 10.5. Given experimental and simulation time periods ΔT_{exp} and ΔT_{sim}, respectively, the local eroded mass m_e, together with the material density ρ and surface area per FVPM particle A, is used to calculate the local erosion depth e_d as

$$e_d = \frac{m_e}{\rho A} \cdot \frac{\Delta T_{exp}}{\Delta T_{sim}}. \tag{10.1}$$

The erosion depth profile after one hour according to the simulation results and experimental profilometry data for impingement at $\theta = 90°$ are presented in Figure 10.4a. The error bars represent the standard deviation: due to azimuthal averaging of the simulation results and due to averaging of two coplanar experimental measurements. The proposed multiscale model agrees well with the experiment, capturing the main features as well as the magnitude of the erosion depth profile. Given that the profile is both a function of the impact condition distributions and the microscale erosion ratio results, it serves as validation of the microscale and macroscale models, as well as their multiscale coupling.

The global erosion ratio, presented in Figure 10.4b, is calculated by summing the eroded mass over all particles and dividing it by the total mass of sediments injected. There is a reasonable agreement between the experimental results and the simulation. The trend of increasing erosion ratio with increasing impingement angle is well captured. The erosion ratio magnitude is predicted with an average relative error of 18 %, which is a significant improvement over the state-of-the-art models based on erosion correlations, as discussed in Section 3.1.

10.3 Results and Verification for Test Case 2

Since all the simulations for test case 2 are performed at an impingement angle $\theta = 90°$, all the results presented hereafter are azimuthal averages around the jet axis.

10.3.1 Distributions of Impact Conditions by Sediment Size

The average impact angle and impact velocity are presented in Figure 10.5 for each of the four sediment sizes studied. Globally, the same behavior explained in the analysis of test case 1 applies for the present results: higher impact angle near the stagnation region, with corresponding low impact velocity, and higher impact velocity away from the stagnation region, with corresponding low impact angle.

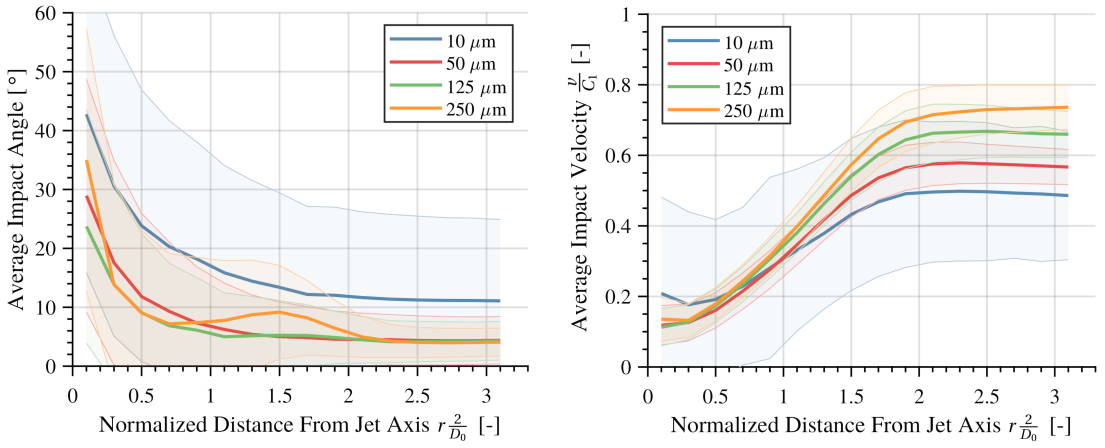

(a) Average impact angle.

(b) Average impact velocity v normalized by the jet velocity C_1.

Figure 10.5 – Distribution of average impact conditions as a function of the radial distance from the jet axis for four sediment sizes. The shaded regions represent ± one standard deviation.

More interesting is the segregation by sediment size. Concerning the impact angle, the $d = 10$ μm sediments stand out both for their higher standard deviation and average value. Being more responsive to the fluid velocity due to their high drag to inertia ratio, their impact conditions are more sensitive to the random turbulent fluctuations. This implies both an overall greater standard deviation due to the turbulence randomness, and a higher average impact angle: whereas the mean flow velocity, parallel to the wall, tends to bring about very low impact angles, the turbulent fluctuations may induce motion perpendicular to the surface, therefore increasing the impact angle. Note that, in general, this increase in impact angle due to greater turbulent fluctuations can occur either because of a higher turbulence intensity or a greater sediment sensitivity to the fluctuations, *i.e.* smaller sediments.

The average impact angle and its standard deviation are inversely proportional to the sediment diameter away from the stagnation region, $r\frac{2}{D_0} >\sim 2.5$, even though for $d = [50,\ 125,\ 250]$ μm

the results are barely distinguishable. This means that there is a very sharp regime change at perhaps $d \simeq 20$ μm below which the sediments become very sensitive to the turbulent fluctuations, although the threshold diameter is probably dependent on the case details such as the turbulence intensity, jet velocity and surface geometry.

A similar segregation by sediment size is evidenced in the impact velocity distributions, Figure 10.5b. Downstream of the stagnation region, the average impact velocity is proportional to the sediment diameter. This behavior is expected because of the drag to inertia ratio: whereas the smaller sediments react swiftly to the deceleration of the flow near the wall, the larger sediments do not, impacting with a greater fraction of their initial velocity C_1. Yet again, the turbulent fluctuations imply a significantly higher standard deviation for the sediment group with $d = 10$ μm.

10.3.2 Distributions of Erosion by Sediment Size

The sediment flux against the wall, normalized by the inlet sediment flux, is presented in Figure 10.6a for the four sediment sizes under study. There is a clear transition mediated by the drag to inertia ratio. The particles with $d = 250$ μm impact directly under the inlet given that they tend not to follow the curved fluid streamlines, and after their first impact they tend to travel with the flow, parallel to the wall, with ever lower flux against the surface. On the contrary, sediments with $d = 10$ μm follow the curved mean flow streamlines closely, so they do not have a preferential impact zone beneath the inlet; however, their propensity to follow the turbulent fluctuations increases their flux against the wall at every radial position. Particles with $d = [50,\ 125]$ μm exhibit a behavior somewhere in between these two extremes, as expected.

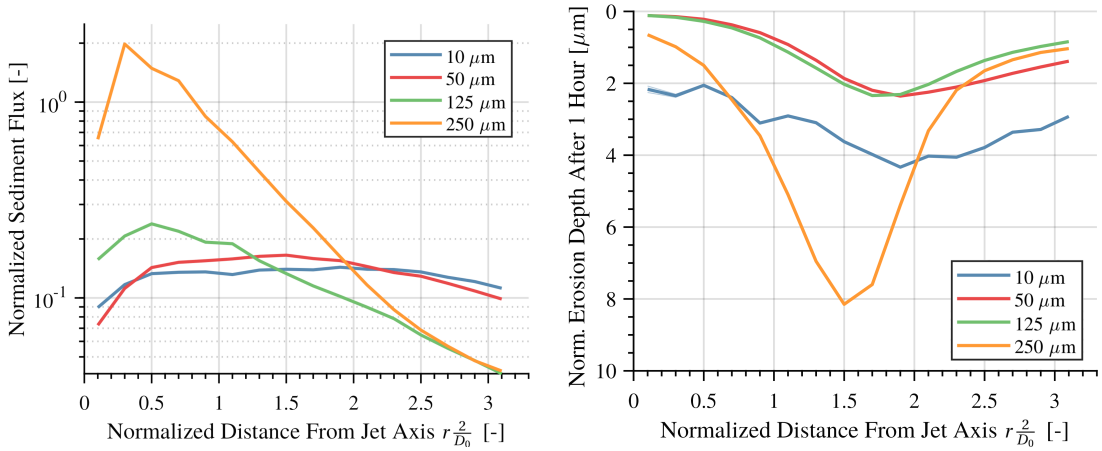

(a) Sediment flux against the wall normalized by the inlet sediment flux.

(b) Erosion ratio per unit area computed using the total sediment mass injected rather than its distribution.

Figure 10.6 – Distributions of sediment flux and erosion ratio per unit area as functions of the radial distance from the jet axis for four sediment sizes.

The erosion distribution can be directly linked with an erosion depth distribution after a given amount of time, as expressed in Equation 10.1. In this test case the erosion depth, presented in Figure 10.6b, is normalized by multiplying it by a factor $\left(\frac{d_0}{d}\right)^3$, where $d_0 = 100$ μm; this normalization makes the erosion depth magnitude of the different sediment size groups comparable. The sediments with $d = 250$ μm induce a sharp erosion scar, whereas particles with $d = 10$ μm generate a wider and more uniform erosion pattern, in agreement with the literature [148]. Particles with $d = [50,\ 125]$ μm exhibit a behavior somewhere in between these two cases. Given that the erosion distribution is a function of the sediment flux and impact condition distributions, the factors already mentioned explain these results too: the drag to inertia ratio and the sediment sensitivity to the turbulent fluctuations.

Table 10.5 – Erosion Results for the Sediment Size Groups of Test Case 2.

Nominal diameter		10	50	125	250	[μm]
Global erosion rate	$\dot{e}$	0.273	16.1	349	3503	[mg · h^{-1}]
Global erosion ratio	e_r	7.95	3.75	3.01	6.53	[mg · kg^{-1}]

The erosion results of test case 2 are compiled in Table 10.5. The amount of sediment mass injected increases as d^3 because each simulation featured the same number of sediments, therefore the erosion rate also scales as d^3. In other words, for a fixed number of sediments, the larger particles are significantly more erosive simply by virtue of their greater mass.

The erosion ratio allows a more interesting interpretation of the results since it is defined per unit mass of sediment injected. The highest erosion ratio is caused by particles with $d = 10$ μm: their high drag to inertia ratio takes them wherever the fluid goes and makes them very sensitive to the turbulent fluctuations, which increases their flux against the wall. The second highest erosion ratio is due to sediments with $d = 250$ μm: their low drag to inertia ratio makes them insensitive to the fluid streamline curvature, directly impacting the wall at high velocity irrespective of the flow. Interestingly, the sediments with $d = [50,\ 125]$ μm cause the lowest erosion ratio: they follow the curved fluid streamlines, avoiding the direct impact against the wall, and are not very sensitive to the turbulent fluctuations that would increase their flux against it.

Nguyen et al. [148] found an opposite trend for the erosion ratio dependence on the particle size. Considering that their results deal with an impinging slurry jet that is five times smaller, 52 % faster, and characterized by a sediment concentration that is five times larger, it is not surprising that the results are significantly different from the ones reported for the present test case. For example, they evidenced a decreasing erosion ratio for sediments larger than $d = 150$ μm, and explained it in terms of the increasing importance of the shielding effect, whereby large sediments, which impact directly below the jet inlet due to their inertia, rebound and interfere with the incoming particles. The shielding effect depends fundamentally on the sediment flux, as explained in Section 2.2.1, that is proportional to the concentration and jet velocity; therefore it is likely that the present results do not follow the same trend due to the sediment flux used, which is about seven times smaller than the one used by Nguyen

et al. Another difference is that they did not evidence the increasing erosion ratio for small sediments. However, the smallest size they used was $d = 50$ μm; perhaps a similar trend would have been found had smaller sediments been considered.

This test case has served to verify the physical correctness of the sediment transport model. It has been evidenced that the two mechanisms that promote the impact of sediments, namely the turbulent fluctuations and the acceleration associated with the fluid curvature, are well captured, as is their dependence on the sediment size. The erosion results highlight the importance of having a good description of the particles: injecting a given mass of sediments generates quite different outcomes depending on their size distribution.

10.4 Results and Validation for Test Case 3

Test case 3 studies the erosion of MSS 13Cr-4Ni, for which there is some uncertainty in the damage model parameters. The microscale erosion ratio results for several sets of these four parameters are first presented, followed by a sensitivity analysis of the macroscale model predictions to this uncertainty.

10.4.1 Sensitivity Analysis of the Microscale Erosion Ratio

The erosion ratio computed on the microscale simulations using the six parameter sets studied is presented in Figure 10.7. Concerning the impact angle dependence, it has been shown that martensitic steel in general [163] and 13Cr-4Ni in particular [176] present a maximum erosion ratio in the range of $\alpha = 60$-$90°$, in agreement with the simulation results. As for the impact velocity dependence, a velocity exponent in the range $n_v = 3.0$-4.0 is found, whereas according to the literature $n_v = 2.0$-3.4 is most common in metals [140, 152, 163, 175].

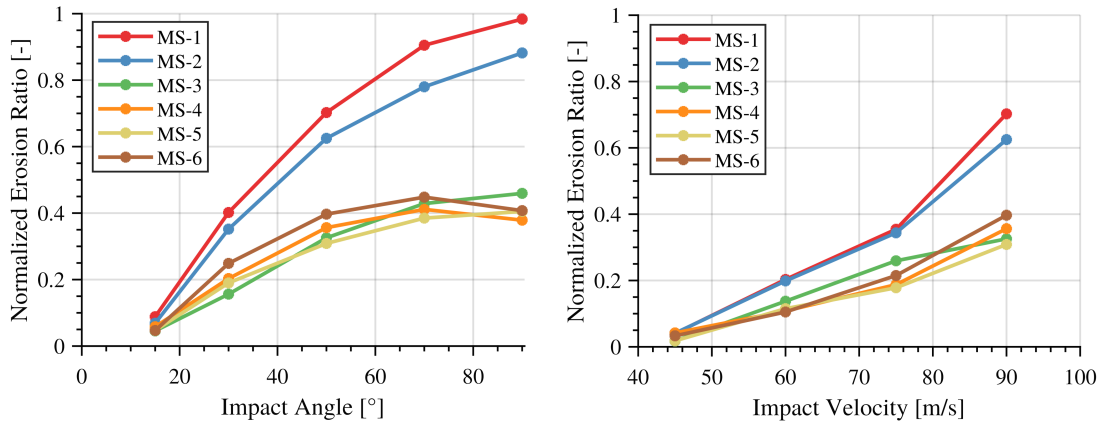

(a) Erosion ratio at $v = 90$ m $\cdot$ s^{-1} as a function of impact angle.

(b) Erosion ratio at $\alpha = 50°$ as a function of impact velocity.

Figure 10.7 – Normalized microscale erosion ratio results for the six parameter sets studied.

The highest variation in the erosion ratio results occurs among parameter sets MS-1, MS-2 and MS-3. These correspond to variations in the Johnson-Cook damage model parameters D_2 and D_3, as presented in Table 10.3, which deal with the influence of the triaxiality state on the failure plastic strain. The exponential dependence presented in Equation 6.61 explains the high sensitivity of the microscale results to the uncertainty intervals of D_2 and D_3. On the contrary, the influence of D_1 and D_4 is relatively low, as revealed by the similar erosion ratio results among parameter sets MS-3, MS-4, MS-5 and MS-6, in spite of the wider uncertainty intervals associated to these parameters.

10.4.2 Sensitivity Analysis of the Macroscale Erosion Ratio

The macroscale simulation erosion ratio results using the six microscale parameter sets are presented in Figure 10.8a for the four cases described in Table 10.4. The shaded regions represent ± one standard deviation whereas the whiskers define the bounds. The average erosion ratio for the ensemble of simulations performed for case A is only 2 % higher than the average experimental value; moreover, the standard deviations are comparable. In other words, for case A the uncertainty introduced by the unknown material model parameters is comparable to the experimental variation between nominally identical tests, and the average erosion ratio is predicted with considerable accuracy.

For cases B, C and D the results are significantly worse: the relative error between the simulation ensemble average and the experiment is 30 %, 43 % and 190 %, respectively. However, note that unlike case A where the experimental sediment size distribution was well characterized, cases B, C and D were performed with unknown particle size distributions for which only the maximum and minimum sediment diameters were specified. As evidenced in test case 2, the distribution of particle diameters has a significant effect on the erosion outcomes; therefore at least part of the error for these three cases is explained by a mismatch between the experiments and the simulations, for which a sediment size distribution had to be assumed.

The macroscale model parameter that brings the greatest uncertainty to the results is the sediment sphericity ϕ_d. According to the literature, the values $\phi_d = [0.66,\ 0.76,\ 0.86]$ correspond to sediment shapes described as fully sharp, semi-sharp and fully round, respectively [135]. The erosion ratio simulation results using the aforementioned values of ϕ_d and the microscale parameter set MS-3 are presented in Figure 10.8b for the four configurations studied. The uncertainty induced by that range of sphericity values tends to be greater than the uncertainty introduced by the microscale material parameters, presented in Figure 10.8a. Case D is the most sensitive to ϕ_d because of the jet impingement angle $\theta = 90°$; at normal impingement the fluid streamline curvature is highest, boosting the importance of the drag to inertia ratio, itself influenced by ϕ_d through the drag coefficient correlation, Equation 6.20.

Such a high uncertainty on the macroscale erosion results would only occur provided no information whatsoever is available about the experimental sediment shape. In practice, however, a set of sediment micrographs would allow reducing the uncertainty range of ϕ_d to perhaps

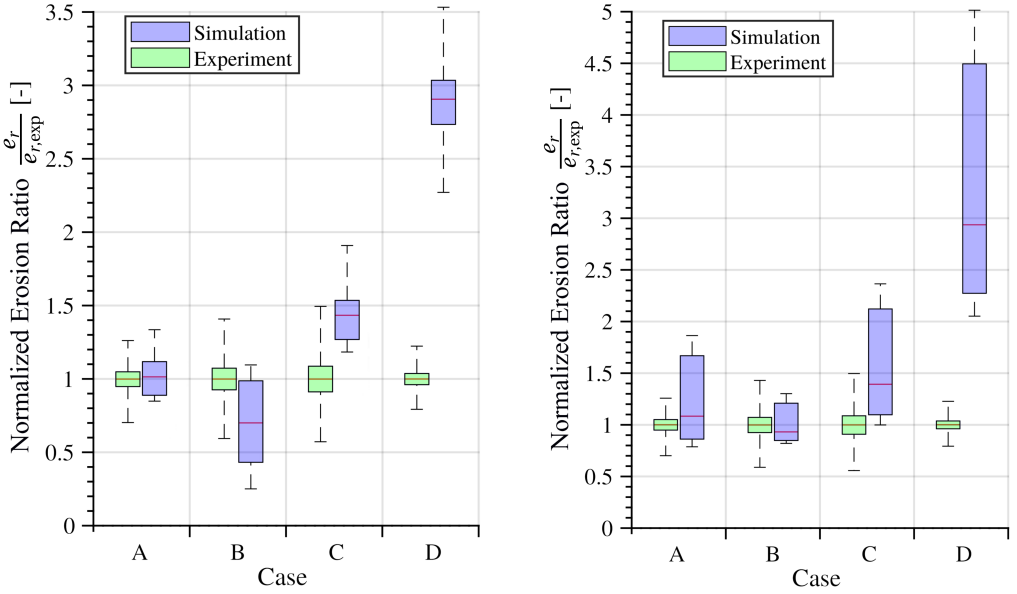

(a) Effect of the microscale model parameters.

(b) Effect of the macroscale sediment sphericity.

Figure 10.8 – Sensitivity analysis of the macroscale erosion ratio to the uncertainty intervals of the model parameters. The simulation results are normalized with respect to the corresponding experimental erosion ratio.

20 % of the one studied, say $\phi_d = 0.76 \pm 0.02$ instead of ± 0.10. Under these circumstances the erosion ratio uncertainty would be comparable to the experimental variability.

The average impact conditions and sediment flux as functions of the radial distance from the jet axis are presented in Figure 10.9 for case D, characterized by an impingement angle $\theta = 90°$. The effect of the sediment sphericity ϕ_d is quite clear in terms of its effect on the particles' drag to inertia ratio. Sediments with higher sharpness, lower ϕ_d, have a greater surface area per unit mass, a higher drag coefficient and therefore are more sensitive to the fluid motion. Consequently, they impact at lower velocity and angle in the stagnation region near the jet axis, whereas rounder sediments maintain to a greater extent their initial velocity and orientation. Similarly, the sediment flux against the wall is highly concentrated below the inlet for the case of rounder particles, less affected by the curved fluid streamlines; the sharper sediments, on the contrary, spread more evenly. These differences in impact conditions and sediment flux explain the variation in erosion ratio as a function of ϕ_d, presented in Figure 10.8b.

10.4.3 Global Erosion Ratio Comparison with the Experimental Data

One of the six material model parameter sets has to be selected for the case studies presented in Chapters 12 and 13; the erosion ratio error relative to the experimental data is used to asses them. A weighted average of the error over the four configurations is used. The highest weight is given to case A since it is the only case for which the experimental sediment size

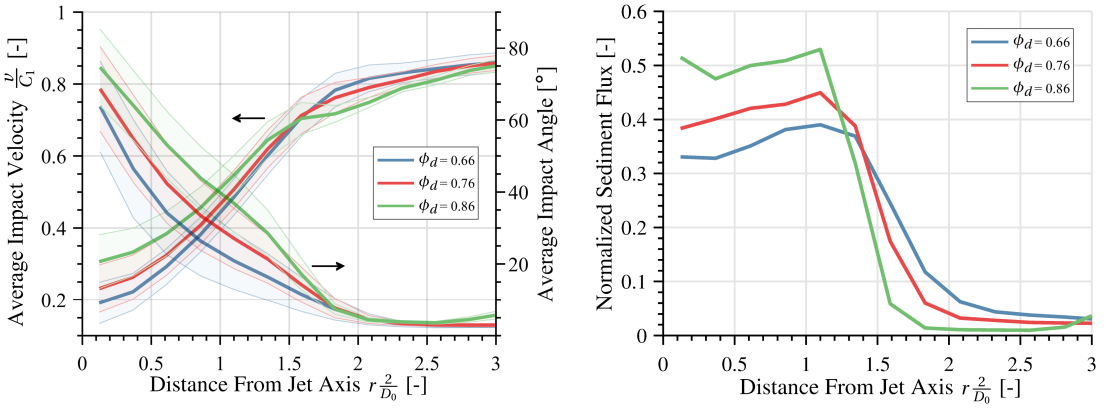

(a) Average impact velocity, normalized by the jet velocity, and impact angle.

(b) Sediment flux against the wall normalized by the inlet sediment flux.

Figure 10.9 – Distributions of average impact conditions and sediment flux as functions of the radial distance from the jet axis for three values of the macroscopic sediment sphericity ϕ_d. The shaded regions represent ± one standard deviation.

distribution was available, allowing an exactly equivalent simulation setup and therefore a fair comparison. The lowest weight is given to case D because it involves impingement at $\theta = 90°$; this configuration is unlike the erosion of a Pelton bucket, where the jet impinges on the splitter at very low angle.

The erosion ratio results, normalized by their experimental counterparts, are presented in Table 10.6 for parameter set MS-3, which achieved the lowest weighted error among the six sets; the results using two values of the sediment sphericity as well as the weight assigned to each case are shown. The weighted average error is in the range of 25-35 %; this figure is judged reasonable, considering the uncertainty on the Johnson-Cook damage model parameters and the average error achieved for test case 1 (18 %) for which all the parameters were known.

Table 10.6 – Normalized Erosion Ratio Results for Parameter Set MS-3.

	Case A	Case B	Case C	Case D	Weighted error
MS-3, $\phi_d = 0.76$	1.084	0.932	1.393	2.935	35 %
MS-3, $\phi_d = 0.66$	0.788	0.821	0.999	2.051	25 %
Case weight	1.00	0.50	0.50	0.25	

10.5 Case Study Discussion

The assumption of constant erosion rate implicit in the choice of extrapolating the results of a short macroscale simulation to compare against an hour-long experiment, as done for test case 1, may be challenged on the grounds of the surface modification induced by the process. For this particular test case, the surface modification is negligible since the erosion depth is

only about 0.3 % of the jet diameter after one hour; it should not induce any significant change in the sediment transport hydrodynamics or effective impact angle. However, for cases where the surface modification becomes significant, the altered hydrodynamics and effective impact angle may lead to a modified erosion rate distribution, in which case the extrapolation from a short macroscale simulation would introduce additional error. For those cases, the projective integration approach should be used, as demonstrated in Chapter 11.

The validation results presented for test case 1 are conclusive. The proposed multiscale model is able to predict the erosion depth profile as well as the global erosion ratio for several jet impingement angles within a mean relative error of 18 %. This constitutes an *improvement over the state-of-the-art* erosion simulations based on correlations, for which an average error of 180 % is expected, as reviewed in Section 3.1. However, a significantly larger set of simulations should be performed to confirm whether the $\approx$ 18 % relative error is maintained, given that the aforementioned 180 % average error is based on a whole suite of jet impingement case studies. Anyhow, the *apparent order of magnitude gain in accuracy* is the result of including the detailed physics of sediment impact simulations into the model; whereas such a level of detail would normally be intractable for a macroscopic problem, the multiscale approach makes it possible.

Test case 2 brings insight about the two mechanisms responsible for the sediment impacts: the acceleration associated with the fluid streamline curvature and the turbulent fluctuations. The physical correctness of the behavior of these mechanisms with respect to different sediment sizes serves as a verification of the macroscale sediment transport model. This test case also highlights the importance of having an accurate description of the sediment size distribution, given that the erosion results depend fundamentally on it.

Having verified and validated the multiscale erosion model, test case 3 is used to study its sensitivity to the uncertainty of some of the model parameters. It has been shown that the variation of the erosion simulation results introduced by the uncertainty of both the microscale material model parameters and the macroscale sediment sphericity is of comparable magnitude to the variability of the experimental erosion results, provided a set of sediment micrographs is used to estimate the sphericity parameter ϕ_d.

Test case 3 also allowed defining the Johnson-Cook damage model parameters for MSS 13Cr-4Ni to be used in the case studies presented in Chapters 12 and 13. Among the six sets that were used to explore the parameter uncertainty intervals, MS-3 achieved the best results over the four jet impingement configurations studied; an average weighted error of 25-35 % was found.

Based on the relative errors calculated on this case study, which cover the range of 18-35 %, it is estimated that the *global error of the multiscale model of erosion* is of the order of 25 %. The convergence analyses of the microscale and macroscale simulations, presented in Appendices B.2 and B.4, respectively, suggest that the *discretization error* is about 5 %. Therefore, the global error of the multiscale model is mainly explained by *modeling error*. As detailed

in Section 3.2, the error of sediment impact simulations can reach 30 %, so most likely the modeling bottleneck occurs within the microscale description. The constitutive and damage modeling of the solid, in this case the Johnson-Cook model, is probably the greatest source of error. Unfortunately, a more accurate description of the solid behavior would have to include an atomistic description of the material, which is by far too expensive for the time being. It appears that an average error of about 25 % is as accurately as the multiscale erosion phenomenon can be predicted with the present knowledge and computational resources.

11 Jet Impingement on a 2D Static Bucket

Having validated the multiscale erosion model on a simple geometry, the second case study applies it to a more challenging problem: a Pelton-like bucket impinged by a slurry jet. The main objective of the case study is to demonstrate the use of the projective integration scheme described in Section 5.3. Given that the approach requires several consecutive macroscale simulations that can be very computationally expensive, this case study is restricted to 2D. Part of the contents of this chapter have been previously published in Leguizamón et al. [114, 115].

11.1 Description of the Case Study

The case study involves a static 2D Pelton-like copper bucket impinged by a slurry jet, as illustrated in Figure 11.1. A sediment size distribution, following the literature reviewed in Section 2.2.1, is described by means of a Weibull distribution. The turbulence intensity and length scale are set to 3.25 % and $0.03D_0$, respectively, based on the assumption of fully developed turbulent flow in the distribution system [173]. The case study geometric parameters are specified in Table 11.1.

Table 11.1 – Geometric Parameters of Case Study 2.

Jet velocity	C_1	40.0	[m · s^{-1}]
Jet diameter	D_0	0.10	[m]
Bucket width	B_2	0.323	[m]
Bucket half-splitter angle	β_b	18.0	[°]
Bucket outlet angle	γ_b	12.0	[°]
Sediment concentration	c_w	1.0	[$\%_w$]
Macroscale sediment sphericity	ϕ_d	0.76	[–]
Weibull shape factor		2.5	[–]
Weibull scale factor		175	[μm]
Lower cutoff diameter		50	[μm]
Upper cutoff diameter		250	[μm]

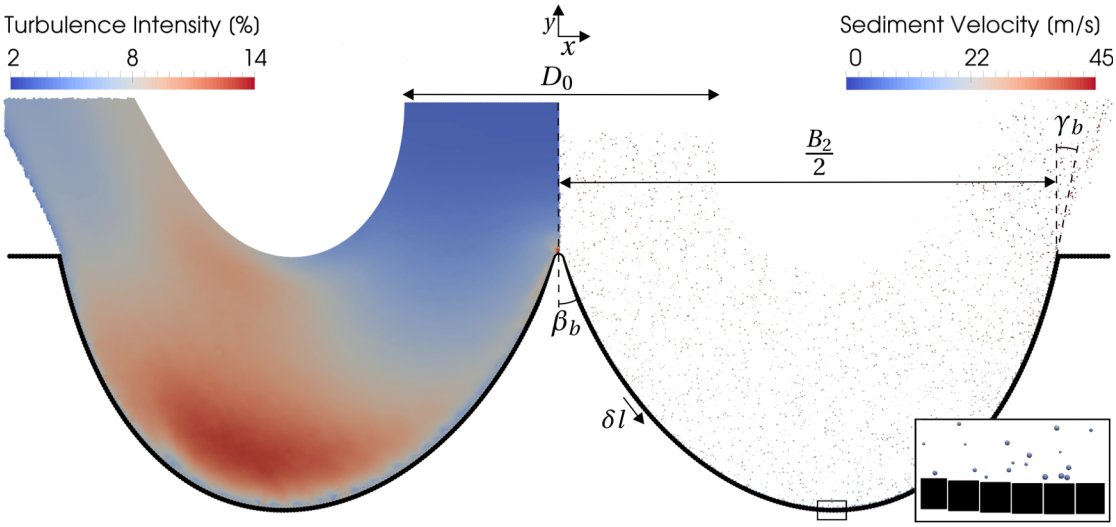

Figure 11.1 – Computational domain of case study 2. The fluid particles and the sediments, illustrated twice their actual size, are visible on the left and right halves, respectively. Although the FVPM particles are spherical, the contact between wall particles and sediments is defined such that the wall is effectively flat, as shown in the inset.

With the objective of generating a realistic bucket geometry, Bézier curves are defined such that the half-splitter and outlet angles are respected and the bucket depth equals $0.25B_2$; these three parameters are within the ranges for Pelton buckets [203]. Importantly, the macroscale domain is about an order of magnitude larger than the ones investigated in case study 1, although the sediments are about the same size. This implies a significantly greater scale separation between the bucket and the sediments, and therefore a test of the code robustness.

The microscale simulation results of quartz sediments impacting oxygen-free copper presented in Chapter 10 are used in this case study; therefore only macroscale simulations are performed. The projective integration scheme described in Section 5.3 is used. The time constants that characterize it are compiled in Table 11.2. The simulation time step is set according to the CFL restriction, discretization size and characteristic wave speed. The inner integration period is set to 10 times the characteristic time $\frac{B_2}{C_1}$ during which 64,000 sediments are injected; it has been verified that the erosion and impact condition distributions on the bucket reach a steady-state. The outer integration period is chosen such that the maximum wall particle displacement due to erosion is equal to half its diameter. A total of 12 outer integration steps are taken, summing up to 80 minutes of physical time.

Table 11.2 – Projective Integration Time Constants for Case Study 2.

Macroscale simulation time step	Δt	2.4×10^{-7}	[s]
Inner integration period	ΔT^i	80.8×10^{-3}	[s]
Outer integration period	ΔT^o	240-900	[s]
Total physical time	$\sum_j \Delta T^o_j$	4,800	[s]

11.2 Results and Qualitative Comparison with Experimental Data

Some of the results presented in this section involve spatial distributions over the bucket surface that have been averaged about the symmetry plane defined by the splitter. Therefore they are presented as distributions spanning from the splitter to the bucket outlet edge along the bucket surface defined by δl, as illustrated in Figure 11.1. The splitter is located at $\frac{l}{B_2} = 0$.

11.2.1 Distributions of Impact Conditions and Erosion Rate

The average sediment impact angle and impact velocity along the bucket surface are presented in Figure 11.2a for three inner integration periods representative of the beginning, middle and end of the simulation. The highest average impact angle, 50°, occurs at the splitter, where the jet impinges perpendicularly. The deflection of the fluid by the splitter disrupts the sediment paths, preventing them from impacting at higher angle. Further downstream the impact angle stabilizes to a fairly small value of about 5°. The minimum average impact velocity occurs at the splitter, due to the stagnation region present, and is equal to about $0.2C_1$; this highlights the fact that the sediments are fairly responsive to the fluid acceleration. Further downstream they tend to impact at higher velocity, reaching $0.8C_1$ near the outlet edge.

The results presented in Figure 11.2a are converged metrics taken at the end of specific inner integration intervals; they are not averages up to a given physical time. Therefore they represent the instantaneous average impact conditions at several moments along the bucket erosion process. It is evidenced that the surface evolution only has a minor effect on the impact conditions, the most significant of which is a small increase of the impact angle near the outlet edge. As discussed in Section 11.2.2, this has to do with the well-known ripple pattern created by the erosion.

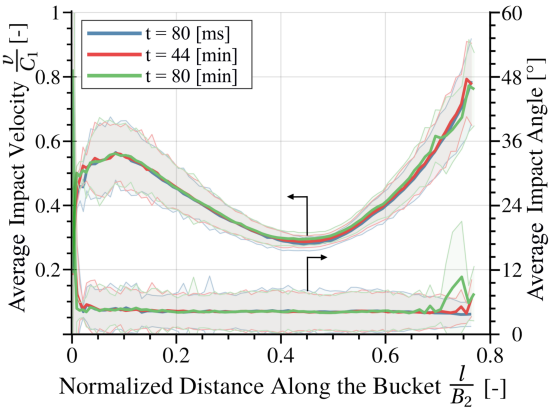

(a) Average impact angle and impact velocity.

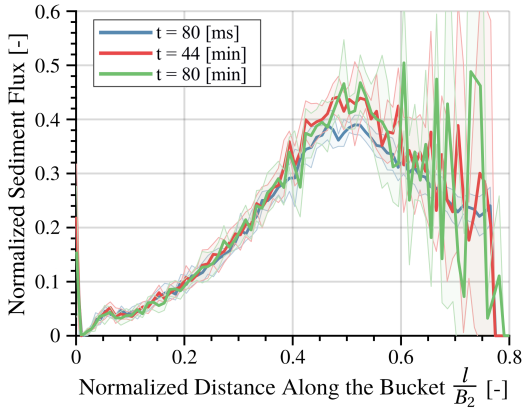

(b) Sediment flux against the bucket surface normalized by the inlet sediment flux.

Figure 11.2 – Average impact conditions and sediment flux on the bucket surface at three instants during the erosion process. The shaded regions represent ± one standard deviation.

The sediment flux against the bucket surface, normalized by the inlet sediment flux, is presented in Figure 11.2b for three inner integration periods representative of the beginning, middle and end of the simulation. The results for the first inner integration (t = 80 ms) show a fairly smooth distribution that has an isolated peak at the splitter, and a maximum about 60 % along the bucket surface. This distribution is tightly linked to the surface curvature and the turbulence intensity, which determine the centrifugal acceleration and the magnitude of the turbulent fluctuations, respectively, that drive the sediments towards the bucket. Indeed, the sediment flux is maximum at the zone of highest curvature near the deepest part of the bucket, which also coincides with the location of highest turbulence intensity, as seen in Figure 11.1.

The surface erosion is not perfectly uniform, so small dents appear as illustrated in the inset of Figure 11.3a. The downstream half of these dents is more likely to be impacted by the passing sediments, whereas the upstream half is relatively sheltered. This preferential impact locations explain the increasingly spiky character of the sediment flux distribution as the simulation advances, especially towards the bucket outlet.

The erosion rate over the bucket surface is presented in Figure 11.3a for three inner integration periods. These distributions depend on where and how the sediments impact, *i.e.* on the aforementioned sediment flux, impact angle and impact velocity distributions. The results for the first inner integration (t = 80 ms) show a smooth erosion rate distribution that peaks towards the bucket outlet, where both the sediment flux and impact velocity are high. As the surface evolves, the erosion rate distribution changes dramatically: strong peaks appear towards the bucket outlet and increase in magnitude as the surface gets eroded. This is partly explained by the appearance of dents whose downstream halves experience an enhanced sediment flux. Furthermore, as illustrated in Figure 11.2a, these dents also imply a local increase of the average impact angle, which generates a greater erosion ratio according to the microscale model results.

The inset of Figure 11.3a illustrates the progressive erosion of the bucket surface near the left outlet edge; the wall particles are colored according to the erosion rate computed on each of the corresponding inner simulations. The surfaces have been shifted horizontally to allow for a clear illustration; the arrows are fixed in space so they serve as reference to assess the surface movement. It is clear that the surface does not evolve evenly, but develops dents and bulges with the aforementioned consequences on the sediment flux and impact angle.

11.2.2 Effect of the Bucket Erosion on the Reaction Force and Outflow Angle

So far the spatial distributions of the quantities of interest over the bucket surface at three instants during its erosion process have been presented. Now the consequences of the surface evolution on certain global parameters are analyzed.

The average outflow angle and the force felt by the bucket in the y-direction as a reaction to the fluid momentum change are presented in Figure 11.3b as functions of time. The inset contains

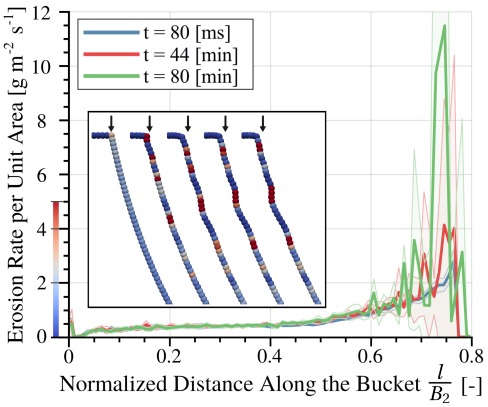

(a) Erosion rate distributions over the bucket surface at three instants during the erosion process. The inset illustrates the evolution of the surface near the left outlet at the following times, from left to right: 0.00133, 44, 68, 76 and 80 min.

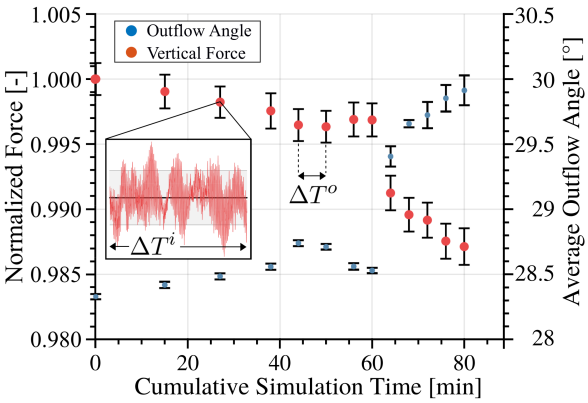

(b) Reaction force on the bucket normalized by its initial value and average outflow angle as functions of the cumulative simulation time, *i.e.* the degree of surface alteration due to erosion. The inset contains the time history of the reaction force on one inner integration interval.

Figure 11.3 – Erosion rate distribution and the effect of the surface state on the reaction force and outflow angle. The shaded regions and error bars represent ± one standard deviation.

the reaction force time history for one inner integration period ΔT^i, *i.e.* along one macroscale simulation instance. The erosion, which is most significant near the outlet, increases the bucket outlet angle γ_b, in turn increasing the outflow angle. As a consequence, the reaction force felt by the bucket decreases due to the reduced momentum change experienced by the fluid in the y-direction. The mechanical power that would be extracted by the bucket, directly proportional to the reaction force, would decrease by 1.5 %, a non-negligible repercussion.

It is common for the fluid not to exit the bucket at exactly the outlet angle γ_b, but rather at a larger angle; the difference between the outflow angle and the bucket outlet angle is typically 5-8° [203]. During the first instants of the simulation, when the water is exiting the bucket for the first time, a thin water sheet with an outflow angle similar to γ_b is evidenced. However, by the time the simulation reaches the steady state illustrated in Figure 11.1, the outlet water sheet is quite thick due to the 2D nature of the simulation. This implies a significantly larger outflow angle, in this case about 16° greater than γ_b, as presented in Figure 11.3b for $t = 0$.

There is an unexpected behavior during the inner integration periods corresponding to $t = [56,\ 60]$ min, followed by an unusual jump of the average outflow angle, and consequently a sudden drop in the reaction force felt by the bucket, at $t = 64$ min. This behavior is in fact a consequence of the non-linear erosion process: it was found that a surface dent, similar to the ones visible in the inset of Figure 11.3a, had formed near the right bucket outlet and induced a local decrease of γ_b that affected the outflow. As the erosion process continued, the dent grew all the way to the outlet edge, causing the sudden increase in outflow angle presented in Figure 11.3b at $t = 64$ min. After this unusual event, the average outflow angle continued to increase, following the trend evidenced since the beginning of the erosion process.

11.2.3 Effect of the Bucket Erosion on the Erosion Rate

The global erosion rate is presented in Figure 11.4a as a function of the cumulative simulation time. In line with the aforementioned erosion distribution results, an increase of the global erosion rate is seen as the erosion process advances. It appears to stabilize towards the end of the simulation, reaching a value that is about 45 % higher than the one calculated using the original bucket geometry, although further outer integration steps would be required to corroborate whether the erosion rate does reach a steady-state.

These results highlight the important feedback between the surface modification caused by erosion and the erosion rate itself. Evidencing this feedback effect could not have been possible without the projective integration scheme, given the temporal scale separation involved.

11.2.4 Qualitative Comparison with Experimental Data

A comparison between the simulation results and available experimental data is not straightforward for a number of reasons. First and foremost, even if the simulated bucket resembles a Pelton bucket, its bidimensionality implies an inherent dissimilarity that makes the results incompatible. Second, the simulated bucket is made of copper due to the unavailability of the stainless steel 13Cr-4Ni material model parameters at the time of simulation. It is clear that the erosion behavior of such a soft metal will be significantly different from the behavior of the martensitic stainless steel typically used in Pelton runners. Third, the case study parameters used, such as the jet velocity, sediment size distribution and bucket curvature, are realistic but do not exactly match any given Pelton turbine installation.

In order to minimize these discrepancies to allow for a qualitative comparison with experimental data, the following actions have been taken. First, the simulated erosion depth profile has been multiplied by a factor $f(l) = 1 - 0.75\frac{l}{l^*}$, where l is the distance along the bucket surface starting at the splitter, and l^* is this distance at the bucket outlet edge. This factor scales down the erosion depth proportionally to the distance from the splitter, such that $f(0) = 1$ at the splitter and $f(l^*) = 0.25$ at the bucket outlet. The motivation for such a correction is the fact that the simulation does not take into account the three-dimensional spreading of the water jet as it travels through the Pelton bucket; as such, the sediment flux and erosion are overrepresented proportionally to the distance from the splitter. The factor slope, 0.75, is chosen based on the observation that the water sheet extension at a Pelton bucket outlet is about four times the jet diameter [191]. Second, the erosion depth distribution is uniformly scaled to have a magnitude comparable to the available experimental data; this normalization partially tackles the difference caused by comparing copper and stainless steel buckets. Third, the erosion depth and spatial coordinates are normalized by the respective bucket width B_2 to compare buckets that are not exactly the same size.

Having followed the aforementioned normalization, the simulation erosion depth at $t = 38$ min is qualitatively compared with field data on uncoated Pelton buckets [165] in Figure 11.4b. The

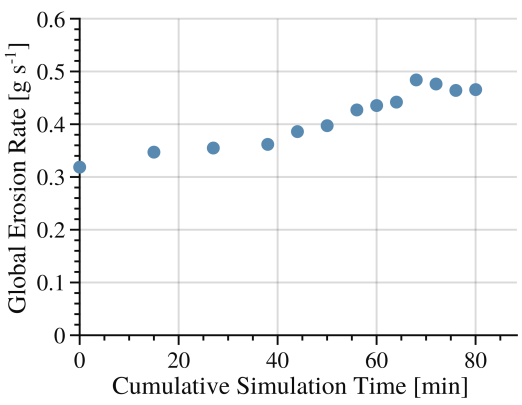

(a) Global erosion rate as a function of the cumulative simulation time.

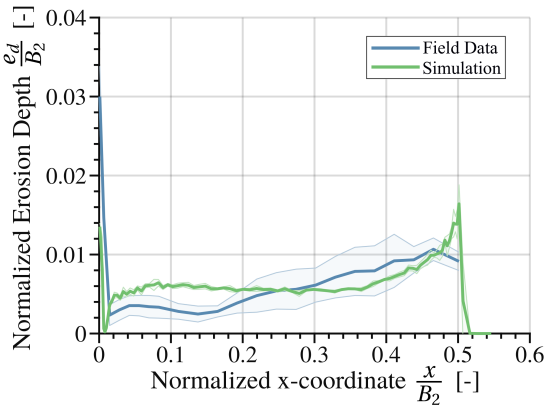

(b) Comparison of the normalized erosion depth between experimental field data [165] and simulation.

Figure 11.4 – Global erosion rate and erosion depth comparison with experimental field data.

experimental data is an average over four profiles: the two halves of the two buckets for which erosion measurements were taken. The standard deviation, represented by the shaded region, illustrates the erosion variation arising under nominally identical conditions. Taking into account the above-stated differences between the simulation and the experiment, the erosion profiles agree qualitatively to a considerable extent. Although the simulation underpredicts the erosion of the splitter, the overall shape of the erosion depth distribution is well captured: an isolated peak at the splitter and an increasing amount of erosion towards the bucket outlet.

As illustrated in Figure 11.1, the initial splitter width is $0.01B_2$, which is more than twice the typical splitter width [203]. Since a given amount of eroded mass will imply a greater erosion depth on a sharper splitter, this difference might partly explain the apparent underestimation of the simulated erosion depth at the splitter.

11.3 Case Study Discussion

The case study serves as a demonstrator of the combination of multiscale modeling and projective integration, which turns out to be instrumental in capturing the long-term effects of erosion. Indeed, without the projective integration scheme it would be impossible to simulate the erosion process for long enough to encounter the aforementioned effects of the surface transformation on the flow, even for this relatively inexpensive 2D simulation. Given $\Delta T^i = 80$ ms and the average $\Delta T^o = 400$ s, reproducing the bucket erosion case study by using only the inner multiscale integrator would have been about 5,000 times more expensive than using the projective integration scheme. This figure translates to about 15 million CPU core-hours for a problem that does not efficiently scale to more than 8 CPU cores, in which case a total of *214 years of computation* would have been required.

Note that the time frame that constitutes the long-term behavior is relative. For the case

of a copper bucket, 80 min is enough to cause significant erosion. For a steel bucket, one would expect a significantly lower erosion rate that would imply a longer physical time to reach a given level of erosion. However, given that the outer integration intervals ΔT^o are only constrained by the maximum wall particle displacement allowable between inner integrations, longer outer integration intervals would be possible thanks to the lower erosion rate. In other words, the simulation would encompass a significantly longer physical time but with a similar number of inner integration steps and therefore a comparable computational cost.

In this case study the wall particles are displaced normal to the surface; furthermore, every time the particles are displaced, the surface normals are recomputed. It should be investigated whether this approach is the most consistent; for example, the wall particles could be displaced following the average sediment impact angle.

The outer integration period was selected based on a reasonable rule of thumb; however, the effect of this parameter on the results should be thoroughly investigated. In other words, the outer integration stability and convergence behavior should be studied as a function of ΔT^o.

The main achievement of this case study is verifying that the proposed multiscale model with projective integration is capable of providing *physically sound insight* into the long-term erosion process of an industrial component. It has been shown that the model captures the effect of the surface curvature and turbulence intensity on the sediment flux against the wall, the details of the impact angle and impact velocity distributions on the surface, the effect of erosion on the average outflow angle and the reaction force felt by the bucket, and the important feedback effect whereby the erosion of the bucket generates a subsequent increase of the rate of erosion.

However, *quantitative validation* of the proposed modeling methodology on 3D Pelton turbine geometries is still required to convincingly demonstrate its capabilities. This is precisely the objective of Chapters 12 and 13.

12 Jet Impingement on a 3D Prototype-Scale Static Pelton Bucket

The main objective of the third case study is to demonstrate and validate the capabilities of the proposed multiscale model of erosion in the context of a 3D prototype-scale Pelton bucket. As a first step, the bucket is considered static in order to limit the case study complexity. The model validation on a 3D rotating prototype-scale Pelton runner is addressed in Chapter 13. Part of the contents of this chapter have been previously published in Leguizamón et al. [111].

12.1 Description of the Case Study

The case study follows the field measurements performed by Rai et al. [165] on the Toss hydro power plant, located in the state of Himachal Pradesh in the Himalayan region of India. The hydroelectric plant features two Pelton runners characterized by a pitch diameter $D_1 = 1.089$ m, $z_b = 17$ buckets and $z_0 = 4$ jets. Their design discharge and head are, respectively, $Q = 3.51\ \mathrm{m}^3 \cdot \mathrm{s}^{-1}$ and $H = 174$ m, and have a rated power of 5 MW.

Rai et al. [165] measured the erosion of one of the machines, an uncoated runner, in a study period lasting from May to October 2015. A 3D-scanner was used to measure the surface location of two buckets at the beginning and end of the study period, yielding the erosion depth distributions. During that period, a total of 12,540 tonnes of sediment passed through each runner during 3,180 hours of operation. The characterization of the sediment parameters is presented in Table 12.1. Both the median sediment size and the average concentration are relatively low. Only the content of minerals harder than steel, which amounts to 88 $\%_w$ of the sediment weight, is presented in the table; only these have any erosion potential given the importance of the hardness ratio, discussed in Section 2.2.1.

Table 12.1 – Experimental Sediment Characteristics of Case Study 3.

Size Distribution [μm]			Concentration [$\%_w$]		Composition [$\%_w$]		
d_{10}	d_{50}	d_{90}	$\overline{c_w}$	max(c_w)	Quartz	Garnet	Feldspar
6	27	134	0.0331	0.1374	65	12	11

The simulation of this case study constitutes a significant jump in complexity with respect to the previous case studies. The scale separation between the industrial-size Pelton turbine and the microscopic sediments poses several problems. First, the number of time steps is enormous given that Δt is restricted by the minimum sediment size. In spite of the dual time stepping scheme described in Section 7.3.3, the time step restriction renders the simulation very expensive. Second, the size difference between the sediments and the FVPM particles used to discretize the wall and the fluid might introduce unexpected errors. Third, the neighbor search algorithm may also be affected by this size difference. To limit the case study complexity, only one static Pelton bucket is simulated. Furthermore, the projective integration scheme demonstrated in Chapter 11 is not used since only one macroscale simulation can be afforded.

The case study domain is illustrated in Figure 12.1, whereas all the corresponding geometric parameters are reported in Table 12.2. Since it was not possible to obtain the original bucket geometry, the design reported by Perrig [160] is used, scaled to exactly match the dimensions of its experimental counterpart. Given that the simulated bucket is not rotating, the experimental relative velocity between the jet and the bucket is used for the simulated jet velocity C_1. The jet length L_j is calculated such that the amount of water injected is equivalent to the amount received by a bucked in the experiment during half a jet pass, by considering the pitch diameter D_1 and the angular separation between buckets. Similarly, the impingement angle θ is chosen to be representative of the rotating runner configuration.

The experimental sediment size distribution is fitted using a log-normal distribution from which the macroscale simulation sediment diameters are randomly drawn. A lower cutoff diameter of 5 μm is used to avoid excessively small sediments that penalize the time step.

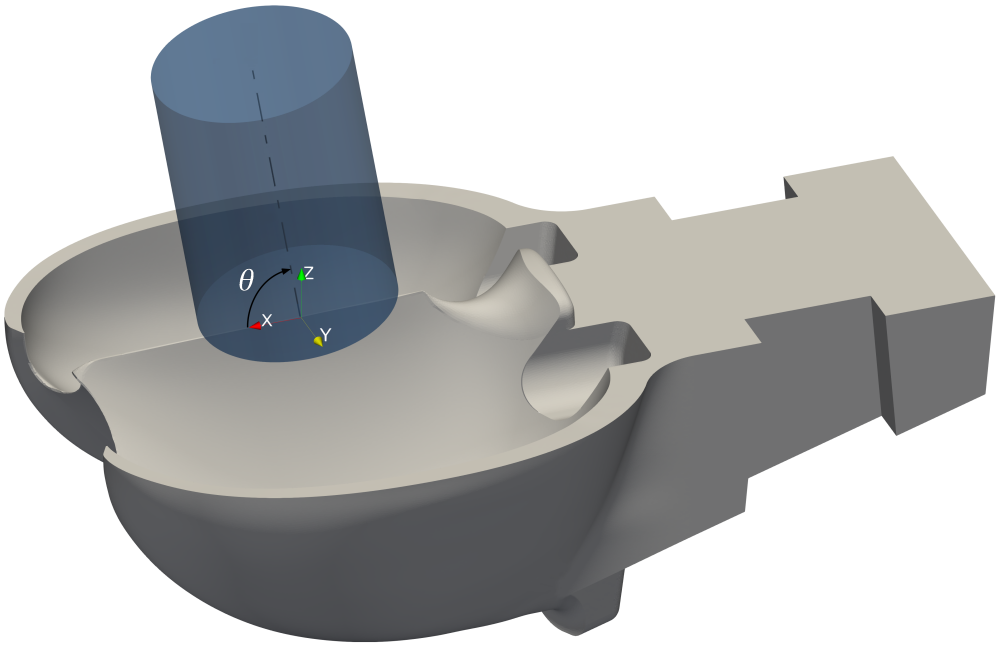

Figure 12.1 – Computational domain of case study 3.

Table 12.2 – Geometric Parameters of Case Study 3.

Jet velocity	C_1	28.5	[m · s^{-1}]
Jet diameter	D_0	0.140	[m]
Jet impingement angle	θ	80	[°]
Jet length	L_j	0.201	[m]
Bucket width	B_2	0.375	[m]
Sediment concentration	c_w	0.1174	[%$_w$]
Macroscale sediment sphericity	ϕ_d	0.76	[–]
Log-normal shape factor		1.25	[–]
Log-normal scale factor		130	[μm]
Lower cutoff diameter		5	[μm]
Upper cutoff diameter		250	[μm]

About 8 % of the experimental sediments are thus neglected given that d_{10} = 6 μm; the impact on the results is probably of the same order of magnitude and considered negligible. A sediment concentration higher than the average experimental concentration is chosen in order to inject enough sediments to have converged erosion results without increasing the jet length and overall simulation duration. A value within the experimental range reported in Table 12.1 is selected. The macroscale sediment sphericity is set to $\phi_d = 0.76$, a typical value for semi-sharp sediments.

The FVPM discretization of the macroscale domain is presented in Figure 12.2. A resolution of 50 particles across the jet diameter is used, following convergence analyses performed for case study 1, as reported in Appendix B.4, and for other Pelton turbine simulations using

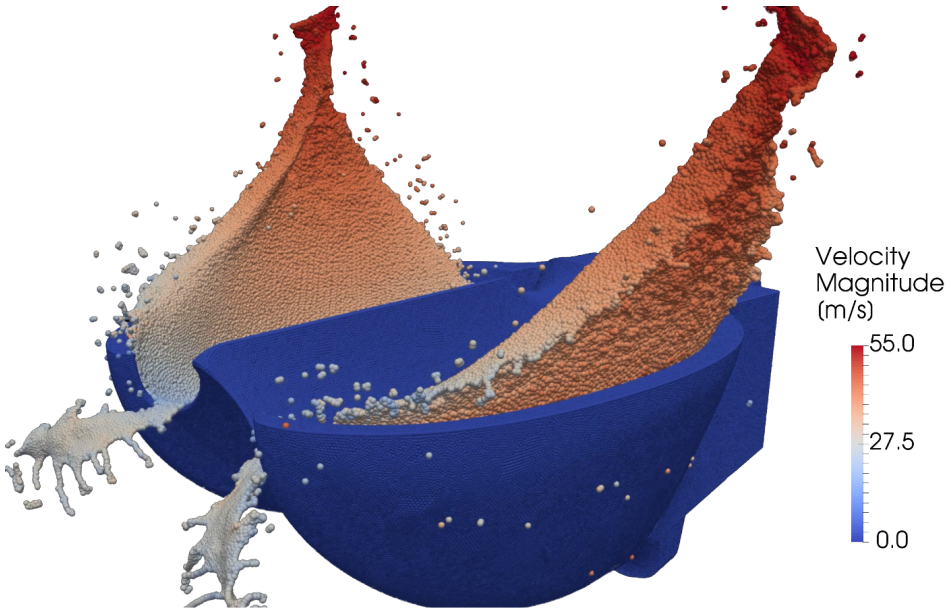

Figure 12.2 – Macroscale domain discretization, where the water is being evacuated from the Pelton bucket. The sediments are too small to be seen.

FVPM [5, 188]. In total, 1.47×10^6 FVPM particles are used, including 0.98×10^6 sediments, a quantity that proved enough to achieve converged impact condition and erosion distributions on the bucket surface. The macroscale simulation took 650 hours using 24 NVIDIA Tesla P100 GPUs for a total of 15,600 node-hours.

The microscale simulation results of sharp quartz sediments impacting MSS 13Cr-4Ni, presented in Section 10.4, are used in this case study. Each of the eight microscale simulations, which contain 85×10^3 FVPM particles, took on average 250 hours using 4 NVIDIA Tesla P100 GPUs for a total of 8,000 node-hours.

12.2 Results and Validation

The impact condition distributions are first presented, followed by the erosion distributions they entail. These results are then extrapolated in time to perform the erosion depth validation with respect to the corresponding experimental data.

12.2.1 Distributions of Impact Conditions

The average sediment impact angle and impact velocity distributions on the bucket surface are presented in Figure 12.3. These averages are computed based on the many impacts that occur at each wall particle; let them be referred to as *particle averages*, with associated *particle standard deviations*. Experimental erosion profiles are available at the pitch diameter, *i.e.* the radial position defined by $r = \frac{D_1}{2}$; given that the distributions of particle averages are somewhat noisy and that there are no particles exactly at $r = \frac{D_1}{2}$, a rectangular stripe of width δr is used to average the particle averages and standard deviations at the aforementioned radial position along the bucket width B_2; the stripe width is illustrated by the rectangle on Figure 12.3. The average along the stripe width δr of particle averages or particle standard deviations is termed a *stripe average*.

Having defined these terms, one can state with precision that the stripe averages of the particle average impact angle and impact velocity are presented in Figure 12.4; the shaded regions represent the stipe average of the impact condition particle standard deviations. On the one hand, the impact velocity is about $0.5C_1$ exactly at the splitter center due to the acceleration experienced by the sediments as a consequence of the low-velocity stagnation zone, although on the splitter edges it is as high as $0.7C_1$. Throughout most of the bucket the impact velocity is about $0.5C_1$, with increasing values towards the bucket outlet, where the maximum average impact velocity of $0.8C_1$ is reached. The standard deviation is rather uniform and equal to about $0.2C_1$. On the other hand, the average impact angle is fairly uniform throughout the bucket with a value of about 5°, except for the splitter where the impacts occur at about 25°. The deflection of the fluid by the splitter disrupts the sediment paths, preventing them from impacting at higher angle. The standard deviation is fairly uniform and equal to about 4°. A similar behavior of the impact conditions is evidenced throughout the bucket surface, as illustrated in Figure 12.3.

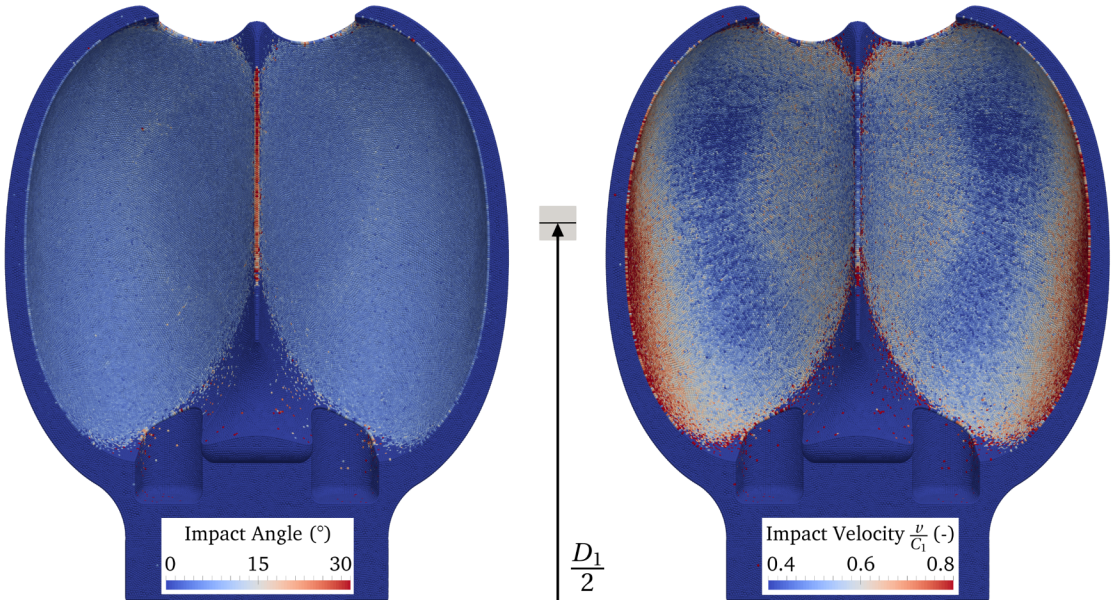

Figure 12.3 – Average impact angle and impact velocity distributions on the bucket surface. The rectangle illustrates the width of the stripe used to average around the position $r = \frac{D_1 \pm \delta r}{2}$.

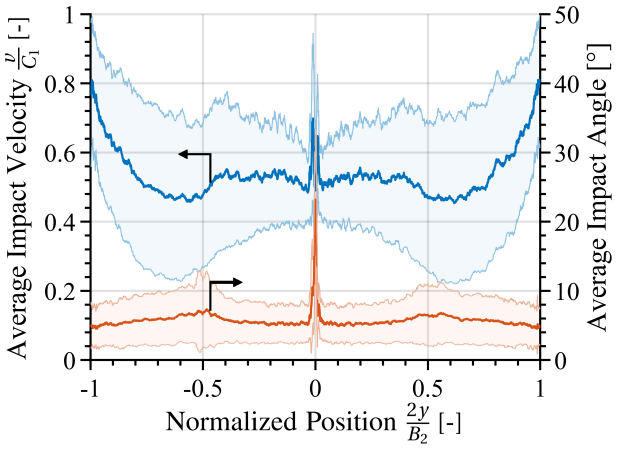

Figure 12.4 – Average impact angle and impact velocity on the stripe defined by $r = \frac{D_1 \pm \delta r}{2}$. The shaded regions represent ± one standard deviation.

12.2.2 Distribution of Erosion and Global Erosion Ratio

Figure 12.5 presents the distributions of impacted erodent mass and eroded mass on the bucket surface; corresponding distributions on the stripe defined by $r = \frac{D_1 \pm \delta r}{2}$ are shown in Figure 12.6. The distribution of erodent mass reveals that most of the sediment impacts occur on the bucket depth, a zone of high bucket curvature. These results highlight the fact that one of the driving mechanisms of sediment flux against the wall, the sediment inertia, is directly linked to the surface curvature. The second region of high sediment flux is the splitter for

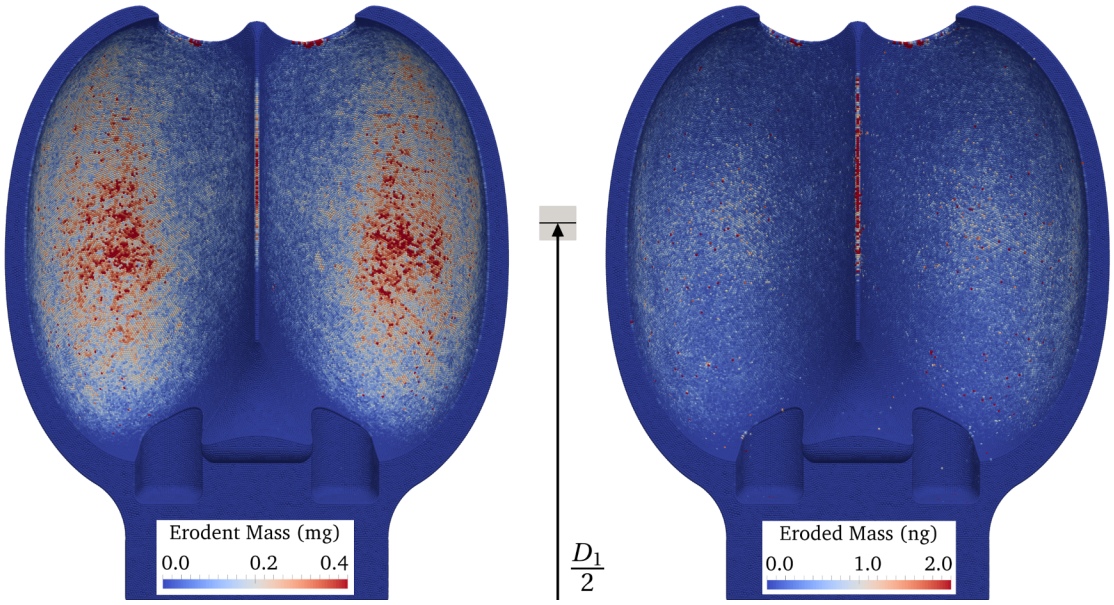

Figure 12.5 – Distributions of erodent mass and eroded mass on the bucket surface. The rectangle illustrates the width of the stripe used to average around the position $r = \frac{D_1 \pm \delta r}{2}$.

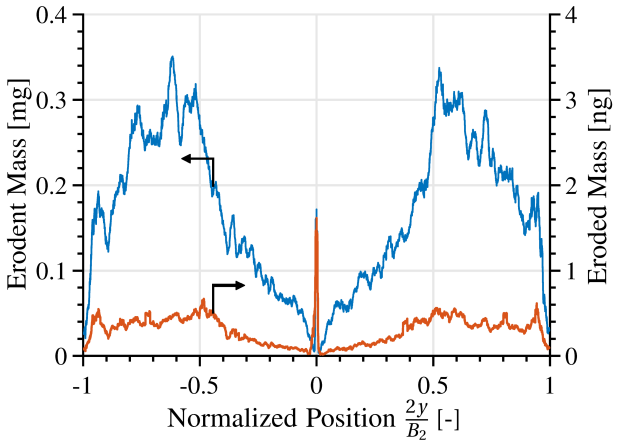

Figure 12.6 – Erodent mass and eroded mass on the stripe defined by $r = \frac{D_1 \pm \delta r}{2}$.

the same reason: most sediments cannot follow the very curved streamlines that maneuver around it. Interestingly, the sum of erodent mass impacted on the surface is equal to 2.66 times the total sediment mass injected, highlighting the fact that sediments tend to impact several times along their trajectory through the bucket.

The superposition of the aforementioned distributions, *i.e.* where the sediments tend to impact and at what angle and velocity, determines the distribution of eroded mass presented in Figures 12.5 and 12.6. The amount of eroded mass has a peak at the splitter and almost vanishes immediately downstream; it gradually increases again towards the bucket outlet.

Importantly, note that the distribution of erosion does not only depend on the sediment flux against the wall: even though the impacted erodent mass is greatest at the bucket depth, the eroded mass is greatest at the splitter because of the higher average impact angle at that location. Similarly, in spite of the relatively low erodent mass that impacted towards the bucket outlet, the amount of mass eroded is maintained due to the high average impact velocity at that location.

The global erosion ratio computed is equal to 4.04 mg $\cdot$ kg^{-1}. In other words, at these sediment and hydrodynamic conditions, the bucket loses about 4.0 kg of material for every 1,000 tonnes of sediment that are injected. According to the following validation, this multiscale simulation prediction is quite near its experimental counterpart.

12.2.3 Validation of the Erosion Depth Distribution

The projective integration approach demonstrated in Chapter 11 is too expensive to apply on this 3D case study since it involves several successive macroscale simulations. In consequence, the long-term erosion distribution is estimated by extrapolating the erosion distribution obtained from the macroscale simulation of the original bucket, not including the surface alteration induced by the process.

The simulation accounts for a total of 3.018 g of sediment injected during a physical time of about 0.03 s. This amount of sediment only represents the fraction of the experimental sediment composition with a hardness greater than that of 13Cr-4Ni, namely 88 %. For this reason, in terms comparable to the experiment, the simulation actually accounts for $\frac{3.018\text{ g}}{0.88} = 3.43$ g of sediment. As discussed in Section 12.1, Rai et al. [165] report on the erosion depth distribution after 3,180 hours of operation during which 12,540 tonnes of sediment have traversed the turbine, *i.e.* 737.647 tonnes through each one of the 17 buckets. The factor used to linearly extrapolate the simulation results to the time frame reported in the field study is therefore $f_{\text{extrap.}} = \frac{737{,}647\text{ kg}}{0.00343\text{ kg}} = 2.151 \times 10^8$.

This extrapolation factor in terms of the sediment load is a generalization of the extrapolation used in Chapter 10, which was based on the ratio of experimental to simulation time. The latter is only applicable provided both the experiment and the simulation are performed at constant and equal sediment concentrations, which is not the case here.

The erosion depth after 3,180 hours of operation is calculated as

$$e_d = f_{\text{extrap.}} \frac{m_e}{\rho A}, \tag{12.1}$$

where m_e is the amount of eroded mass accumulated on each FVPM particle, ρ is the base material density, and A is the surface area per FVPM particle. That is, the eroded mass distribution presented in Figure 12.5 can be directly linked to a distribution of erosion depth that is then extrapolated to the time frame of the experiment by means of $f_{\text{extrap.}}$.

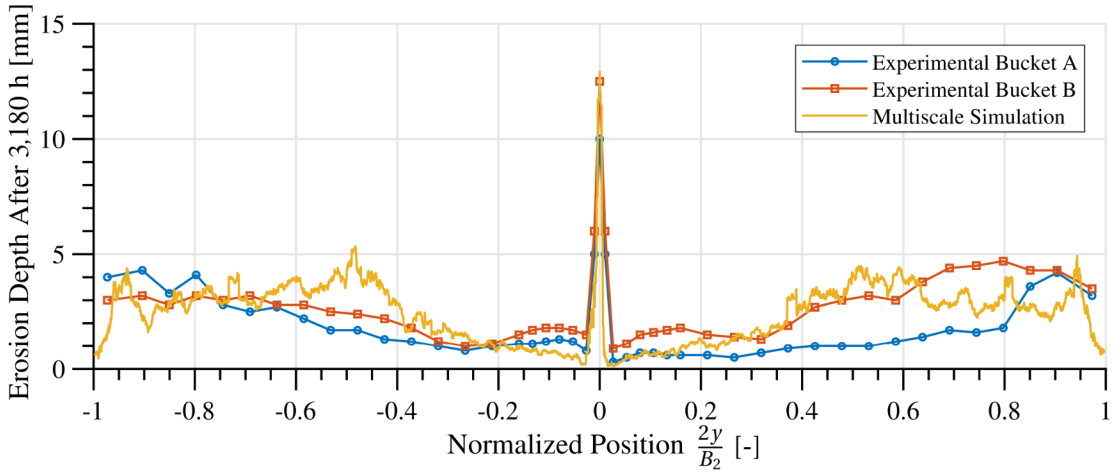

Figure 12.7 – Experimental [165] and simulated erosion depth distribution on the stripe defined by $r = \frac{D_1 \pm \delta r}{2}$ after 3,180 hours of operation.

The multiscale simulation prediction of the erosion depth distribution on the stripe defined by $r = \frac{D_1 \pm \delta r}{2}$, *i.e.* at the pitch diameter position, is presented in Figure 12.7. The corresponding measurements reported by Rai et al. [165] on two different buckets are also displayed. The remarkable agreement between the simulation and the experiment is highlighted, considering the complexity and astounding range of time and length scales involved. Notice that the differences between the two experimental buckets and even between the two sides of each bucket is of comparable magnitude to the difference between the experimental data and the simulation results. The smoothness of the erosion profiles calculated by the multiscale model is bound to increase if a higher number of sediments is injected: as with any process influenced by randomness, in this case the turbulent fluctuations, the signal-to-noise ratio would increase by having more samples.

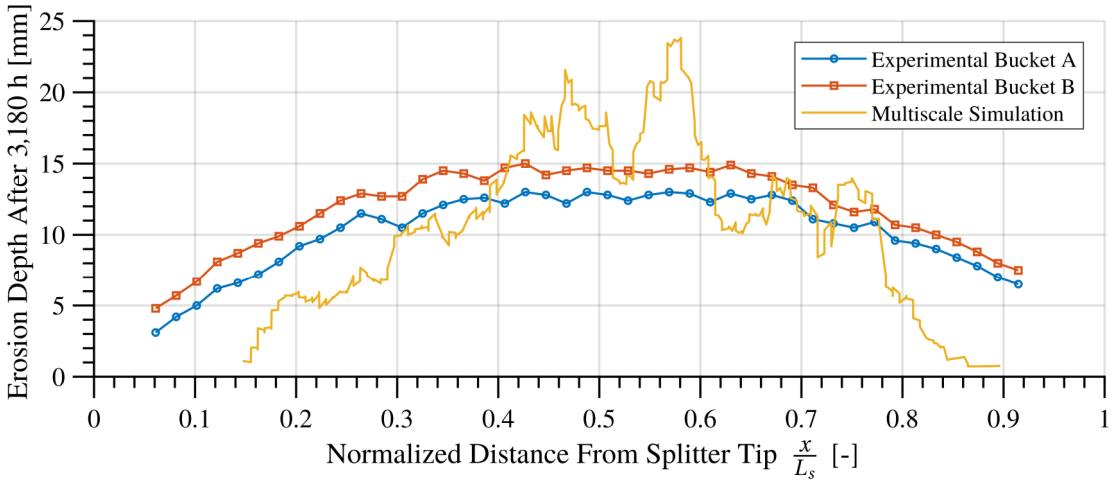

Figure 12.8 – Experimental [165] and simulated erosion depth distributions on the bucket splitter. The distance from the splitter tip x is normalized by the splitter length L_s.

The multiscale simulation prediction of the erosion depth distribution on the bucket splitter is presented in Figure 12.8 together with the corresponding measurements reported by Rai et al. [165] on two different buckets. Whereas the experimental erosion is widely distributed along the splitter, the simulated erosion is concentrated towards its center. Indeed, as the experimental bucket rotates, the jet is allowed to impinge at different locations along the splitter, whereas in the simulated static bucket it only impinges at its center. Apart from this discrepancy and the overall lack of smoothness evidenced in the simulated erosion depth, the results agree to a significant extent.

12.3 Case Study Discussion

After an initial validation of the multiscale erosion model on the case study presented in Chapter 10, jet impingement on a flat plate, the model has now been successfully validated on a significantly more complex configuration: the erosion of an industrial-scale Pelton bucket. Physically sound distributions of the sediment impact conditions on the bucket surface explain the erosion distribution results obtained, which are in quantitative agreement with the corresponding experimental data. In spite of the relatively noisy erosion distributions obtained, a consequence of the very short simulation duration and the associated low number of sediments injected, the erosion predictions agree with the experimental data both on the overall trends as well as on the magnitudes. Such quantitative agreement with the long-term erosion of an industrial-scale component is unprecedented in the literature, where oftentimes only a qualitative agreement with experiments is reached.

These results have to be framed with a caveat: several errors are probably canceling each other out to a certain extent. First, the bucket geometry used in the simulation is not identical to the experimental one. Second, the fact that a non-rotating bucket configuration was selected implies a degree of noncomparability with the experimental data. Third, the surface alteration was not taken into account in the long-term estimation of the erosion; according to the results presented in Chapter 11, the erosion rate is expected to increase somewhat as the bucket gets eroded such that an extrapolation to the time frame of the field study using the erosion rate distribution computed from the original geometry should introduce some error. Given that it is impossible to disentangle these sources of error, only the third of which is attributable to the modeling methodology, a quantification of the global error of the multiscale model is not possible for this case study.

In order to assess whether the 30 ± 5 % global error estimation derived in Chapter 10 for the case of MSS 13Cr-4Ni holds for significantly more complex problems, the discrepancies between simulation and experiment have to be reduced. With this objective, Chapter 13 deals with the erosion of a prototype-scale rotating Pelton runner for which the bucket geometry is known.

13 Jet Impingement on a 3D Prototype-Scale Rotating Pelton Runner

The fourth case study deals with the erosion of a prototype-scale rotating Pelton runner for which both the bucket geometry and the experimental erosion data are available. It is the final validation of the proposed multiscale modeling methodology and a demonstrator of its use in a problem of interest to the industry. Part of the contents of this chapter have been previously published in Leguizamón et al. [109].

13.1 Description of the Case Study

The case study follows the field measurements performed by General Electric in a Pelton hydroelectric plant located in the Himalayas. Each runner is characterized by a pitch diameter $D_1 = 2.870$ m, $z_b = 21$ buckets and $z_0 = 6$ jets. The design discharge and head are, respectively, $Q = 22.4\ \mathrm{m}^3 \cdot \mathrm{s}^{-1}$ and $H = 435$ m, for a rated power of 84 MW. Compared to the case study presented in Chapter 12, the present machine is significantly larger, implying a greater scale separation between the sediments and the bucket and consequently a higher computational cost.

A study period of 21 months comprising 12,114 hours of operation is considered. The characterization of the sediment parameters is presented in Table 13.1. The sediment size distribution is relatively wide whereas the average concentration is very low. Only the content of minerals harder than steel is presented in the table, *i.e.* the fraction of the particles with any erosion potential; they amount to 48 $\%_w$ of the sediment weight.

The macroscale simulation computational domain, illustrated in Figure 13.1a, includes one jet and three rotating buckets: the first and third buckets are necessary to ensure that the

Table 13.1 – Experimental Sediment Characteristics of Case Study 4.

Size Distribution [μm]			Concentration [$\%_w$]		Composition [$\%_w$]		
d_{10}	d_{50}	d_{90}	$\overline{c_w}$	$\max(c_w)$	Quartz	Feldspar	Garnet
13	85	272	0.00328	0.0135	41	5	2

interaction between the jet and the middle one is representative of steady-state turbine operation. As such, only the erosion results of the middle bucket are considered. The macroscale simulation lasts for 0.072 s, equivalent to an angular displacement $\theta = 130°$, enough for a complete evacuation of the water from the bucket under evaluation.

All the geometric parameters of the case study are reported in Table 13.2. The experimental sediment size distribution is fitted using a log-normal distribution from which the macroscale simulation sediment diameters are randomly drawn. A lower cutoff diameter of 8.5 μm is used to avoid excessively small sediments that penalize the time step while not contributing significantly to the erosion. The macroscale sediment sphericity is set to $\phi_d = 0.76$, a typical value for semi-sharp sediments, based on micrographs of a different hydroelectric plant also located in the Himalayas.

Since the average sediment concentration on the study period is very low, an artificially high concentration is selected in order to ensure that enough particles are injected such that converged distributions on the bucket surface are obtained with only one jet pass. The concentration is artificially increased by having five different sediment groups in the simulation: whereas sediments in one group do not interact in any way with those in other groups, they do interact with the bucket and with sediments in the same group. In this way, a high enough *numerical concentration* is obtained, but sediments behave according to the *physical concentration* of each group, selected to be equal to the average experimental concentration. Since the sediment transport model is based on one-way coupling, the fluid dynamics is unaltered by the increased concentration. Therefore this approach is equivalent to simulating five jet passes using the average physical sediment concentration, but significantly less expensive.

A snapshot of the macroscale simulation, showing the FVPM discretization used, is presented in Figure 13.2. A resolution of 45 particles across the jet diameter is used, following convergence analyses performed for case study 1, see Appendix B.4, and for other Pelton turbine simulations run using the same code [5, 188]. A total of 2.25×10^6 FVPM particles are used,

Table 13.2 – Geometric Parameters of Case Study 4.

Jet velocity	C_1	90.2	$[\mathrm{m \cdot s^{-1}}]$
Jet diameter	D_0	0.220	[m]
Turbine pitch diameter	D_1	2.870	[m]
Rotational speed	ω	31.416	$[\mathrm{rad \cdot s^{-1}}]$
Bucket width	B_2	0.786	[m]
Physical sediment concentration	c_w	0.00328	$[\%_w]$
Numerical sediment concentration	c_w^n	0.0164	$[\%_w]$
Macroscale sediment sphericity	ϕ_d	0.76	[–]
Log-normal shape factor		0.883	[–]
Log-normal scale factor		95.5	[μm]
Lower cutoff diameter		8.5	[μm]
Upper cutoff diameter		300	[μm]

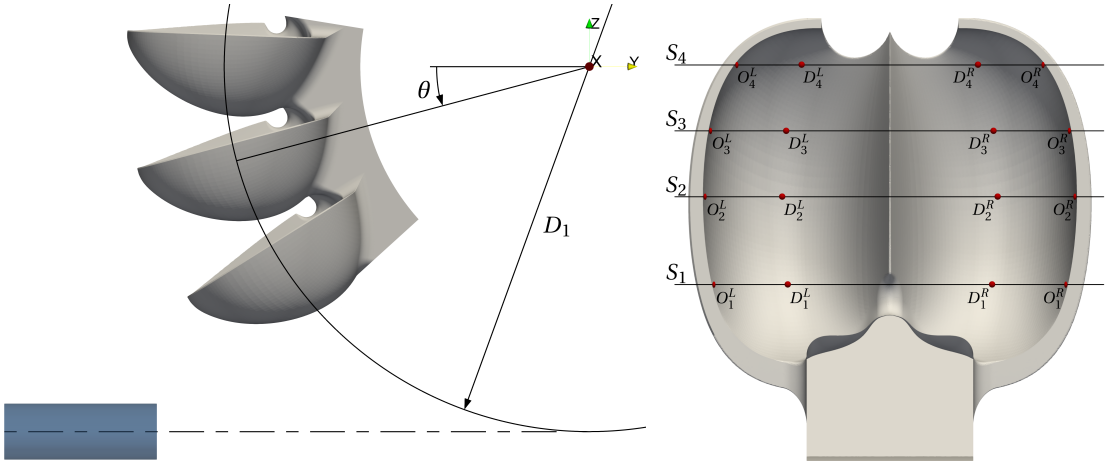

(a) (b)

Figure 13.1 – Computational domain and erosion sample points of case study 4.

including 0.93×10^6 sediments of which 0.65×10^6 are located on the portion of the jet that interacts with the middle bucket. A snapshot of the macroscale simulation showing only the sediments as they traverse the bucket is presented in Figure 13.3.

The macroscale simulation took 1,000 hours using 32 NVIDIA Tesla P100 GPUs for a total of 32,000 node-hours, *i.e.* the present case study is twice as expensive as the static bucket case study presented in Chapter 12. The projective integration scheme demonstrated in Chapter 11 is not used since only one macroscale simulation can be afforded. The long-term erosion is therefore extrapolated from the erosion rate calculated on the original bucket geometry.

Similar to case study 3, the microscale simulation results of sharp quartz sediments impacting MSS 13Cr-4Ni, presented in Section 10.4, are used here. Each of the eight microscale simulations, which contain 85×10^3 FVPM particles, took on average 250 hours using 4 NVIDIA Tesla P100 GPUs for a total of 8,000 node-hours.

The experimental erosion data provided by General Electric was measured using templates along four sections S_i, as illustrated in Figure 13.1b. These templates conform to the theoretical bucket design, *i.e.* the one used on the simulation, offset by 1.6 mm perpendicular to the surface. At the beginning of the study period, which coincides with the commissioning of completely new runners, the gap between the template and each bucket is measured. It is not exactly equal to 1.6 mm along each section and for each bucket; the discrepancy is due to manufacturing inaccuracies. The gap is measured again for each bucket at the end of the study period and compared with the first measurement, yielding an estimation of the erosion depth that takes into account the differences among buckets resulting from the runner manufacturing process.

The experimental erosion depth is available at 4 points on each of the 4 sections, as illustrated in Figure 13.1b. For each section, the sample points are located at the deepest part on each

bucket half and near both outlets; they are named $D_i^{L,R}$ and $O_i^{L,R}$, respectively. A total of 336 data points are therefore available: 16 sample points on each of the 21 buckets. Given the bucket symmetry, only half of the sample points on each bucket constitute distinct erosive conditions; therefore the data is arranged into 8 points, each of which includes 42 samples that correspond to the two halves of each one of the 21 buckets. Apart from these point values, an average erosion depth for each section is also available for each one of the buckets; these measurements are named P_i. An estimation of the total eroded mass is available as well. The experimental results presented in Section 13.2.3 use the standard deviation of the samples, 21 for P_i and 42 for D_i and O_i, to illustrate how variable the erosion depth is, even under nominally identical conditions.

The simulation erosion depth is calculated by extrapolating the results to the time period under study. As explained in Chapter 12, the extrapolation factor is computed based on the ratio of experimental to numerical sediment load. The experimental sediment load is estimated based on average values of the concentration and discharge, taking into account the uncertainties associated with these values, as discussed in Section 13.3. The average concentration is $c_w = 0.00328 \pm 0.00034\ \%_w$, whereas the amount of water that traverses the turbine during the study period is computed based on the known $12,114 \pm 1$ hours of operation and the average discharge $\overline{Q} = 18.69 \pm 1.19\ \mathrm{m}^3 \cdot \mathrm{s}^{-1}$, itself estimated from the known energy production in the study period. Note that it is not surprising that the average discharge is lower than the nominal discharge because Pelton turbines maintain their efficiency at partial load and are oftentimes operated in that regime. The experimental sediment load on the study

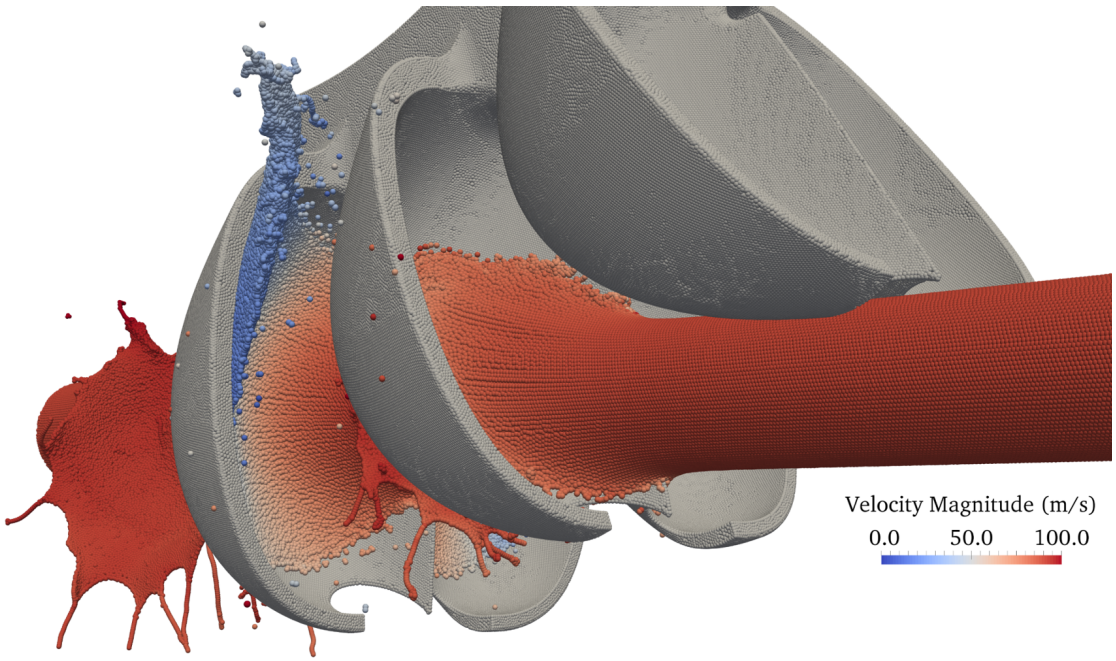

Figure 13.2 – Snapshot of the macroscale simulation discretization where only the fluid and wall FVPM particles are visible.

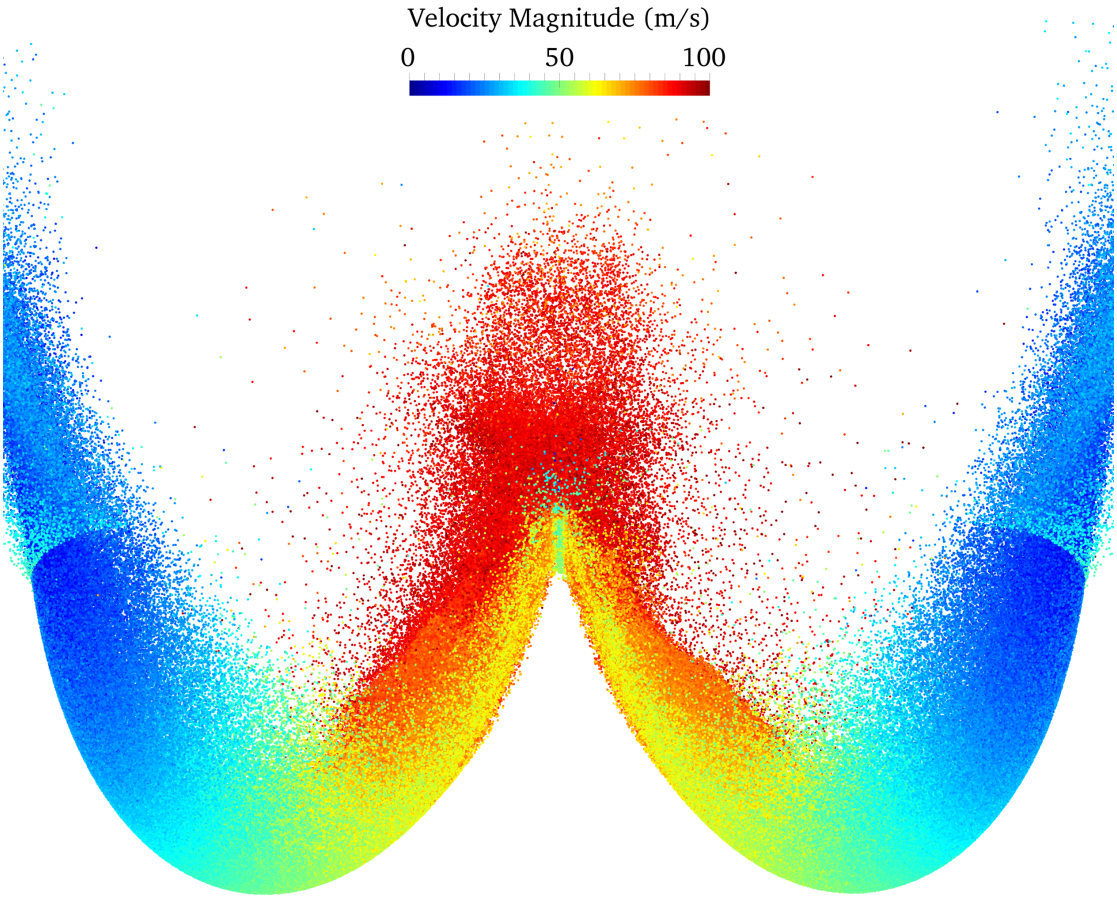

Figure 13.3 – Snapshot of the macroscale simulation, where only the sediments near the middle bucket are visible. They are all illustrated, irrespective of their actual size, by disks of $d = 1.7$ mm, *i.e.* 20 times the median sediment diameter.

period is thereby estimated to be about $26,680 \pm 5,192$ tonnes, *i.e.* $1,270 \pm 247$ tonnes per bucket. The ± 19.5 % standard deviation of the experimental sediment load is the result of uncertainty propagation calculated using the Monte Carlo method, based on the estimated standard deviations of the variables used to calculate it, as discussed in Section 13.3.

The numerical sediment load follows from the simulation setup. A total of 2.566 g of sediment are injected in the fraction of the jet that impinges on the middle bucket; this amount only represents the fraction of the experimental sediment composition with a hardness greater than that of MSS 13Cr-4Ni, namely 48 %. Therefore, in terms comparable to the experiment, the simulation actually accounts for $\frac{2.566 \text{ g}}{0.48} = 5.345$ g of sediment. The extrapolation factor is then $f_{\text{extrap.}} = \frac{1,270,000 \text{ kg}}{0.005345 \text{ kg}} = 2.377 \times 10^8$, with a standard deviation of ± 19.5 % inherited from the experimental sediment load estimation.

As in case study 3, Equation 12.1 is used to link the simulation eroded mass distribution with a distribution of erosion depth that is then extrapolated to the time frame of the experiment by means of $f_{\text{extrap.}}$.

13.2 Results and Validation

First, the distributions of average sediment impact conditions on the bucket surface and on the stripe defined by the pitch diameter are presented. These are then used, together with the distribution of erodent mass, to explain the resulting distribution of eroded mass. Finally, the extrapolated erosion depth is validated against the experimental data.

13.2.1 Distributions of Impact Conditions

The average impact angle and velocity distributions on the bucket surface are presented in Figure 13.4. As with the third case study, a rectangular stripe of width δr is used to average the particle averages and standard deviations at the radial position $r = \frac{D_1}{2}$ along the bucket width B_2. Following the terminology introduced in Section 12.2.1, one can state that the stripe averages of the particle average impact angle and impact velocity are presented in Figure 13.5; the shaded regions represent the stripe average of the impact condition particle standard deviations.

The average impact velocity is about $0.35W$ exactly at the splitter center, where W is the relative velocity between the jet and the bucket. The low velocity stagnation zone accelerates the sediments, explaining their relatively low impact velocity. The stagnation zone, characterized by high pressure, also deviates some sediments that end up impacting the splitter edges at up to $0.8W$, the highest average impact velocity found. There is a gradual reduction of the impact velocity further downstream, reaching its minimum value of about $0.3W$ on the deepest part of the bucket; it gradually increases again towards the outlet, where it reaches $0.5W$. The standard deviation is quite uniform and equal to about $0.12W$.

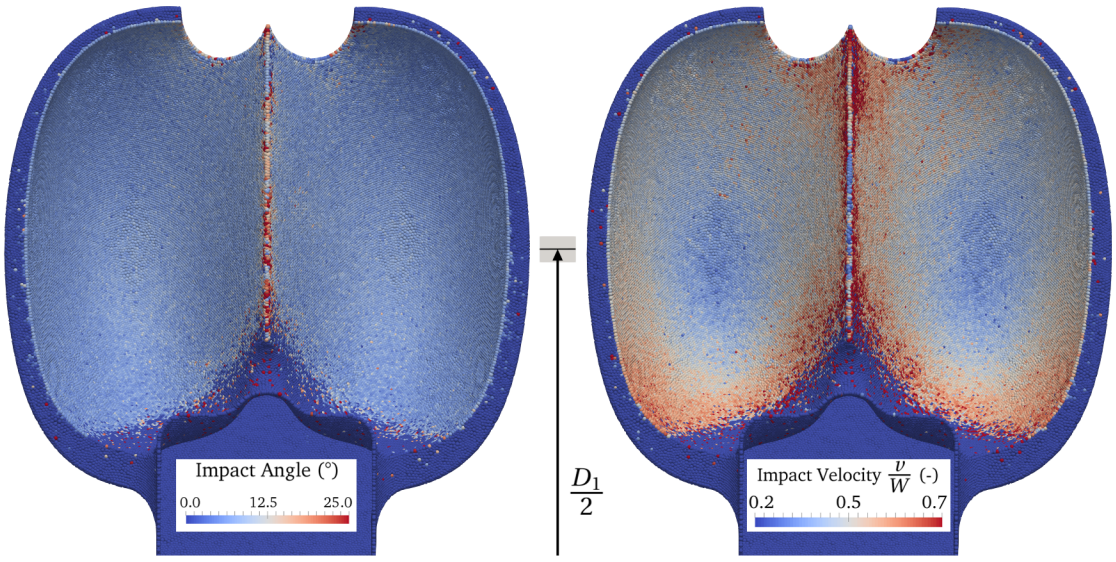

Figure 13.4 – Average impact angle and impact velocity distributions on the bucket surface. The rectangle illustrates the width of the stripe used to average around the position $r = \frac{D_1 \pm \delta r}{2}$.

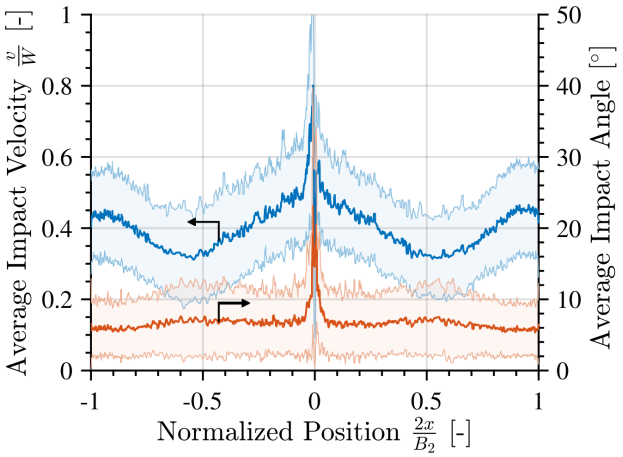

Figure 13.5 – Average impact angle and impact velocity on the stripe defined by $r = \frac{D_1 \pm \delta r}{2}$. The shaded regions represent ± one standard deviation.

The average impact angle is fairly uniform and equal to 6° throughout the bucket, except at the splitter where it reaches 25°. These low impact angle values highlight the strong influence that the fluid has on the sediment dynamics, preventing impacts at normal incidence. The standard deviation is about 5° throughout most of the bucket, although it reaches 15° at the splitter.

These distributions of impact conditions are comparable but not quite equal to the ones obtained on the third case study. It can be said that the model is sensitive enough to capture the erosion differences caused by the variation of the runner geometry, the hydrodynamic conditions and the sediment properties.

13.2.2 Distribution of Erosion and Global Erosion Ratio

The distribution of impacted erodent mass on the bucket surface is presented in Figure 13.6; the corresponding distribution on the stripe defined by $r = \frac{D_1 \pm \delta r}{2}$ is shown in Figure 13.7. The highest sediment flux occurs at the splitter and the cutout, the places where the fluid experiences the highest acceleration; the sediments therefore separate from the fluid streamlines and have a higher chance of impacting the bucket. Similarly but to a lower extent, the high-curvature bucket depth is also characterized by a high erodent flux.

The sum of erodent mass that impacted the second bucket is equal to 4.35 times the total sediment mass that interacted with it, *i.e.* sediments tend to impact several times along their trajectory through the bucket; this value is 64 % greater than the one computed on the third case study. The ratio of centrifugal to drag force experienced by a sediment, which approximates the likelihood of sediment impacts, is proportional to $\frac{d}{B_2}$, see Equation 2.6. Although for the present case study B_2 is 2.10 times higher than that of the previous case study,

the median sediment diameter is 3.15 times greater, leading to an overall increase of 50 % on the likelihood of sediment impacts according to the dimensional analysis described in Equation 2.6. This trend is confirmed by the aforementioned simulation results.

The distribution of eroded mass on the bucket surface, also presented in Figures 13.6 and 13.7, illustrates the interaction among the distributions of impact conditions and sediment flux. It is maximum at the splitter tip and at the cutout, followed by the bucket depth, in approximate correspondence with the sediment flux distribution. However, the eroded mass on the bucket depth is not as high as the erodent mass would indicate due to the relatively low impact velocity in that zone; on the contrary, it increases slightly towards the bucket outlet, unlike the sediment flux, due to a local increase of the impact velocity. The eroded mass on the splitter is higher than the erodent mass would suggest due to the relatively high average impact angle on that location.

The global erosion ratio computed is equal to 13.02 mg $\cdot$ kg^{-1}, 3.22 times greater than the one computed on the third case study. This difference is mostly explained by the greater relative velocity between the jet and the bucket, which is 1.58 times higher, and correspondingly higher average impact velocities; since the erosion ratio typically depends on a power 2-3 of the impact velocity, a given increase in velocity implies a more significant increase in erosion. In short, at these sediment and hydrodynamic conditions, the bucket loses about 13 kg of material for every 1,000 tonnes of sediment that traverse it. As demonstrated in the following section, this prediction of the multiscale model is in good agreement with the experimental data available.

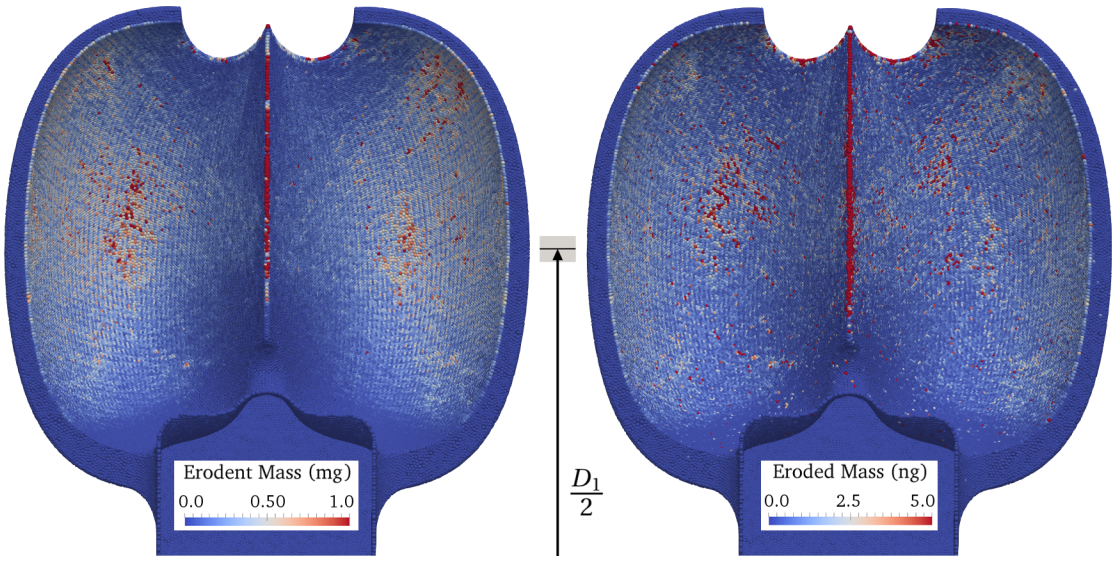

Figure 13.6 – Distributions of erodent mass and eroded mass on the bucket surface. The rectangle illustrates the width of the stripe used to average around the position $r = \frac{D_1 \pm \delta r}{2}$.

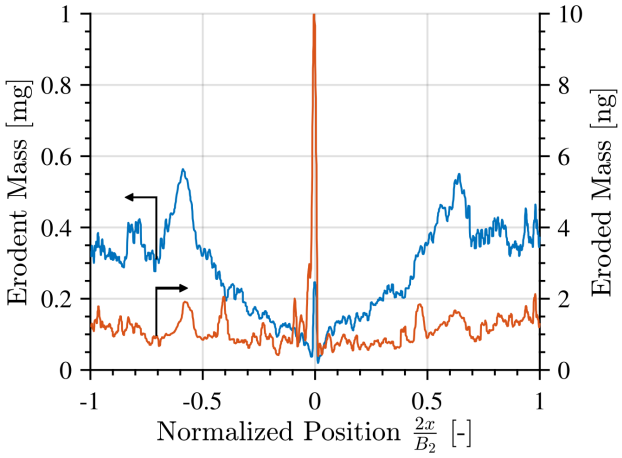

Figure 13.7 – Erodent mass and eroded mass on the stripe defined by $r = \frac{D_1 \pm \delta r}{2}$.

13.2.3 Validation of the Erosion Depth Distribution

The erosion depth predicted by the multiscale simulation at eight points on the bucket, normalized by the corresponding average experimental measurements, is presented in Figure 13.8. The simulation results are calculated using a weighted average over the FVPM particles around each sample point in order to mitigate the noise inherent to the results. A Gaussian kernel is used as weighting function; it is defined by $\phi = \exp\left[-3.0\left(\frac{\|\boldsymbol{x}-\boldsymbol{x}_0\|}{r_g}\right)^2\right]$, where $\boldsymbol{x}$ is the particle position, $\boldsymbol{x}_0$ is the sample point position, and the Gaussian radius is set to $r_g = 0.05\ B_2$. The kernel is truncated, *i.e.* $\phi = 0$ if $\|\boldsymbol{x} - \boldsymbol{x}_0\| > r_g$. The same procedure is used to calculate the standard deviation.

As seen in Figure 13.8, the spread of both the simulation and the experimental erosion depth results is significant. In the case of the simulation, the spread is a measure of the numerical result variability around each sample point. In the case of the experiment, the spread is a measure of the results variability among the 42 samples that constitute each point. Whereas in the former case the noise is not surprising given the short simulation duration and therefore the relatively low number of sediment impacts, in the latter case the erosion variability under nominally identical experimental conditions is indeed notable.

There is a considerable overlap between the simulation predictions and the corresponding experimental results, although the difference of mean values is significant. The erosion depth is considerably underpredicted on the bucket depth, especially at points D_1 and D_4. It is difficult to understand the root cause of these differences because the results depend on too many parameters, submodels and processes. The average relative error of these pointwise comparisons is 35 %, somewhat higher than on previous test cases. However, consider that previously only integral quantities have been assessed; the error of pointwise comparisons is expected to be higher because errors do not cancel out, as is the case with integral comparisons.

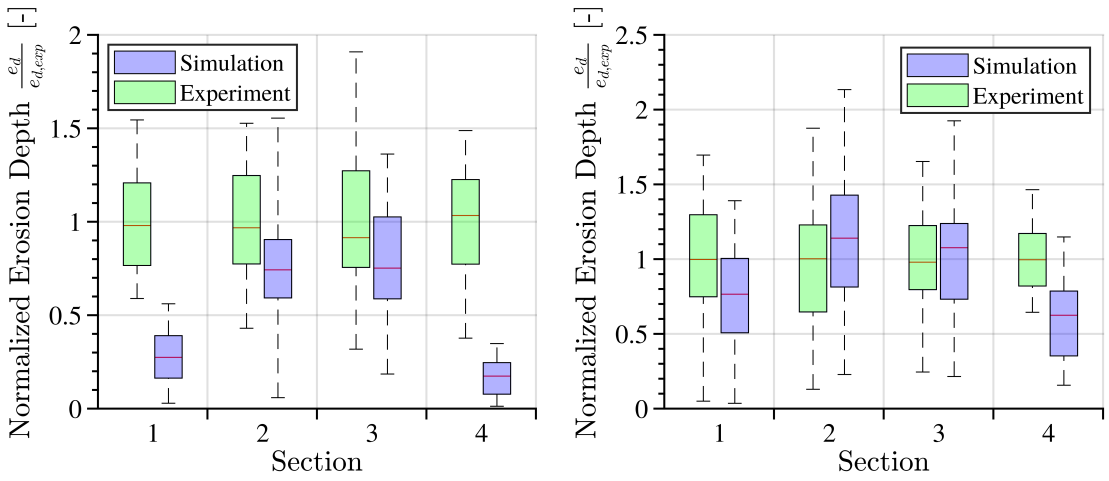

(a) Bucket depth points D_i.

(b) Bucket outlet points O_i.

Figure 13.8 – Erosion depth at eight points on the bucket, normalized by the corresponding average experimental measurements. The red lines, lower and upper box bounds, and whiskers represent the median, 25th and 75th percentiles, and extreme values, respectively.

The average erosion depth on each of the four sections S_i is presented in Figure 13.9, where both the experimental measurements and the multiscale simulation results are normalized by the corresponding average experimental values. Here again a significant spread of the results is evidenced, as well as an important overlap of experimental and numerical results. The average relative error, calculated using the mean values, is only 14.3 %, lower than the

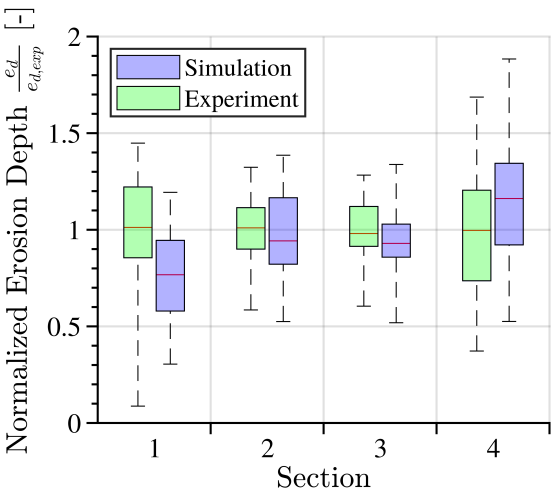

Figure 13.9 – Average erosion depth along four profiles on the bucket, normalized by the corresponding average experimental measurements. See the box plot description in the caption of Figure 13.8.

standard deviation of the experimental results. As previously mentioned, this comparison is forgiving thanks to the cancellation of errors that occurs in the averaging procedure.

An additional metric is used for validation: the total eroded mass. The results are compiled in Table 13.3. The relative error is 3.9 %; given that this metric is an average over the whole bucket surface, the error is expected to be lower than in the previous comparisons because there is ample opportunity for the under- and overpredictions to cancel each other out.

Table 13.3 – Eroded Mass During the Study Period for Case Study 4.

		Per bucket	Total
Field study	[kg]	17.21	361.4
Multiscale simulation	[kg]	16.54	347.3
Relative error	[%]	3.9	

13.3 Case Study Discussion

This final case study has served as a demonstrator of the capabilities of the multiscale model of erosion. It has been shown to provide insight into the erosion of a prototype-scale Pelton runner by means of physically sound distributions of sediment flux and impact conditions that help to understand the erosion distribution obtained. The simulation predictions of the erosion depth distribution have been successfully validated with the field data available. The relative errors obtained in this case study are comparable to the ones found on the previous case studies, in spite of the significantly more challenging problem.

There is a series of uncertainties in the experimental study that propagates into the simulation setup and hinders a precise estimation of the modeling error. First and foremost, the total sediment load: it is estimated based on average values of the concentration and discharge, themselves uncertain, instead of their time histories. The average concentration is calculated from monthly average concentrations available for the first year of operation; since the study period lasts for almost two years, it had to be assumed that the monthly concentrations available are good approximations for the second year as well. The standard deviation of the average concentration is estimated to be ±7 % based on the interannual variability of the sediment concentration of the Jialing River [36] in the period 1992-2006; no data of similar scope was found for a river closer to the investigated power plant. The average discharge is computed based on the total energy production of the plant, which features four Pelton turbines. Three presumptions are made: the turbine efficiency, equal repartition of energy production among the turbines, and constant available head. The standard deviations of these variables are estimated based on the known efficiency behavior of Pelton turbines as a function of discharge, the standard deviation of the energy production for successive years, and the expectedly small head variation on Pelton turbine installations, respectively. The error propagation from these uncertain variables to the estimation of the average discharge is done with the Monte Carlo method, yielding a standard deviation of ±6.4 %. The same method is

used to propagate the uncertainty of the average concentration and discharge to the resulting estimation of the experimental sediment load, resulting in a standard deviation of ±9.5 %. Finally, note that even if exact values of the average concentration and discharge were known, neglecting the time histories introduces some error. For example, if a lower than average discharge was exploited on the months of high sediment concentration, the total sediment load calculation based on the averages would be overestimated.

A second uncertainty relates to the macroscale sediment sphericity $\phi_d = 0.76$ that is estimated based on micrographs of a different hydroelectric plant, albeit located on the same mountain range, due to the unavailability of a visual characterization of the actual sediments. As presented in Chapter 10, variations in ϕ_d can significantly affect the turbulent sediment transport process and resulting erosion distribution. However, it is difficult to know whether the estimated value of ϕ_d is a good approximation. All things considered, it is presumed that $\phi_d = 0.76 \pm 0.4$, which according to the sensitivity analysis presented in Section 10.4.2 would introduce an uncertainty in the simulation results characterized by a standard deviation of about ±20 %.

A third uncertainty is due to the sediment composition. It is assumed that it is independent of the sediment size, such that after neglecting the sediments with no erosion potential, as done during the simulation to avoid the unnecessary tracking of irrelevant sediments, the size distribution is preserved. This assumption is incorrect; for example, when considering only the sediments with $d < 90$ μm the fraction of hard particles increases to 65 % from the original 48 % obtained when considering all particle sizes. For this reason, the sediment size distribution used in the simulation is somewhat approximative. Yet again, it is difficult to assess the degree to which this simplification affects the validation results. However, based on the second test case presented in Chapter 10 in which the erosion ratio is estimated for four different sediment sizes, it is presumed that the variation of the simulation results due to the uncertainty associated with the sediment size distribution would be about ±10 %.

These three main uncertainties between the experiment and the simulation render a precise quantification of the modeling error hopeless. However, approximate error bounds can be estimated by considering the uncertainty of the comparison between simulation and experiment. The Monte Carlo method of error propagation is used to combine the three aforementioned uncertainties, yielding a standard deviation of ±24 %.

Taking the average over the 13 comparisons performed in Section 13.2.3, namely the erosion depth at 8 points, its average value on 4 sections and the total eroded mass, the average relative difference between the simulation and experiment results is equal to 26.5 %. Taking into account the comparison uncertainty previously described, the multiscale modeling error for this case study is estimated to be 26.5 ± 24 %.

As presented in Chapter 11, the erosion rate is expected to increase as the bucket surface is transformed. An increase of 45 % was evidenced at the end of that simulation; by then the bucket had suffered considerable erosion. If one factors in this effect into the extrapolation

factor used in the present case study, *i.e.* by multiplying it by $1 + \frac{0.45}{2}$ in order to have an estimation of the erosion depth at the end of the study period that considers the increase of the erosion rate as the process advances, the aforementioned estimation of the multiscale modeling error would instead be equal to 28 ± 24 %. Although multiplying the extrapolation factor by $1 + \frac{0.45}{2}$ induces an overall increase of the erosion depth, the fact that at some points the erosion is underpredicted whereas at other points it is overpredicted explains the very slight increase of the average relative error induced by the correction. Based on these considerations, the global multiscale model error for this case study is estimated to be 28 ± 24 %.

The estimation of the global model error derived in case study 1 for the case of stainless steel 13Cr-4Ni was 30 ± 5 %. Although the uncertainties inherent to the present case study do not allow an estimation of comparable precision, the expected value is about the same. It is remarkable that the proposed multiscale model performs as well on a short laboratory-scale experiment as it does on a very long prototype-scale unsteady problem. This behavior is explained by the appropriate integration of all the physical models required to approximate the average erosion response of the system. The multiscale model accuracy and transferability and its overall performance under realistic erosive conditions on a problem of interest to the industry has been demonstrated.

Part IV
Conclusions and Perspectives

We can only see a short distance ahead, but we can see plenty there that needs to be done.

—*Alan Turing*

14 Conclusions

Hydropower is a key player in many greenhouse gas emission mitigation scenarios thanks to its low lifecycle emission intensity and its capacity to integrate intermittent renewables into the electrical grid. One of the problems commonly faced by hydropower plants is the erosion of the turbines caused by the sediment-laden water, which has undesirable consequences such as efficiency degradation and outage for repairs that ultimately represent a loss of revenue and flexibility. The technical capacity to predict the erosion process is essential to optimize the runner designs and the hydroelectric plant operation strategies, but neither laboratory experiments nor traditional numerical simulations are capable of delivering quantitative predictions.

The challenging aspect of simulating the erosion process is its inherently multiscale character. Traditional numerical simulations approach the problem by neglecting the details of the sediment impacts altogether, settling instead for the use of erosion correlations to close the system; however, these correlations dramatically reduce the model accuracy and transferability. A novel multiscale numerical model of erosion, tailored to the multiscale nature of the phenomenon, is presented in this thesis. A microscale model is used to explicitly simulate the sediment impacts, thus resulting in a significant increase in accuracy with respect to the use of erosion correlations. A macroscale model is used to describe the turbulent sediment transport and erosion accumulation on the domain of interest. By uncoupling the problem into two independent submodels, the problematic scale separation is bypassed. A sequential multiscale coupling approach is used to reproduce the original coupled problem, whereas a projective integration scheme can be used to extend the temporal scope of the model to include the long-term surface alteration and its effect on the hydrodynamics.

14.1 Concerning the Multiscale Model Validation

Four case studies are used to assess, verify and validate the proposed multiscale model. The main conclusions and observations are drawn hereafter.

The first case study, presented in Chapter 10, deals with the erosion of a flat plate by impinging slurry jets of a few millimeters in diameter; three independent test cases are considered. In the first test case the multiscale model is validated: it is shown to be able to predict the erosion depth distribution as well as the global erosion ratio for several jet impingement angles within a mean relative error of 18 % for the case of copper. The second test case verifies the physical correctness of the two mechanisms responsible for the sediment impacts, namely the acceleration associated with the fluid streamline curvature and the turbulent fluctuations, in regards to variations of the sediment size. The importance of having an accurate description of the particle size distribution is highlighted. The third test case is used to study the sensitivity of the erosion predictions to uncertainties in the microscale material model parameters and the macroscale sediment sphericity. The variation of the erosion results is shown to be of comparable magnitude to the variability of the experimental results, provided a set of sediment micrographs is used to estimate the sphericity parameter ϕ_d. With respect to the experimental data for the erosion ratio, an average relative error of 30 ± 5 % is found for the case of martensitic stainless steel 13Cr-4Ni, higher than that for copper because of the uncertainty in the microscale material model parameters.

The global multiscale model error is estimated to be about 25 ± 10 % based on the results of the first case study. The convergence analyses of the microscale and macroscale simulations, presented in Appendices B.2 and B.4, respectively, suggest that the discretization error is about 5 %, pointing to the fact that the global error is mostly explained by modeling error.

The second case study, presented in Chapter 11, is used to demonstrate the use of the multiscale model together with projective integration to investigate the long-term effects of erosion of a 2D bucket of industrial size. The model correctly predicts the expected outflow angle increase and subsequent reduction of the reaction force as the surface is transformed by the erosion process. It is shown that without the projective integration scheme it would be impossible to simulate the process for long enough to encounter the aforementioned effects of the surface transformation on the hydrodynamics. It is also shown that the model correctly captures the effect of the surface curvature and turbulence intensity on the sediment flux against the wall, and predicts physically sound distributions of impact conditions that explain the obtained erosion distribution.

The second case study evidences an important feedback effect whereby the erosion of the bucket generates a subsequent increase of the rate of erosion. The erosion rate appears to stabilize at a level that is about 45 % higher than the one calculated using the original bucket geometry.

The third case study, presented in Chapter 12, deals with the erosion of a static prototype-scale Pelton bucket impinged by a sediment-laden jet, a significantly more challenging problem compared to the previous case studies due to the greater scale separation between the dynamics of the fluid and the sediments. Yet again, physically sound distributions of the sediment impact conditions on the bucket surface explain the erosion distribution obtained, which is in

quantitative agreement with the available experimental data. Although these results serve as a second validation of the multiscale model, they have to be framed with a caveat: a series of discrepancies between the field study and the simulation setup rule out a proper estimation of the global error of the multiscale model. The discrepancies include the non-identicality of the bucket geometries, the non-rotating bucket configuration used in the simulation, and the fact that the erosion depth distribution is calculated from the erosion rate distribution computed on the uneroded bucket geometry, *i.e.* neglecting the aforementioned feedback effect.

The fourth case study, presented in Chapter 13, investigates the erosion of a different prototype-scale Pelton runner impinged by a sediment-laden jet. Contrary to the third case study, the simulation configuration closely follows the field study, *i.e.* the runner geometry is known and a rotating configuration is adopted. The sediment impact conditions are very similar to the ones obtained in the non-rotating configuration and explain the resulting erosion distribution. A quantitative validation including the erosion depth at eight points on the bucket, the average erosion depth along four sections on the bucket, and the total eroded mass is done with respect to experimental data on the corresponding runner; this third validation yields satisfactory results and is an illustration of the capacity of the multiscale model to deliver quantitative predictions of the erosion of industrial-scale hydraulic turbines under realistic erosive conditions.

However, a series of uncertainties in the experimental study that propagates into the simulation setup hinders a precise estimation of the global modeling error once again. The uncertainties are related to the total sediment load on the study period, the macroscale model sediment sphericity ϕ_d, and the sediment composition and size distribution. A detailed analysis of the sources of uncertainty and the propagation of their expected effect on the erosion predictions yields an estimation of the standard deviation of the simulations results of ± 24 %. This uncertainty regarding the comparison between the experimental and simulation results propagates to the calculation of the global model error, thus estimated to be 28 ± 24 % based on the validation results. This figure is very similar to the one estimated from the first case study, highlighting that the multiscale model performs as well on a short laboratory-scale experiment as it does on a very long prototype-scale unsteady problem. The model accuracy and transferability and its overall performance under realistic erosive conditions on a problem of interest to the industry is thus demonstrated.

14.2 Concerning the Contributions of the Thesis

On the one hand, the validation results for the flat plate erosion case study, for which the relative error is about 25 ± 10 %, are a significant improvement over the state-of-the-art erosion simulations based on correlations; as reviewed in Section 3.1, an average error of 180 % is expected for that case. The gain in accuracy is a consequence of including detailed models that capture the physical phenomena involved in the microscopic impacts, namely the high strain rate material response and the sediment shape and elasticity. Such a level of detail would

normally be intractable for a macroscopic problem, but the multiscale approach renders it possible.

On the other hand, the simulation results presented for the third and fourth case studies, namely quantitative predictions of the erosion of prototype-scale runners, are unprecedented in the literature. Even if the average error is somewhat greater than for the first case study, for the first time it becomes possible to investigate this very challenging problem of interest to the industry. Not only is the model able to predict the erosion distribution, it brings insight about the underlying sediment flux and impact condition distributions that are responsible for it.

In conclusion, it can be said that the proposed multiscale model is a bold step towards the buildup of the technical capacity to predict the erosion of hydraulic machines, itself an instrumental asset for the design of optimum turbines in the context of sediment-laden hydraulic conditions of ever-increasing importance.

15 Perspectives

The objective of this chapter is to provide some perspective in regard to possible investigation directions, model improvements, limitations and loose ends.

15.1 On Methodological Improvements

In the microscale model it is assumed that the sediment orientation probability at the moment of impact is uniform, *i.e.* there is no preferential orientation. However, it is possible that the interaction between the fluid and the sediment orients the latter according to a drag minimization principle, for example, exposing the sharpest edges towards the solid. It should be investigated whether sediments have a preferential orientation upon impact and modify the microscale model accordingly in order for its results to be representative of the slurry erosion phenomenon.

The fluid is not considered in the microscale model on the grounds that its effect at the instant of impact is unimportant. This assumption introduces errors that might not be negligible, especially for small sediments impacting at low velocity, as illustrated in Figure 5.7. A detailed assessment of the effect of this assumption should be pursued and, if justified, the microscale model should be modified in order to account for the fluid. One approach would be to implement a damping force, function of the Stokes number, affecting the microscale sediments only when they are in contact with the solid.

The projective integration scheme, demonstrated in Chapter 11 on a 2D bucket geometry, should be thoroughly studied. The most immediate task should be to investigate its convergence and stability behavior as a function of the outer integration period ΔT^o. The effect of this parameter on the results should be studied in detail and guidelines to assist in selecting a suitable value should be drawn.

As discussed in Chapters 12 and 13, each macroscale simulation of an industrial-sized machine is very expensive; therefore the ordinary use of projective integration is not practical for those cases since it involves multiple instances of the macroscale model. However, it would be

beneficial to run at least one such simulation in order to estimate the relative increase of the erosion rate that is caused by the alteration of the runner surface. These results would allow to partially correct subsequent simulations where only the macroscale simulation of the uneroded geometry is feasible. In other words, by characterizing the erosion rate as a function of the runner surface state, a better extrapolation of the results of subsequent simulations from the erosion rate calculated on the original geometries would be possible.

15.2 On Modeling Improvements

In spite of the overall good results achieved, the physical models used within the multiscale model are surprisingly simple, almost primitive; there is infinitely more detail to be captured within both the microscale and the macroscale.

It is highly likely that most of the modeling error is introduced within the microscale description. On the one hand, the constitutive and damage modeling of the solid could be improved. For example, several corrections to the Johnson-Cook model exist, such as a second strain rate dependent term [30], a modification of the failure strain dependence on the stress triaxiality [13] and modifications to the damage criterion [21]. It is possible that these corrections could improve the model accuracy, but the price to pay would be a greater number of material model parameters that need characterization. A different approach would be to use molecular dynamics instead of a continuum description of the material; although by far too expensive for the time being, future researchers might be able to leverage quantum computing to benefit from such a first-principles approach. Molecular dynamics simulations of the material, including all the details of the microstructure, would bypass the barely justifiable assumptions of homogeneity and isotropy, and obviate the need for continuum constitutive and damage models and all of the associated parameters that need characterization.

On the other hand, the friction model employed is quite simple; it could be improved by including a force component proportional to the slip velocity, the pre-sliding effect, the lubricant effect, and the hysteresis behavior [124]. Yet again, a possible accuracy gain could be achieved at the expense of additional model parameters.

Independent of whether the material model is improved, a complete characterization of martensitic stainless steel 13Cr-4Ni, unlike the partial one presented in Chapter 9, is recommended in order to improve the model accuracy and reduce the uncertainty of the results. The characterization should be performed at as high a strain rate as possible, to limit the degree of extrapolation inherent to the simulation of sediment impacts.

The Johnson-Cook damage model is applicable to ductile metals because it assumes that failure occurs as a consequence of the accumulation of plastic deformation. An important research direction would be to include a second material model tailored to brittle materials such as the hard coatings occasionally used in hydraulic machines; in that case, the failure mechanism is fatigue by repeated elastic deformation without plastic strain. Provided an

appropriate material model is implemented, only minor modifications to the multiscale model would be needed.

Similarly, the sediment material model should be improved to account for their brittle fracture during impact, which may have an effect on the microscale model calculation of the erosion ratio and the restitution coefficients [68, 70, 187]. According to the literature, the most appropriate choice would be the Johnson-Holmquist constitutive and damage models [69, 196].

Several modeling improvements and investigation topics are also available in the macroscale model. First, the effects of the surface roughness, which tends to increase as a consequence of erosion, have been neglected thus far, but they might be important. On the one hand, the surface roughness affects the boundary layer development and thus the turbulence production; the higher turbulence intensity induced would heighten the sediment flux against the wall and therefore increase the erosion. On the other hand, when the roughness scale is comparable to the sediment diameter it has to be taken into account in the contact calculation. The former effect can be introduced by a simple modification of the wall function parameter E_k [57, 162, 173], whereas the latter effect can be captured through a suitable modification of the contact detection algorithm.

Second, the use of more refined near-wall modeling should be assessed. The standard wall function used assumes equilibrium of turbulence production and dissipation, a simplification that is certainly very crude for the violent unsteady flows found in hydraulic machinery. A non-equilibrium wall function would be the first candidate for evaluation, although circumventing the use of wall functions altogether, by using a low Reynolds number turbulence formulation, is another possibility.

Third, the effect of different turbulence models on the erosion results has not been verified in this thesis, and it should. Even though according to the literature the standard k-ϵ model gives the best results for sediment transport simulations, as reviewed in Section 6.6, it is worth testing whether more sophisticated models might be advantageous in the specific field of hydraulic turbomachines. Candidates for evaluation are the k-ω SST model [133], its scale-adaptive variant [42, 134], and even turbulence models that bypass the isotropy assumption [52] that is certainly incorrect near the wall, affecting the sediment dynamics prior to impact. Another possible improvement is the implementation of turbulence attenuation or augmentation by the sediments, *i.e.* a two-way coupling scheme, for example using the approach proposed by Mandø et al. [129].

15.3 On Discretization Improvements

The multiscale model of erosion and all of the underlying submodels are independent of the discretization scheme used to solve them. It is worth evaluating whether the finite volume particle method, described in Chapter 7, is the most suitable scheme for the simulation of the model in the case of hydraulic turbines. Its greatest disadvantages are the very high

computational cost and the formally first-order accuracy.

The finite element method would probably be the best alternative for the discretization of the microscale model. The high-order accuracy FEM is capable of would be very convenient to describe the sharp gradients that occur on the solid whenever it is impacted by a sediment. The high-order accuracy also implies a significantly lower computational cost for a given discretization error, compared to FVPM.

A mesh-based finite volume method would likewise be a good alternative for the discretization of the macroscale model. Although the mesh generation is time-consuming, the advantages of mesh refinement near the turbine surfaces, high-order accuracy and the significantly lower computational cost would most likely result in an overall gain in solution accuracy and a reduction of the time-to-solution.

15.4 On Further Model Validation and Identification of Limitations

Irrespective of whether any of the above-stated improvements is implemented, further model validation is recommended for the rotating prototype-scale Pelton runner case study. A considerable effort should be made to gather detailed descriptions of the experimental conditions in order to minimize the comparison uncertainty with the simulation results.

As discussed in Chapter 13, it is fundamental to have a good approximation of the total sediment load the turbine is subject to during the study period. The average sediment concentration and total discharge might not be enough; concentration and discharge time histories would be best. Furthermore, appropriate characterization of the sediments, both their size distribution and shape, should be obtained. Finally, it would be advantageous to have erosion depth measurements on at least 40 points on each bucket to reconstruct the erosion distribution on the internal surface. Only then will a reliable estimation of the global multiscale model error for this industrial-scale problem be available.

Apart from such a global validation on a complex problem, it is worth investigating each of the submodels in some detail in order to validate the multiscale model bottom-up. As highlighted before, each part of the model is characterized by significant simplifications and assumptions, whose implications were not fully explored in this thesis. There is plenty of uncertainty within each building block and further investigation is needed to identify their limitations and the key accuracy bottlenecks. With this in mind, an overview of all the model parameters is presented in Appendix C, where they are classified according to the degree to which they have physical meaning and according to how easily characterizable they are.

Appendices Part V

A Derivations and Demonstrations

A.1 Derivation of the Momentum Equation for a Weakly Compressible Newtonian Fluid

The Navier-Stokes equations for a compressible Newtonian fluid read [52]

$$\frac{\partial}{\partial t}\left(\rho \boldsymbol{C}_f\right) + \nabla \cdot \left(\rho \boldsymbol{C}_f \otimes \boldsymbol{C}_f\right) = -\nabla p + \nabla \cdot \boldsymbol{\tau}, \tag{A.1}$$

where ρ is the density, $\boldsymbol{C}_f$ is the velocity, p is the pressure and $\boldsymbol{\tau}$ is the viscous stress. By distributing the partial derivative and the divergence operator, and replacing the mass conservation equation into the resulting $\frac{\partial \rho}{\partial t}$, we can write

$$\rho \frac{\partial \boldsymbol{C}_f}{\partial t} + \boldsymbol{C}_f \left[-\boldsymbol{C}_f \cdot \nabla \rho - \rho \nabla \cdot \boldsymbol{C}_f\right] + \rho \nabla \cdot \left(\boldsymbol{C}_f \otimes \boldsymbol{C}_f\right) + \left(\boldsymbol{C}_f \otimes \boldsymbol{C}_f\right) \cdot \nabla \rho = -\nabla p + \nabla \cdot \boldsymbol{\tau}. \tag{A.2}$$

Knowing that $\nabla \cdot \left(\boldsymbol{C}_f \otimes \boldsymbol{C}_f\right) = \boldsymbol{C}_f \cdot \nabla \boldsymbol{C}_f + \boldsymbol{C}_f \left(\nabla \cdot \boldsymbol{C}_f\right)$ and removing the two terms that cancel each other out, we can write the left hand side as a material derivative $\frac{d}{dt}$

$$\rho \frac{d \boldsymbol{C}_f}{dt} = -\nabla p + \nabla \cdot \boldsymbol{\tau}. \tag{A.3}$$

By performing either a Reynolds average or a Favre average, the resulting time-averaged equations are

$$\rho \frac{d \boldsymbol{C}_f}{dt} = -\nabla p + \nabla \cdot \left(\boldsymbol{\tau} + \boldsymbol{\tau}_t\right), \tag{A.4}$$

where the averaged variables have the same notation as the instantaneous ones, and $\boldsymbol{\tau}_t$ is the Reynolds stress tensor. The assumed Newtonian character of the fluid leads to the following definition [106]

$$\boldsymbol{\tau} = 2\mu \left[\boldsymbol{S} - \frac{1}{3}\left(\nabla \cdot \boldsymbol{C}_f\right) \boldsymbol{I}\right] + \mu_b \left(\nabla \cdot \boldsymbol{C}_f\right) \boldsymbol{I}, \tag{A.5}$$

where μ is the dynamic viscosity, $\boldsymbol{S}$ is the strain rate, $\boldsymbol{I}$ is the identity and μ_b is the bulk viscosity,

also termed second viscosity.

Boussinesq's approximation for the Reynolds stress reads

$$\boldsymbol{\tau}_t = 2\mu_t \left[\boldsymbol{S} - \frac{1}{3}\left(\nabla \cdot \boldsymbol{C}_f\right) \boldsymbol{I} \right] - \frac{2}{3}\rho k \boldsymbol{I}, \tag{A.6}$$

where μ_t is the turbulent, or eddy, viscosity. The momentum equation can then be written as

$$\rho \frac{d\boldsymbol{C}_f}{dt} = -\nabla p + \nabla \cdot \left\{ 2\left(\mu + \mu_t\right) \left[\boldsymbol{S} - \frac{1}{3}\left(\nabla \cdot \boldsymbol{C}_f\right) \boldsymbol{I} \right] - \frac{2}{3}\rho k \boldsymbol{I} + \mu_b \left(\nabla \cdot \boldsymbol{C}_f\right) \boldsymbol{I} \right\}. \tag{A.7}$$

An additional artificial term is used to apply dissipation in order to limit spurious oscillations that lead to instability. The artificial viscosity is applied as $\mu_a \left(\nabla \cdot \boldsymbol{C}_f\right) \boldsymbol{I}$, so it has the same effect as the bulk viscosity: dissipating energy when the fluid is compressing or dilating. Including the artificial viscosity term, the momentum equation for the weakly compressible Newtonian fluid reads

$$\rho \frac{d\boldsymbol{C}_f}{dt} = -\nabla p + \nabla \cdot \left\{ 2\left(\mu + \mu_t\right) \left[\boldsymbol{S} - \frac{1}{3}\left(\nabla \cdot \boldsymbol{C}_f\right) \boldsymbol{I} \right] - \frac{2}{3}\rho k \boldsymbol{I} + \left(\mu_b + \mu_a\right) \left(\nabla \cdot \boldsymbol{C}_f\right) \boldsymbol{I} \right\}, \tag{A.8}$$

where μ_a is the artificial viscosity parameter.

A.2 Derivation of the Time Derivative of the Cauchy Stress

The linear stress-strain constitutive relation used in the elastic regime is written as

$$\boldsymbol{\sigma} = K_e \operatorname{tr}(\boldsymbol{\varepsilon})\, \boldsymbol{I} + 2G_e \left(\boldsymbol{\varepsilon} - \frac{1}{3} \operatorname{tr}(\boldsymbol{\varepsilon})\, \boldsymbol{I} \right), \tag{A.9}$$

where $\boldsymbol{\sigma}$ is Cauchy's stress, K_e is the bulk modulus, G_e is the shear modulus, and $\boldsymbol{\varepsilon}$ is the elastic strain.

The Jaumann rate of the Cauchy stress is defined as

$$\overset{\triangle}{\boldsymbol{\sigma}} = \dot{\boldsymbol{\sigma}} + \boldsymbol{\sigma} \cdot \boldsymbol{\omega} - \boldsymbol{\omega} \cdot \boldsymbol{\sigma} = K_e \operatorname{tr}(\dot{\boldsymbol{\varepsilon}})\, \boldsymbol{I} + 2G_e \left(\dot{\boldsymbol{\varepsilon}} - \frac{1}{3} \operatorname{tr}(\dot{\boldsymbol{\varepsilon}})\, \boldsymbol{I} \right), \tag{A.10}$$

where $\dot{\boldsymbol{\sigma}}$ is the time derivative of the Cauchy stress, $\boldsymbol{\omega}$ is the material spin, defined by Equation 6.51, and $\dot{\boldsymbol{\varepsilon}}$ is the strain rate, defined as

$$\dot{\boldsymbol{\varepsilon}} = \frac{1}{2} \left[\nabla \boldsymbol{C}_m + (\nabla \boldsymbol{C}_m)^T \right]. \tag{A.11}$$

The time derivative of the Cauchy stress can therefore be written as

$$\dot{\boldsymbol{\sigma}} = K_e \operatorname{tr}(\dot{\boldsymbol{\varepsilon}})\, \boldsymbol{I} + 2G_e \left(\dot{\boldsymbol{\varepsilon}} - \frac{1}{3} \operatorname{tr}(\dot{\boldsymbol{\varepsilon}})\, \boldsymbol{I} \right) - \boldsymbol{\sigma} \cdot \boldsymbol{\omega} + \boldsymbol{\omega} \cdot \boldsymbol{\sigma}. \tag{A.12}$$

By decomposing the Cauchy stress as $\boldsymbol{\sigma} = -p\boldsymbol{I} + \boldsymbol{s}$, where the pressure $p = -\frac{1}{3}\operatorname{tr}(\boldsymbol{\sigma})$, $\boldsymbol{I}$ is the identity and $\boldsymbol{s}$ is the deviatoric stress, and knowing that $K_e = -V\frac{\partial p}{\partial V}$, where V is the volume, one can write

$$\dot{\boldsymbol{\sigma}} = -V\frac{\partial p}{\partial V}\, (\nabla \cdot \boldsymbol{C}_m)\, \boldsymbol{I} + 2G_e \left(\dot{\boldsymbol{\varepsilon}} - \frac{1}{3} \operatorname{tr}(\dot{\boldsymbol{\varepsilon}})\, \boldsymbol{I} \right) - \boldsymbol{s} \cdot \boldsymbol{\omega} + \boldsymbol{\omega} \cdot \boldsymbol{s} + p\, (\boldsymbol{I} \cdot \boldsymbol{\omega} - \boldsymbol{\omega} \cdot \boldsymbol{I}). \tag{A.13}$$

Knowing that $V\frac{\partial p}{\partial V}\, (\nabla \cdot \boldsymbol{C}_m) = \frac{\partial p}{\partial t} = \dot{p}$, the equation simplifies to

$$\dot{\boldsymbol{\sigma}} = -\dot{p}\boldsymbol{I} + 2G_e \left(\dot{\boldsymbol{\varepsilon}} - \frac{1}{3} \operatorname{tr}(\dot{\boldsymbol{\varepsilon}})\, \boldsymbol{I} \right) - \boldsymbol{s} \cdot \boldsymbol{\omega} + \boldsymbol{\omega} \cdot \boldsymbol{s} = -\dot{p}\boldsymbol{I} + \dot{\boldsymbol{s}}. \tag{A.14}$$

This demonstration simply states that, in virtue of the fact that the trace of a tensor is invariant to rotations, the definition of the objective Jaumann rate of stress can directly be used on the deviatoric stress $\boldsymbol{s}$, since the pressure results unaffected by the correcting terms.

A.3 FVPM Demonstrations

First, let us consider the third term of Equation 7.7. In order to derive its approximation, we first define the time derivative of the volume intersection between two particles

$$\dot{V}_{ij} = \frac{d}{dt}V_{ij} = \frac{d}{dt}\int_\Omega \psi_i\psi_j dV = \int_\Omega \frac{\partial\left(\psi_i\psi_j\right)}{\partial t}dV + \int_{\partial\Omega}\psi_i\psi_j\left(\dot{\boldsymbol{x}}\cdot\boldsymbol{n}\right)dS, \tag{A.15}$$

where the last equality is due to Reynolds's transport theorem.

It has been demonstrated [86] that

$$\int_\Omega \psi_i\frac{\partial\psi_j}{\partial t}dV - \int_\Omega \psi_j\frac{\partial\psi_i}{\partial t}dV = -\left(\dot{\boldsymbol{x}}_j\cdot\boldsymbol{\Gamma}_{ij} - \dot{\boldsymbol{x}}_i\cdot\boldsymbol{\Gamma}_{ji}\right). \tag{A.16}$$

These two equations allow us to write

$$\int_\Omega \psi_j\frac{\partial\psi_i}{\partial t}dV = \frac{1}{2}\left[\dot{V}_{ij} - \int_{\partial\Omega}\psi_i\psi_j\left(\dot{\boldsymbol{x}}\cdot\boldsymbol{n}\right)dS + \left(\dot{\boldsymbol{x}}_j\cdot\boldsymbol{\Gamma}_{ij} - \dot{\boldsymbol{x}}_i\cdot\boldsymbol{\Gamma}_{ji}\right)\right] \tag{A.17}$$

and

$$\int_\Omega \psi_i\frac{\partial\psi_j}{\partial t}dV = \frac{1}{2}\left[\dot{V}_{ij} - \int_{\partial\Omega}\psi_i\psi_j\left(\dot{\boldsymbol{x}}\cdot\boldsymbol{n}\right)dS - \left(\dot{\boldsymbol{x}}_j\cdot\boldsymbol{\Gamma}_{ij} - \dot{\boldsymbol{x}}_i\cdot\boldsymbol{\Gamma}_{ji}\right)\right]. \tag{A.18}$$

We can then express the third term of Equation 7.7 as

$$\sum_{j=1}^{N}\boldsymbol{U}_j(t)\int_\Omega \psi_j(\boldsymbol{x},t)\frac{\partial\psi_i(\boldsymbol{x},t)}{\partial t}dV = \sum_{j=1}^{N}\boldsymbol{U}_j\frac{1}{2}\left[\dot{V}_{ij} - \int_{\partial\Omega}\psi_i\psi_j\left(\dot{\boldsymbol{x}}\cdot\boldsymbol{n}\right)dS + \left(\dot{\boldsymbol{x}}_j\cdot\boldsymbol{\Gamma}_{ij} - \dot{\boldsymbol{x}}_i\cdot\boldsymbol{\Gamma}_{ji}\right)\right], \tag{A.19}$$

and write the analogous expression

$$\sum_{j=1}^{N}\boldsymbol{U}_i\int_\Omega \psi_i\frac{\partial\psi_j}{\partial t}dV = \sum_{j=1}^{N}\boldsymbol{U}_i\frac{1}{2}\left[\dot{V}_{ij} - \int_{\partial\Omega}\psi_i\psi_j\left(\dot{\boldsymbol{x}}\cdot\boldsymbol{n}\right)dS - \left(\dot{\boldsymbol{x}}_j\cdot\boldsymbol{\Gamma}_{ij} - \dot{\boldsymbol{x}}_i\cdot\boldsymbol{\Gamma}_{ji}\right)\right] = 0, \tag{A.20}$$

where the last equality follows from $\sum_{j=1}^{N}\int_\Omega \psi_i\frac{\partial\psi_j}{\partial t}dV = 0$, itself a consequence of $\sum_{j=1}^{N}\psi_j = 1$.

By subtracting these equations and neglecting the first-order terms, we have

$$\sum_{j=1}^{N}\boldsymbol{U}_j\int_\Omega \psi_j\frac{\partial\psi_i}{\partial t}dV \overset{\mathcal{O}(h)}{\approx} \sum_{j=1}^{N}\left[\frac{1}{2}\left(\boldsymbol{U}_i+\boldsymbol{U}_j\right)\otimes\left(\dot{\boldsymbol{x}}_j\cdot\boldsymbol{\Gamma}_{ij} - \dot{\boldsymbol{x}}_i\cdot\boldsymbol{\Gamma}_{ji}\right) + \frac{1}{2}\left(\boldsymbol{U}_i-\boldsymbol{U}_j\right)\int_{\partial\Omega}\psi_i\psi_j\left(\dot{\boldsymbol{x}}\cdot\boldsymbol{n}\right)dS\right]. \tag{A.21}$$

However, note that $\int_{\partial\Omega}\psi_i\psi_j\left(\dot{\boldsymbol{x}}\cdot\boldsymbol{n}\right)dS \neq 0$ only when $i=j$, in which case $\boldsymbol{U}_i - \boldsymbol{U}_j = 0$, meaning that the last term is always equal to zero. Therefore, the first-order approximation to the third

term of Equation 7.7 is

$$\sum_{j=1}^{N} \boldsymbol{U}_j(t) \int_\Omega \psi_j(\boldsymbol{x},t) \frac{\partial \psi_i(\boldsymbol{x},t)}{\partial t} dV \overset{\mathscr{O}(h)}{\approx} \sum_{j=1}^{N} \left[\frac{1}{2} \left(\boldsymbol{U}_i + \boldsymbol{U}_j \right) \otimes \left(\dot{\boldsymbol{x}}_j \cdot \boldsymbol{\Gamma}_{ij} - \dot{\boldsymbol{x}}_i \cdot \boldsymbol{\Gamma}_{ji} \right) \right]. \tag{A.22}$$

Now let us consider the fifth term of Equation 7.7. We first note that

$$\int_{\partial\Omega} \psi_i \psi_j \boldsymbol{n} dS = \int_\Omega \nabla \left(\psi_i \psi_j \right) dV = \int_\Omega \psi_i \nabla \psi_j dV + \int_\Omega \psi_j \nabla \psi_i dV, \tag{A.23}$$

which follows from Gauss's divergence theorem. Furthermore, it has been demonstrated [77, 86] that

$$\int_\Omega \psi_i \nabla \psi_j dV - \int_\Omega \psi_j \nabla \psi_i dV = \int_\Omega \psi_i \frac{\nabla W_j}{\sigma_w} dV - \int_\Omega \psi_j \frac{\nabla W_i}{\sigma_w} dV = \boldsymbol{\Gamma}_{ij} - \boldsymbol{\Gamma}_{ji}. \tag{A.24}$$

Based on these two equation, we have

$$\int_\Omega \psi_j \nabla \psi_i dV = \frac{1}{2} \left[\int_{\partial\Omega} \psi_i \psi_j \boldsymbol{n} dS - \left(\boldsymbol{\Gamma}_{ij} - \boldsymbol{\Gamma}_{ji} \right) \right] \tag{A.25}$$

and

$$\int_\Omega \psi_i \nabla \psi_j dV = \frac{1}{2} \left[\int_{\partial\Omega} \psi_i \psi_j \boldsymbol{n} dS + \left(\boldsymbol{\Gamma}_{ij} - \boldsymbol{\Gamma}_{ji} \right) \right]. \tag{A.26}$$

We can then express the fifth term of Equation 7.7 as

$$\sum_{j=1}^{N} \boldsymbol{F}_j \cdot \int_\Omega \psi_j \nabla \psi_i dV = \sum_{j=1}^{N} \frac{1}{2} \boldsymbol{F}_j \cdot \left[\int_{\partial\Omega} \psi_i \psi_j \boldsymbol{n} dS - \left(\boldsymbol{\Gamma}_{ij} - \boldsymbol{\Gamma}_{ji} \right) \right] \tag{A.27}$$

and write the analogous expression

$$\sum_{j=1}^{N} \boldsymbol{F}_i \cdot \int_\Omega \psi_i \nabla \psi_j dV = \sum_{j=1}^{N} \frac{1}{2} \boldsymbol{F}_i \cdot \left[\int_{\partial\Omega} \psi_i \psi_j \boldsymbol{n} dS + \left(\boldsymbol{\Gamma}_{ij} - \boldsymbol{\Gamma}_{ji} \right) \right] = 0, \tag{A.28}$$

where the last equality follows from $\sum_{j=1}^{N} \int_\Omega \psi_i \nabla \psi_j dV = 0$, itself a consequence of $\sum_{j=1}^{N} \psi_j = 1$.

Subtracting these equations yields

$$\sum_{j=1}^{N} \boldsymbol{F}_j \cdot \int_\Omega \psi_j \nabla \psi_i dV = -\sum_{j=1}^{N} \frac{1}{2} (\boldsymbol{F}_i + \boldsymbol{F}_j) \cdot \left(\boldsymbol{\Gamma}_{ij} - \boldsymbol{\Gamma}_{ji} \right) - \sum_{j=1}^{N} \frac{1}{2} (\boldsymbol{F}_i - \boldsymbol{F}_j) \cdot \int_{\partial\Omega} \psi_i \psi_j \boldsymbol{n} dS. \tag{A.29}$$

Yet again, $\int_{\partial\Omega} \psi_i \psi_j \boldsymbol{n} dS \neq 0$ only when $i = j$, in which case $\boldsymbol{F}_i - \boldsymbol{F}_j = 0$, which means that the last term is always equal to zero. Therefore, the fifth term of Equation 7.7 is exactly

$$\sum_{j=1}^{N} \boldsymbol{F}_j(t) \cdot \int_\Omega \psi_j(\boldsymbol{x},t) \nabla \psi_i(\boldsymbol{x},t) dV = -\sum_{j=1}^{N} \left[\frac{1}{2} \left(\boldsymbol{F}_i + \boldsymbol{F}_j \right) \cdot \left(\boldsymbol{\Gamma}_{ij} - \boldsymbol{\Gamma}_{ji} \right) \right]. \tag{A.30}$$

B Complementary Results

B.1 Realistic Sediment Shape Generation Algorithm

A novel algorithm to generate particle-based discretizations for sediments is hereafter presented. Part of the contents of this appendix have been previously published in Leguizamón et al. [110].

As presented in Figure B.1, quartz sediments have very complicated shapes that are not easy to describe systematically. One common metric to characterize the shape of sediments is the sphericity ϕ_d, defined as

$$\phi_d = \frac{\pi^{\frac{1}{3}} (6V)^{\frac{2}{3}}}{A}, \tag{B.1}$$

where V is the sediment volume and A is its surface area. Another common approach is to use an ordinal scale, *e.g.* round, semi-round, sharp, very sharp.

Representing the particle geometry as polyhedra has been the choice taken by researchers who want to improve upon the assumption of sphericity. With the aim of further refining the description of the impacting particles, an algorithm to generate random FVPM discretizations for sediments is presented. The algorithm takes three inputs:

- the objective sediment characteristic size $d_\circ$, taken to be the average Feret diameter,
- the discretization resolution $r_s = \frac{d_\circ}{\Delta x}$, where Δx is the average spacing between the FVPM particles,
- the particle shape parameter ϕ_s, where $0.1 < \phi_s < 1.0$.

The algorithm outputs an arbitrary number of random sediment discretizations of equal characteristic size and similar sphericity $\phi_d = f(\phi_s)$.

The first step involves generating a ball of FVPM particles. A homogeneous distribution is achieved by building the ball with i successive spherical layers of increasing radii $r_i = i\frac{d_\circ}{r_s}$.

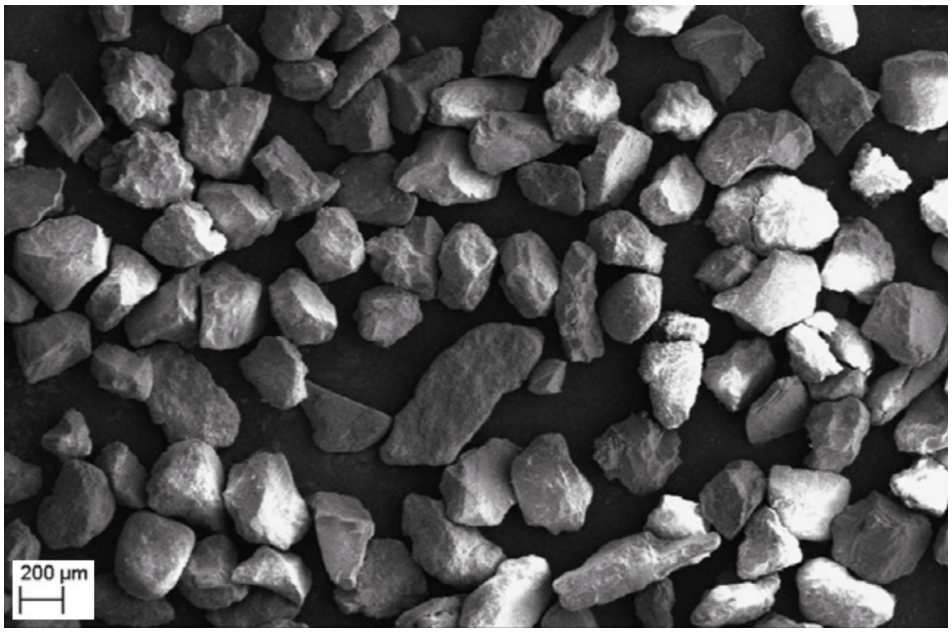

Figure B.1 – Scanning electron micrograph of typical quartz sediments responsible for the erosion of hydraulic machines, adapted from [99].

The particles are distributed on each sphere following a Fibonacci lattice as described in [63], resulting in a very even distribution. The number of layers n_L is determined according to

$$n_L = \left\lceil \frac{r_s}{2} \frac{1}{\phi_s + \frac{1-\phi_s}{3}} \right\rceil . \tag{B.2}$$

The second step consists in cutting the ball with a given number of planes n_P oriented in random directions, conserving only its central portion. This approach is based on the fact that sediments tend to have intersecting flat faces that lead to sharp edges, see Figure B.1. It has been found that $n_P \simeq$ 13-15 leads to satisfactory results; fewer cuts result in part of the original ball being conserved, whereas more cuts result in a similar sharpness but a smaller sediment. The distance from the ball center to any given cutting plane is randomly chosen in the interval $R_{min} = \frac{d_\circ}{2}[\phi_s,\ 1.0]$. When $\phi_s = 1.0$ the planes do not cut the ball, resulting in a spherical sediment. However, as $\phi_s \to 0.0$ the ball is cut ever closer to its center, resulting in sharper sediment discretizations. As seen in Equation B.2, the number of layers increases as ϕ_s decreases, resulting in a larger initial ball. Consequently, the final sediment has the desired characteristic size $d_\circ$ in spite of the material removed during the cutting procedure.

The third step involves slightly moving the FVPM particles that were near a cutting plane in the direction of the plane normal such that the resulting faces are flatter. This step improves the general aspect of the discretization and allows for better defined edges. Figure B.2 presents sediment discretizations generated with the aforementioned algorithm using three different values of the input shape parameter ϕ_s and $r_s = 24$.

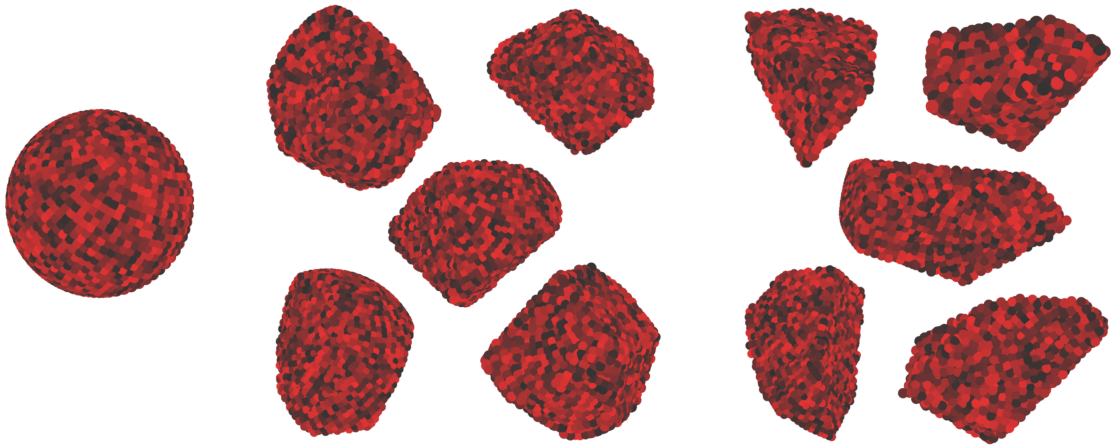

Figure B.2 – Random sediment FVPM discretizations for different values of the shape parameter ϕ_s. Each FVPM particle is colored with a random shade of red to aid visualization.

In order to verify the consistency of the algorithm output, 3^3 sediments are generated for each of five shape parameter values $\phi_s = [1.0,\ 0.8,\ 0.6,\ 0.4,\ 0.2]$; the sphericity ϕ_d, characteristic size d and volume V are then computed for each sediment. The algorithm is run with an objective characteristic size $d_\circ = 100$ μm and resolution $r_s = 32$, in line with the microscale simulations performed in Part III.

The sediment sphericity ϕ_d as a function of the input shape parameter ϕ_s is presented in Figure B.3. The range ϕ_s = 0.1-1.0 results in sphericity values in the range ϕ_d = 0.68-1.0. According to Messa et al. [135], the particle sphericity commonly lies within ϕ_d = 0.66-0.86, whereas Li et al. [119] report that quartz angular particles of d = 45-90 μm present a sphericity $\phi_d = 0.81 \pm 0.062$, *i.e.* 95 % of sediments are in the range ϕ_d = 0.69-0.93. These characterizations suggest that the proposed particle generation algorithm is able to reproduce the sphericity range of typical quartz sediments. Furthermore, the standard deviation plotted in Figure B.3 indicates that the sphericity variability is small within a population of sediments generated with a given shape parameter value, especially for higher values. The consistent mapping $\phi_d = f(\phi_s)$ can be approximated by the polynomial $\phi_d = 0.328\phi_s^2 - 0.005\phi_s + 0.677$.

The resulting sediment characteristic size d and volume V as functions of the input shape parameter ϕ_s are presented in Figure B.4; these metrics are normalized by the input characteristic size $d_\circ$ and associated spherical volume $V_\circ$, respectively. It is evidenced that the algorithm is able to generate sediments that closely follow the objective characteristic size irrespective of the shape; in most situations the agreement is within 1 %. The sediment volume is shown to decrease with increasing sharpness even if the characteristic size remains unchanged. In other words, a sphere is able to accommodate the greatest volume within a given Feret diameter, with sharper shapes necessarily resulting in a smaller volume. As presented in Appendix B.3, this fact increases the erosion ratio of sharper particles, compared to spherical sediments of the same characteristic size.

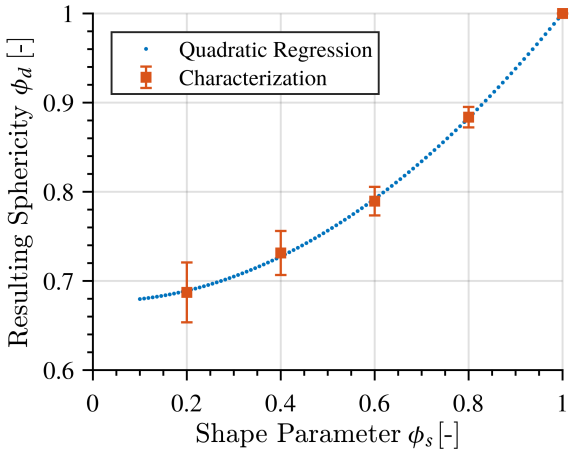

Figure B.3 – Characterization of the resulting sediment sphericity ϕ_d as a function of the input shape parameter ϕ_s. The error bars represent the standard deviation.

In short, the algorithm verification shows that, provided an objective sphericity ϕ_d and characteristic size $d_\circ$, the algorithm is able to generate an arbitrary number of random shapes that closely follow the objective metrics.

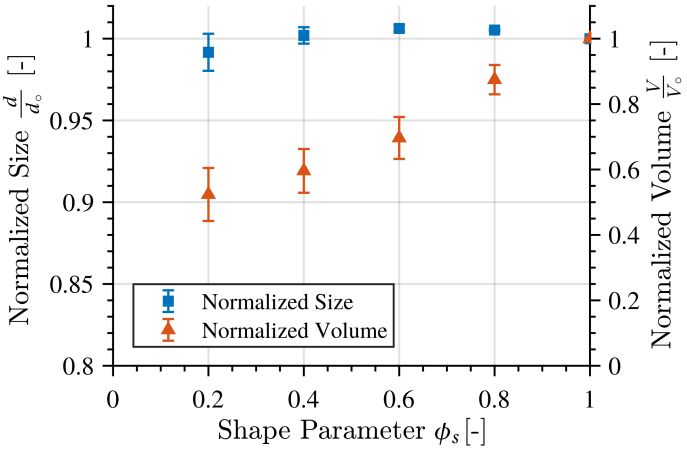

Figure B.4 – Characterization of the resulting sediment characteristic size d and volume V as functions of the input shape parameter ϕ_s. The error bars represent the standard deviation.

B.2 Microscale Model Convergence and Parametric Analyses

The configuration of the microscale model simulations has been studied in detail by means of convergence and parametric analyses to ensure that the results are independent of the setup. A short description of these analyses is provided hereafter, although only the most relevant results are plotted. Part of the contents of this appendix have been previously published in Leguizamón et al. [110].

As illustrated in Figure B.5, the microscale solid domain is hemispherical, with a central refined zone where the impacts occur. The effect of the solid specimen size was studied and it was verified that after a threshold value of about 6 times the sediment diameter d, the impact results became independent. Therefore, the solid hemisphere outer diameter is set to $d_t = 7.0 \cdot d$. The sediments are allowed to impact on a circular area with a diameter equal to $d_i = 1.0 \cdot d$, which was found to be the smallest area that still retains the erosion ratio results of impact simulations on a significantly larger area. The diameter of the central refined hemispherical volume is set to $d_r = 2.0 \cdot d$, such that all the strong gradients associated with the sediment impacts occur within the refined region. Away from the central region, the discretization is gradually coarsened with an expansion ratio of 1.12.

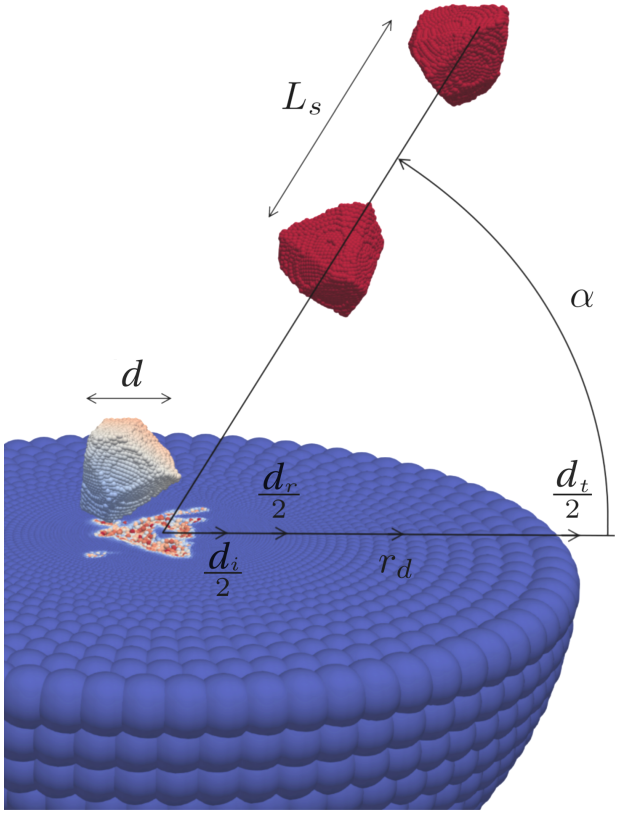

Figure B.5 – Definition of the main geometric parameters that define the microscale domain.

The damping to avoid spurious elastic wave reflections is applied on the outer shell bounded by the hemisphere of diameter equal to $4.0 \cdot d$ and the solid specimen boundary, *i.e.* $r_d = 2.0 \cdot d$. A damping coefficient $k_d = 0.05$ was found to prevent the spurious wave reflections without altering the impact results, namely the plastic strain and damage accumulation.

The separation between successive sediments is set to $L_s = 2.5 \cdot d$, which was found to be enough delay to ensure no interaction between the sediments. Furthermore, it was verified that, together with the artificial damping applied on the outer shell, this separation between sediments guarantees that the solid specimen reaches a stationary state before each new impact.

A convergence analysis was performed using resolutions r_s = [8, 16, 32, 64], where r_s is the number of FVPM particles per sediment diameter; the same discretization resolution is used on the refined region on the specimen. A single impact of a spherical quartz sediment at 100 m $\cdot$ s^{-1} normal to a MSS 13Cr-4Ni specimen is considered. The time histories of the normalized sediment velocity and the volume integral of the damage parameter δ over the specimen are presented in Figure B.6. Even though the convergence behavior is non-monotonic, it is evidenced that the impact results for $r_s = 32$ and $r_s = 64$ are very similar, with a difference of less than 1 %. A discretization resolution of $r_s = 32$ is used in the microscale simulations of MSS 13Cr-4Ni presented in Chapters 10, 12 and 13. However, for the microscale simulations of copper, presented in Chapters 10 and 11, a discretization resolution of $r_s = 16$ was used because they were run using the CPU version of the code, which is significantly less performant than the GPU version.

The effect of the contact parameter k_c was studied in order to select a value that represents a good compromise between accuracy and computational time. Like any penalty-based

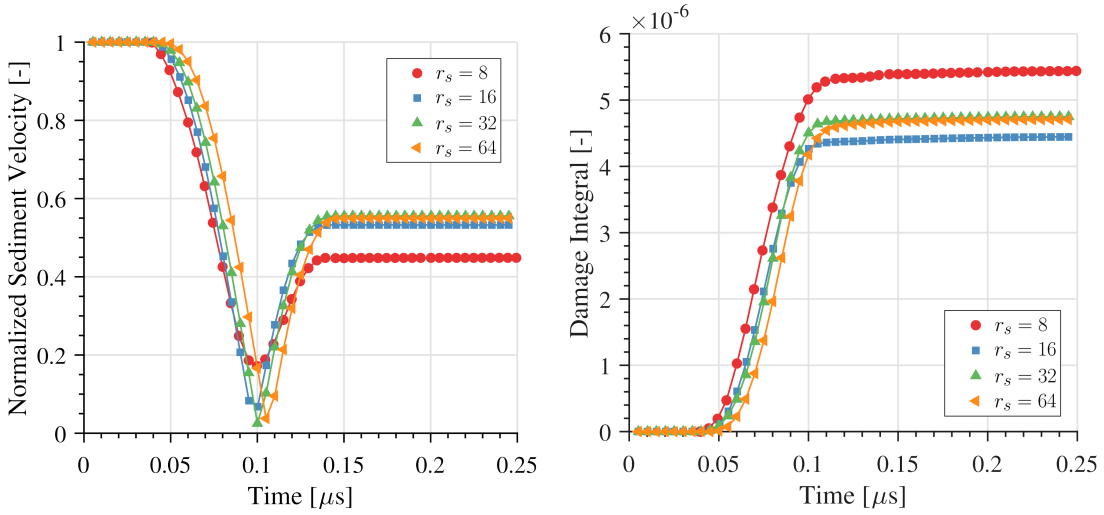

(a) Normalized sediment velocity.

(b) Damage integral on the specimen.

Figure B.6 – Time history of the normalized sediment velocity and damage integral on the specimen as functions of the domain discretization resolution.

contact model, the higher k_c, the more accurate the respect of the non-penetration constraint; however, with increasing values of k_c also come instabilities and time step restrictions linked to the stiffness of the contact. A single-impact test case was performed to determine a suitable value of the contact parameter; a spherical sediment impacting normal to the surface at 75 m $\cdot$ s^{-1} is considered. Figure B.7 presents the time history of the normalized sediment velocity for different values of k_c. The difference between $k_c = 10$ and $k_c = 20$ is less than 2 %, whereas the simulations with $k_c = 40$ developed instabilities that were only solved by significantly decreasing the time step. Based on these results, a value of $k_c = 20$ is chosen for all simulations.

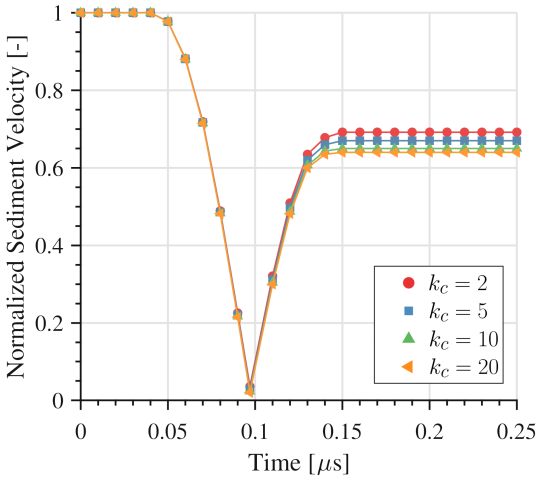

Figure B.7 – Time history of the normalized sediment velocity as a function of k_c.

B.3 Effect of the Sediment Shape and Elasticity

Results on the effect of the sediment shape and elasticity on impact erosion are reported in this appendix, which includes content published in Leguizamón et al. [110].

The time history of the volume integral over the specimen of the damage parameter δ, normalized by its maximum value, is presented in Figure B.8 for the case of a single spherical quartz sediment impact against MSS 13Cr-4Ni. The impact conditions are $v = 100$ m $\cdot$ s^{-1} and $\alpha = 30°$. The effect of the sediment elasticity is assessed by performing two simulations: one using the physical value of the material's Young's modulus E_e, and another one using an effectively rigid sediment with a Young's modulus of $500 \cdot E_e$. Although both impacts have a similar duration, the rigid sediment causes significantly more damage; the simplification of assuming a rigid sediment introduces a relative error of 38 % with respect to an elastic sediment impact. Given the link between the damage integral and the erosion ratio, it is expected that the rigid sediment will generate greater erosion compared to its elastic counterpart, although the magnitude of this effect cannot be precisely estimated from these single impact simulations.

Given that the Young's modulus of MSS 13Cr-4Ni is comparable to that of quartz, the sediment accommodates an elastic deformation comparable to the one experienced by the specimen. Consequently, compared to an impact with a rigid sediment, the specimen is subject to a lower strain rate, the contact area increases and a lower fraction of the impact energy is available to generate plastic deformation and damage.

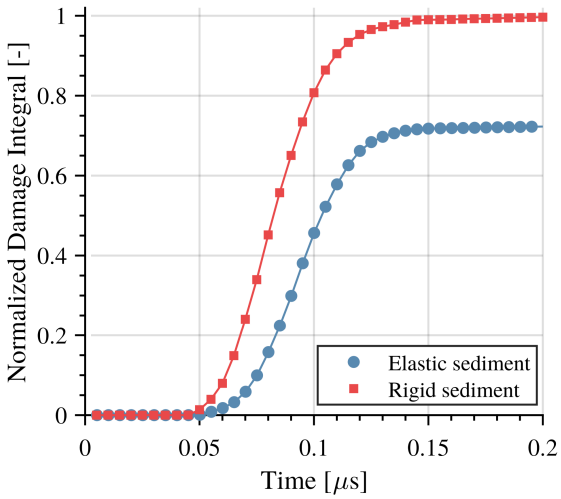

Figure B.8 – Normalized damage integral after one impact with $v = 100$ m $\cdot$ s^{-1} and $\alpha = 30°$.

The effect of the shape of elastic sediments impacting at $v = 100$ m $\cdot$ s^{-1} and $\alpha = 30°$ on copper is illustrated in Figure B.9a, which contains the volume integral of the specimen damage after one impact, normalized by its value for spherical sediments. For the non-spherical particle cases, $\phi_s = [0.6,\ 0.2]$, 20 independent simulations of a single impact are performed and their results averaged. As evidenced by the standard deviation, represented by the error bars, the

damage caused by the non-spherical particles is highly variable: depending on whether the particle impacts with an edge or with a blunt face.

On average, sharp particles cause an increase in damage of up to 72 % with respect to spherical particles, as shown in Figure B.9a. Note that for a fixed characteristic size d, the sharp sediments have a lower volume and therefore a lower mass than similarly-sized spherical ones, as presented in Figure B.4; for example, sediments characterized by $\phi_s = 0.2$ are on average only 53 % as massive as a spherical sediment of the same characteristic size. To provide a fair comparison among the different sediment shapes, the damage integral per unit of sediment mass is computed based on the results presented in Figures B.4 and B.9a. The resulting damage per unit of sediment mass, comparable to the way the erosion ratio is defined, results in an increased effect of the sediment shape, as also presented in Figure B.9a, because of the aforementioned reduction in sediment mass for increasing particle angularity. For example, it is equal to $\frac{1.72}{0.53}$ for $\phi_s = 0.2$, implying an increase of 225 % with respect to its value for spherical particles. A comparable effect on the erosion ratio is anticipated, although it cannot be quantified based on the results of a single sediment impact.

The steady-state erosion ratio is computed for the case of elastic sediments of different shapes impacting a MSS 13Cr-4Ni specimen at $v = 100$ m $\cdot$ s^{-1} and $\alpha = [15, 30, 50, 70, 90]°$. The results are presented in Figure B.9b, where the error bars represent the standard deviation of the erosion ratio estimation, which varies depending on what portion of the eroded mass *vs.* erodent mass curve is considered for the slope calculation. Whereas the slope estimation for the case of spherical particle impacts is unambiguous, similar to Figure 5.3a, it is less so for the case of sharp particles because their orientation-dependent damage potential makes the eroded mass *vs.* erodent mass curve somewhat less consistent.

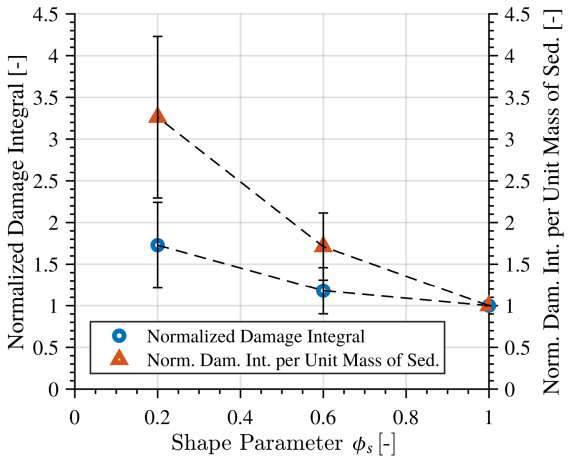

(a) Normalized damage integral and normalized damage integral per unit mass of sediment for the case of copper after one impact at $v = 100$ m $\cdot$ s^{-1} and $\alpha = 30°$ as functions of the sediment shape parameter ϕ_s.

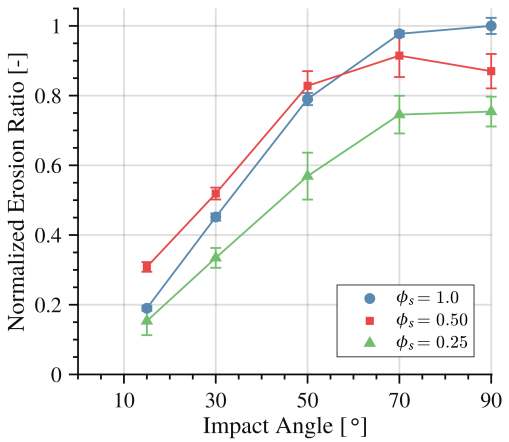

(b) Normalized steady-state erosion ratio of MSS 13Cr-4Ni at $v = 100$ m $\cdot$ s^{-1} as a function of impact angle for three values of the sediment shape parameter ϕ_s.

Figure B.9 – Effect of the shape of elastic sediments on impact erosion.

For spherical sediments, MSS 13Cr-4Ni exhibits a rather brittle erosion behavior, with the greatest erosion ratio at normal incidence. The effect of using sharper sediments, $\phi_s = 0.50$, is clear. At 90° the erosion ratio decreases by 13 %, whereas it increases by 62 % for the lowest impact angle studied, 15°. It remains about the same at an impact angle of 50°. The erosion ratio as a function of impact angle for sediments characterized by $\phi_s = 0.25$ is very similar to the case of $\phi_s = 0.50$, although lower in magnitude almost uniformly.

As highlighted in Section 2.2.1, angular particles cause more damage than spherical ones. Sharp edges act as stress concentrators, so angular sediments generate deeper cuts and scratches. The fact that the sediment sharpness increases the damage, particularly at low impact angles, has been verified both experimentally [35] and by numerical simulation [125] for the case of metals that exhibit a ductile erosion behavior, for instance copper. In agreement with these results, the present simulations evidence a significant increase in the damage caused by sharp sediments impacting on copper at $\alpha = 30°$. Given its ductile character, the dominant erosion mechanisms are cutting and ploughing, which are active at the impact angle considered, and are enhanced by the sediment sharpness.

Estimations of the erosion ratio caused by sharp particles compared to spherical ones lie in the range of 1.7 [150] to 4.0 [118]. The simulation results for sediment impacts at $\alpha = 30°$ on copper predict a damage per unit of sediment mass of 1.7 and 3.3 relative to spherical particles for $\phi_s = 0.6$ and $\phi_s = 0.2$, respectively; a comparable effect on the rationalized erosion rate is expected, in agreement with the aforementioned trends.

It has been shown that martensitic steel in general [163] and 13Cr-4Ni in particular [176] present a maximum erosion ratio in the range of $\alpha = 60$-$90°$, in agreement with the simulation results. The increase of sediment sharpness from $\phi_s = 1.0$ to $\phi_s = 0.5$ entails an increase of the erosion ratio at low impact angle, similar to the aforementioned trends in metals that exhibit a ductile erosion behavior. However, the magnitude of the effect was found to be weaker than it is for copper. Given that the erosion behavior of 13Cr-4Ni is significantly less ductile than that of copper, these results are not surprising. That is, the cutting action of the sediments, which is enhanced by their sharpness, is less important in MSS 13Cr-4Ni, which is less prone to this erosion mechanism thanks to its relatively high hardness. The sediment inertia, the most important parameter in brittle erosion, is invariant to the sediment shape. Given that the erosion behavior of MSS 13Cr-4Ni is in between brittle and ductile, the sediment sharpness has an effect similar to that evidenced in copper, but of significantly weaker magnitude.

For the case of very flat and sharp sediments characterized by $\phi_s = 0.25$, the erosion ratio of MSS 13Cr-4Ni is found to be on average 30 % lower than for $\phi_s = 0.50$, with an angle dependence somewhere in between the curves for $\phi_s = 0.50$ and $\phi_s = 1.0$. The analysis of the simulations revealed that some of the FVPM particles in the sediment edge in contact with the solid reached the maximum stress criterion and were thus removed from the system. This occurs predominantly for $\phi_s = 0.25$, where the very sharp and narrow edges concentrate significant deformation upon contact with the solid. Given that the quartz material model is

not able to describe the fracture by crack propagation as would be expected in brittle materials, the sediments do not fracture into pieces as shown by Hadavi et al. [69, 70]; instead, they only suffer material removal at the contact location. For this reason, the results for $\phi_s = 0.25$ in Figure B.9b are most likely inaccurate.

B.4 Macroscale Model Convergence Analysis

A convergence analysis was performed to determine the FVPM discretization resolution and number of sediments required to ensure configuration-independent results on the macroscale simulations. The first case study, jet impingement on a flat plate, is chosen for the analysis. The following are azimuthally-averaged results for test case 1, as described in Section 10.1.1, at an impingement angle $\theta = 90°$. Part of the contents of this appendix have been published in Leguizamón et al. [112].

The average sediment impact angle and velocity as functions of the normalized radial distance from the jet axis are presented in Figure B.10. They show converged results with respect to the number of sediments, see next paragraph. Four resolutions, measured as the number of particles across the inlet diameter, are studied: 16, 32, 40 and 48. It can be seen that the impact angle dependence on the discretization resolution is highest for the lower radial distances. On the contrary, the impact velocity shows greater variation for the larger radial distances. For both cases, the difference between the resolutions R40 and R48 is well within the distributions' standard deviation, represented by the error bars. Based on these results, all the simulations of Part III are performed with a resolution of 40 particles across the inlet diameter or higher. Other variables such as the sediment flux and average sediment diameter show a similar convergence behavior.

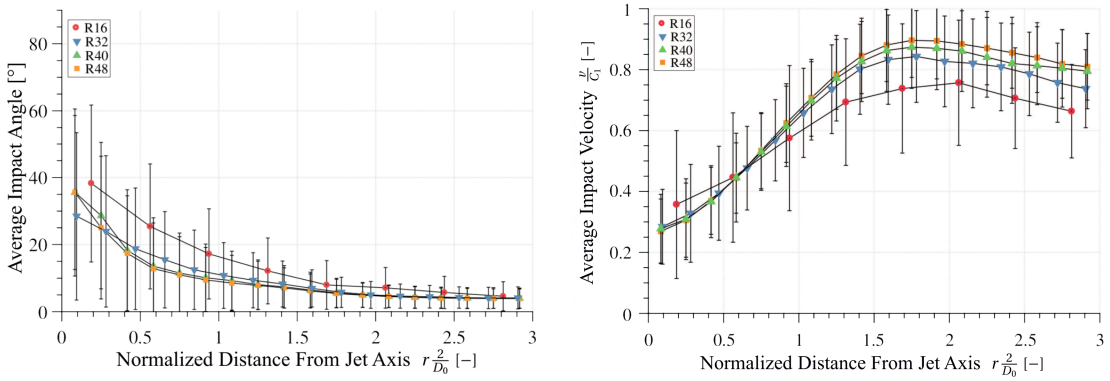

(a) Average sediment impact angle for four discretization resolutions as a function of the distance from the jet axis r normalized by the jet radius $\frac{D_0}{2}$. The error bars represent ± one standard deviation.

(b) Average sediment impact velocity for four discretization resolutions as a function of the normalized distance from the jet axis. The impact velocity v is normalized by the jet velocity C_1. The error bars represent ± one standard deviation.

Figure B.10 – Convergence behavior of the sediment impact angle and velocity distributions.

The random sampling of sediment diameters, inlet positions and turbulent fluctuations followed by the deterministic sediment trajectory calculation can be understood as a Monte Carlo process. As such, enough trajectories must be sampled in order to accurately reveal the set of underlying impact condition distributions that give rise to the erosion. In Figure B.11, the global erosion rate for three jet impingement angles as a function of the total number of

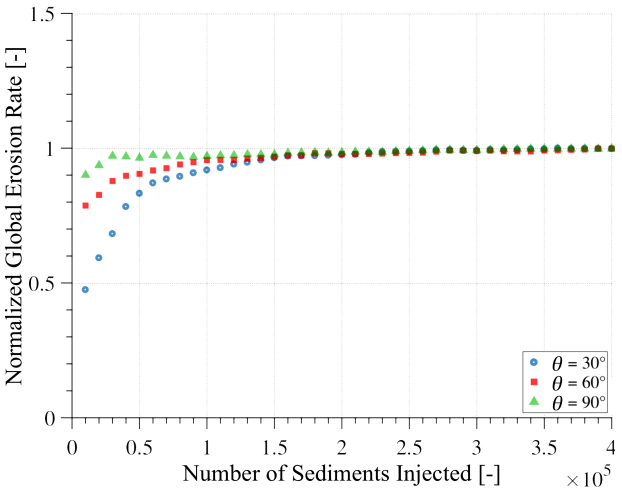

Figure B.11 – Normalized global erosion rate as a function of the number of sediments injected for three jet impingement angles.

sediments injected, *i.e.* the physical simulation time, is presented. This figure shows that at least 2.0×10^5 sediment are required to achieve converged results. The same behavior was noticed for the other variables of interest such as the impact condition distributions. Based on this convergence behavior, all the simulations of Part III include at least 2.0×10^5 sediments.

B.5 Implementation Verification of the Standard k-ϵ Model

The 2D channel flow test case is used to verify the correctness of the standard k-ϵ model implementation by comparing SPHEROS's simulation results against the results of a commercial CFD code. The channel is 0.1 m high and 2.0 m long. The inlet boundary is defined by a uniform velocity $C_\circ = 2\ \mathrm{m} \cdot \mathrm{s}^{-1}$ and a turbulence intensity of 5 %. The working fluid is water, yielding a Reynolds number $\mathrm{Re}_{\frac{L}{2}} = 2 \times 10^6$ defined using the channel half-length. The velocity and turbulence profiles are assessed at downstream distances $L_x = [1.0,\ 1.5]$ m, as illustrated in Figure B.12. Both the FVPM and commercial software discretizations are defined by $y^+ = 50$.

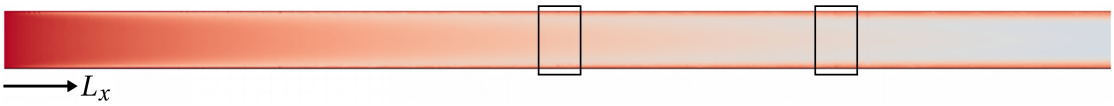

Figure B.12 – Computational domain of the 2D channel flow test case. The rectangles define the regions over which the velocity and turbulence profiles are averaged and assessed. The fluid is colored according to its turbulence intensity.

The velocity profiles at $L_x = [1.0,\ 1.5]$ m, normalized by the reference velocity $C_\circ$, are presented in Figure B.13 for two cases: without and with the turbulence model activated in SPHEROS. The activation of the turbulence model, together with its wall function, significantly modify the velocity profiles near the wall, as expected. Figure B.13b evidences that the turbulence model implementation is correct: the velocity profile difference between SPHEROS and the commercial software is negligible; furthermore, the same profile development trend as a function of downstream distance is obtained.

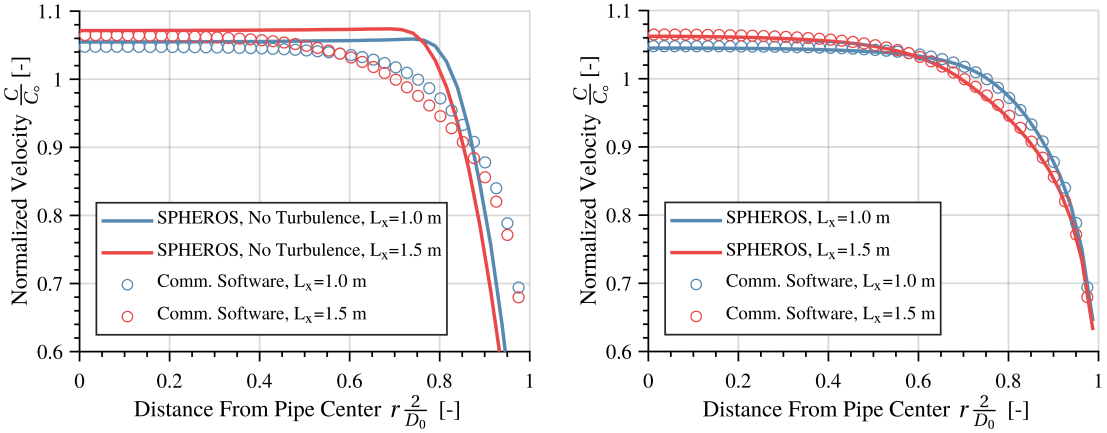

(a) Without the turbulence model.

(b) With the turbulence model.

Figure B.13 – Velocity profiles at two downstream distances L_x.

The turbulence model implemented describes the eddy viscosity by means of two variables that give it its name: the turbulence kinetic energy k and its dissipation rate ϵ. Profiles of these variables at $L_x = [1.0,\ 1.5]$ m are presented in Figure B.14. Yet again, very good agreement is

evidenced between SPHEROS and the commercial software for the turbulence profiles and their development trend as a function of the downstream distance. These results evidence that the standard k-ϵ turbulence model implementation in SPHEROS is correct.

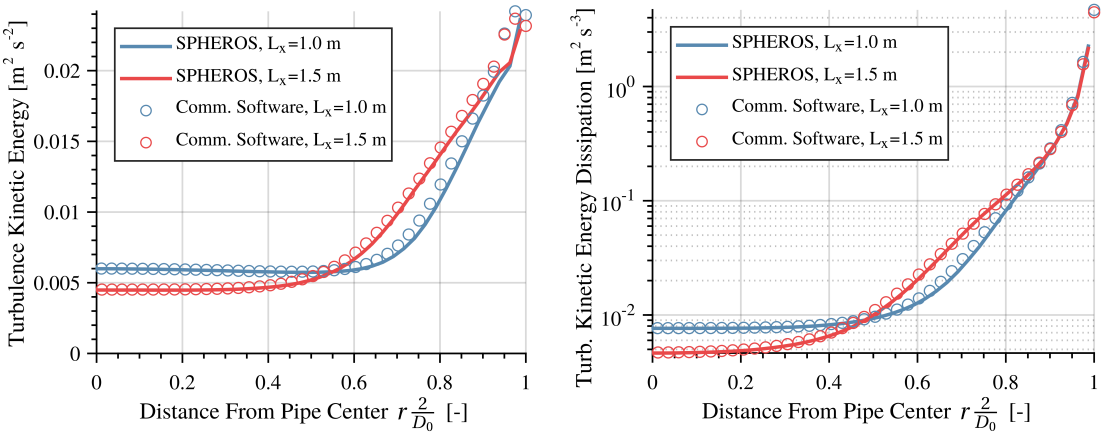

(a) Turbulence kinetic energy k.

(b) Turbulence kinetic energy dissipation ϵ.

Figure B.14 – Turbulence profiles at two downstream distances L_x.

A similar test case with $C_\circ = 200\ \mathrm{m} \cdot \mathrm{s}^{-1}$, implying a Reynolds number $\mathrm{Re}_{\frac{L}{2}} = 2 \times 10^8$, was used to assess the influence of y^+ on the velocity and turbulence profiles. It was verified that as long as about 10 FVPM particles are within the boundary layer, results comparable to much finer discretizations are obtained.

B.6 Discrete and Continuous Random Walk Models

The turbulent fluctuating velocity $\boldsymbol{C}_{f,t}$ used in the sediment transport model can be computed using a random walk model. These fall into one of two categories: discrete random walk models, such as the eddy interaction model of Gosman and Ioannides [64], and continuous random walk models, such as the use of the stochastic Langevin equation [33]. To illustrate the difference between these models, the 2D channel flow test case was used; the fluctuating velocity at three locations defined by $\frac{n}{\delta_t} = [0.2,\ 1.2,\ 2.2]$ was monitored, where n is the normal distance from the wall and δ_t is the boundary layer thickness.

A time history of the magnitude of the fluctuating velocity $C_{f,t}$ normalized by the reference velocity $C_\circ$ is presented in Figures B.15 and B.16 for the aforementioned discrete and continuous random walk models, respectively. The eddy interaction model assumes that the sediment interacts with one discrete eddy at a time that induces a constant velocity throughout the interaction duration; this yields the piecewise-constant behavior illustrated in Figure B.15. On the contrary, the Langevin equation updates the fluctuating velocity at every time step, resulting in the continuously-changing velocity presented in Figure B.16.

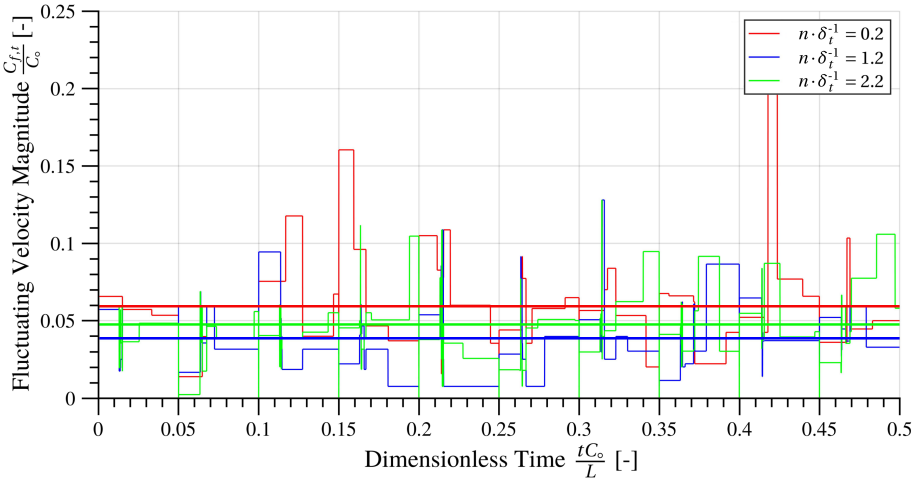

Figure B.15 – Time history of the fluctuating velocity computed using a discrete random walk model. The bold horizontal lines represent the averages.

Both models are physical in the sense that the fluctuations depend on properties of the turbulence field, such as turbulent time and length scales. Consequently, the average magnitude of the velocity fluctuations is greatest inside the boundary layer, as expected. However, only the continuous random walk model is physical in the sense that velocity fluctuations caused by turbulence are continuous, not piecewise-constant as assumed by the discrete random walk model. Not only do the fluctuations of the continuous model look more realistic; it was evidenced that in the first case study, jet impingement against a flat plate, fewer sediments were required to reach converged erosion and impact condition distributions. For these reasons, the continuous random walk model based on the Langevin equation was adopted for all the case studies presented in this thesis.

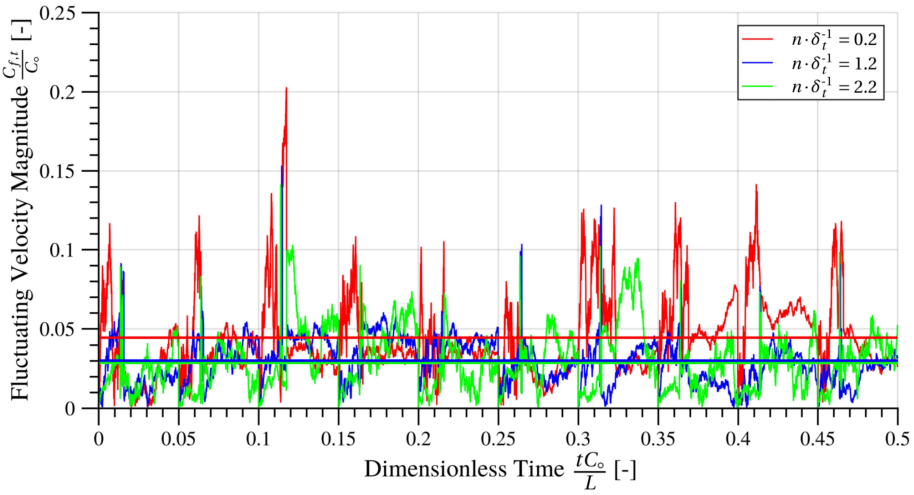

Figure B.16 – Time history of the fluctuating velocity computed using a continuous random walk model. The bold horizontal lines represent the averages.

The continuous random walk model of turbulent dispersion was verified in a 2D test case where the drift of sediments of various sizes under homogeneous turbulence was studied. Spherical sediments of diameters $d = [5,\ 50,\ 500,\ 5000]$ μm were positioned in the center of a square patch of fluid with zero mean velocity and constant turbulence properties defined by $k = 0.01$ m$^2 \cdot$ s^{-2} and $\epsilon = 1.0$ m$^2 \cdot$ s^{-3}. The position time histories, normalized by the patch size L, are presented in Figure B.17. As expected, the smallest sediment is very sensitive to the turbulent fluctuations, as revealed by its wiggly path. As the sediment inertia increases, the paths are significantly shorter and less prone to changes of direction, since they are less sensitive to the high frequency forcing applied by the turbulence.

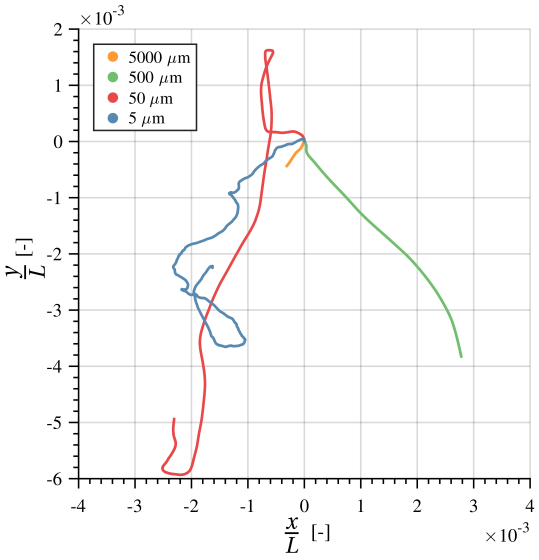

Figure B.17 – Sediment trajectories on homogeneous turbulence.

C Overview of the Model Parameters

The multiscale model of erosion contains a large set of parameters that can be grouped into four categories:

- Physical model parameters that can be characterized with low uncertainty and are oftentimes found in the literature
- Physical model parameters that can be characterized with a relatively high uncertainty and are oftentimes not found in the literature
- Calibration model parameters that have been tuned to simple experiments and whose standard values are found in the literature, and numerical parameters that can be straightforwardly selected based on sensitivity or parametric analyses
- Calibration model parameters that are case-dependent and whose values vary significantly in the literature

All the parameters found in the microscale and macroscale models are illustrated in Figures C.1 and C.2, respectively; each parameter is color-coded according to the aforementioned categories. Note that the submodels that have no parameters are not illustrated.

Most of the parameters in the microscale, Figure C.1, pertain to the first category, *i.e.* they are material model parameters with a clear physical meaning and whose values can be found in the literature or through simple experimentation. Examples include the densities, melting temperatures and the solid yield stress. Other material model parameters pertain to the second category given that sophisticated characterization campaigns are needed to obtain them, and even then, not without considerable uncertainty; these include most of the Johnson-Cook material model parameters. The sediment shape parameter ϕ_s also falls under the second category because it depends on the sediment sphericity ϕ_d, which requires advanced characterization for a representative population of sediments.

Two numerical parameters, the static-to-dynamic decay factor of the friction model and the penetration penalty parameter of the contact force, are examples of the third category: they can be selected based on a parametric study, as presented in Section B.2 for the latter, or based on the literature and a sensitivity analysis, for the former.

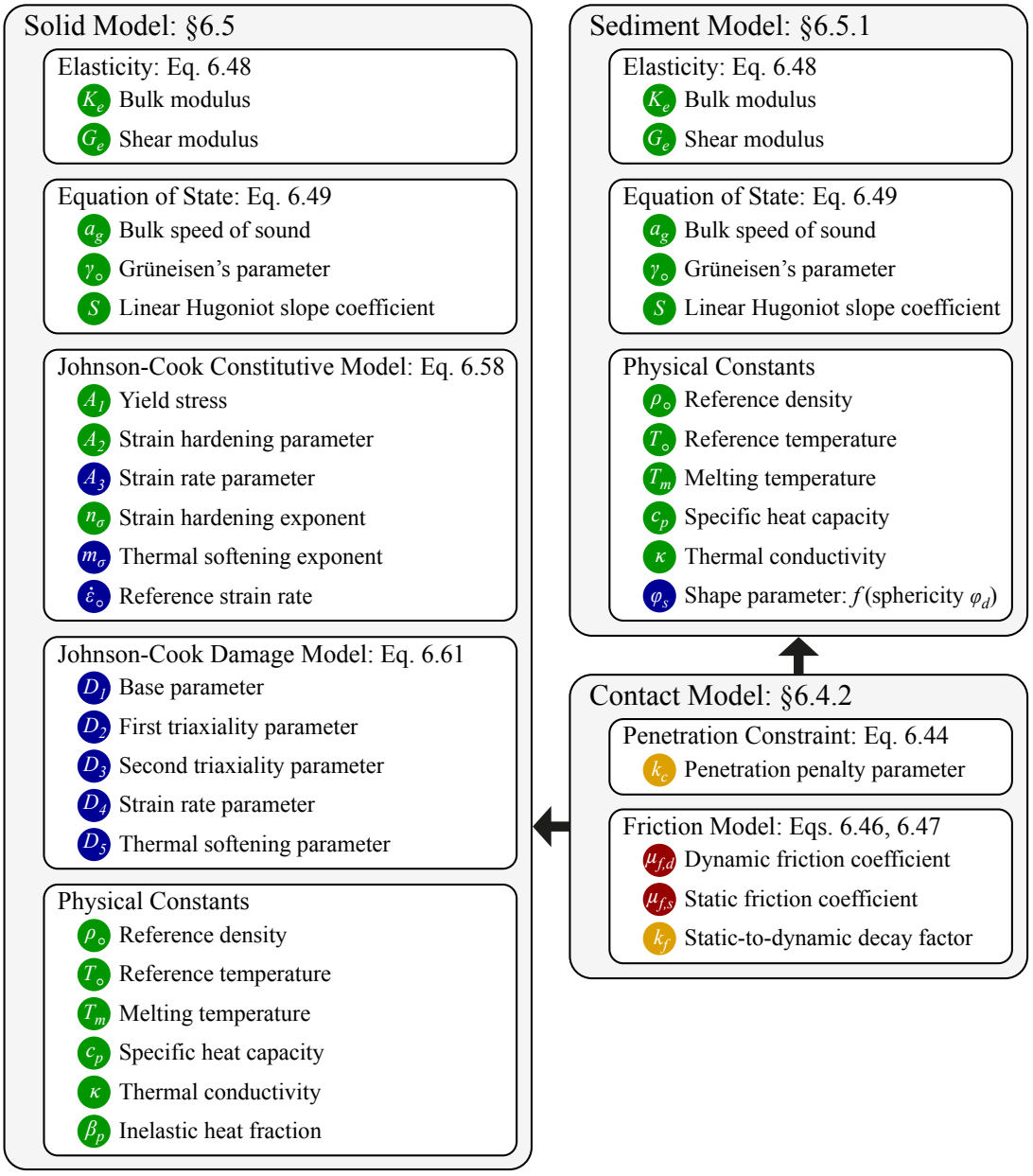

Figure C.1 – List of parameters within the microscale model.

Perhaps the most problematic parameters are the static and dynamic friction coefficients, members of the fourth category: even though they have a physical interpretation, experiments result in a very wide range of values; as such, they can be interpreted as calibration parameters rather than well-defined physical parameters. As discussed in Section 10.1.3, the friction coefficients in this thesis were selected based on the particle impact simulation literature and were not tuned to fit the experimental erosion results. However, given that the values used in the simulation literature fall within a small range compared to the experimental range, the variability of the erosion results to significant changes in these parameters should be tested.

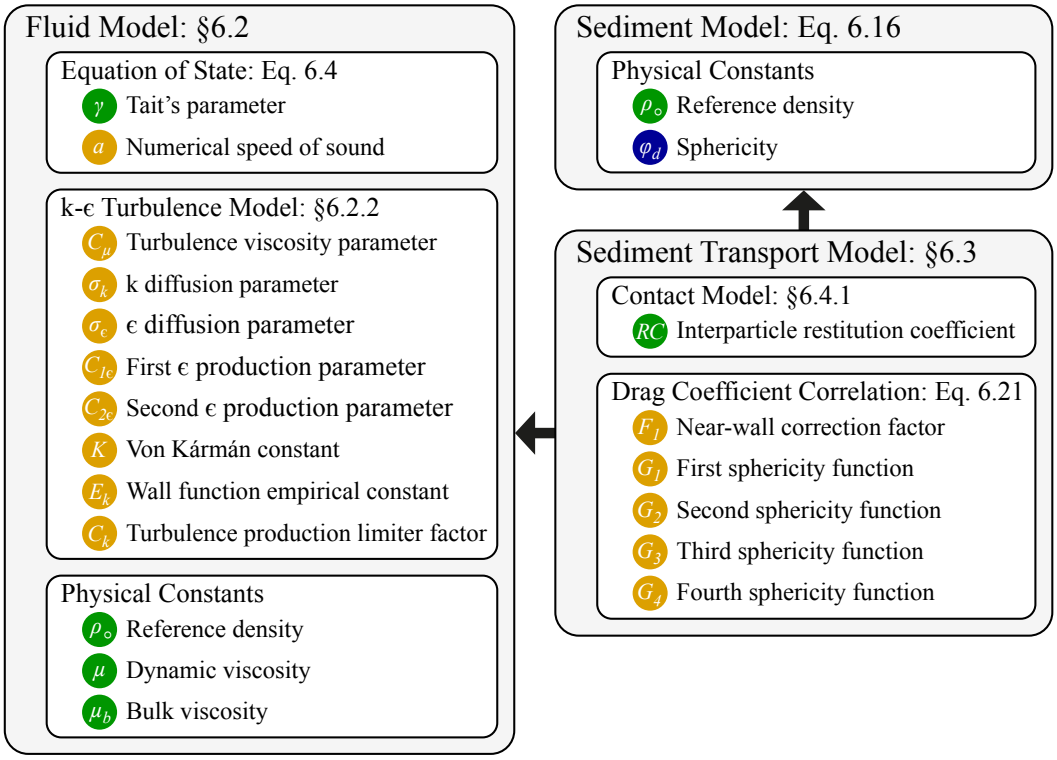

Figure C.2 – List of parameters within the macroscale model.

Most of the parameters in the macroscale, Figure C.2, pertain to the third category, *i.e.* they are model parameters that have been previously calibrated using experimental data and whose values can be found in the literature. Examples include the turbulence model parameters and the drag coefficient correlation. The macroscale model also includes a few parameters of the first category such as the water density and viscosities.

The most problematic parameter in the macroscale is the sediment sphericity. It is a member of the third category because an elaborate characterization over a representative population of sediments is required to find it. Alternatively, a set of micrographs can also be used to approximate it, although a significant uncertainty is introduced in the erosion results, as discussed in Section 10.4.

Bibliography

[1] A. Abdulle, E. Weinan, B. Engquist, and E. Vanden-Eijnden. The heterogeneous multiscale method. *Acta Numerica*, 21:1–87, 2012. doi:10.1017/S0962492912000025.

[2] S. Alimirzazadeh. *GPU-accelerated finite volume particle simulation of free jet deviation by multijet rotating Pelton runner*. PhD thesis, École Polytechnique Fédérale de Lausanne (EPFL), 2019.

[3] S. Alimirzazadeh, E. Jahanbakhsh, A. Maertens, S. Leguizamón, and F. Avellan. GPU-SPHEROS: A GPU-accelerated versatile solver based on the finite volume particle method. In *12th International SPHERIC Workshop*, Ourense, ES, 2017.

[4] S. Alimirzazadeh, E. Jahanbakhsh, A. Maertens, S. Leguizamón, and F. Avellan. GPU-accelerated 3-D finite volume particle method. *Computers & Fluids*, 171:79–93, 2018. doi:10.1016/j.compfluid.2018.05.030.

[5] S. Alimirzazadeh, T. Kumashiro, S. Leguizamón, E. Jahanbakhsh, A. Maertens, C. Vessaz, K. Tani, and F. Avellan. GPU-accelerated numerical analysis of jet interference in a six-jet Pelton turbine using finite volume particle method. *Submitted to Renewable Energy*, 2019.

[6] S. Alimirzazadeh, T. Kumashiro, S. Leguizamón, A. Maertens, E. Jahanbakhsh, K. Tani, and F. Avellan. RANS simulation of a Pelton turbine using the finite volume particle method accelerated on GPU. In *13th International SPHERIC Workshop*, Galway, IR, 2018.

[7] S. Alimirzazadeh, T. Kumashiro, S. Leguizamón, A. Maertens, E. Jahanbakhsh, K. Tani, and F. Avellan. GPU-accelerated Pelton turbine simulation using finite volume particle method coupled with linear eddy viscosity models. *IOP Conference Series: Earth and Environmental Science*, 240:072018, 2019. doi:10.1088/1755-1315/240/7/072018.

[8] H. J. Amarendra, P. Kalhan, G. P. Chaudhari, S. K. Nath, and S. Kumar. Slurry erosion response of heat treated 13Cr-4Ni martensitic stainless steel. *Materials Science Forum*, 710:500–505, 2012. doi:10.4028/www.scientific.net/MSF.710.500.

[9] R. Andersson, M. Syk, J. Powell, and C. Magnusson. Development of high strain rate equations for stainless steels. *Journal of Materials Engineering and Performance*, 14:553–562, 2005. doi:10.1361/105994905X64549.

[10] F. Avellan. EPFL hydraulic turbomachines course: Formulary. Technical report, Laboratory for Hydraulic Machines, 2018.

[11] T. R. Bajracharya, B. Acharya, C. B. Joshi, R. P. Saini, and O.G. Dahlhaug. Sand erosion of Pelton turbine nozzles and buckets: A case study of Chilime hydropower plant. *Wear*, 264:177–184, 2008. doi:10.1016/j.wear.2007.02.021.

[12] P. Balu, F. Kong, S. Hamid, and R. Kovacevic. Finite element modeling of solid particle erosion in AISI 4140 steel and nickel-tungsten carbide composite material produced by the laser-based powder deposition process. *Tribology International*, 62:18–28, 2013. doi:10.1016/j.triboint.2013.01.021.

[13] Y. Bao and T. Wierzbicki. On fracture locus in the equivalent strain and stress triaxiality space. *International Journal of Mechanical Sciences*, 46:81–98, 2004. doi:10.1016/j.ijmecsci.2004.02.006.

[14] G. K. Batchelor. *An Introduction to Fluid Dynamics*. Cambridge University Press, 2000. doi:10.1017/CBO9780511800955.

[15] Y. Bazilevs, V. M. Calo, J. A. Cottrell, T. J. R. Hughes, A. Reali, and G. Scovazzi. Variational multiscale residual-based turbulence modeling for large eddy simulations of incompressible flows. *Computer Methods in Applied Mechanics and Engineering*, 197:173–201, 2007. doi:10.1016/j.cma.2007.07.016.

[16] A. K. Behera, N. K. Singh, and M. K. Singha. Compressive behavior of AISI-416 stainless steel at different rates of loading. In *Proceedings of the World Congress on Engineering*. WCE, 2012. URL: http://www.iaeng.org/publication/WCE2012/WCE2012_pp1879-1883.pdf.

[17] J. G. A. Bitter. A study of erosion phenomena: Part I. *Wear*, 6:5–21, 1963. doi:10.1016/0043-1648(63)90003-6.

[18] J. G. A. Bitter. A study of erosion phenomena: Part II. *Wear*, 6:169–190, 1963. doi:10.1016/0043-1648(63)90073-5.

[19] R. M. Boes. Kontinuierliche messung von schwebstoffkonzentration und –korngrössenverteilung im triebwasser und quantifizierung der hydroabrasion an einer peltonturbine (Continuous measurements of SSC and PSD in the turbine water and quantification of hydro-abrasive erosion on a Pelton turbine). *Wasser Energy Luft*, 102:101–107, 2010.

[20] R. M. Boes. Real-time monitoring of suspended sediment concentration and particle size distribution in the headwater way of a high-head hydropower plant. In *Proceedings of the 33rd IAHR Congress: Water Engineering for a Sustainable Environment*, pages 4037–4044, 2010.

[21] P. A. Du Bois, S. Kolling, M. Feucht, and A. Haufe. A comparative review of damage and failure models and a tabulated generalization. *Keynote Lecture 10: 6^{th} European LS-DYNA User's Conference*, 2007.

[22] Y. Ait Bouziad. *Physical modelling of leading edge cavitation: Computational methodologies and application to hydraulic machinery*. PhD thesis, École Polytechnique Fédérale de Lausanne (EPFL), 2005. doi:10.5075/epfl-thesis-3353.

[23] T. Bruckner, I. A. Bashmakov, Y. Mulugetta, H. Chum, A. de la Vega Navarro, J. Edmonds, A. Faaij, B. Fungtammasan, A. Garg, E. Hertwich, D. Honnery, D. Infield, M. Kainuma, S. Khennas, S. Kim, H. B. Nimir, K. Riahi, N. Strachan, R. Wiser, and X. Zhang. Energy Systems. In O. Edenhofer, R. Pichs-Madruga, Y. Sokona, E. Farahani, S. Kadner, K. Seyboth, A. Adler, I. Baum, S. Brunner, P. Eickemeier, B. Kriemann, J. Savolainen, S. Schlömer, C. von Stechow, T. Zwickel, and J. C. Minx, editors, *Climate Change 2014: Mitigation of Climate Change. Contribution of Working Group III to the Fifth Assessment Report of the Intergovernmental Panel on Climate Change*. Cambridge University Press, Cambridge, United Kingdom, 2014. URL: www.cambridge.org/9781107641655.

[24] T. Børvik, O.S. Hopperstad, S. Dey, E.V. Pizzinato, M. Langseth, and C. Albertini. Strength and ductility of Weldox 460 E steel at high strain rates, elevated temperatures and various stress triaxialities. *Engineering Fracture Mechanics*, 72:1071–1087, 2005. doi:10.1016/j.engfracmech.2004.07.007.

[25] Swiss National Supercomputing Centre. Piz Daint Fact Sheet. Technical report, CSCS, 2018. URL: https://www.cscs.ch/fileadmin/user_upload/contents_publications/factsheets/piz_daint/FSPizDaint_Final_2018_EN.pdf.

[26] A. K. Chauhan, D. B. Goel, and S. Prakash. Erosion behaviour of hydro turbine steels. *Bulletin of Materials Science*, 31:115–120, 2008. URL: https://www.ias.ac.in/article/fulltext/boms/031/02/0115-0120.

[27] M. Chen and J. B. McLaughlin. A new correlation for the aerosol deposition rate in vertical ducts. *Journal of Colloid and Interface Science*, 169:437–455, 1995. doi:10.1006/jcis.1995.1054.

[28] Z. Chongji, X. Yexiang, Z. Wei, Y. Yangyang, C. Lei, and W. Zhengwei. Pelton turbine needle erosion prediction based on 3D three-phase flow simulation. *IOP Conference Series: Earth and Environmental Science*, 22:052019, 2014. doi:10.1088/1755-1315/22/5/052019.

[29] S. Coulson. Changes in hydro turbine design – The last 40 years, and into the future. *Invited Lecture: 29^{th} IAHR Symposium on Hydraulic Machinery and Systems, Kyoto*, 2018.

[30] H. Couque. The use of the direct impact Hopkinson pressure bar technique to describe thermally activated and viscous regimes of metallic materials. *Philosophical Transactions of the Royal Society A*, 372:20130218, 2014. doi:10.1098/rsta.2013.0218.

[31] G. R. Cowper and P. S. Symonds. Strain-hardening and strain-rate effects in the impact loading of cantilever beams. Technical report, Division of Applied Mathematics, Brown University, 1957. URL: http://www.dtic.mil/dtic/tr/fulltext/u2/144762.pdf.

[32] O. G. Dahlhaug, P.E. Skare, V. Mossing, and A. Gutierrez. Erosion resistant coatings for Francis runners and guidevanes. *International Journal of Hydropower and Dams*, 17:109–112, 2010.

[33] A. Dehbi. Turbulent particle dispersion in arbitrary wall-bounded geometries: A coupled CFD-Langevin-equation based approach. *International Journal of Multiphase Flow*, 34:819–828, 2008. doi:10.1016/j.ijmultiphaseflow.2008.03.001.

[34] Z. Van der Westhuizen. World energy resources: Hydropower. Technical report, World Energy Council, 2017. URL: https://www.worldenergy.org/wp-content/uploads/2017/03/WEResources_Hydropower_2016.pdf.

[35] G. R. Desale, B. K. Gandhi, and S. C. Jain. Effect of erodent properties on erosion wear of ductile type materials. *Wear*, 261:914–921, 2006. doi:10.1016/j.wear.2006.01.035.

[36] W. Ding and H. El Kateb. Annual discharge and sediment load variation in Jialing river during the past 50 years. *Journal of Mountain Science*, 8:664–676, 2011. doi:10.1007/s11629-011-1031-0.

[37] Y. Ding, Wang M, Z.Li, and H. Haob. Damage evaluation of the steel tubular column subjected to explosion and post-explosion fire condition. *Engineering Structures*, 55:44–55, 2013. doi:10.1016/j.engstruct.2012.01.013.

[38] X. W. Dong, G. R. Liu, Z. Li, and W. Zeng. A smoothed particle hydrodynamics (SPH) model for simulating surface erosion by impacts of foreign particles. *Tribology International*, 95:267–278, 2016. doi:10.1016/j.triboint.2015.11.038.

[39] C. G. Duan, V. Y. Karelin, H. Brekke, Y. L. Wu, M. Matsumura, B. Chen, A. I. Denisov, and B. Y. Cai. *Abrasive Erosion and Corrosion of Hydraulic Machinery*, volume 2 of *Series on Hydraulic Machinery*. Imperial College Press, London, 2003. doi:10.1142/p272.

[40] C. Dubois. *Hydropower - Andritz Hydro*. Druckerei Schüpfheim, Kriens, 2010.

[41] W. E. Principles of multiscale modeling, 2011. URL: https://web.math.princeton.edu/~weinan/papers/weinan_book.pdf.

[42] Y. Egorov, F. R. Menter, R. Lechner, and D. Cokljat. The scale-adaptive simulation method for unsteady turbulent flow predictions. Part 2: Applications to complex flows. *Flow, Turbulence and Combustion*, 85:139–165, 2010. doi:10.1007/s10494-010-9265-4.

[43] S. Elghobashi. Particle-laden turbulent flows: direct simulation and closure models. In R. V. A. Oliemans, editor, *Computational Fluid Dynamics for the Petrochemical Process Industry*, pages 301–314. Springer Dordrecht, 1991. doi:10.1007/978-94-011-3632-7_4.

[44] M. S. ElTobgy, E. Ng, and M. A. Elbestawi. Finite element modeling of erosive wear. *International Journal of Machine Tools and Manufacture*, 45:1337–1346, 2005. doi:10.1016/j.ijmachtools.2005.01.007.

[45] EPFL-LMH. HYPERBOLE report summary. Technical report, European Commission Projects, 2017. URL: https://cordis.europa.eu/result/rcn/208601_en.html.

[46] A. M. Espinoza. Managing sediment in Peru's Pativilca river basin. *Hydro Review Worldwide*, 24:24–29, 2016. URL: https://www.hydroworld.com/articles/print/volume-24/issue-4/features/managing-sediment-in-peru-s-pativilca-river-basin.html.

[47] R. Fatehi and M. T. Manzari. A consistent and fast weakly compressible smoothed particle hydrodynamics with a new wall boundary condition. *International Journal for Numerical Methods in Fluids*, 68:905–921, 2012. doi:10.1002/fld.2586.

[48] D. Felix. *Experimental investigation on suspended sediment, hydro-abrasive erosion and efficiency reductions of coated Pelton turbines*. PhD thesis, Eidgenössische Technische Hochschule Zürich (ETHZ), 2017. doi:10.3929/ethz-b-000161430.

[49] D. Felix, A. Abgottspon, I. Albayrak, and R. Boes. Hydro-abrasive erosion on coated Pelton runners: Partial calibration of the IEC model based on measurements in HPP Fieschertal. *IOP Conference Series: Earth and Environmental Science*, 49:122009, 2016. doi:10.1088/1755-1315/49/12/122009.

[50] D. Felix, I. Albayrak, A. Abgottspon, and R. Boes. Hydro-abrasive erosion of hydraulic turbines caused by sediment - A century of research and development. *IOP Conference Series: Earth and Environmental Science*, 49:122001, 2016. doi:10.1088/1755-1315/49/12/122001.

[51] A. Ferrante and S. Elghobashi. On the physical mechanisms of two-way coupling in particle-laden isotropic turbulence. *Physics of Fluids*, 15:315–329, 2003. doi:10.1063/1.1532731.

[52] J. Ferziger and M. Perić. *Computational Methods for Fluid Dynamics*. Springer-Verlag Berlin Heidelberg, 1996. doi:10.1007/978-3-642-97651-3.

[53] Richard Feynman. *The Character of Physical Law*. Cornell University, 1965. URL: http://www.cornell.edu/video/playlist/richard-feynman-messenger-lectures.

[54] C. B. Field, V. R. Barros, D. J. Dokken, K. J. Mach, M. D. Mastrandrea, T. E. Bilir, M. Chatterjee, K. L. Ebi, Y. O. Estrada, R. C. Genova, B. Girma, E. S. Kissel, A. N. Levy, S. MacCracken, P. R. Mastrandrea, and L. L. White. *Climate Change 2014: Impacts, Adaptation, and Vulnerability. Part A: Global and Sectorial Aspects. Contribution of Working Group II to the Fifth Assessment Report of the Intergovernmental Panel on Climate Change*. Cambridge University Press, Cambridge, United Kingdom, 2014. URL: www.cambridge.org/9781107641655.

[55] I. Finnie. Erosion of surfaces by solid particles. *Wear*, 3:87–103, 1960. doi:10.1016/0043-1648(60)90055-7.

[56] I. Finnie. Some observations on the erosion of ductile materials. *Wear*, 19:81–90, 1972. doi:10.1016/0043-1648(72)90444-9.

[57] K. A. Flack and M. P. Schultz. Roughness effects on wall-bounded turbulent flows. *Physics of Fluids*, 26:101305, 2014. doi:10.1063/1.4896280.

[58] R. O. Fox. A quadrature-based third-order moment method for dilute gas-particle flows. *Journal of Computational Physics*, 227:6313–6350, 2008. doi:10.1016/j.jcp.2008.03.014.

[59] J. P. Franc. Incubation time and cavitation erosion rate of work-hardening materials. *ASME Journal of Fluids Engineering*, 131:021303–1, 2009. doi:10.1115/1.3063646.

[60] C. W. Gear and I. G. Kevrekidis. Projective methods for stiff differential equations: Problems with gaps in their eigenvalue spectrum. *SIAM Journal on Scientific Computing*, 24:1091–1106, 2006. doi:10.1137/S1064827501388157.

[61] NASA Goddard Space Flight Center. How many stars in the Milky Way? URL: https://asd.gsfc.nasa.gov/blueshift/index.php/2015/07/22/how-many-stars-in-the-milky-way/.

[62] P. P. Gohil and R. P. Saini. Coalesced effect of cavitation and silt erosion in hydro turbines - A review. *Renewable and Sustainable Energy Reviews*, 33:280–289, 2014. doi:10.1016/j.rser.2014.01.075.

[63] A. Gonzáles. Measurement of areas on a sphere using Fibonacci and latitude-longitude lattices. *Mathematical Geosciences*, 42:49:1–19, 2010. doi:10.1007/s11004-009-9257-x.

[64] A. Gosman and E. Ioannides. Aspects of computer simulation of liquid-fuelled combustors. In *19th Aerospace Sciences Meeting*. AIAA, 1981. doi:10.2514/6.1981-323.

[65] H. Grein and A. Schachenmann. Solving problems of abrasion in hydroelectric machinery. *Water Power and Dam Construction*, 44:19–24, 1992. URL: https://www.researchgate.net/publication/293094121_Solving_problems_of_abrasion_in_hydroelectric_machinery.

[66] H. S. Grewal, S. Bhandari, and H. Singh. Parametric study of slurry-erosion of hydroturbine steels with and without detonation gun spray coatings using Taguchi technique. *Metallurgical and Materials Transactions A*, 43:3387, 2012. doi:10.1007/s11661-012-1148-y.

[67] H. S. Grewal, H. Singh, and E. S. Yoon. Interplay between erodent concentration and impingement angle for erosion in dilute water-sand flows. *Wear*, 332-333:1111–1119, 2015. doi:10.1016/j.wear.2015.02.039.

[68] V. Hadavi, N.H. Arani, and M. Papini. Numerical and experimental investigations of particle embedment during the incubation period in the solid particle erosion of ductile materials. *Tribology International*, 129:38–45, 2019. doi:10.1016/j.triboint.2018.08.013.

[69] V. Hadavi, C.E. Moreno, and M. Papini. Numerical and experimental analysis of particle fracture during solid particle erosion, Part I: Modeling and experimental verification. *Wear*, 356-357:135–145, 2016. doi:10.1016/j.wear.2016.03.008.

[70] V. Hadavi, C.E. Moreno, and M. Papini. Numerical and experimental analysis of particle fracture during solid particle erosion, Part II: Effect of incident angle, velocity and abrasive size. *Wear*, 356-357:146–157, 2016. doi:10.1016/j.wear.2016.03.009.

[71] A. Haider and O. Levenspiel. Drag coefficient and terminal velocity of spherical and non-spherical particles. *Powder Technology*, 58:63–70, 1989. doi:10.1016/0032-5910(89)80008-7.

[72] J. O. Hallquist. LS-DYNA Theory Manual. Technical report, Livermore Software Technology Corporation, 2006. URL: https://www.dynasupport.com/manuals/additional/ls-dyna-theory-manual-2005-beta/view.

[73] M. Hashish. A modeling study of metal cutting with abrassive waterjets. *Journal of Engineering Materials and Technology*, 106:88–100, 1984. doi:10.1115/1.3225682.

[74] X. He, H. Wei, J. Shi, J. Liu, S. Li, W. Chen, and X. Mo. Experimental measurement of bulk viscosity of water based on stimulated Brillouin scattering. *Optics Communications*, 285:4120–4124, 2012. doi:10.1016/j.optcom.2012.05.062.

[75] P. Henry. *Turbomachines hydrauliques: Choix illustré de réalisations marquantes*. Presses polytechniques et universitaires romandes, 1992. URL: https://www.ppur.org/produit/133/9782880742096/Turbomachines%20hydrauliques%20.

[76] J. S. Hesthaven. *Numerical Methods for Conservation Laws: From Analysis to Algorithms*. SIAM, 2018. URL: http://bookstore.siam.org/cs18/.

[77] D. Hietel, K. Steiner, and J. Struckmeier. A finite-volume particle method for compressible flows. *Mathematical Models and Methods in Applied Sciences*, 10:1363–1382, 2000. doi:10.1142/S0218202500000604.

[78] A. Higgins, J. C. Restrepo, L. J. Otero, J. C. Ortiz, and M. Conde. Vertical distribution of suspended sediment in the mouth area of the Magdalena River, Colombia. *Latin American Journal of Aquatic Research*, 45:724–736, 2017. doi:10.3856/vol45-issue4-fulltext-9.

[79] I. M. Hutchings and R. E. Winter. Particle erosion of ductile metals: A mechanism of material removal. *Wear*, 27:121–128, 1974. doi:10.1016/0043-1648(74)90091-X.

[80] J. M. Hyman. Patch dynamics for multiscale problems. *Computing in Science and Engineering*, 7:47–53, 2005. doi:10.1109/MCSE.2005.57.

[81] ICOLD. Sedimentation and sustainable use of reservoirs and river systems. Technical report, International Commission on Large Dams, Paris, 2009. URL: http://www.icold-cigb.org/userfiles/files/CIRCULAR/CL1793Annex.pdf.

[82] IPCC. *Global Warming of 1.5 °C: an IPCC special report on the impacts of global warming of 1.5 °C above pre-industrial levels and the related global greenhouse gas emission pathways, in the context of strengthening the global response to the threat of climate change, sustainable development, and efforts to eradicate poverty*. Intergovernmental Panel on Climate Change, 2018. URL: https://www.ipcc.ch/sr15/.

[83] E. Jahanbakhsh. *Simulation of silt erosion using particle-based methods*. PhD thesis, École Polytechnique Fédérale de Lausanne (EPFL), 2014. doi:10.5075/epfl-thesis-6284.

[84] E. Jahanbakhsh, A. Maertens, N. Quinlan, C. Vessaz, and F. Avellan. Exact finite volume particle method with spherical-support kernels. *Computer Methods in Applied Mechanics and Engineering*, 317:102–127, 2017. doi:10.1016/j.cma.2016.12.015.

[85] E. Jahanbakhsh, C. Vessaz, and F. Avellan. Silt motion simulation using finite volume particle method. *IOP Conference Series: Earth and Environmental Science*, 22:052015, 2014. doi:10.1088/1755-1315/22/5/052015.

[86] E. Jahanbakhsh, C. Vessaz, A. Maertens, and F. Avellan. Development of a finite volume particle method for 3-D fluid flow simulations. *Computer Methods in Applied Mechanics and Engineering*, 298:80–107, 2016. doi:10.1016/j.cma.2015.09.013.

[87] F. T. Johnson, E. N. Tinoco, and N. J. Yu. Thirty years of development and application of CFD at Boeing commercial airplanes, Seattle. *Computers & Fluids*, 34:1115–1151, 2005. doi:10.1016/j.compfluid.2004.06.005.

[88] G. R. Johnson and W. H. Cook. Fracture characteristics of three metals subjected to various strains, strain rates, temperatures and pressures. *Engineering Fracture Mechanics*, 21:31–48, 1985. doi:10.1016/0013-7944(85)90052-9.

[89] A. Karimi and R. K. Schmid. Ripple formation in solid-liquid erosion. *Wear*, 156:33–47, 1992. doi:10.1016/0043-1648(92)90142-U.

[90] M. Karplus. Nobel Lecture: Development of multiscale models for complex chemical systems. Technical report, The Norwegian Nobel Institute, 2013. URL: https://www.nobelprize.org/uploads/2018/06/karplus-lecture.pdf.

[91] M. Kato and B. E. Launder. The modelling of turbulent flow around stationary and vibrating square cylinders. In *9^{th} Symposium on Turbulent Shear Flows*. STSF, 1993. URL: https://www.researchgate.net/publication/247931894_The_Modelling_of_Turbulent_Flow_Around_Stationary_and_Vibrating_Square_Cylinders.

[92] M. E. Kavousanakis, R. Erban, A. G. Boudouvis, C. W. Gear, and I. G. Kevrekidis. Projective and coarse projective integration for problems with continuous symmetries. *Journal of Computational Physics*, 225:382–407, 2007. doi:10.1016/j.jcp.2006.12.003.

[93] H. Keck and M. Sick. Thirty years of numerical flow simulation in hydraulic turbomachines. *Acta Mechanica*, 201:211–229, 2008. doi:10.1007/s00707-008-0060-4.

[94] T. Kempe and J. Fröhlich. Collision modelling for the interface-resolved simulation of spherical particles in viscous fluids. *Journal of Fluid Mechanics*, 709:445–489, 2012. doi:10.1017/jfm.2012.343.

[95] I. G. Kevrekidis, C. W. Gear, and G. Hummer. Equation-free: The computer-aided analysis of complex multiscale systems. *American Institute of Chemical Engineers Journal*, 50:1346–1355, 2004. doi:10.1002/aic.10106.

[96] I. G. Kevrekidis, C. W. Gear, J. M. Hyman, P. G. Kevrekidis, O. Runborg, and C. Theodoropoulos. Equation-free, coarse-grained multiscale computation: enabling microscopic simulators to perform system-level analysis. *Communications in Mathematical Sciences*, 1:715–762, 2003. doi:10.4310/CMS.2003.v1.n4.a5.

[97] I. G. Kevrekidis and G. Samaey. Equation-free multiscale computation: Algorithms and applications. *Annual Review of Physical Chemistry*, 60:321–344, 2009. doi:10.1146/annurev.physchem.59.032607.093610.

[98] K. Khayrat and P. Jenny. A multi-scale network method for two-phase flow in porous media. *Journal of Computational Physics*, 342:194–210, 2017. doi:10.1016/j.jcp.2017.04.023.

[99] B. Kishor, G. P. Chaudhari, and S. K. Nath. Slurry erosion of thermo-mechanically processed 13Cr-4Ni stainless steel. *Tribology International*, 93:50–57, 2016. doi:10.1016/j.triboint.2015.08.048.

[100] The Kockmann Research Group at ETHZ. From atoms to the macroscale: the nonlocal quasicontinuum method. URL: http://www.mm.ethz.ch/research_QC.html.

[101] B. J. Kohn. Compilation of Hugoniot equations of state. Technical report, Air Force Weapons Laboratory, Kirtland Air Force Base, New Mexico, 1969. URL: http://www.dtic.mil/dtic/tr/fulltext/u2/852300.pdf.

[102] P. Koumoutsakos and J. Feigelman. Multiscale stochastic simulations of chemical reactions with regulated scale separation. *Journal of Computational Physics*, 244:290–297, 2013. doi:10.1016/j.jcp.2012.11.030.

[103] T. Kumashiro, S. Alimirzazadeh, A. Maertens, E. Jahanbakhsh, S. Leguizamón, F. Avellan, and K. Tani. Numerical investigation of the jet velocity profile and its influence on the Pelton turbine performance. *IOP Conference Series: Earth and Environmental Science*, 240:072006, 2019. doi:10.1088/1755-1315/240/7/072006.

[104] T. Kumashiro, H. Fukuhara, and K. Tani. Unsteady CFD simulation for bucket design optimization of Pelton turbine runner. *IOP Conference Series: Earth and Environmental Science*, 49:022003, 2016. doi:10.1088/1755-1315/49/2/022003.

[105] H. Kurtaran, M. Buyuk, and A. Eskandarian. Ballistic impact simulation of GT model vehicle door using finite element method. *Theoretical and Applied Fracture Mechanics*, 40:113–121, 2003. doi:10.1016/S0167-8442(03)00039-9.

[106] L. D. Landau and E. M. Lifshitz. *Fluid Mechanics*. Pergamon Press, New York, 1965. URL: http://users-phys.au.dk/srf/hydro/Landau+Lifschitz.pdf.

[107] L. E. Laverde. Evaluación del impacto de los embalses por retención de sedimentos sobre la morfología del cauce del río Magdalena. Technical report, Universidad de la Salle, Bogotá, Colombia, 2016. URL: http://repository.lasalle.edu.co/bitstream/handle/10185/18663/40102950_2016.pdf.

[108] S. L. Lee and C. W. Gear. Second-order accurate projective integrators for multiscale problems. *Journal of Computational and Applied Mathematics*, 201:258–274, 2007. doi:10.1016/j.cam.2006.02.018.

[109] S. Leguizamón, S. Alimirzazadeh, E. Jahanbakhsh, and F. Avellan. Multiscale simulation of erosive wear in a prototype-scale Pelton runner. *Submitted to Renewable Energy*, 2019.

[110] S. Leguizamón, E. Jahanbakhsh, S. Alimirzazadeh, A. Maertens, and F. Avellan. FVPM numerical simulation of the effect of particle shape and elasticity on impact erosion. *Wear*, 430-431:108–119, 2019. doi:10.1016/j.wear.2019.04.023.

[111] S. Leguizamón, E. Jahanbakhsh, S. Alimirzazadeh, A. Maertens, and F. Avellan. Multiscale simulation of the hydroabrasive erosion of a Pelton bucket: Bridging scales to improve the accuracy. *International Journal of Turbomachinery, Propulsion and Power*, 4:9, 2019. doi:10.3390/ijtpp4020009.

[112] S. Leguizamón, E. Jahanbakhsh, A. Maertens, S. Alimirzazadeh, and F. Avellan. A multi-scale model for sediment impact erosion simulation using the finite volume particle method. *Wear*, 392-393:202–212, 2017. doi:10.1016/j.wear.2017.10.002.

[113] S. Leguizamón, E. Jahanbakhsh, A. Maertens, S. Alimirzazadeh, and F. Avellan. A multi-scale model for the simulation of sediment impact erosion of metallic targets using the finite volume particle method. In *12^{th} International SPHERIC Workshop*, Ourense, ES, 2017.

[114] S. Leguizamón, E. Jahanbakhsh, A. Maertens, S. Alimirzazadeh, and F. Avellan. Multiscale simulation with projective integration of the erosion process of a Pelton bucket using the finite volume particle method. In *13^{th} International SPHERIC Workshop*, Galway, IR, 2018.

[115] S. Leguizamón, E. Jahanbakhsh, A. Maertens, S. Alimirzazadeh, and F. Avellan. Simulation of the hydroabrasive erosion of a bucket: A multiscale model with projective integration to circumvent the spatio-temporal scale separation. *IOP Conference Series: Earth and Environmental Science*, 240:072014, 2019. doi:10.1088/1755-1315/240/7/072014.

[116] S. Leguizamón, E. Jahanbakhsh, A. Maertens, C. Vessaz, S. Alimirzazadeh, and F. Avellan. Impact erosion prediction using the finite volume particle method with improved constitutive models. *IOP Conference Series: Earth and Environmental Science*, 49:122010, 2016. doi:10.1088/1755-1315/49/12/122010.

[117] S. Leguizamón, C. Ségoufin, P. Hai-Trieu, and F. Avellan. On the efficiency alteration mechanisms due to cavitation in Kaplan turbines. *ASME Journal of Fluids Engineering*, 139-6:0613011, 2017. doi:10.1115/1.4035928.

[118] A. V. Levy and P. Chik. The effects of erodent composition and shape on the erosion of steel. *Wear*, 89:151–162, 1983. doi:10.1016/0043-1648(83)90240-5.

[119] M. Li, D. Wilkinson, and K. Patchigolla. Comparison of particle size distributions measured using different techniques. *Particulate Science and Technology*, 23:265–284, 2005. doi:10.1080/02726350590955912.

[120] S. Li. Cavitation enhancement of silt erosion - An envisaged micro model. *Wear*, 260:1145–1150, 2006. doi:10.1016/j.wear.2005.07.002.

[121] W. Y. Li, J. Wang, H. Zhu, and C. Huang. On ultrahigh velocity micro-particle impact on steels – A multiple impact study. *Wear*, 309:52–64, 2014. doi:10.1016/j.wear.2013.10.011.

[122] W. Y. Li, J. Wang, H. Zhu, H. Li, and C. Huang. On ultrahigh velocity micro-particle impact on steels – A single impact study. *Wear*, 305:216–227, 2013. doi:10.1016/j.wear.2013.06.011.

[123] S. Lin, I. J. Hsieh, K. M. Huang, and C. H. Wang. Influence of the Yangtze river and grain size on the spatial variations of heavy metals and organic carbon in the East China Sea continental shelf sediments. *Chemical Geology*, 182:377–394, 2002. doi:10.1016/S0009-2541(01)00331-X.

[124] Y. F. Liu, J. Li, Z. M. Zhang, X. H. Hu, and W. J. Zhang. Experimental comparison of five friction models on the same test-bed of the micro stick-slip motion system. *Mechanical Sciences*, 6:15–28, 2015. doi:10.5194/ms-6-15-2015.

[125] Z. G. Liu, S. Wan, V. B. Nguyen, and Y. W. Zhang. A numerical study on the effect of particle shape on the erosion of ductile materials. *Wear*, 313:135–142, 2014. doi:10.1016/j.wear.2014.03.005.

[126] I. Llanos, J. A. Villar, I. Urresti, and P. J. Arrazola. Finite element modeling of oblique machining using an arbitrary Lagrangian-Eulerian formulation. *Machining Science and Technology*, 13:385–406, 2009. doi:10.1080/10910340903237921.

[127] F. Lucci, A. Ferrante, and S. Elghobashi. Modulation of isotropic turbulence by particles of Taylor length-scale size. *Journal of Fluid Mechanics*, 650:5–55, 2010. doi:10.1017/S0022112009994022.

[128] A. Maertens, E. Jahanbakhsh, and F. Avellan. A novel approach to surface tension modelling with the finite volume particle method. *Computer Methods in Applied Mechanics and Engineering*, 341:409–428, 2018. doi:10.1016/j.cma.2018.02.010.

[129] M. Mandø, M. F. Lightstone, L. Rosendahl, C. Yin, and H. Sørensen. Turbulence modulation in dilute particle-laden flow. *International Journal of Heat and Fluid Flow*, 30:331–338, 2009. doi:10.1016/j.ijheatfluidflow.2008.12.005.

[130] B. S. Mann. High-energy particle impact wear resistance of hard coatings and their application in hydroturbines. *Wear*, 237:140–146, 2000. doi:10.1016/S0043-1648(99)00310-5.

[131] R. Mei. An approximate expression for the shear lift force on a spherical particle at finite Reynolds number. *International Journal of Multiphase Flow*, 18:145–147, 1992. doi:10.1016/0301-9322(92)90012-6.

[132] H. C. Meng and K. C. Ludema. Wear models and predictive equations: Their form and content. *Wear*, 181-183:443–457, 1995. doi:10.1016/0043-1648(95)90158-2.

[133] F. R. Menter. Zonal two equation k-ω turbulence models for aerodynamic flows. In *24th Fluid Dynamics, Plasmadynamics and Lasers Conference*. AIAA, 1993. doi:10.2514/6.1993-2906.

[134] F. R. Menter and Y. Egorov. The scale-adaptive simulation method for unsteady turbulent flow predictions. Part 1: Theory and model description. *Flow, Turbulence and Combustion*, 85:113–138, 2010. doi:10.1007/s10494-010-9264-5.

[135] G. V. Messa and S. Malavasi. The effect of sub-models and parametrizations in the simulation of abrasive jet impingement tests. *Wear*, 370-371:59–72, 2017. doi:10.1016/j.wear.2016.10.022.

[136] G. V. Messa and S. Malavasi. A CFD-based method for slurry erosion prediction. *Wear*, 398-399:127–145, 2018. doi:10.1016/j.wear.2017.11.025.

[137] G. V. Messa, M. Malin, and S. Malavasi. Numerical prediction of fully-suspended slurry flow in horizontal pipes. *Powder Technology*, 256:61–70, 2014. doi:10.1016/j.powtec.2014.02.005.

[138] G. V. Messa, S. Mandelli, and S. Malavasi. Hydro-abrasive erosion in Pelton turbine injectors: A numerical study. *Renewable Energy*, 130:474–488, 2019. doi:10.1016/j.renene.2018.06.064.

[139] D. Mohr. Split Hopkinson Bar Systems: Lecture Notes. Technical report, Department of Mechanical and Process Engineering, ETH Zürich, 2015. URL: https://www.ethz.ch/content/dam/ethz/special-interest/mavt/virtual-manufacturing/ivp-dam/Studium/Vorlesungsunterlagen/Dynamic%20Behavior%20of%20Materials%20and%20Structures/Downloads/Lecture2/Lecture%202.pdf.

[140] J. F. Molinari and M. Ortiz. A study of solid-particle erosion of metallic targets. *International Journal of Impact Engineering*, 27:347–358, 2002. doi:10.1016/S0734-743X(01)00055-0.

[141] J. J. Monaghan. Smoothed particle hydrodynamics. *Reports on Progress in Physics*, 68:1703–1759, 2005. doi:10.1088/0034-4885/68/8/R01.

[142] L. F. Mori, S. Lee, Z. Y. Xue, A. Vaziri, D. T. Queheillalt, K. P. Dharmasena, H. N. G. Wadley, J. W. Hutchinson, and H. D. Espinosa. Deformation and fracture modes of sandwich structures subjected to underwater impulsive loads. *Journal of Mechanics of Materials and Structures*, 2:1982–2006, 2007. doi:10.2140/jomms.2007.2.1981.

[143] S. M. Nahvi, P. H. Shipway, and D. G. McCartney. Particle motion and modes of wear in the dry sand-rubber wheel abrasion test. *Wear*, 267:2083–2091, 2009. doi:10.1016/j.wear.2009.08.013.

[144] Y. Nakanishi and T. Kubota. Scale effect of jet interference in multinozzle Pelton turbines. In E. Cabrera, V. Espert, and F. Martínez, editors, *Hydraulic Machinery and Cavitation*, pages 333–341. Springer Dordrecht, 1996. doi:10.1007/978-94-010-9385-9_33.

[145] H. P. Neopane. *Sediment erosion in hydro turbines*. PhD thesis, Norwegian University of Science and Technology (NTNU), 2010. URL: http://hdl.handle.net/11250/233519.

[146] R. M. Nestor, M. Basa, M. Lastiwka, and N. J. Quinlan. Extension of the finite volume particle method to viscous flow. *Journal of Computational Physics*, 228:1733–1749, 2009. doi:10.1016/j.jcp.2008.11.003.

[147] I. Newton. *Philosophiae Naturalis Principia Mathematica*. Jussu Societatis Regiæ ac Typis Josephi Streater, 1687.

[148] V. Nguyen, Q. Nguyen, Y. Zhang, C. Lim, and B. Khoo. Effect of particle size on erosion characteristics. *Wear*, 348-349:126–137, 2016. doi:10.1016/j.wear.2015.12.003.

[149] V. B. Nguyen, Q. B. Nguyen, Z. G. Liu, S. Wan, C. Y. H. Lim, and Y. W. Zhang. A combined numerical-experimental study on the effect of surface evolution on the water-sand multiphase flow characteristics and the material erosion behavior. *Wear*, 319:96–109, 2014. doi:10.1016/j.wear.2014.07.017.

[150] T. Nozaki. Estimation of repair cycle of turbine due to abrasion caused by suspended sand and determination of desilting basin capacity. Technical report, Japan International Cooperation Agency, Tokyo, 1990.

[151] National Institute of Standards and Technology. Thermophysical properties of fluid systems, 2018. URL: https://webbook.nist.gov/chemistry/fluid/.

[152] Y. I. Oka, , K. Okamura, and T. Yoshida. Practical estimation of erosion damage caused by solid particle impact: Part 1: Effects of impact parameters on a predictive equation. *Wear*, 259:95–101, 2005. doi:10.1016/j.wear.2005.01.039.

[153] Y. I. Oka, H. Ohnogi, T. Hosokawa, and M. Matsumura. The impact angle dependence of erosion damage caused by solid particle impact. *Wear*, 203-204:573–579, 1997. doi:10.1016/S0043-1648(96)07430-3.

[154] G. Ozturk. Numerical and experimental investigation of perforation of ST-37 steel plates by oblique impact. Technical report, Middle East Technical University, 2010. URL: http://citeseerx.ist.psu.edu/viewdoc/download?doi=10.1.1.632.5548&rep=rep1&type=pdf.

[155] M. K. Padhy and R. P. Saini. A review on silt erosion in hydro turbines. *Renewable and Sustainable Energy Reviews*, 12:1974–1987, 2008. doi:10.1016/j.rser.2007.01.025.

[156] M. K. Padhy and R. P. Saini. Effect of size and concentration of silt particles on erosion of Pelton turbine buckets. *Energy*, 34:1477–1483, 2009. doi:10.1016/j.energy.2009.06.015.

[157] M. K. Padhy and R. P. Saini. Study of silt erosion mechanism in Pelton turbine buckets. *Energy*, 39:286–293, 2012. doi:10.1016/j.energy.2012.01.015.

[158] E. Parkinson. EPFL hydraulic turbomachines course: Design of Pelton turbines. Technical report, Andritz Hydro, Vevey, Switzerland, 2018.

[159] A. Passalacqua and R. O. Fox. Simulation of mono- and bidisperse gas-particle flow in a riser with a third-order quadrature-based moment method. *Industrial & Engineering Chemistry Research*, 52:187–198, 2013. doi:10.1021/ie300424m.

[160] A. Perrig. *Hydrodynamics of the free surface flow in Pelton turbine buckets*. PhD thesis, École Polytechnique Fédérale de Lausanne (EPFL), 2007. doi:10.5075/epfl-thesis-3715.

[161] P. Peyre, I. Chaieb, and C. Braham. FEM calculation of residual stresses induced by laser shock processing in stainless steels. *Modelling and Simulation in Materials Science and Engineering*, 15:205–221, 2007. doi:10.1088/0965-0393/15/3/002.

[162] S. B. Pope. *Turbulent Flows*. Cambridge University Press, 2000. doi:10.1017/CBO9780511840531.

[163] C. M. Preece and N. H. Macmillan. Erosion. *Annual Review of Material Science*, 7:95–121, 1977. doi:10.1146/annurev.ms.07.080177.000523.

[164] N. J. Quinlan, L. Lobovsky, and R. M. Nestor. Development of the meshless finite volume particle method with exact and efficient calculation of interparticle area. *Computer Physics Communications*, 185:1554–1563, 2014. doi:10.1016/j.cpc.2014.02.017.

[165] A. Rai, A. Kumar, and T. Staubli. Hydro-abrasive erosion in Pelton buckets: Classification and field study. *Wear*, 392-393:8–20, 2017. doi:10.1016/j.wear.2017.08.016.

[166] K. T. Ramesh. High strain rate and impact experiments. In W. Sharpe, editor, *Springer Handbook of Experimental Solid Mechanics*. Springer US, 2008. URL: https://www.springer.com/cda/content/document/cda_downloaddocument/9780387268835-c2.pdf.

[167] REN21. Renewables 2018 global status report. Technical report, Renewable Energy Policy Network for the 21st Century (REN21) Secretariat, Paris, 2018. URL: http://www.ren21.net/wp-content/uploads/2018/06/17-8652_GSR2018_FullReport_web_final_.pdf.

[168] C. M. Rhie and W. L. Chow. Numerical study of the turbulent flow past an airfoil with trailing edge separation. *AIAA Journal*, 21:1525–1532, 1983. doi:10.2514/3.8284.

[169] P. Rosakis, A. J. Rosakis, G. Ravichandran, and J. Hodowany. A thermodynamic internal variable model for the partition of plastic work into heat and stored energy in metals. *Journal of the Mechanics and Physics of Solids*, 48:581–607, 2000. doi:10.1016/S0022-5096(99)00048-4.

[170] A. Ruiz-Angulo and M. L. Hunt. Measurement of the coefficient of restitution for particle collisions with ductile surfaces in a liquid. *Granular Matter*, 12:185–191, 2010. doi:10.1007/s10035-010-0166-y.

[171] R. I. Saye and J. A. Sethian. Multiscale modeling of membrane rearrangement, drainage, and rupture in evolving foams. *Science*, 340:720–724, 2013. doi:10.1126/science.1230623.

[172] A. Schleiss, G. De Cesare, and J. Althaus. Verlandung der stauseen gefährdet die nachhaltige nutzung der wasserkraft (Sedimentation of reservoirs compromises the sustaninable use of hydropower). *Wasser Energy Luft*, 102:31–40, 2010. URL: https://infoscience.epfl.ch/record/147714/files/Schleiss_DeCesare_Jenzer_wel_2010_Verlandung.pdf.

[173] H. Schlichting and K. Gersten. *Boundary-Layer Theory*. Springer-Verlag Berlin Heidelberg, 2017. doi:10.1007/978-3-662-52919-5.

[174] G. L. Sheldon and I. Finnie. On the ductile behavior of nominally brittle materials during erosive cutting. *Journal of Engineering for Industry*, 88:387–392, 1966. doi:10.1115/1.3672666.

[175] P. Shewmon and G. Sundararajan. The erosion of metals. *Annual Review of Material Science*, 13:301–318, 1983. doi:10.1146/annurev.ms.13.080183.001505.

[176] R. C. Shivamurthy, M. Kamaraj, R. Nagarajan, S. M. Shariff, and G. Padmanabham. Influence of microstructure on slurry erosive wear characteristics of laser surface alloyed 13Cr–4Ni steel. *Wear*, 267:204–212, 2009. doi:10.1016/j.wear.2008.12.027.

[177] R. Singh, S. K. Tiwari, and S. K. Mishra. Cavitation erosion in hydraulic turbine components and mitigation by coatings: Current status and future needs. *Journal of Materials Engineering and Performance*, 21:1539–1551, 2012. doi:10.1007/s11665-011-0051-9.

[178] G. W. Stachowiak and A. W. Batchelor. *Engineering Tribology*. Butterworth-Heinemann, 2014. doi:10.1016/C2011-0-07515-4.

[179] K. Sugiyama, K. Harada, and S. Hattori. Influence of impact angle of solid particles on erosion by slurry jet. *Wear*, 265:713–720, 2008. doi:10.1016/j.wear.2008.01.020.

[180] M. Takaffoli and M. Papini. Material deformation and removal due to single particle impacts on ductile materials using smoothed particle hydrodynamics. *Wear*, 274-275:50–59, 2012. doi:10.1016/j.wear.2011.08.012.

[181] B. S. Thapa, B. Thapa, and O. G. Dahlhaug. Empirical modelling of sediment erosion in Francis turbines. *Energy*, 41:386–391, 2012. doi:10.1016/j.energy.2012.02.066.

[182] TOP500. 50^{th} edition of the TOP500 Supercomputers list: November 2017. Technical report, TOP500, 2017. URL: https://www.top500.org/lists/2017/11/.

[183] TOP500. 52^{nd} edition of the TOP500 Supercomputers list: November 2018. Technical report, TOP500, 2018. URL: https://www.top500.org/lists/2018/11/.

[184] TOP500. 52^{nd} edition of the TOP500 Supercomputers list: Piz Daint. Technical report, TOP500, 2018. URL: https://www.top500.org/system/177824.

[185] A. A. Torrance. Modelling abrasive wear. *Wear*, 258:281–293, 2005. doi:10.1016/j.wear.2004.09.065.

[186] D. Umbrello, R. M'Saoubi, and J.C. Outeiro. The influence of Johnson–Cook material constants on finite element simulation of machining of AISI 316L steel. *International Journal of Machine Tools and Manufacture*, 47:462–470, 2007. doi:10.1016/j.ijmachtools.2006.06.006.

[187] A. Uzi and A. Levy. Energy absorption by the particle and the surface during impact. *Wear*, 404-405:92–110, 2018. doi:10.1016/j.wear.2018.03.007.

[188] C. Vessaz. *Finite particle flow simulation of free jet deviation by rotating Pelton buckets*. PhD thesis, École Polytechnique Fédérale de Lausanne (EPFL), 2015. doi:10.5075/epfl-thesis-6470.

[189] C. Vessaz, P. Cerrutti, and F. Avellan. LMH NeXtScale using SLURM. Technical report, Laboratory for Hydraulic Machines, 2014.

[190] C. Vessaz, E. Jahanbakhsh, and F. Avellan. FPM simulations of a high-speed water jet - Validation with CFD and experimental results. In P. Gourbesville, J. Cunge, and G. Caigneart, editors, *Advances in Hydroinformatics*, Springer Hydrogeology, pages 419–431. Springer Singapore, 2013. doi:10.1007/978-981-4451-42-0_34.

[191] C. Vessaz, E. Jahanbakhsh, and F. Avellan. Flow simulation of jet deviation by rotating Pelton buckets using finite volume particle method. *ASME Journal of Fluids Engineering*, 137:074501, 2015. doi:10.1115/1.4029839.

[192] C. S. von Bartheld, J. Bahney, and S. Herculano-Houzel. The search for true numbers of neurons and glial cells in the human brain: A review of 150 years of cell counting. *Journal of Comparative Neurology*, 524:3865–3895, 2016. doi:10.1002/cne.24040.

[193] J. H. Walther, M. Praprotnik, E. M. Kotsalis, and P. Koumoutsakos. Multiscale simulation of water flow past a C-540 fullerene. *Journal of Computational Physics*, 231:2677–2681, 2012. doi:10.1016/j.jcp.2011.12.015.

[194] M. H. Wang, C. Huang, K. Nandakumar, P. Minev, J. Luo, and S. Chiovelli. Computational fluid dynamics modelling and experimental study of erosion in slurry jet flows. *International Journal of Computational Fluid Dynamics*, 23:155–172, 2009. doi:10.1080/10618560902744412.

[195] X. Wang and J. Shi. Validation of Johnson-Cook plasticity and damage model using impact experiment. *International Journal of Impact Engineering*, 60:67–75, 2013. doi:10.1016/j.ijimpeng.2013.04.010.

[196] Y. F. Wang and Z. G. Yang. Finite element model of erosive wear on ductile and brittle materials. *Wear*, 265:871–878, 2008. doi:10.1016/j.wear.2008.01.014.

[197] Y. F. Wang and Z. G. Yang. A coupled finite element and meshfree analysis of erosive wear. *Tribology International*, 42:373–377, 2009. doi:10.1016/j.triboint.2008.07.009.

[198] S. Y. Yang, H. S. Jung, M. S. Choi, and C. X. Li. The rare earth element compositions of the Changjiang (Yangtze) and Huanghe (Yellow) river sediments. *Earth and Planeraty Science Letters*, 201:407–419, 2002. doi:10.1016/S0012-821X(02)00715-X.

[199] B. Yildirim and S. Muftu. Simulation and analysis of the impact of micron-scale particles onto a rough surface. *International Journal of Solids and Structures*, 49:1375–1386, 2012. doi:10.1016/j.ijsolstr.2012.02.018.

[200] B. Yildirim, S. Muftu, and A. Gouldstone. Modeling of high velocity impact of spherical particles. *Wear*, 270:703–713, 2011. doi:10.1016/j.wear.2011.02.003.

[201] M. Yousefzadeh and I. Battiato. Physics-based hybrid method for multiscale transport in porous media. *Journal of Computational Physics*, 344:320–338, 2017. doi:10.1016/j.jcp.2017.04.055.

[202] J. Zhang, B. S. McLaury, and S. A. Shirazi. Application and experimental validation of a CFD based erosion prediction procedure for jet impingement geometry. *Wear*, 394-395:11–19, 2018. doi:10.1016/j.wear.2017.10.001.

[203] Z. Zhang. *Pelton Turbines*. Springer International Publishing AG Switzerland, 2016. doi:10.1007/978-3-319-31909-4.

[204] Z. Zhang and Q. Chen. Comparison of the Eulerian and Lagrangian methods for predicting particle transport in enclosed spaces. *Atmospheric Environment*, 41:5236–5248, 2007. doi:10.1016/j.atmosenv.2006.05.086.

Sebastián Leguizamón

Avenue du Grammont 6
1007 Lausanne, Switzerland
(+41) 76 804 0289
sebastian.legui@epfl.ch
Born on February 22, 1989
Colombian national, married

Education

2015–2019 **Ph.D. in Energy**, *École Polytechnique Fédérale de Lausanne (EPFL), Laboratory for Hydraulic Machines*.
Thesis: Multiscale modeling and simulation of erosive wear in Pelton turbines.
Research done in the context of the project GPU-SPHEROS, in cooperation with General Electric Renewable Energy. The main achievement was the development and validation of a computational model with applications to the design optimization of Pelton turbines.

2012–2014 **M.Sc. in Mechanical Engineering**, *EPFL*.
GPA: 5.72/6.00.
Thesis: Assessment and validation of numerical simulation methodologies for the prediction of cavitation in hydraulic turbomachines. Executed during an internship at General Electric.
Semester projects:
- Numerical simulation of wind turbine wakes: Evaluation of turbulence models
- Temperature estimation in luminescent laser-generated cavitation bubbles
- Energy integration of a polypropylene production plant

2007–2012 **B.Sc. in Mechanical Engineering**, *Universidad de los Andes (Uniandes)*, Bogotá.
GPA: 4.44/5.00, First-Class Honours.
Thesis: Parametric simulation of unsteady flapping-wing aerodynamics.

Experience

2015–2019 **Doctoral Assistant at the Laboratory for Hydraulic Machines, EPFL**.
Apart from the computational model development and implementation associated with my Ph.D. investigation, my responsibilities included: writing research proposals, most of which succeded in securing additional funding; serving as Teaching Assistant for the Master's course on Hydraulic Turbomachines, which involved one-on-one teaching, writing and correcting exams; communicating effectively through reports and presentations.

2014, 6 months **Intern at General Electric Renewable Energy (Formerly Alstom Power)**.
With the goal of assessing and validating two cavitation simulation methodologies, my responsabilities went from mesh generation to results analysis and reporting. The excellent outcomes improved the company's simulation methodology and were published in a journal article.

2011–2013 **Course Assistant at EPFL and Uniandes**,
Advanced Energetics (Master's at EPFL), Analysis III and General Physics I (Bachelor's at EPFL), and Energy Conversion Systems (Bachelor's at Uniandes).
Responsible of the exercise sessions, including one-on-one teaching and exercise corrections.

2007–2011, part-time 40% **Show Jumping Horse Trainer at El Rancho Country Club**.
Responsible for the daily training of several horses, with distinguished results on national competitions. Time management way key to achieving my Bachelor's degree simultaneously.

Computer Skills

Advanced C++, CFX, MATLAB, Fluent, Paraview
Intermediate Linux environment, AutoGrid, FINE/Turbo, ICEM, LaTeX, MS Office
Beginner CUDA, Python, OpenFOAM, Adobe Creative Suite

Languages

Spanish	Native language
English	Proficient (C2)
French	Upper intermediate/Advanced (B2/C1)
German	Beginner (A1)

Awards and Distinctions

2019 Best Paper Award, 13$^{\text{th}}$ European Conference on Turbomachinery Fluid Dynamics & Thermodynamics, Lausanne, Switzerland.

2019 Young Researcher Award Runner-Up, International Hydropower Association.

2017 EPFL ACCES Visualization Contest: Third prize in the Dynamic Category and Special Mention for Computational Thinking.

2017 Best Poster Award in engineering, PASC17 Conference, Lugano, Switzerland.

2012 Scholarship for graduate studies abroad, granted by Colfuturo.

2012 B.Sc. Cum laude distinction: Granted to students whose GPA is among the highest 3% of all the Engineering Faculty graduates of the previous 5 years.

2012 Top 0.2% in the National Standardized Test after higher education (ECAES).

2007 Top 0.1% in the National Standardized Test before higher education (ICFES).

Additional Academic Activities

2017, 2019 **Reviewer**, *Wear*, monthly journal published by Elsevier.

2018 **Reviewer**, *29th Symposium on Hydraulic Machinery and Systems*, Kyoto, Japan.
Organized by The International Association for Hydro-Environment Engineering and Research.

2018 **Presenter**, *Short Course on Hydraulic Machines Engineering: Simulating hydroabrasive erosion with SPHEROS*, Lausanne, Switzerland.
Organized by the Laboratory for Hydraulic Machines, EPFL.

2017 **Training Program**, *Ph.D. School: Meshfree and immersed boundary methods for fluid-structure interaction*, Lugano, Switzerland.
Organized by the Swiss Graduate Program on Foundations in Mathematics and Informatics for Computer Simulations in Science and Engineering (FOMICS).

2017 **Jury Member**, *Master's thesis: Influence of the flow characteristics and profile geometry on the cavitation of a Darrieus turbine*, Nicolas Vargas Cabrera, Uniandes.

2016 **Conference Organization Volunteer**, *HYDRO 2016*, Montreux, Switzerland.
Organized by The International Journal on Hydropower & Dams.

2016 **Training Program**, *Ph.D. School: Understanding the transition needed to reach the Swiss Energy Strategy 2050*, Leukerbad, Switzerland.
Organized by the Swiss Competence Center for Energy Research (SCCER).

2016 **Co-adviser**, *Bachelor's thesis: CFD study of the cavitating flow in a Venturi tube*, Luis Niño Forero, Uniandes.

2014 **Presenter**, *Seminar on Computational Mechanics: Assessment and validation of methodologies for cavitation simulation in hydraulic turbines*, Bogotá, Colombia.
Organized by the Computational Mechanics group at Uniandes.

Publications

Journal Articles

1. **S. Leguizamón**, S. Alimirzazadeh, E. Jahanbakhsh, F. Avellan, Multiscale simulation of erosive wear in a prototype-scale Pelton runner, *Submitted to Renewable Energy*.
2. S. Alimirzazadeh, T. Kumashiro, **S. Leguizamón**, E. Jahanbakhsh, A. Maertens, C. Vessaz, K. Tani, F. Avellan, GPU-accelerated numerical analysis of jet interference in a six-jet Pelton turbine using finite volume particle method, *Submitted to Renewable Energy*.
3. **S. Leguizamón**, E. Jahanbakhsh, S. Alimirzazadeh, A. Maertens, F. Avellan, FVPM numerical simulation of the effect of particle shape and elasticity on impact erosion, *Wear* 430-431 (2019) 108–119. doi:10.1016/j.wear.2019.04.023.
4. **S. Leguizamón**, E. Jahanbakhsh, S. Alimirzazadeh, A. Maertens, F. Avellan, Multiscale simulation of the hydroabrasive erosion of a Pelton bucket: Bridging scales to improve the accuracy, *International Journal of Turbomachinery, Propulsion and Power* 4 (2019) 9. doi:10.3390/ijtpp4020009.
5. S. Alimirzazadeh, E. Jahanbakhsh, A. Maertens, **S. Leguizamón**, F. Avellan, GPU-accelerated 3-D finite volume particle method, *Computers & Fluids* 171 (2018) 79–93. doi:10.1016/j.compfluid.2018.05.030.
6. **S. Leguizamón**, E. Jahanbakhsh, A. Maertens, S. Alimirzazadeh, F. Avellan, A multiscale model for sediment impact erosion simulation using the finite volume particle method, *Wear* 392-393 (2017) 202–212. doi:10.1016/j.wear.2017.10.002.
7. **S. Leguizamón**, C. Ségoufin, P. Hai-Trieu, F. Avellan, On the efficiency alteration mechanisms due to cavitation in Kaplan turbines, *ASME Journal of Fluids Engineering* 139-6 (2017) 0613011. doi:10.1115/1.4035928.

Conferences with Online Proceedings

1. **S. Leguizamón**, E. Jahanbakhsh, A. Maertens, S. Alimirzazadeh, F. Avellan, Simulation of the hydroabrasive erosion of a bucket: A multiscale model with projective integration to circumvent the spatio-temporal scale separation, in: 29^{th} *IAHR Symposium on Hydraulic Machinery and Systems*, IOP Conference Series: Earth and Environmental Science Vol. 240, Kyoto, JP, 2019. doi:10.1088/1755-1315/240/7/072014.
2. S. Alimirzazadeh, T. Kumashiro, **S. Leguizamón**, A. Maertens, E. Jahanbakhsh, K. Tani, F. Avellan, GPU-accelerated Pelton turbine simulation using finite volume particle method coupled with linear eddy viscosity models, in: 29^{th} *IAHR Symposium on Hydraulic Machinery and Systems*, IOP Conference Series: Earth and Environmental Science Vol. 240, Kyoto, JP, 2019. doi:10.1088/1755-1315/240/7/072018.
3. T. Kumashiro, S. Alimirzazadeh, A. Maertens, E. Jahanbakhsh, **S. Leguizamón**, F. Avellan, K. Tani, Numerical investigation of the jet velocity profile and its influence on the Pelton turbine performance, in: 29^{th} *IAHR Symposium on Hydraulic Machinery and Systems*, IOP Conference Series: Earth and Environmental Science Vol. 240, Kyoto, JP, 2019. doi:10.1088/1755-1315/240/7/072006.
4. **S. Leguizamón**, E. Jahanbakhsh, A. Maertens, C. Vessaz, S. Alimirzazadeh, F. Avellan, Impact erosion prediction using the finite volume particle method with improved constitutive models, in: 28^{th} *IAHR Symposium on Hydraulic Machinery and Systems*, IOP Conference Series: Earth and Environmental Science Vol. 49, Grenoble, FR, 2016. doi:10.1088/1755-1315/49/12/122010.
5. **S. Leguizamón**, O. López, Parametric study of low Reynolds number flapping wing aerodynamics, in: 21^{th} *AIAA Computational Fluid Dynamics Conference*, American Institute of Aeronautics and Astronautics, San Diego, CA, U.S.A., 2013. doi:10.2514/6.2013-2954.
6. O. López, N. Ochoa, J. Mahecha, **S. Leguizamón**, J. Escobar, S. Ramirez, R. Jimenez, A. Giraldo, C. Silva, Numerical simulation of NASA trap-wing model as a colombian contribution to the high-lift prediction workshop, in: 30^{th} *AIAA Applied Aerodynamics Conference*, American Institute of Aeronautics and Astronautics, New Orleans, LA, U.S.A., 2012. doi:10.2514/6.2012-2921.

Ce document a été imprimé au Centre d'impression EPFL,
imprimerie climatiquement neutre, certifiée myClimate.